

# The Relation between Defect Interactions, Local Structure and Oxygen Ion Conductivity in the Bulk of Doped Ceria

Von der Fakultät für Mathematik, Informatik und Naturwissenschaften der  
RWTH Aachen University zur Erlangung des akademischen Grades eines  
Doktors der Naturwissenschaften genehmigte Dissertation

vorgelegt von

Julius Rütger Köttgen M.Sc.

geb. Berghoff

aus Recklinghausen

Berichter: Universitätsprofessor Dr. Manfred Martin  
apl. Professor Dr. Peter C. Schmidt  
apl. Professor Dr. Ullrich Englert

Tag der mündlichen Prüfung: 07.02.2017

Diese Dissertation ist auf den Internetseiten der Universitätsbibliothek online verfügbar.



## Abstract

### **The Relation between Defect Interactions, Local Structure and Oxygen Ion Conductivity in the Bulk of Doped Ceria**

For the development of solid oxide fuel cells (SOFC) and high-temperature electrolysis an electrolyte, which has a high oxygen ion conductivity and a low electronic conductivity, is required. Potential candidates are fluorite-structured oxides such as doped zirconia ( $\text{ZrO}_2$ ) and doped ceria ( $\text{CeO}_2$ ). The latter allows a reduction in the operating temperature from 900 °C to 600 °C, and is, therefore, the main focus of this thesis. The central aim of this thesis is the detailed understanding of the relationship between defect interactions, the local structure (microscopic level) and the macroscopic oxygen ion conductivity in the bulk of fluorite-structured oxides. By combining *ab initio* density functional theory with Kinetic Monte Carlo simulations, both the local structure and the oxygen ion conductivity are predicted as a function of the doping concentration. These results are verified by accompanying experiments. In this way, a deeper understanding of the underlying mechanism is obtained in order to make better predictions about material properties. Therefore, this work provides a contribution to the study of sustainable and efficient energy storages.

### **Zusammenhang zwischen Defekt-Wechselwirkungen, Lokaler Struktur und Sauerstoffionenleitung in der Bulk Domäne von Dotiertem Ceroxid**

Im Rahmen der Entwicklung von Festoxidbrennstoffzellen (SOFC) und der Hochtemperaturelektrolyse werden Elektrolyte mit einer hohen Sauerstoffionenleitfähigkeit und geringen elektronischen Leitfähigkeit benötigt. Potenzielle Kandidaten sind fluoritstrukturierte Oxide wie dotierte Zirkoniumoxide ( $\text{ZrO}_2$ ) und dotierte Ceroxide ( $\text{CeO}_2$ ), wobei Letztere eine Verringerung der Betriebstemperatur von 900 °C auf 600 °C ermöglichen und im Mittelpunkt dieser Arbeit stehen. Das zentrale Ziel der Arbeit ist es, den Zusammenhang zwischen Defektwechselwirkungen und der lokalen Struktur (mikroskopische Ebene) sowie der makroskopischen Sauerstoffionenleitung in der bulk Domäne von fluoritstrukturierten Oxiden im Detail zu verstehen. Durch Kombination von *ab initio* Dichtefunktionaltheorie-Methoden mit Kinetic Monte Carlo-Simulationen wird sowohl die lokale Struktur als auch die Sauerstoffionenleitfähigkeit in Abhängigkeit von der Dotierungskonzentration vorhergesagt. Diese Ergebnisse werden durch begleitende Experimente überprüft. Auf diese Weise wird ein tieferes Verständnis für zugrunde liegende Mechanismen gewonnen, um bessere Vorhersagen über Materialeigenschaften treffen zu können. Diese Arbeit leistet damit einen Beitrag zur Erforschung einer nachhaltigen und effizienten Energiespeicherung.

This work has been carried out at the Chair of Physical Chemistry I of the Institute of Physical Chemistry (RWTH Aachen University) under the supervision of Prof. Dr. Manfred Martin. A preliminary work is the master thesis “Sauerstoffionenleitfähigkeit in dotierten Ceroxiden aus experimenteller und quantenmechanischer Sicht” by the author himself.<sup>[1]</sup> Single crystal samples were prepared at the Institute of Chemistry (TU Berlin). External measurements for this work were carried out at the Institute of Crystallography (RWTH Aachen University), the German Electron Synchrotron (DESY, Hamburg) and the On-Line Isotope Mass Separator (ISOLDE at CERN, Geneva). Theoretical calculations were conducted in cooperation with Steffen Grieshammer (MMC) and Benjamin Grope (KMC of model 2014). The author thanks the Jülich Aachen Research Alliance High Performance Computing (JARA-HPC) for granting computing time within the projects jara0035, jara0071 and jara0141. The author gratefully acknowledges the computing time granted on the supercomputers JUROPA and JURECA at Jülich Supercomputing Centre (JSC).

## Acknowledgment

I would like to thank Prof. Dr. Manfred Martin for the opportunity to work on this exciting topic in his group, for his constant support as well as his scientific supervision. I would like to express my sincere gratitude to Prof. Dr. Peter C. Schmidt and Prof. Dr. Ullrich Englert for being my second and third examiner. My heartfelt gratitude goes to my parents and grandparents who have been an indispensable source of support.

I am grateful to Tobias Zacherle, Benjamin Grope and especially Steffen Grieshammer for the countless number of fruitful discussions. My sincere thanks to Dr. Roger De Souza, Dr. Michael Schroeder, Thomas Beckers, Philipp Hein, Annalena Genreith-Schriever, Andreas Falkenstein and Stefan Beschnitt who have provided valuable ideas for this work. Many thanks go to Fabian Draber, Andreas Falkenstein, Steffen Grieshammer, Philipp Hein, Christine Hendriks, Christian Schwab and Stephan Waldow who proofread this thesis and provided valuable feedback.

I thank Prof. Dr. Peter C. Schmidt, Tomáš Bučko and Prof. Dr. Rolf Schäfer for their support and discussions on molecular dynamics simulations as well as Jens Röder from ISOLDE (CERN), Dr. Lars Peters and Angelika von Berg from the Institute of Crystallography (RWTH Aachen University) and Prof. Dr. Martin Lerch and Gregor Ulbrich from the Institute of Chemistry (TU Berlin) for their support of experiments in this work. Many thanks go to Roman Chernikov from HASYLAB (DESY, Hamburg), Miliias Liu, Thomas Beckers and Henning Schraknepper for their support during the EXAFS beam time. Special thanks go to Thomas Leichtweiß (JLU Gießen) for the opportunity to work with thin films and Martha Pietrowski, Miliias Liu and Judith Hinterberg for introductions to experimental setups used in this work.

Many thanks go to my students Rachid Touzani, Mark Bispinghoff, Tai-Lam Nghiem, Gerald Dück, Fabian Draber, Hyung-Jong Choi, Yu Hashimoto and Ryota Sonoda for their great work, which is partly presented in this thesis.

I also gratefully acknowledge Bernd Huppertz and Thorsten Marioneck representatively for the electrical and mechanical workshops, Resi Zaunbrecher and Dieter Kerschgens for their experimental help as well as Dr. Thomas Kirschgen, Andreas Lucht, Brigitte Pauquet and Sebastian Kirchmeyer for their administrative support during this work. Special thanks go to my office colleagues as well as the whole group for their friendship and the great atmosphere throughout the whole time. Furthermore, I would like to thank everyone who contributed to the success of this work without being mentioned here.

**Parts of this work have been published in the following articles:**

1. S. Grieshammer, B.O.H. Grope, J. Koettgen and M. Martin, “A combined DFT+U and Monte Carlo study on rare-earth doped ceria”, *Physical Chemistry Chemical Physics* 16 (2014), 9974-9986
2. J. Koettgen, T. Zacherle, S. Grieshammer and M. Martin, “Ab initio calculation of the attempt frequency of oxygen diffusion in pure and samarium doped ceria”, submitted

**and oral presentations and posters:**

3. B.O.H. Grope, S. Grieshammer, J. Koettgen, M. Martin, “Doped ceria: A DFT and Monte Carlo study”, poster at *Frontiers in Electronic Materials*, Aachen, Germany, June 19, 2012
4. S. Grieshammer, B.O.H. Grope, J. Koettgen and M. Martin, “A combined DFT+U and Monte Carlo study on rare-earth doped ceria”, presentation at Seoul National University, Korea, April 02, 2014
5. J. Koettgen, T. Zacherle, S. Grieshammer and M. Martin, “A First-Principles Approach to the Attempt Frequency of Oxygen Ion Jumps in Doped Ceria”, presentation at 39th International Conference & Exposition on Advanced Ceramics & Composites (39th ICACC), Daytona Beach, Florida, USA, January 28, 2015
6. S. Grieshammer, B.O.H. Grope, J. Koettgen and M. Martin, “Long-term Degradation Due to Cation Ordering in rare-earth Doped Ceria”, presentation at 39th International Conference & Exposition on Advanced Ceramics & Composites (39th ICACC), Daytona Beach, Florida, USA, January 29, 2015
7. J. Koettgen, T. Zacherle, S. Grieshammer and M. Martin, “Ab initio calculation of the attempt frequency for oxygen diffusion in pure and samarium doped ceria”, presentation at 114th General Assembly of the German Bunsen Society for Physical Chemistry (Bunsentagung 2015), Bochum, Germany, May 15, 2015
8. J. Koettgen, T. Zacherle, S. Grieshammer and M. Martin, “A First-Principles Approach to the Attempt Frequency of Oxygen Ion Jumps in Doped Ceria”, presentation at 20th International Conference on Solid State Ionics (SSI-20), Keystone, Colorado, USA, June 16, 2015
9. J. Koettgen, T. Zacherle, S. Grieshammer and M. Martin, “A first-principles approach to the attempt frequency for oxygen diffusion in pure and doped ceria”, presentation at Workshop on CeO<sub>2</sub>-based materials in catalysis and electrochemistry, Rauischholzhausen, Germany, July 28, 2015

# Contents

<b>1</b>	<b>Introduction</b>	<b>1</b>
<b>2</b>	<b>Transport Properties in Pure and Doped Ceria</b>	<b>5</b>
2.1	Properties of Ceria . . . . .	5
2.1.1	Ceria . . . . .	5
2.1.2	Doped Ceria . . . . .	6
2.1.3	Non-Stoichiometric Ceria . . . . .	8
2.2	Conductivity and Diffusion . . . . .	9
2.3	Transition State Theory . . . . .	11
2.3.1	Historical Developments Concerning the Rate Constant . . . . .	11
2.3.2	Transition State Theory according to Eyring . . . . .	11
2.3.3	Transition State Theory according to Vineyard . . . . .	15
2.3.4	Equivalence of the Eyring and Vineyard Theory . . . . .	16
2.4	Conductivity in Doped Ceria . . . . .	18
2.4.1	The Total Conductivity . . . . .	18
2.4.2	The Bulk Conductivity . . . . .	20
2.4.3	Dopant Fraction with the Highest Conductivity . . . . .	24
2.4.4	The Activation Enthalpy of the Bulk Domain . . . . .	26
2.5	The Influence of Doping . . . . .	30
2.5.1	Varying the Dopant Fraction . . . . .	30
2.5.2	Varying the Type of Dopant . . . . .	32
<b>3</b>	<b>Methods</b>	<b>35</b>
3.1	Experimental Methods . . . . .	35
3.1.1	Composition . . . . .	35
3.1.2	Macroscopic Structure . . . . .	36
3.1.3	Local Structure . . . . .	36
3.1.4	Conductivity and Diffusion . . . . .	38
3.2	Computational Methods . . . . .	40
3.2.1	Quantum Mechanical Calculations . . . . .	40
3.2.2	Monte Carlo Simulations . . . . .	42

<b>4</b>	<b>Experimental and Computational Details</b>	<b>45</b>
4.1	Experimental Details . . . . .	45
4.1.1	Synthesis and Sample Preparation . . . . .	45
4.1.2	Composition . . . . .	46
4.1.3	Macroscopic Structure: Varying the Sintering Temperature and Duration . . . . .	47
4.1.4	Local Structure . . . . .	50
4.1.5	Conductivity . . . . .	54
4.2	Computational Details . . . . .	59
4.2.1	Quantum Mechanical Calculations . . . . .	59
4.2.2	Monte Carlo Simulations . . . . .	63
<b>5</b>	<b>Defect Interactions and Local Structures</b>	<b>65</b>
5.1	Defect Interactions and Association Energies . . . . .	65
5.1.1	Diluted Defects . . . . .	65
5.1.2	High Defect Concentrations . . . . .	72
5.2	Local Structure . . . . .	74
5.2.1	Metropolis Monte Carlo Simulations . . . . .	74
5.2.2	Coordination Numbers in EXAFS Experiments . . . . .	76
<b>6</b>	<b>Attempt Frequency</b>	<b>83</b>
6.1	Calculation of the Attempt Frequency: Doping at the Migration Edge . . . . .	84
6.1.1	Pure Ceria: Influence of the Phonon Mesh . . . . .	86
6.1.2	Sm Doped Ceria . . . . .	86
6.1.3	Gd and Yb Doped Ceria . . . . .	88
6.1.4	Attempt Frequency at Constant Pressure . . . . .	90
6.2	Calculation of the Attempt Frequency: Doping in Nearest Neighborhood . . . . .	94
6.3	Experimental Attempt Frequencies . . . . .	96
6.3.1	Experimental Values for Pure Ceria . . . . .	96
6.3.2	Reasons for Scattering . . . . .	98
6.3.3	Experimental Values for Doped Ceria . . . . .	103
6.4	KMC Simulations with Varying Attempt Frequencies . . . . .	106
<b>7</b>	<b>Activation Energy</b>	<b>109</b>
7.1	Calculating the Migration Energy . . . . .	109
7.1.1	Widening of the Edges Cation Distance . . . . .	110
7.1.2	Supercell Size . . . . .	114
7.2	Modeling the Migration Energy . . . . .	124
7.2.1	Mathematics: Linear and Additive Models . . . . .	124
7.2.2	Evaluation of Models . . . . .	126
7.2.3	Choice of Model and Parameters . . . . .	128

7.2.4	Influence of Dopants on a Jump . . . . .	135
7.2.5	Influence of Vacancies on a Jump . . . . .	159
7.2.6	Comparing Model and DFT Energies . . . . .	161
7.2.7	Jumps at Experimental Defect Concentrations . . . . .	162
7.2.8	Comparison with Models in Literature . . . . .	164
7.3	Simulating the Ionic Conductivity for Different Models . . . . .	167
<b>8</b>	<b>Oxygen Ion Conductivity</b>	<b>173</b>
8.1	The Influence of Sample Preparation: Varying the Sintering Temperature and Duration . . . . .	173
8.2	The Influence of Doping . . . . .	181
8.2.1	Simulating the Ionic Conductivity . . . . .	181
8.2.2	Sm Doped Ceria . . . . .	194
8.2.3	The Best Dopant: Sm or Gd? . . . . .	196
8.2.4	Co-Doped Ceria: Sm-Zr and Gd-Zr . . . . .	202
8.2.5	Lu Doped Ceria . . . . .	205
8.2.6	Comparing Simulations and Experiments . . . . .	208
8.3	The Influence of Time: Long-term Degradation Due to Cation Ordering . . . . .	209
<b>9</b>	<b>Summary and Outlook</b>	<b>213</b>
	<b>References</b>	<b>217</b>
	<b>Appendix</b>	<b>241</b>
	<b>List of Abbreviations</b>	<b>253</b>
	<b>List of Figures</b>	<b>255</b>
	<b>List of Tables</b>	<b>269</b>



# 1 Introduction

The increasing use of renewable energy sources highlights the importance of energy conversion and storage.<sup>[1,2]</sup> For water, wind and solar power, energy production and demand can occur at different times, which makes efficient energy storage a central issue in the global energy industry.

Electric energy can be stored mechanically using water pump storages, compressed air reservoirs and, for small applications, flywheels.<sup>[3]</sup> Alternatively, energy can be stored electrochemically using batteries or a combination of water electrolysis and fuel cells. For the latter, water is converted into hydrogen and oxygen in times of high energy production (water electrolysis). Hydrogen or both gases can be stocked, for example underground.<sup>[4-6]</sup> When the energy demand exceeds production, hydrogen and oxygen are converted back to water in a fuel cell.

Fuel cells separate the oxidation of hydrogen and reduction of oxygen on both sides of an electrolyte, which in most cases only allows either positively charged hydrogen ions or negatively charged oxygen ions to pass. Examples are Proton Exchange Membrane Fuel Cells (PEMFCs) or Solid Oxide Fuel Cells (SOFCs), respectively. For the latter, other fuels than hydrogen can be used. Proton conducting fuel cells are operated at up to about 200 °C and oxygen ion conducting fuel cells at high temperature up to 1000 °C. SOFCs provide high energy conversion efficiency, long-term stability and excellent fuel flexibility and are therefore a promising candidate for future energy applications.<sup>[7]</sup>

In a Solid Oxide Fuel Cell (Fig. 1.1), air or pure oxygen is fed to a gas-permeable and electrically conductive cathode. Oxygen is incorporated into the solid while being reduced. The oxygen ions move through a dense solid electrolyte to the anode. The anode is also porous and electrically conductive. A fuel gas is fed and oxidized. If hydrogen is used as a fuel, water is produced. The electrons, which are released during oxidation, move through an external circuit to the cathode since the electrolyte has a low electronic conductivity. The electrons transport the electrical energy that is gained in the chemical reaction. Thus, chemical energy is directly converted into electric energy.<sup>[8]</sup>

SOFCs can be used for energy conversion in combination with Solid Oxide Electrolyser Cells, where water is electrolyzed at high temperature.<sup>[9]</sup> Alternative applications for SOFCs are, for example, the domestic production of electricity and warm water fed by natural gas pipelines, battery chargers for cell phones or fuel cell vehicles.<sup>[10]</sup>

The main component in SOFCs is the dense solid electrolyte, which is permeable for oxygen ions and impenetrable for electrodes or gas molecules. For more than 150 years, research has been carried out on this topic. Solid electrolytes have been discovered in 1853 (Gaugain) or 1854 (Buff) by connecting the enhanced conductivity of glasses and ceramics with their electrolytic nature.<sup>[11-13]</sup>

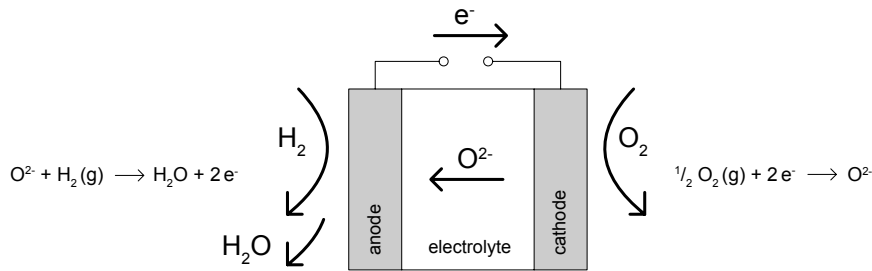


Figure 1.1: Configuration of a Solid Oxide Fuel Cell (SOFC).

At the turn of the 20<sup>th</sup> century, solid electrolytes attracted a lot of attention when Nernst presented an alternative to the carbon filament lamp.<sup>[14]</sup> Due to practical reasons, the Nernst lamp could not compete against tungsten-filament lamps, which were discovered shortly afterwards. However, now the high oxygen ion conductivity of yttria-stabilized zirconia,  $(Y_2O_3)_{0.15}(ZrO_2)_{0.85}$ , at high temperature had been identified.<sup>[15]</sup> The conduction mechanism in solids was systematically investigated by Frenkel, Schottky and Wagner between 1926 and 1935 with fundamental works on the disorder of ionic crystals.<sup>[16]</sup> The first SOFC with zirconia was presented by Baur in 1937.<sup>[17]</sup> Not until 1943, the existence of vacancies in the anion sublattice was realized by Wagner, which are responsible for the high oxygen ion conductivity.<sup>[18]</sup> Finally in 1951, Hund confirmed the existence of oxygen vacancies by X-ray crystallographic and pycnometric measurements.<sup>[19]</sup>

Besides SOFCs, solid electrolytes with oxygen ion conductivity can be used as oxygen sensors. An example is the lambda sensor<sup>[20]</sup> in cars to control the combustion of fuel. Other applications are oxygen membranes, which feature both ionic and electronic conductivity and can be used to separate air and oxygen.<sup>[21–23]</sup> Currently, pure oxygen for industrial and medical applications is produced by cryogenic distillation, which has a high energy demand. Oxygen membranes can also be used in power plants for combustion in pure oxygen, which allows the capturing of  $CO_2$  for storage.<sup>[24]</sup>

The most common material for electrolytes, yttria-stabilized zirconia, requires operation temperatures around 900 °C, which lead to thermal degradation of materials and chemical reactions between components. At lower temperatures, the oxygen ion conductivity decreases rapidly. As an alternative, doped ceria ( $CeO_2$ ) was found, which allowed the reduction of the operating temperature to intermediate temperatures around 600 °C.<sup>[25]</sup> Pure cerium oxide itself is not a good ionic conductor.<sup>[26]</sup> In contrast, doping with lower valent oxides like rare-earth (RE) oxides creates oxygen vacancies, which results in a significant increase in oxygen ion conductivity. In particular, doping with samarium oxide ( $Sm_2O_3$ ) leads to high conductivities as revealed by impedance spectroscopy experiments (Fig. 1.2 left).<sup>[27]</sup>

The ionic conductivity first increases and then decreases with increasing dopant fraction with a maximum at  $Ce_{0.8}Sm_{0.2}O_{1.9}$ . For different dopants ( $Ce_{0.8}RE_{0.2}O_{1.9}$ ), a correlation between ionic conductivity and dopant radius was found (Fig. 1.2 right).<sup>[27,29–31]</sup> Here, often the ionic radii according to Shannon are given.<sup>[32]</sup> Compared to pure ceria, doping can also decrease the ionic conductivity

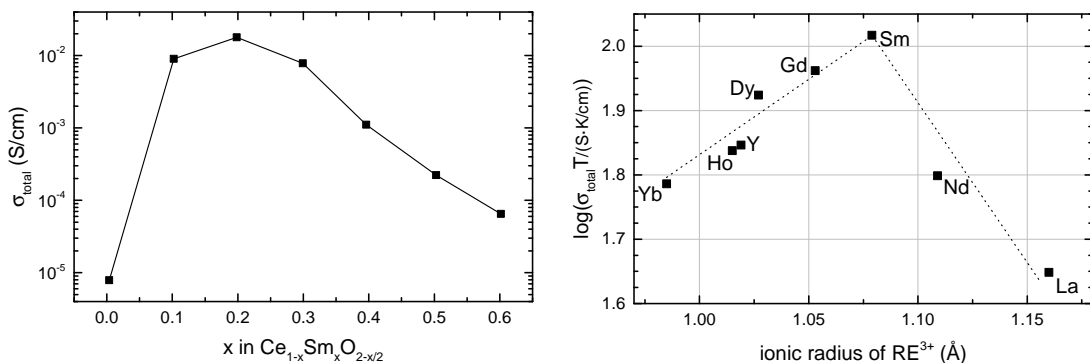


Figure 1.2: Ionic conductivity of Sm doped ceria at 600 °C (left)<sup>[28]</sup> and  $\text{Ce}_{0.8}\text{RE}_{0.2}\text{O}_{1.9}$  at 800 °C (right).<sup>[27]</sup> Lines are a guide to the eye only.

e.g. by doping with Sc.<sup>[33]</sup>

The influence of the dopant fraction and the type of dopant on the conductivity has been a topic of research for half a century. Initially, analytical models were employed.<sup>[34–37]</sup> For more than 30 years semi-empirical<sup>[38–41]</sup> and since the turn of the 21<sup>st</sup> century *ab initio* calculations have been performed.<sup>[42–45]</sup> Despite the development of various models, the detailed understanding of the underlying mechanism that determines the magnitude of the oxygen ion conductivity and the optimal dopant concentration is still missing.

In this work, this mechanism is closely investigated by presenting the relation between defect interactions, local structure and oxygen ion conductivity. Only if all three properties and their interdependencies are known, the behavior in the bulk of doped ceria can be understood.

The local structure is investigated experimentally using Extended X-Ray Absorption Fine Structure (EXAFS) and theoretically using Metropolis Monte Carlo (MMC) simulations. The novel direct comparison of EXAFS coordination numbers based on atomic distances in ceria with simulations based on *ab initio* data provides insights into the local structure and its influence on the conductivity.

The diffusion is traced back to microscopic jumps using Kinetic Monte Carlo (KMC) simulations. The jump rate  $\Gamma = \nu_0 \cdot e^{-\frac{\Delta E_{\text{mig}}}{k_B T}}$  is separated into electronic and vibrational contributions, commonly known as pre-factor of diffusion and migration energy. Both are investigated using *ab initio* methods.

The pre-factor of diffusion in pure and doped ceria is studied in unprecedented detail, which allows a complete *ab initio* understanding of processes at high temperature compared to standard *ab initio* calculations at zero temperature. Migration energies are closely investigated by using models with high complexity but few and intuitive *ab initio* parameters, which correlate with material properties. These models provide a detailed understanding of the underlying mechanism that determines the influence of different dopants and their concentration on the oxygen ion conductivity.

For comparison, Sm and Lu doped ceria are investigated for their oxygen ion conductivity in impedance spectroscopy experiments. Here, more compositions are examined than previously shown in literature. Finally, the degradation of doped ceria due to cation diffusion is, for the first time, directly compared between experiments and simulations based on *ab initio* data.



# 2 Transport Properties in Pure and Doped Ceria

## 2.1 Properties of Ceria

### 2.1.1 Ceria

Ceria ( $\text{CeO}_2$ ) has the fluorite structure (space group 225:  $Fm\bar{3}m$ ) for temperatures between room temperature and melting point.<sup>[1,25,31,46]</sup> The cations are positioned in a face-centered cubic lattice while the anions fill the tetrahedral holes leading to a primitive cubic anion lattice (see Fig. 2.1).

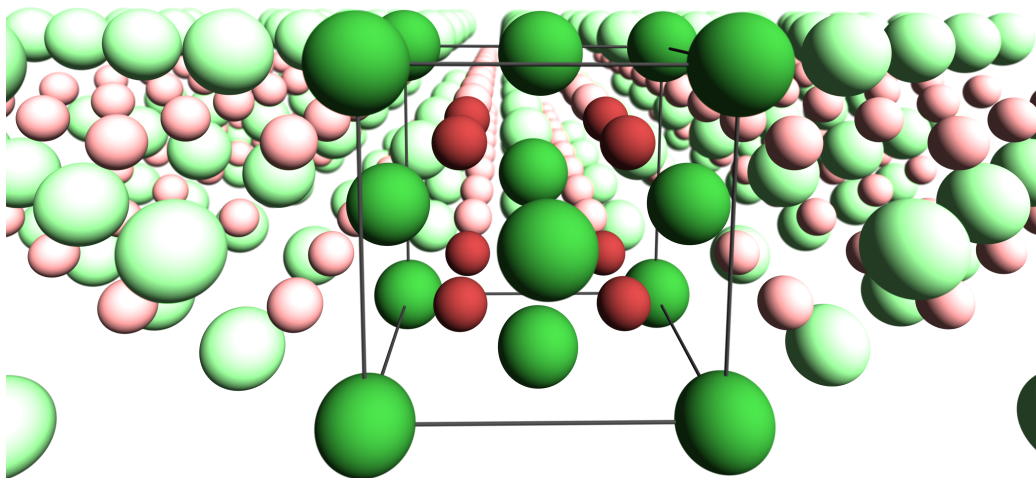


Figure 2.1: Crystal structure of cerium oxide. Cerium ions (green) and oxygen ions (red). The unit cell of the fluorite structure is highlighted.

A fundamental requirement for oxygen ion conductivity is the existence of defects, i.e. interstitial ions or vacant lattice sites (vacancies). A perfect defect-free crystal exists only at 0 K. For higher temperatures, the number of ‘intrinsic’ defects increases: In NaCl cations and anions leave their lattice sites and move to the surface (Schottky disorder), in AgCl cations move to interstitial sites (Frenkel disorder) and in  $\text{CaF}_2$  anions move to interstitial sites (Anti-Frenkel disorder).<sup>[47–49]</sup> In pure ceria, the anti-Frenkel disorder is favored.<sup>[50,51]</sup> For low oxygen partial pressures, oxygen va-

cancies are created by reduction (see Chapter 2.1.3).<sup>[50–53]</sup> In air, the concentration of defects is low. Therefore, the ionic conductivity of pure CeO<sub>2</sub> is low (10<sup>−6</sup> – 10<sup>−5</sup> S/cm at 600 °C).<sup>[25,26]</sup>

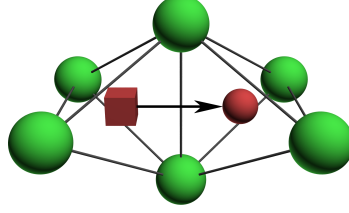


Figure 2.2: Migration configurations in ceria. Cerium ions (green), oxygen ions (red spheres) and oxygen vacancy (red box).

Oxygen vacancies lead to ionic conductivity as oxygen ions can jump to a vacant lattice site (hopping mechanism). For the oxygen ion conductivity, jumps of oxygen ions or vacancies occur mainly between adjacent tetrahedral oxygen sites in (100) direction<sup>[54]</sup> with the experimental jump distance  $l = 2.7055 \text{ \AA}$  given by half of the unit cell length at room temperature.<sup>[25]</sup> Along the migration pathway, the migrating oxygen ion passes between two adjacent cations, which form a migration edge as shown in Fig. 2.2.<sup>[55]</sup>

Stoichiometric ceria is an insulator with band gap of  $E_{\text{gap}}[\text{O}(2p) \rightarrow \text{Ce}(5d)] = 6 \text{ eV}$ ,<sup>[56]</sup> in which unoccupied Ce(4f)-states with  $E_{\text{gap}}[\text{O}(2p) \rightarrow \text{Ce}(4f)] = 3 \text{ eV}$ <sup>[57]</sup> can be found. Therefore, the electronic conductivity is low (10<sup>−7</sup> – 10<sup>−6</sup> S/cm at 600 °C).<sup>[26,58]</sup>

### 2.1.2 Doped Ceria

Defects can also be created by doping and are then called ‘extrinsic’.<sup>[59]</sup> In this work, cerium oxide  $\overset{+IV}{\text{Ce}} \overset{-II}{\text{O}_2}$  is doped with lower valent oxides, mostly rare-earth oxides  $\overset{+III}{\text{RE}} \overset{-II}{\text{O}_3}$ . This leads to the creation of oxygen vacancies as shown in Eq. 2.1 in Kröger-Vink notation.<sup>[25]</sup> Lower valent dopant atoms are called acceptors. As dopant fractions in experiments are high (cp. Fig. 2.3), ceria is actually rather substituted than doped with rare-earth oxides.



As a result, oxygen vacancies are the majority defects with a concentration controlled by the dopant fraction according to  $[\text{RE}'_{\text{Ce}}] = 2[\text{V}_{\text{O}}^{\bullet\bullet}]$ . In this work, dopant fractions are given as RE<sub>1</sub>O<sub>1.5</sub> mol%, though in literature also RE<sub>2</sub>O<sub>3</sub> mol% is used (for conversion see appendix, Fig. 9.1). Intrinsic defects can be neglected and the concentration of oxygen vacancies is independent of temperature. Even for commercially available ceria with high purity, small amounts of impurities lead to higher concentration of extrinsic defects than the concentration of intrinsic defects (see Chapter 6.3).

Doping is limited by solubility. While for some dopants solubilities above  $x = 0.4$  were reported,<sup>[25]</sup> contradicting information about the solubility limits are found in literature as described in the following. Often X-Ray Diffraction (XRD) analysis cannot confirm the development of secondary

phases, as they are very similar to the fluorite structure of ceria. For the dopants investigated in this work, most studies report solubilities above  $x > 0.25$  (cp. Fig. 2.3),<sup>[60,61]</sup> while Balazs and Glass found for  $x = 0.2$  minor impurity phases for small (Lu, Yb, Tm) and large dopants (Nd, La) compared to  $\text{Ce}^{4+}$ .<sup>[62]</sup> For the even smaller dopant Sc, the solubility limit is already reached at 3–5%.<sup>[25,33]</sup> For the large dopant La, the solid solution  $\text{Ce}_{0.8}\text{La}_{0.2}\text{O}_{1.9}$  appears to be only metastable.<sup>[63,64]</sup>

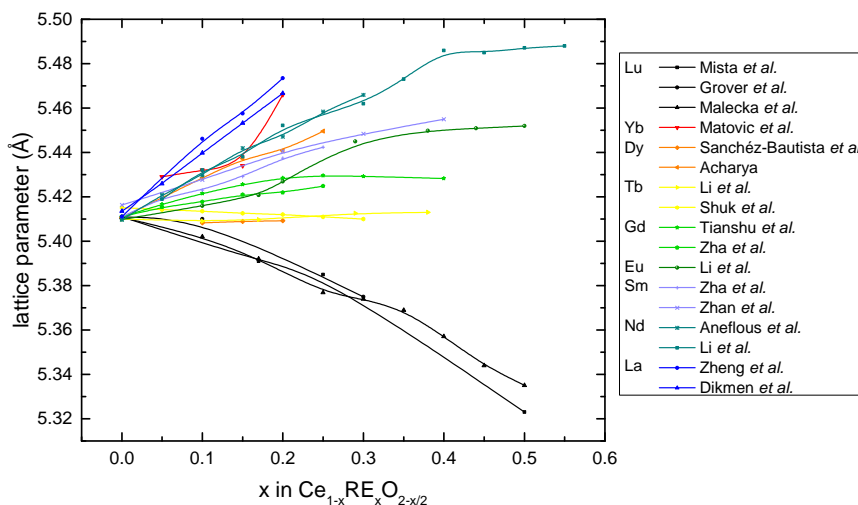


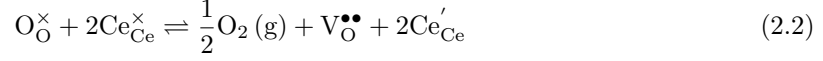
Figure 2.3: Experimental lattice parameter in air at room temperature for Lu,<sup>[65–67]</sup> Yb,<sup>[68]</sup> Dy,<sup>[69,70]</sup> Tb,<sup>[71,72]</sup> Gd,<sup>[64,73]</sup> Eu,<sup>[71]</sup> Sm,<sup>[73,74]</sup> Nd<sup>[75,76]</sup> and La doped ceria.<sup>[63,77]</sup> Lines are a guide to the eye only.

The lattice parameter in doped ceria depends on the ionic radius of the dopant. For  $\text{Ce}_{0.8}\text{RE}_{0.2}\text{O}_{1.9}$ , the lattice parameter increases linearly with the dopant radius obeying Vegard’s law.<sup>[27,29,62,78]</sup> Figure 2.3 shows that the lattice parameter decreases (for small dopants) or increases (for large dopants) with increasing dopant fraction until a constant value is reached, which indicates the solubility limit.<sup>[63,76]</sup> For Yb, Dy and Eu doped ceria, a few derivations from this rule can be found. Earlier measurements from Brauer and Gradinger showed lower lattice parameters, which are not shown here.<sup>[79]</sup> Some studies even assume a relationship between the association of oxygen vacancies with dopants and the change in behavior of the lattice parameter as a function of dopant fraction.<sup>[61,64,71]</sup>

Oxygen ion conductivities of doped ceria are shown in Chapter 2.4. The electronic conductivity of stoichiometric doped ceria is low. However, in SOFCs, the driving force for the ionic conductivity is a gradient of the chemical potential ( $p_{\text{O}_2}$  (anode)  $<$   $p_{\text{O}_2}$  (cathode)). For low oxygen partial pressures, ceria can become oxygen-deficient or non-stoichiometric (see next section).

### 2.1.3 Non-Stoichiometric Ceria

At low oxygen partial pressure or high temperature, ceria can be easily reduced to  $\text{CeO}_{2-\delta}$ . Here, cerium ions  $\text{Ce}^{4+}$  are reduced to  $\text{Ce}^{3+}$  and oxygen vacancies  $\text{V}_{\text{O}}^{\bullet\bullet}$  are created:<sup>[25,51]</sup>



The formation of oxygen vacancies is compensated by the formation of electrons, which makes non-stoichiometric ceria an n-type conductor.<sup>[80]</sup> The additional electron is localized at the host cation in a distorted local environment and is therefore called polaron.<sup>[81–84]</sup> Polarons migrate by thermally activated jumps and therefore are responsible for electronic conductivity.<sup>[25,85]</sup>

The equilibrium in Eq. 2.2 is influenced by doping with lower valent cations since doping also creates oxygen vacancies.<sup>[25]</sup> Therefore, doping decreases the concentration of trivalent cerium ions  $\text{Ce}'_{\text{Ce}}$ . On the other hand, experiments show that doping promotes the reduction of  $\text{Ce}^{4+}$ -ions at lower temperatures.<sup>[86–92]</sup>

If it is assumed that no interactions between defects exist, e.g. for small defect concentrations, the law of mass action can be applied with unity activity coefficients: Hence, for pure ceria, the non-stoichiometry  $\delta$  depends on the oxygen partial pressure according to  $\delta \propto p_{\text{O}_2}^{-1/6}$ . In doped ceria  $\text{Ce}_{1-x}\text{RE}_x\text{O}_{2-\frac{x}{2}-\delta}$ , the relation  $\delta \propto p_{\text{O}_2}^{-1/4}$  applies. Experimentally, both partial pressure dependencies were detected, respectively, for pure and doped ceria with low non-stoichiometry.<sup>[26,91,93]</sup> For large non-stoichiometry ( $\delta > 0.006$ ), significant deviations from the expected partial pressure dependencies can be observed.<sup>[25,82,90,91,94–100]</sup> These deviations may indicate interactions between defects or the ordering of defects.

In addition to the high oxygen ion conductivity in doped ceria, the electronic conductivity must be low for an ideal electrolyte material. However, the electronic conductivity increase with non-stoichiometry according to Eq. 2.2.

In the investigated conditions in this work ( $p_{\text{O}_2} = 0.21$  atm), the non-stoichiometry is very small. For example, at 1500 °C, the oxygen partial pressure has to be as low as  $10^{-2}$  atm to create a non-stoichiometry of  $\delta \approx 0.02$ .<sup>[25]</sup> Electrolyte materials should possess an electronic conductivity, which is at least one order of magnitude smaller than the ionic conductivity (ionic domain) for the entire range of application. This is the case for doped ceria at intermediate temperatures (Fig. 2.4).

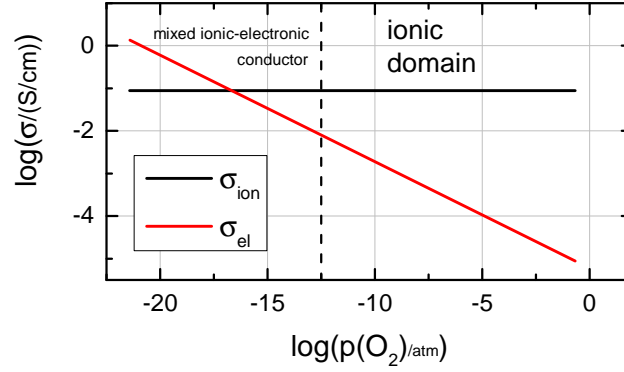


Figure 2.4: Ionic and electronic conductivity of  $\text{Ce}_{0.8}\text{Gd}_{0.2}\text{O}_{1.9-\delta}$  at 800 °C according to Yokokawa *et al.*<sup>[101]</sup>

## 2.2 Conductivity and Diffusion

The ionic conductivity  $\sigma_i$  of the oxygen ions ( $i = \text{O}^{2-}$ ) or vacancies ( $i = \text{V}_{\text{O}}^{\bullet\bullet}$ ) is proportional to their squared charge  $z_i^2 e^2$ , concentration  $n_i$  and mechanical mobility  $b_i$  (Eq. 2.3). The mobility is related to the diffusion coefficient  $D_i$  by the classical Einstein relation for non-interacting defects with the Boltzmann constant  $k_{\text{B}}$  and the absolute temperature  $T$ .<sup>1</sup> Both diffusion coefficients ( $D_{\text{O}^{2-}}$  and  $D_{\text{V}_{\text{O}}^{\bullet\bullet}}$ ) depend on the weighted mean jump rate of all oxygen ions ( $\bar{\Gamma}_{\text{O}^{2-}}$ ) or vacancies ( $\bar{\Gamma}_{\text{V}_{\text{O}}^{\bullet\bullet}}$ ) to one nearest neighbor site.<sup>2</sup> In Eq. 2.3  $l$  is the jump distance and  $\gamma$  is the geometrical factor, which includes the number of jump sites  $n_{\text{p}}$  and the dimension of diffusion  $d$  and is  $\gamma = \frac{n_{\text{p}}}{2d} = 1$  in a primitive cubic lattice, e.g. the oxygen sublattice in ceria.<sup>[103,104]</sup> The jump rate can be described by an Arrhenius equation (Eq. 2.4) with the activation enthalpy at constant pressure  $\Delta H_{\text{a}}(p, T)$ . The activation enthalpy describes the experimentally determined dependence of the diffusion coefficient on temperature and can be calculated from the slope of a plot  $\ln \bar{\Gamma}_i$  versus  $1/T$ .

$$\sigma_i = n_i \cdot z_i^2 e^2 \cdot b_i, \text{ where } b_i = \frac{D_i}{k_{\text{B}} T} \text{ and } D_i = \gamma l^2 \cdot \bar{\Gamma}_i. \quad (2.3)$$

$$\bar{\Gamma}_i(p, T) = \bar{\nu}_{\text{exp}, i}(p, T) \cdot e^{-\frac{\Delta H_{\text{a}}(p, T)}{k_{\text{B}} T}} \quad (2.4)$$

Therefore, the pre-exponential factor for diffusion  $D_{0,i} = \gamma l^2 \cdot \bar{\nu}_{\text{exp}, i}(p, T)$  depends on the frequency  $\bar{\nu}_{\text{exp}, i}(p, T)$ . The latter can be interpreted as mean experimental attempt frequency of all oxygen vacancies or oxygen ions to jump to one nearest neighbor site at constant pressure. It should be noted that several definitions of the term ‘attempt frequency’ exist, which will be discussed in section 2.3.2. Naturally, deviations in the activation enthalpy, which appears in the exponential term, possess a stronger influence on the jump rate than deviations in the attempt frequency.

<sup>1</sup>For high defect concentrations, an ‘exact Nernst-Einstein’ relation using the chemical potential can be applied.<sup>[102]</sup>

<sup>2</sup>In fact, jumps to other lattice sites may be possible, which are neglected here according to Nakayama and Martin.<sup>[54]</sup>

## 2 Transport Properties in Pure and Doped Ceria

For doped ceria, the concentration of charge carriers is independent of temperature, while conductivity, mobility, diffusion coefficient and jump rate increase for increasing temperature.<sup>[105]</sup> In a restricted temperature range, the activation enthalpy is often assumed to be independent of temperature.

The conductivity of an oxygen ion conductor (Eq. 2.3) can be defined for both oxygen ions and vacancies whereat both conductivities are equal in value. Likewise, the absolute value of the oxygen ions charge is equal to the Kröger-Vink charge of the oxygen vacancies. Therefore, the diffusion coefficients of ions  $D_{\text{O}^{2-}}$  and vacancies  $D_{\text{V}_{\text{O}}^{\bullet\bullet}}$  differ according to

$$D_{\text{O}^{2-}} = \frac{n_{\text{V}_{\text{O}}^{\bullet\bullet}}}{n_{\text{O}^{2-}}} D_{\text{V}_{\text{O}}^{\bullet\bullet}}, \quad (2.5)$$

with the concentration of oxygen ions  $n_{\text{O}^{2-}}$  and oxygen vacancies  $n_{\text{V}_{\text{O}}^{\bullet\bullet}}$  (cf. ‘jump balance’). The same applies to the mean jump rate  $\bar{\Gamma}_i$  and the mean attempt frequency  $\bar{\nu}_{\text{exp},i}(p,T)$ . In a pure ceria crystal with isolated defects, all oxygen vacancies have the same attempt frequency  $\bar{\nu}_{\text{exp},\text{V}_{\text{O}}^{\bullet\bullet}} = \nu_{\text{exp},\text{V}_{\text{O}}^{\bullet\bullet}}$  where  $\nu_{\text{exp},\text{V}_{\text{O}}^{\bullet\bullet}}$  is the attempt frequency for the jump of one individual oxygen ion to a vacant lattice site. This is the elementary frequency for a jump process where both the jumping oxygen vacancy and the jumping oxygen ion have the same jump attempt frequency and which is calculated in this work. In the transition state theory, attempt frequencies of individual defects are calculated. Since oxygen ions can only jump when a neighboring vacancy exists, the mean attempt frequency of all oxygen ions  $\bar{\nu}_{\text{exp},\text{O}^{2-}}$  depends on the fraction of oxygen vacancies (Fig. 2.5). Often it is assumed that the attempt frequency of an oxygen vacancy  $\nu_{\text{exp},\text{V}_{\text{O}}^{\bullet\bullet}}$  is not influenced by other vacancies. Therefore, the attempt frequency and the diffusion coefficient of the oxygen ions increase with increasing oxygen vacancy fraction according to Eq. 2.5.

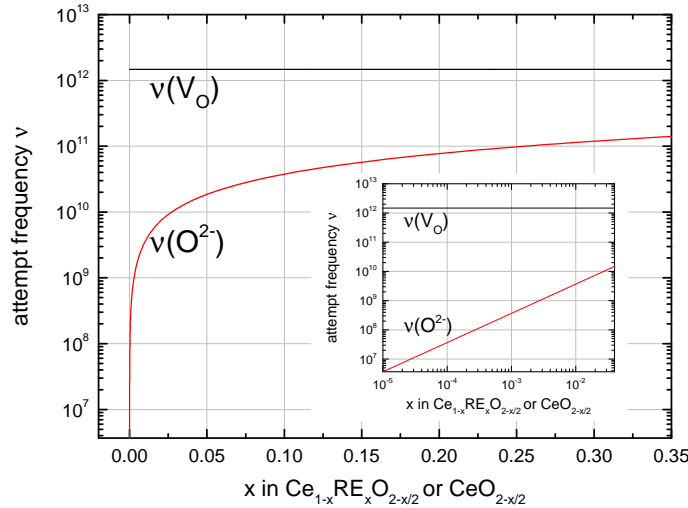


Figure 2.5: Attempt frequency of oxygen ions and vacancies as a function of dopant fraction or non-stoichiometry for a constant oxygen vacancy attempt frequency according to Eq. 2.5. The attempt frequency of the oxygen ions increases with increasing oxygen vacancy fraction.

In doped ceria, a variety of ionic configurations occurs, which leads to a variety of jump envi-

ronments and possibly different local attempt frequencies. As a macroscopic property, the mean experimental attempt frequency  $\bar{\nu}_{\text{exp},i}(p,T)$  is influenced by all local attempt frequencies that affect the diffusion.

## 2.3 Transition State Theory

### 2.3.1 Historical Developments Concerning the Rate Constant

Reaction rate theory was majorly influenced by Arrhenius,<sup>[106]</sup> Trautz and Lewis,<sup>[107,108]</sup> Eyring<sup>[109]</sup> and Vineyard.<sup>[110]</sup> The Arrhenius equation<sup>[106]</sup> (Eq. 2.4), originally formulated in 1889 for the temperature-dependent rate constant of a chemical reaction, assumes that a minimum amount of activation energy at constant volume (or enthalpy at constant pressure) is necessary to transform reactants into products. Thus, the reaction rate is proportional to the product of a pre-exponential factor and the probability an activated state occurs. While Arrhenius assumed a constant prefactor, about 25 years later, Max Trautz and William Lewis<sup>[107,108]</sup> proposed a minor temperature dependence of the pre-exponential factor. According to their collision theory, a reaction occurs if the kinetic energy along the line-of-centers at contact exceeds a specific value.<sup>[111]</sup> However, other degrees of freedom can also contribute to the formation of the activated state,<sup>[112]</sup> and discrepancies between theoretical and experimental results were observed.

### 2.3.2 Transition State Theory according to Eyring

In the year 1935 Eyring<sup>[109]</sup> published an essential contribution to the transition state theory or absolute-rate theory. He proposed between initial state (IS) and transition state (TS) a quasi-equilibrium  $\text{IS} \rightleftharpoons \text{TS}$ . The corresponding equilibrium constant is  $K = c_{\text{TS}}/c_{\text{IS}}$  where  $c_{\text{TS}}$  and  $c_{\text{IS}}$  are the concentrations of the reactants in both respective states. Once the transition state configuration is reached, every complex decomposes to the product (P) with the decomposition frequency  $\nu_d$ ,  $\text{IS} \rightleftharpoons \text{TS} \xrightarrow{\nu_d} \text{P}$ . Then, the reaction rate for the formation of the product P can be written as

$$\text{reaction rate} = \nu_d c_{\text{TS}} = \underbrace{\nu_d K}_{k} c_{\text{IS}}. \quad (2.6)$$

Here  $k$  is the reaction rate constant. A transmission factor  $\kappa \leq 1$  could be included in Eq. 2.6 to account for ‘return jumps’, though it cannot be evaluated in the frame of the transition state theory.<sup>1</sup> Hence, the classical transition state theory is an upper bound to the true reaction rate.<sup>[119]</sup>

The equilibrium constant  $K$  in Eq. 2.6 can be expressed by the partition functions of the initial state  $Z_{\text{IS}}$  and the transition state  $Z_{\text{TS}}$ .<sup>[120]</sup> Both of them can be written as a product of an electronic partition function  $Z_{\text{el}}$  and a vibrational partition function  $Z_{\text{vib}}$  assuming no coupling between

<sup>1</sup>A ‘return jumps’ rate is taken into account by the Kramers approach,<sup>[113]</sup> and the short-memory augmented-rate theory (SM-ART) framework of Toller et al.<sup>[112,114–118]</sup>

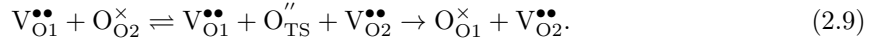
vibrational and electronic excitation (Eq. 2.7). For temperatures far below the Fermi temperature, the electronic partition function is primarily determined by the electronic ground state. Therefore, the ratio of the electronic partition functions results in  $\exp\left(-\frac{\Delta E_{\text{el}}^0}{k_{\text{B}}T}\right)$  where  $\Delta E_{\text{el}}^0$  is the electronic energy difference between the activated complex and the reactants for temperatures far below the Fermi temperature. This quantity is typically obtained in *ab initio* calculations at absolute zero.

$$K = \frac{Z_{\text{TS}}}{Z_{\text{IS}}} = \frac{Z_{\text{TS,vib}}}{Z_{\text{IS,vib}}} \frac{Z_{\text{TS,el}}}{Z_{\text{IS,el}}} = \frac{Z_{\text{TS,vib}}}{Z_{\text{IS,vib}}} e^{-\frac{\Delta E_{\text{el}}^0}{k_{\text{B}}T}} \quad (2.7)$$

Until now, all transition state related properties like the concentrations  $c_{\text{TS}}$ , the equilibrium constant  $K$ , and the vibrational partition function  $Z_{\text{TS,vib}}$  contained the decomposition vibration. However, the vibrational mode, which corresponds to the decomposition vibration, has to be excluded from these properties for the calculation of the free energy. Therefore, the partition function for the critical vibration can be separated from the vibrational partition function according to  $Z_{\text{TS,vib}} = \frac{k_{\text{B}}T}{h\nu_{\text{d}}} Z'_{\text{TS,vib}}$ .<sup>1</sup> Here,  $Z'_{\text{TS,vib}}$  is the vibrational partition function for all normal coordinates except the decomposition vibration, similar to a modified equilibrium constant  $K' = c'_{\text{TS}}/c_{\text{IS}} = (h\nu_{\text{d}})/(k_{\text{B}}T) K$ . Therefore, the transition state partition function  $Z'_{\text{TS,vib}}$  has one degree of freedom less than the initial state partition function  $Z_{\text{IS,vib}}$ . The final expression for the reaction rate constant is

$$k = \frac{k_{\text{B}}T}{h} \frac{Z'_{\text{TS,vib}}}{Z_{\text{IS,vib}}} e^{-\frac{\Delta E_{\text{el}}^0}{k_{\text{B}}T}}. \quad (2.8)$$

Equation 2.8 can be applied to the diffusion process as follows: The migration of an oxygen ion  $\text{O}_{\text{O}}^{\times}$  from a lattice site 2 to a lattice site 1 can be described by the following quasi-chemical reaction:



In the initial state (IS), the oxygen ion occupies lattice site 2, while the oxygen vacancy occupies a neighboring lattice site 1. In the transition state (TS), the oxygen ion is located on the saddle point between both empty lattice sites 1 and 2. Finally, in the product state P, the oxygen ion occupies lattice site 1 and the vacancy occupies lattice site 2. The corresponding electronic energy profile is

---

<sup>1</sup>The decomposition vibration can be described as classical harmonic oscillator where the weighted number of states consists of the kinetic and potential energy weighted by the Boltzmann factor, integrated over phase space and ‘arbitrarily’ divided by the Planck constant. This is similar to a quantum harmonic oscillator without zero point energy and in high temperature limit ( $k_{\text{B}}T \gg h\nu_{\text{d}}$ ). Instead of describing the decomposition motion as a vibration, a translational degree of freedom can be used. Then, the reaction rate can be defined as product of the concentration of the transition state  $c_{\text{TS}}$ , the translational partition function for the particle in an one-dimensional box  $Z_{\text{translational}} = \frac{\sqrt{2\pi mk_{\text{B}}T}}{h} \delta$  with the box length  $\delta$  and the effective mass associated with the translation along the reaction coordinate  $m$ . This modified transition state concentration is multiplied with the mean velocity given by an one-dimensional Maxwell-Boltzmann distribution  $\bar{v} = \sqrt{\frac{k_{\text{B}}T}{2\pi m}}$  and the inverse box length  $1/\delta$ .<sup>[112,120–122]</sup>

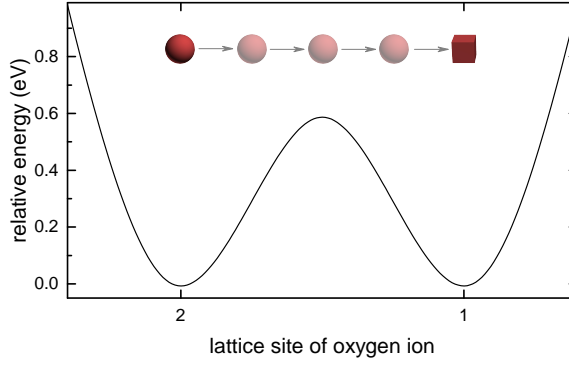


Figure 2.6: Sketch of the electronic energy profile for an oxygen jump in pure ceria according to Eq. 2.9.

shown in Fig. 2.6. Comparing Eqs. 2.9 and 2.6 indicates that the jump rate  $\Gamma$  for this elementary site exchange process corresponds to the reaction rate constant  $k$  discussed before.

The partition functions  $Z'_{\text{TS,vib}}$  and  $Z_{\text{IS,vib}}$  in Eq. 2.8 can be described by means of the quantum harmonic oscillator excluding the decomposition frequency (see next subsection). For a system at constant volume, both partition functions correlate with the free energy  $F$  according to  $F(V,T) = -k_{\text{B}}T \ln Z(V,T)$ . Introducing the vibrational free energy difference of initial and transition state,  $\Delta F_{\text{vib}} = F_{\text{vib,TS}} - F_{\text{vib,IS}}$ , finally the Eyring formula for the jump rate at constant volume (Eq. 2.10) is obtained.

$$\Gamma(V,T) = \underbrace{\frac{k_{\text{B}}T}{h} e^{-\frac{\Delta F_{\text{vib}}(V,T)}{k_{\text{B}}T}}}_{\nu_0(V,T)} e^{-\frac{\Delta E_{\text{el}}^0(V)}{k_{\text{B}}T}} \quad (2.10)$$

Similar to the Arrhenius equation (Eq. 2.4), the Eyring formula (Eq. 2.10) is a product of an attempt frequency, here  $\nu_0(V,T)$ , and an exponential term containing the electronic energy difference,  $\Delta E_{\text{el}}^0(V)$ , whereat the latter is temperature independent. The definition of the attempt frequency according to Eyring in Eq. 2.10 is commonly used in literature since  $\nu_0(V,T)$  is independent of temperature at high temperatures (see section 6.1) and can be easily used in combination with the electronic energy difference  $\Delta E_{\text{el}}^0$  which is the standard result for *ab initio* calculations.

In addition, the total free energy difference between transition state and initial state can be used, again, with the assumption of no excited electronic states for temperatures far below the Fermi temperature

$$\Delta F = \Delta E_{\text{el}}^0 + \underbrace{\Delta E_{\text{vib}} - T \Delta S_{\text{vib}}}_{\Delta F_{\text{vib}}}, \quad (2.11)$$

where  $\Delta E_{\text{vib}}$  is the vibrational energy difference and  $\Delta S_{\text{vib}}$  the entropy difference of initial and transition state. Thus, Eq. 2.10 can be written as

$$\begin{aligned} \Gamma(V,T) &= \frac{k_{\text{B}}T}{h} e^{-\frac{\Delta F(V,T)}{k_{\text{B}}T}} \\ &= \underbrace{\frac{k_{\text{B}}T}{h} e^{\frac{\Delta S_{\text{vib}}(V,T)}{k_{\text{B}}}} e^{-\frac{\Delta E_{\text{vib}}(V,T)}{k_{\text{B}}T}}}_{\nu_0(V,T)} e^{-\frac{\Delta E_{\text{el}}^0(V)}{k_{\text{B}}T}}. \end{aligned} \quad (2.12)$$

Until now, it was assumed that the volume of the solid is constant during the migration, while experiments are usually performed at a constant pressure of  $p = 1$  bar. This leads to a change in volume during the jump of the oxygen ion from the initial to the transition state, which is limited as atomic displacements in a solid proceed with the speed of sound.<sup>[123–125]</sup> Nevertheless, the attempt frequency can be calculated at constant pressure. Similar to Eqs. 2.6 and 2.8 the reaction rate is

$$\text{reaction rate} = \nu_d \underbrace{\frac{k_B T}{h \nu_d}}_{c_{\text{TS}}} c_{\text{TS}}' = \nu_d \underbrace{\frac{k_B T}{h \nu_d}}_k K' c_{\text{TS}}. \quad (2.13)$$

Therefore, the activated states with the concentration  $c_{\text{TS}}$  decompose to the product with the unknown decomposition frequency  $\nu_d$ , while for the modified concentration  $c_{\text{TS}}'$  the prefactor  $k_B T/h$  is e.g.  $1.9 \cdot 10^{13} \text{ s}^{-1}$  at 900 K. Using the change in standard Gibbs free energy between transition and initial state  $\Delta G = -k_B T \ln K'$  according to the Van't Hoff isotherm results in the jump rate:<sup>[122,126]</sup>

$$\Gamma(p, T) = \frac{k_B T}{h} e^{-\frac{\Delta G(p, T)}{k_B T}} = \underbrace{\frac{k_B T}{h} e^{-\frac{\Delta S_{\text{vib}}(p, T)}{k_B}}}_{\nu_s(p, T)} e^{-\frac{\Delta H(p, T)}{k_B T}}, \quad (2.14)$$

with the Gibbs free energy difference  $\Delta G = \Delta H - T \Delta S_{\text{vib}}$  while assuming no change in the electronic entropy. Here, all thermodynamic quantities are in standard state i.e. their pure form at 1 bar. Of course, this derivation can also be used for the constant volume case. The enthalpy of migration at constant pressure is  $\Delta H = \Delta E_{\text{el}}^0 + \Delta E_{\text{vib}} + p \Delta V$ . In this work, the electronic energy difference  $\Delta E_{\text{el}}^0$ , the attempt frequency  $\nu_0(p, T)$ , the vibrational energy difference  $\Delta E_{\text{vib}}$  and the migration volume  $\Delta V$  are calculated for a system at zero pressure (see section 6.1) which is a good approximation for  $p = 1$  bar. The resulting pressure-volume work of migration  $p \Delta V$  with  $p = 1$  bar is rather small (about  $10^{-6}$  eV) and will be neglected here:<sup>[119]</sup>

$$\Gamma(p, T) = \underbrace{\frac{k_B T}{h} e^{-\frac{\Delta S_{\text{vib}}(p, T)}{k_B}} e^{-\frac{\Delta E_{\text{vib}}(p, T)}{k_B T}}}_{\nu_0(p, T)} e^{-\frac{\Delta E_{\text{el}}^0(p)}{k_B T}}. \quad (2.15)$$

While theoretical calculations use the enthalpy of migration  $\Delta H$  to calculate the jump rate according to Eq. 2.14, experimental measurements rely on the activation enthalpy  $\Delta H_a$  (Eq. 2.4). Using the definition of the activation enthalpy  $\Delta H_a = k_B T^2 (\partial \ln \Gamma(p, T) / \partial T)$  according to Eq. 2.4 in Eq. 2.14, the relation between both energies can be formulated by  $\Delta H_a = \Delta H + k_B T$  leading to

$$\Gamma(p, T) = \underbrace{\frac{k_B T}{h} e^{-\frac{\Delta S_{\text{vib}}(p, T)}{k_B}} e^1}_{\nu_{\text{exp, V}\bullet\text{O}}(p, T)} e^{-\frac{\Delta H_a(p, T)}{k_B T}}. \quad (2.16)$$

In theoretical calculations, the attempt frequency  $\nu_0(p, T)$  according to the Eyring theory is combined with the electronic energy difference at zero temperature  $\Delta E_{\text{el}}^0(p, T)$  to calculate the reaction rate (Eq. 2.15). In experiments, the measured quantities are the experimental attempt frequency  $\nu_{\text{exp, V}\bullet\text{O}}(p, T)$  and the activation enthalpy  $\Delta H_a(p, T)$  (Eq. 2.16). Therefore, both equations cannot be directly compared, in general. However, for ceria and Sm doped ceria the vibrational energy  $\Delta E_{\text{vib}}$  is calculated in this work to be approximately  $-k_B T$  at high temperature. This corresponds

exactly to the value of the missing vibrational degree of freedom of the transition state that consists of kinetic and potential energy. As a result, calculated attempt frequencies  $\nu_0(p, T)$  and experimental attempt frequencies  $\nu_{\text{exp}, \text{V}\ddot{\text{O}}}(p, T)$  can be directly compared. In conductivity and diffusion experiments, only a macroscopic attempt frequency  $\bar{\nu}_{\text{exp}, \text{V}\ddot{\text{O}}}(p, T)$  and activation enthalpy can be extracted. Hence, calculated and experimental attempt frequencies can only be directly compared according to Eq. 2.4 if all jump environments are equivalent.

The attempt frequency is commonly assumed to be ‘a typical value’ between  $10^{12} \text{ s}^{-1}$  and  $10^{13} \text{ s}^{-1}$ .<sup>[103,127,128]</sup> This is based on the assumption that the vibrational partition functions of initial and activated state in Eyring’s formula (Eq. 2.8) are similar<sup>[119]</sup> resulting in the frequency  $k_{\text{B}}T/h$  that is  $6.2 \cdot 10^{12} \text{ s}^{-1}$  at room temperature and  $1.9 \cdot 10^{13} \text{ s}^{-1}$  at 900 K.

### 2.3.3 Transition State Theory according to Vineyard

Vineyard<sup>[110]</sup> adapted Eyring’s concept to the movement of defects in solids in 1957. Even though only one atom jumps in the elementary process, the movement of defects is essentially a many-body process since the migrating defect interacts with neighboring atoms. The absolute rate theory is in its general form already a many-body process; however, most authors had oversimplified solid state processes to one-body models or assumed that all surrounding atoms are fixed. Vineyard avoided these reductions. A hyper-surface is defined, which passes through the transition state and is orthogonal to contours of equal potential energy separating the initial and the final jump position. The jump rate is given by the ratio of representative points on one side of the hyper-surface to the number of points crossing the hyper-surface from just this site. Any representative point of the system that reaches the hyper-surface with finite velocity will unavoidably cross to the product site. This corresponds to the transition state in the Eyring theory, which always decomposes to the product. Using the theory of small vibrations, a high-temperature approximation and a reduction to the Gamma Point, the attempt frequency can be calculated by the Vineyard formula

$$\nu_0 = \frac{\prod_i^N \nu_i}{\prod_j^{N-1} \nu_j}, \quad (2.17)$$

where  $\nu_i$  and  $\nu_j$  are the normal frequencies for vibration in the initial and transition state at the Gamma point, respectively. Thereby, the product for the initial state features one additional normal frequency compared to the transition state product. Limitations of the Vineyard theory were illustrated by Bennett<sup>[129,130]</sup> and Da Fano *et al.*<sup>[131]</sup> A similar solution to the Vineyard method was formulated by Rice in 1985.<sup>[132–134]</sup> Further historical developments include various modifications to account for quantum effects during hydrogen diffusion.<sup>[135–138]</sup>

### 2.3.4 Equivalence of the Eyring and Vineyard Theory

Many authors refer to the equivalence of the Eyring and the Vineyard method in the harmonic approximation at high temperature in case only phonons at the Gamma point are considered in both methods.<sup>[103,139,140]</sup> Indeed many groups calculate phonon modes for the Gamma point only<sup>[141–143]</sup> unless thermodynamic properties derived from the phonon dispersion on the whole reciprocal lattice grid are of special interest.<sup>[141,142,144–147]</sup> According to this, the vibrational free energy is sometimes calculated for several phonon wave vectors  $\mathbf{q}$  ( $\mathbf{q}$ -point mesh),<sup>[103,148–151]</sup> extending the Eyring method to the full Brillouin zone. In fact, also the Vineyard method can be applied to a phonon mesh with several wave vectors, but this possibility is only mentioned by Fedorov and Sadreev.<sup>[152]</sup> To the authors knowledge, there is no example in literature in which the equivalence of the Eyring and the Vineyard method is shown without restriction to the Gamma point. For this reason, this derivation will be described in the following.

The canonical partition function for  $M$  discrete wave vectors with the index  $q$  is defined as

$$Z_{\text{vib}} = \prod_q^M \left( \prod_i^N \sum_n e^{-\frac{E_{q,i,n}}{k_B T}} \right)^{\frac{1}{M}}, \quad (2.18)$$

where the  $N$  phonon bands, equivalent to the degrees of freedom, have the index  $i$  and the microstates have the index  $n$ .<sup>1</sup> For the vibrational partition function, the harmonic approximation and therewith the energy eigenvalues  $E_{q,i,n} = h\nu_{q,i}(1/2 + n)$  of the quantum harmonic oscillator with its frequency  $\nu_{q,i}$  can be used (see also Maradudin<sup>[153]</sup> and Wimmer *et al.*<sup>[140]</sup>). The vibrational energy  $F_{\text{vib}}$  can be calculated from the partition function  $F_{\text{vib}} = -k_B T \ln Z_{\text{vib}}$  resulting in

$$\begin{aligned} F_{\text{vib}} &= \sum_{q,i} \left\{ \frac{h\nu_{q,i}}{2M} + \frac{k_B T}{M} \ln \left[ 1 - \exp \left( -\frac{h\nu_{q,i}}{k_B T} \right) \right] \right\} \\ &= \frac{k_B T}{M} \sum_{q,i} \ln \left( 2 \sinh \frac{h\nu_{q,i}}{2k_B T} \right). \end{aligned} \quad (2.19)$$

Here  $\sum_{q,i} h\nu_{q,i}/2M$  is independent of temperature and can be regarded as zero point energy correction to the energy barrier  $\Delta E_{\text{el}}^0$ . The attempt frequency can be calculated corresponding to the Eyring theory (Eq. 2.10):

$$\begin{aligned} \nu_0 &= \frac{k_B T}{h} \frac{\prod_q^M \prod_i^N \left( 2 \sinh \frac{h\nu_{q,i}}{2k_B T} \right)^{\frac{1}{M}}}{\prod_m^M \prod_j^{N-1} \left( 2 \sinh \frac{h\nu_{m,j}}{2k_B T} \right)^{\frac{1}{M}}} \\ &\approx \frac{k_B T}{h} \frac{\prod_q^M \prod_i^N \left( 1 - e^{-\frac{h\nu_{q,i}}{k_B T}} \right)^{\frac{1}{M}}}{\prod_m^M \prod_j^{N-1} \left( 1 - e^{-\frac{h\nu_{m,j}}{k_B T}} \right)^{\frac{1}{M}}}. \end{aligned} \quad (2.20)$$

---

<sup>1</sup>The partition function is calculated as geometric mean for all discrete wave vectors, just as the arithmetic mean of all wave vectors would be used for the phonon density of states to satisfy its normalization condition.

The indices  $i$  (phonon band) and  $q$  (wave vector) for the initial state correspond to the indices  $j$  and  $m$  for the transition state. The transition state has one degree of freedom less than the initial state. For the last part in Eq. 2.20, which is given for comparison with literature, it is assumed that the difference in zero point energy can be neglected, which might be valid at high temperature.<sup>[154]</sup>

As a further approach that is often performed in literature, the Taylor expansion of the hyperbolic sine can be simplified for high temperatures (see Eq. 2.21) to  $\sinh x \approx x$ . Equation 2.21 is often referred to as the classical limit<sup>[155]</sup> of the vibrational free energy of the ‘quantum mechanical’ vibrational free energy in Eq. 2.19.

$$F_{\text{vib}} = \frac{k_{\text{B}}T}{M} \sum_{q,i} \ln \left( \frac{h\nu_{q,i}}{k_{\text{B}}T} \right) \quad (2.21)$$

Inserting Eq. 2.21 in the Eyring formula (Eq. 2.10) leads to

$$\nu_0 = \frac{\prod_q^M \prod_i^N \nu_{q,i}^{\frac{1}{M}}}{\prod_m^M \prod_j^{N-1} \nu_{m,j}^{\frac{1}{M}}}. \quad (2.22)$$

The resulting attempt frequency (Eq. 2.22) allows the general use of the classical Vineyard method for high temperatures and any phonon mesh. If only the Gamma point is considered ( $M = 1$ ), the classical Vineyard formula (Eq. 2.17) is obtained.

## 2.4 Conductivity in Doped Ceria

In this chapter, ionic conductivities or precisely oxygen ion conductivities of doped ceria according to experiments are presented. Interpretations of these conductivities according to literature are summarized in Chapter 2.5.

Direct current (DC) measurements show the total conductivity of a polycrystalline sample. Impedance spectroscopy (AC) measurements allow the separation of the resistivity in the grains (grain interior, bulk) and the resistivity in the grain boundaries, which are both inverse (cp. Chapter 4.1.5) to the macroscopic conductivity.

### 2.4.1 The Total Conductivity

#### Sm Doped Ceria

Sm doped ceria has one of the highest conductivities reported for a ternary cerium oxide. The total conductivity of polycrystalline Sm doped ceria at 600 °C is shown in Fig. 2.7 as a function of dopant fraction  $x$  in  $\text{Ce}_{1-x}\text{Sm}_x\text{O}_{2-x/2}$ . The curve progression and its interpretation is the main objective of this work.

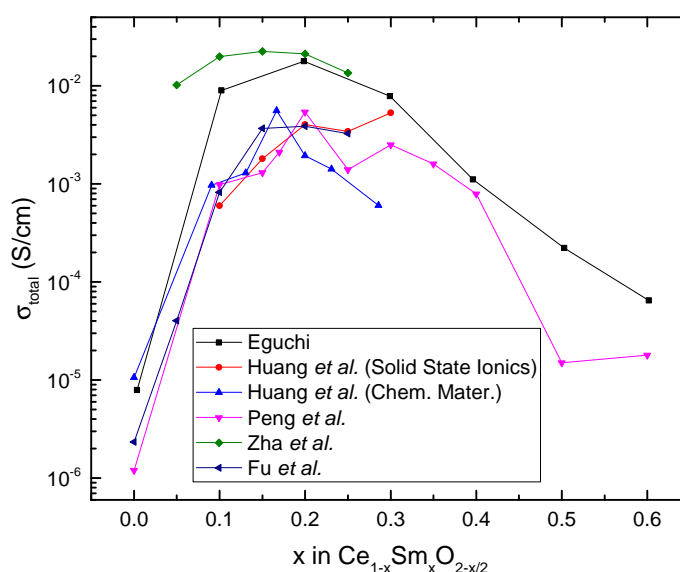


Figure 2.7: Total ionic conductivity of polycrystalline Sm doped ceria at 600 °C. <sup>[28,73,156–158]</sup> Lines are a guide to the eye only.

The conductivity first increases and then decreases with increasing dopant fraction. The dopant fraction leading to the maximum in conductivity is referred to as  $x_{\text{max}}$ . A summary of all  $x_{\text{max}}$  is shown in Table 2.1. Each research group found for the entire investigated temperature range the same  $x_{\text{max}}$ .

reference	$x_{\max}$	temperature
Yu <i>et al.</i> <sup>[159]</sup>	0.12	230 – 900 °C
Zha <i>et al.</i> <sup>[73]</sup>	0.15	400 – 850 °C
Huang <i>et al.</i> (Chem. Mater.) <sup>[160]</sup>	0.17 <sup>a</sup>	200 – 600 °C
Eguchi <sup>[28]</sup>	0.2	500 – 900 °C
Huang <i>et al.</i> (Solid State Ionics) <sup>[156]</sup>	0.2–0.3	200 – 640 °C
Peng <i>et al.</i> <sup>[158]</sup>	0.2	600 °C
Fu <i>et al.</i> <sup>[157]</sup>	0.2	500 – 800 °C

Table 2.1: Dopant fractions that lead to the highest total ionic conductivity for polycrystalline  $\text{Ce}_{1-x_{\max}}\text{Sm}_{x_{\max}}\text{O}_{2-x_{\max}/2}$  samples in the measured temperature range.

<sup>a</sup>The grain size is comparably small with 100 – 500 nm.

At high dopant fractions, few measurements show again an increase in conductivity with increasing dopant fraction (Fig. 2.7). Both the measurements from Huang *et al.*<sup>[156]</sup> and Peng *et al.*<sup>[158]</sup> show an increase in total conductivity from  $x = 0.25$  to  $x = 0.3$ . For the measurements of Huang *et al.*,<sup>[156]</sup> this is even the global maximal conductivity.

The conductivities measured by different groups scatter for about one order of magnitude. Reasons for that are investigated in this work in Chapter 8.1 and a strong influence of the synthesis on the conductivity is found.

## Other Rare-Earth Dopants

Different trivalent rare-earth dopants lead to different conductivities. Often, only a single dopant fraction is investigated for comparison. This dopant fraction may be different from the dopant fraction leading to the maximum in conductivity and  $x_{\max}$  may vary between different dopants. Therefore, the investigation of a single dopant fraction gives only a hint to the optimal dopant leading to the highest conductivity.

Figure 2.8 shows the total ionic conductivity of  $\text{Ce}_{1-x}\text{RE}_x\text{O}_{2-x/2}$  according to Balazs and Glass,<sup>[62]</sup> Yahiro *et al.*<sup>[29,161]</sup> and Eguchi *et al.*<sup>[27]</sup> ( $x = 0.2$ ) and Kudo and Obayashi ( $x = 0.3$ )<sup>[162]</sup> using the ionic radii of  $\text{RE}^{3+}$  according to Shannon.<sup>[32]</sup> The work of Yahiro *et al.* was slightly modified by the same group later, especially the conductivity of Gd doped ceria. Eguchi *et al.* found similar results. Balazs and Glass found smaller conductivities for the same compositions. As expected, higher temperatures lead to higher conductivities.

For  $x = 0.2$ , doping with Sm leads to the highest total ionic conductivity. For dopants with higher or lower ionic radii, the total ionic conductivity is lower. Especially the results of Yahiro *et al.* and Eguchi *et al.* suggest a linear relationship between ionic radius and total conductivity. A fit for the linear relationship is shown with the red and blue line, for Balazs and Glass arbitrary values were

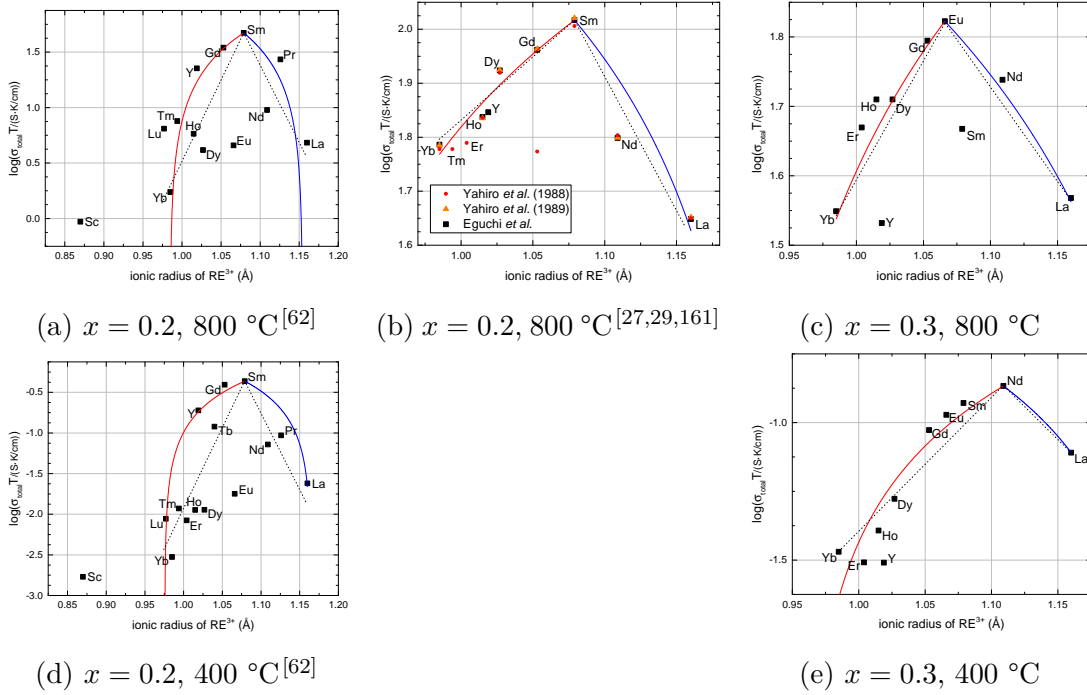


Figure 2.8: Total ionic conductivity of  $\text{Ce}_{1-x}\text{RE}_x\text{O}_{2-x/2}$  for  $x = 0.2$ , [27,29,62,161] and  $0.3$ . [162] The lines show a possible linear relationship between the ionic radius and the conductivity (solid lines) or the logarithm of the conductivity (dashed lines).

chosen. For comparison, the dashed lines in Fig. 2.8 show a linear relationship between the ionic radius and the logarithm of the total conductivity. The relation between different conductivities as a function of dopant is similar at  $400\text{ °C}$  and  $800\text{ °C}$ .

For  $x = 0.3$ , the order of precedence for ‘best’ dopant changes and is temperature dependent. At  $400\text{ °C}$ , Eu and Gd lead to large ionic conductivities while the conductivity of Sm doped ceria is low. At  $800\text{ °C}$ , Nd, Sm, Eu and Gd lead to large ionic conductivities.

### 2.4.2 The Bulk Conductivity

For polycrystalline samples, the total conductivity is influenced by the bulk and grain boundary domain. In the bulk domain, oxygen ions jump through the regular lattice. In the grain boundary domain, jumps take place along or across dislocations and in space charge zones. The separation of both domains is possible using e.g. impedance spectroscopy measurements and will be discussed in Chapter 4.1.5. Influences on the grain boundary domain will be discussed in Chapter 8.1. In the present work, the bulk domain is of particular interest as it represents the inherent property of the doped material largely without influences of the microstructure of the sample. Therefore, the bulk conductivity is measured and simulated in this work.

Figure 2.9 shows the influences of bulk and grain boundary conductivity on the total conductivity

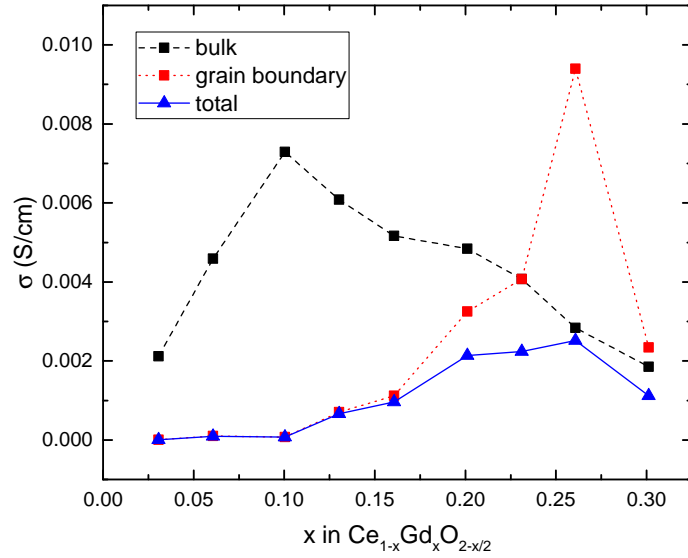


Figure 2.9: Bulk, grain boundary and total ionic conductivity of Gd doped ceria at 500 °C according to Steele.<sup>[86]</sup> Lines are a guide to the eye only.

of Gd doped ceria at 500 °C. The curve progressions are significantly different. For small dopant fractions, the total conductivity is limited by the low grain boundary conductivity, which is discussed further in Chapter 4.1.5. For large dopant fractions, the conductivity is limited by the low bulk conductivity. Compared to the total domain,  $x_{\max}$  is small for the bulk conductivity.

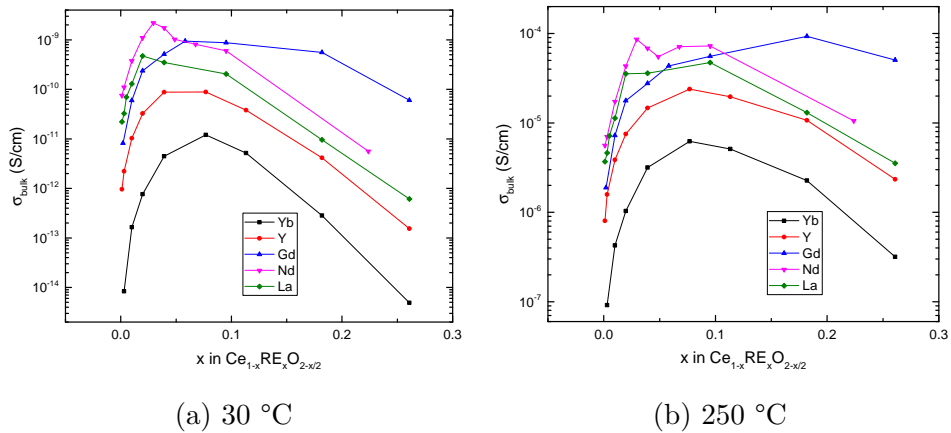


Figure 2.10: Bulk ionic conductivity of doped ceria at 30 °C (left) and 250 °C (right) according to an Arrhenius fit of the data of Faber *et al.* for measurements between 30 °C and 330 °C.<sup>[163]</sup> Lines are a guide to the eye only.

The bulk conductivity depends significantly on the type of dopant and the investigated temperature. Figure 2.10 shows the bulk ionic conductivity of Yb, Y, Gd, Nd and La doped ceria at 30 °C and 250 °C according to Faber *et al.*<sup>[163]</sup>

For small dopant fractions, Nd doped ceria possess the highest bulk conductivities with a max-

imum at  $x_{\max} = 0.03$ . For large dopant fractions, Gd doped ceria possess the highest bulk conductivities with a maximum at  $x_{\max} = 0.06-0.18$ . The dopant fraction leading to the maximum in conductivity decreases with increasing dopant radius, with the exception of Gd doped ceria at 250 °C. This behavior is further investigated in the next section. The relation between conductivities of different dopants is similar at 30 °C and 250 °C. Nowick *et al.*<sup>[164]</sup> showed for Y doped ceria at 181 °C similar conductivities as the Arrhenius fit of the data of Faber *et al.*

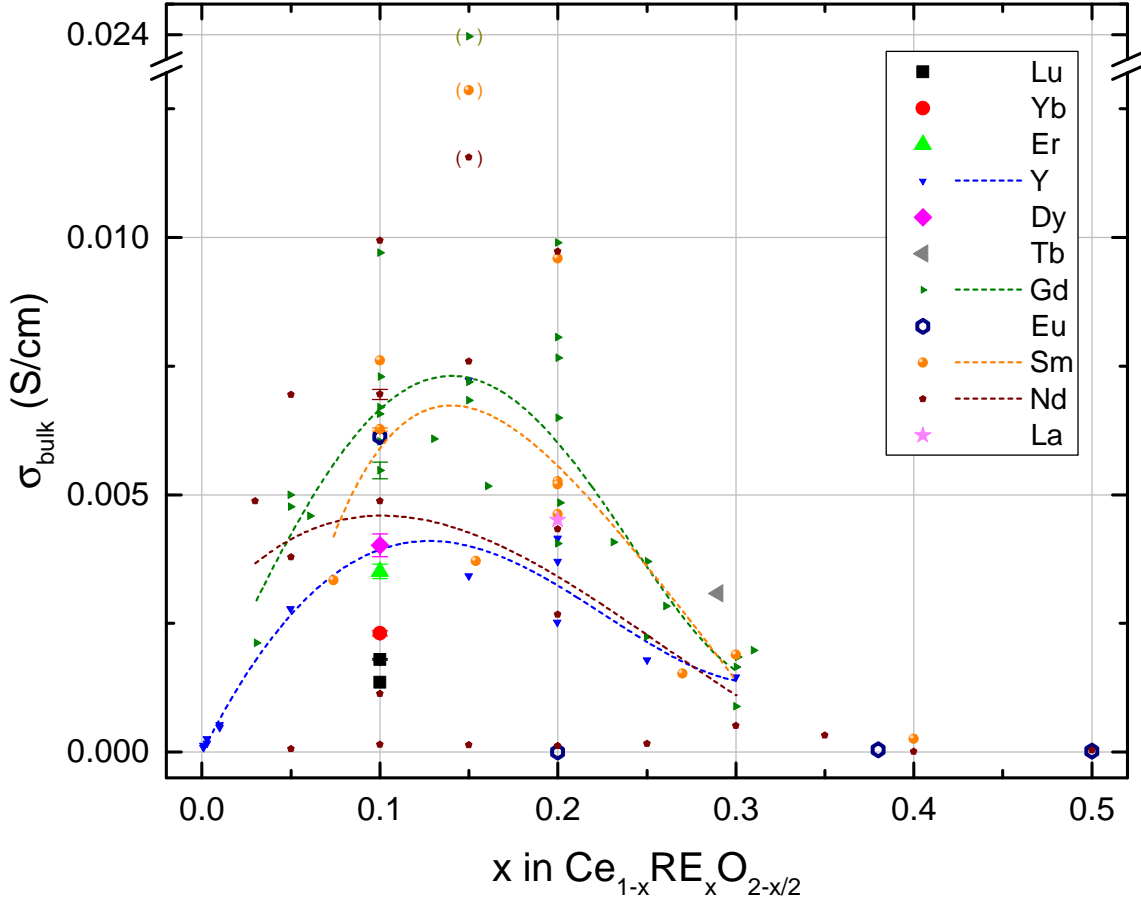


Figure 2.11: Bulk ionic conductivity at 500 °C for Lu,<sup>[165,166]</sup> Yb,<sup>[166]</sup> Er,<sup>[166]</sup> Y,<sup>[163,166-172]</sup> Dy,<sup>[166]</sup> Tb,<sup>[71]</sup> Gd,<sup>[64,86,166,169-177]</sup> Eu,<sup>[71,178]</sup> Sm,<sup>[74,166,169-172,179-181]</sup> Nd<sup>[75,76,166,170,182,183]</sup> and La doped ceria.<sup>[169]</sup> Fourth order polynomials were fitted to the data with exception of the data of Zajac and Molenda (in parentheses), which was disregarded due to its strong deviation compared to other literature data, as a guide to the eye only to show the general trend of the data (dashed lines).

For 500 °C, a summary of several experiments is shown in Fig. 2.11. A strong scattering between different experiments is found. The dopant fractions leading to the maximum in conductivity differ significantly and will be investigated in the next section.

Nevertheless, a general increase and decrease in conductivity with increasing dopant radius with

a maximum around Gd and Sm doped ceria is found. For example, Mogensen *et al.*<sup>[184]</sup> found decreasing conductivities at 1000 °C in the series Gd, Y, La and Sc doped ceria ( $x = 0.1$ ). Omar *et al.*<sup>[166]</sup> investigated Lu, Yb, Er, Y, Dy, Gd, Sm, Nd doped ceria ( $x = 0.1$ ) and found between 400–600 °C an increasing conductivity with increasing dopant radius, which is in disagreement with the other studies. Zajac<sup>[170]</sup> studied Y, Gd, Sm and Nd doped ceria ( $x = 0.15$ ) at 700 °C where Gd doped ceria has the largest conductivity. Pérez-Coll *et al.*<sup>[169]</sup> investigated Y, Gd, Sm and La doped ceria ( $x = 0.2$ ) and found between 200–700 °C the largest conductivity for Sm doped ceria.

It is surprising that only a few dopant fractions of Sm doped ceria were examined despite its high conductivity. Polycrystalline samples were analyzed for  $x = 0.1, 0.2$  and  $0.3$ ,<sup>[74,166,169,171,172,180,181]</sup> or  $0.15$ ,<sup>[170]</sup> while Sanghavi *et al.*<sup>[179]</sup> investigated single crystal thin films for few different dopants fractions. For a complete picture, Sm doped ceria was investigated in this work and results will be presented in Chapter 8.2.2.

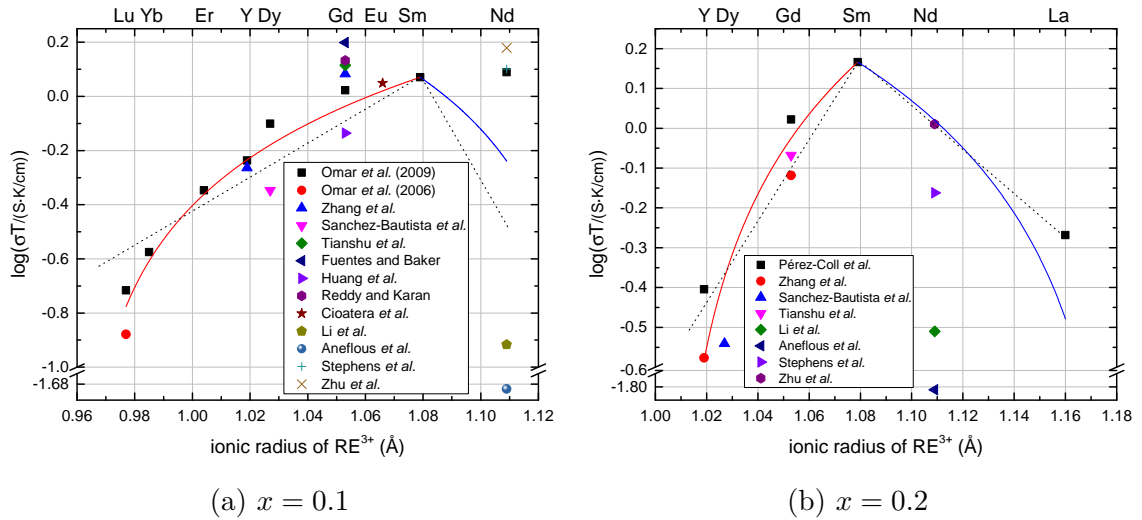


Figure 2.12: Bulk ionic conductivity at 400 °C of  $\text{Ce}_{1-x}\text{RE}_x\text{O}_{2-x/2}$  for  $x = 0.1$ ,<sup>[64,69,75,76,165,166,168,174,177,178,182,183,185]</sup> and  $0.2$ .<sup>[64,69,75,76,168,169,182,183]</sup> The lines show a possible linear relationship between the ionic radius and the conductivity (solid lines) or the logarithm of the conductivity (dashed lines).

Again, the conductivity for a single dopant fraction can be investigated. In Fig. 2.12, the bulk conductivity at 400 °C for  $x = 0.1$  and  $0.2$  is extracted. For  $x = 0.2$ , doping with Sm leads to the highest bulk ionic conductivity as seen before for the total conductivity. For  $x = 0.1$  the conductivity of Gd, Eu, Sm and Nd doped ceria is similar as seen before for the total conductivity at  $x = 0.3$ . A linear relationship between ionic radius and bulk conductivity cannot clearly be verified due to strong scattering, especially for Nd doped ceria. A fit of the linear relationship is shown with the red line; the linear relationship shown by the blue line is a guide to the eye only. For comparison, the dashed lines show a linear relationship between the ionic radius and the logarithm of the bulk conductivity.

### 2.4.3 Dopant Fraction with the Highest Conductivity

The dopant fraction leading to the maximum in conductivity depends on the type of dopant and the measured temperature range and varies between different research groups. In this chapter, an overview of  $x_{\max}$  for the total and bulk conductivity is given.

#### The Total Conductivity

For the total conductivity, the dopant fraction leading to the maximum in conductivity is shown in Table 2.2 and Fig. 2.13a. The nearest measured dopant fractions, compared to  $x_{\max}$ , with lower conductivity are shown in Fig. 2.13a using error bars.

dopant	$x_{\max}$	temperature	reference
Yb	0.15	500 °C	Ou <i>et al.</i> <sup>[186]</sup>
Y	0.10	300 – 500 °C	
	0.20	600 – 900 °C	Van herle <i>et al.</i> <sup>[187]</sup>
	0.25	1000 °C	
	0.16	400 – 800 °C	Balazs <i>et al.</i> <sup>[62,188]</sup>
Dy	0.1	200 – 900 °C	Sánchez-Bautista <i>et al.</i> <sup>[69]</sup>
	0.2	400 – 600 °C	Acharya <i>et al.</i> <sup>[189]</sup>
Gd	0.20	430 – 870 °C	Kudo and Obayashi <sup>[190]</sup>
	0.30	870 – 980 °C	
	0.12	160 – 710 °C	Hohnke <sup>[36]</sup>
	0.20	710 – 1400 °C	
	0.26	500 °C	Steele <sup>[86]</sup>
	0.15	300 – 400 °C	Tianshu <i>et al.</i> <sup>[64]</sup>
	0.20	400 – 800 °C	
	0.15	400 – 850 °C	Zha <i>et al.</i> <sup>[73]</sup>
Sm	0.12–0.2		see Table 2.1
Nd	0.15	250 – 800 °C	Zhu <i>et al.</i> <sup>[183]</sup>
La	0.1	500 °C	Zheng <i>et al.</i> <sup>[77]</sup>
	0.15	600 – 800 °C	
	0.15	300 – 600 °C	Dikmen <i>et al.</i> <sup>[63]</sup>

Table 2.2: Dopant fractions that lead to the highest *total* ionic conductivity for  $\text{Ce}_{1-x_{\max}}\text{RE}_{x_{\max}}\text{O}_{2-x_{\max}/2}$  samples in the measured temperature range.

For the total conductivity,  $x_{\max}$  is found between 0.1 and 0.3. The distribution of  $x_{\max}$  is very

broad especially for medium ionic radii, which lead to the highest conductivities. Measurements at low temperature lead rather to low  $x_{\max}$ , while measurements at high temperature lead rather to high  $x_{\max}$ . This is shown in Fig. 2.13a using a blue and a red line. The reason for the temperature dependence is the increase in activation enthalpy with increasing dopant fraction, which is shown in the next section. For all dopants, at least one reference is found with a dopant fraction leading to the maximum in conductivity of  $x_{\max} = 0.15$ . The lowest  $x_{\max}$  is found for the total conductivity at 0.1.

For Pr<sup>[191,192]</sup> and Dy doped ceria,<sup>[72]</sup> impedance measurements show an increase in conductivity with increasing dopant content for low and intermediate temperatures. This is caused by a decrease in ionic transference number and, therefore, an increase in electronic contribution with increasing dopant fraction.

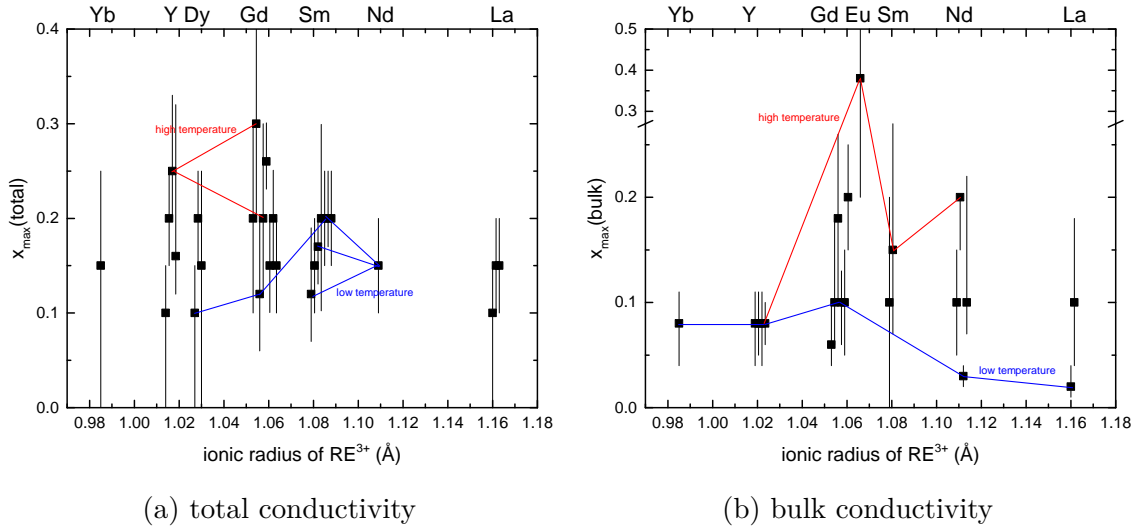


Figure 2.13: Dopant fractions that lead to the highest ionic conductivity for  $\text{Ce}_{1-x_{\max}}\text{RE}_{x_{\max}}\text{O}_{2-x_{\max}/2}$  samples in the measured temperature range. Errors bars indicate the nearest measured dopant fraction with lower conductivity.  $x_{\max}$  for low and high temperature measurements are marked (lines).

## The Bulk Conductivity

For the bulk conductivity, the dopant fraction leading to the maximum in conductivity is found between  $x_{\max} = 0.02$  and  $0.38$  (Table 2.3 and Fig. 2.13b). The distribution of  $x_{\max}$  is even broader compared to the total conductivity especially again for medium ionic radii, which lead to the highest conductivities. Similar to the total conductivity, the measured temperature range and  $x_{\max}$  correlate. Measurements at low temperature lead rather to low  $x_{\max}$ , while measurements at high temperature lead rather to high  $x_{\max}$  (Fig. 2.13b). For all dopants, at least one reference is found with a dopant fraction leading to  $x_{\max}$  in conductivity of about  $x_{\max} = 0.1$ , which is the lowest  $x_{\max}$

found for the total conductivity. Generally,  $x_{\max}$  for the bulk domain is smaller than for the total domain as already expected from Fig. 2.9.

dopant	$x_{\max}$	temperature	reference
Yb	0.08	30 – 330 °C	Faber <i>et al.</i> <sup>[163]</sup>
Y	0.08	181 °C	Nowick <i>et al.</i> <sup>[164]</sup>
	0.08	80 – 200 °C	Wang <i>et al.</i> <sup>[167]</sup>
	0.08	80 – 330 °C	Faber <i>et al.</i> <sup>[163]</sup>
	0.08	500 – 700 °C	Tian and Chan <sup>[193,194]</sup>
Gd	0.06	30 °C	
	0.10	80 °C	Faber <i>et al.</i> <sup>[163]</sup>
	0.18	130 – 330 °C	
	0.10	500 °C	Steele <sup>[86]</sup>
	0.10	350 – 450 °C	
	0.20	450 – 500 °C	Tianshu <i>et al.</i> <sup>[64]</sup>
Eu	0.38	400 – 600 °C	Li <i>et al.</i> <sup>[71]</sup>
Sm	0.1	250 – 550 °C	Zhan <i>et al.</i> <sup>[74]</sup>
	0.15	500 – 700 °C	Sanghavi <i>et al.</i> <sup>[179]</sup>
Nd	0.10	300 – 500 °C	
	0.20	500 – 800 °C	Zhu <i>et al.</i> <sup>[183]</sup>
	0.03	30 – 280 °C	
	0.10	330 °C	Faber <i>et al.</i> <sup>[163]</sup>
La	0.02	30 – 170 °C	
	0.10	170 – 330 °C	Faber <i>et al.</i> <sup>[163]</sup>

Table 2.3: Dopant fractions that lead to the highest *bulk* ionic conductivity for  $\text{Ce}_{1-x_{\max}}\text{RE}_{x_{\max}}\text{O}_{2-x_{\max}/2}$  samples in the measured temperature range.

#### 2.4.4 The Activation Enthalpy of the Bulk Domain

The temperature dependent behavior of the conductivity in doped ceria can be shown in an Arrhenius plot (Fig. 2.14 left) according to Eqs. 2.3 and 2.4. While most literature sources show a linear relationship between  $\ln(\sigma T)$  and  $1/T$  and determine an activation enthalpy  $\Delta H_a$ , several groups find a distinct temperature dependence for low and high temperature. Then, the resulting  $\Delta H_a$  is high for the low temperature region and low for the high temperature region. This leads to a kink in the Arrhenius plot around 350–600 °C.<sup>[74,166,168,169,174,181,182,195]</sup> However, the difference in activation

enthalpy between low and high temperature region, which is referred to as experimental RE-V association enthalpy or association energy for an  $(\text{RE}'_{\text{Ce}}\text{V}_{\text{O}}^{\bullet\bullet})^{\bullet}$  associate, varies. While Omar *et al.* find association energies between only 0.02-0.05 eV for different dopants,<sup>[166]</sup> Gerhardt-Anderson and Nowick determine the association energy for Sc doped ceria to be 0.67 eV.<sup>[33]</sup> The (experimental) association energies are shown in Fig. 2.14 (right). From  $x = 0.001$  to 0.02 a decrease in association energy for Y doped ceria was found.<sup>[167]</sup> The same is true for Nd doped ceria from  $x = 0.01$  to 0.03.<sup>[182]</sup> From  $x = 0.03$  to 0.4 an increase in association energy for Y, Gd, Sm and Nd doped ceria was found.<sup>[74,168,182]</sup> Stephens and Kilner use the lowest migration energy of different dopant fractions as a reference to calculate the association energy.

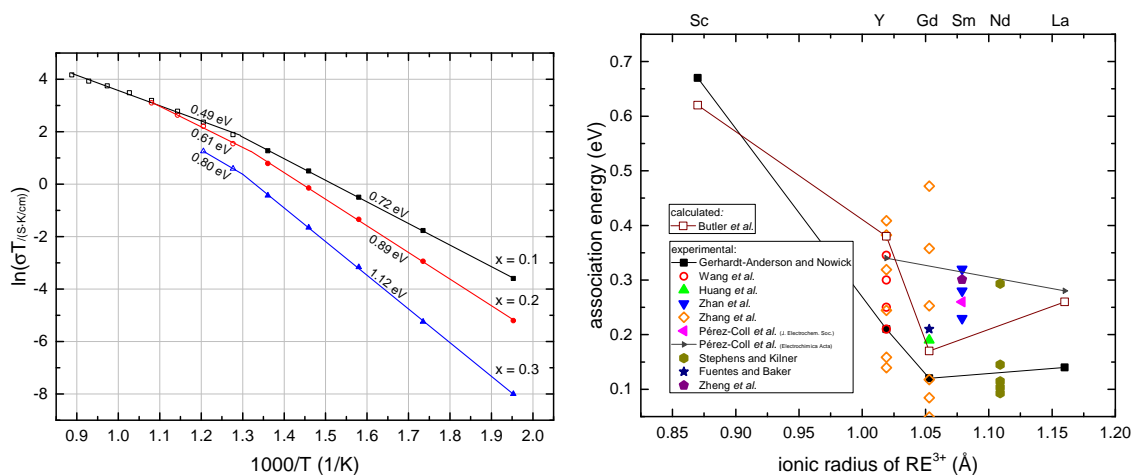


Figure 2.14: Arrhenius behavior of the ionic conductivity in  $\text{Ce}_{1-x}\text{Sm}_x\text{O}_{2-x/2}$  according to Zhan *et al.* (left).<sup>[74]</sup> Association energies according to literature (right).<sup>[33,39,74,166–169,174,181,182,185,195]</sup> For the latter, Lines are a guide to the eye only.

The activation enthalpy for rare-earth doped ceria is shown in Fig. 2.15 from measurements between room temperature and 330 °C and in Fig. 2.16 from measurements up to 1000 °C. Both temperature ranges show a similar behavior. Activation enthalpies scatter significantly, e.g. between 0.63 eV and 0.82 eV for  $\text{Ce}_{0.9}\text{Gd}_{0.1}\text{O}_{1.95}$  and between 0.80 eV and 0.94 eV for  $\text{Ce}_{0.8}\text{Gd}_{0.2}\text{O}_{1.9}$ . For Sm and Nd doped ceria, activation enthalpies scatter between 0.46 eV and 0.72 eV for  $\text{Ce}_{0.9}\text{Sm}_{0.1}\text{O}_{1.95}$  and between 0.65 eV and 0.82 eV for  $\text{Ce}_{0.9}\text{Nd}_{0.1}\text{O}_{1.95}$ .

In general, activation enthalpies first decrease and then increase as a function of dopant fraction, similar to other fluorite-structured oxides.<sup>[36]</sup> For example, a decreases between  $x = 0.001$ –0.02 was found for Y or Nd doped ceria.<sup>[167,182]</sup> An increases between  $x = 0.03$ –0.4 was found for Sm, Y, Gd or Nd doped ceria.<sup>[74,168,182]</sup>

The dopant fraction leading to a minimum in activation enthalpy is large for small dopants and small for large dopants. For example, Faber *et al.*<sup>[163]</sup> found minima in the activation enthalpy at  $x = 0.02$ –0.04 (for Nd), 0.08 (Yb), 0.04 (Y), 0.06 (Gd) and 0.02 (La).

At a single dopant fraction, the activation enthalpy decreases for an increasing dopant radius

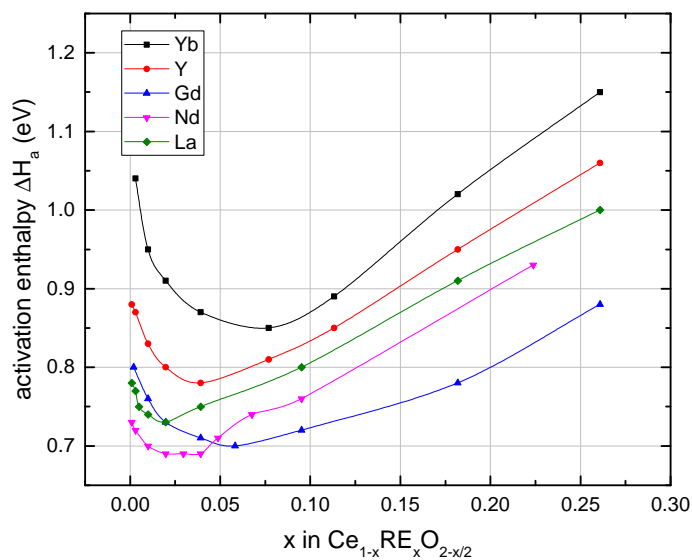


Figure 2.15: Activation enthalpy for the bulk ionic conductivity of doped ceria between room temperature and 330 °C according to Faber *et al.*<sup>[163]</sup> Lines are a guide to the eye only.

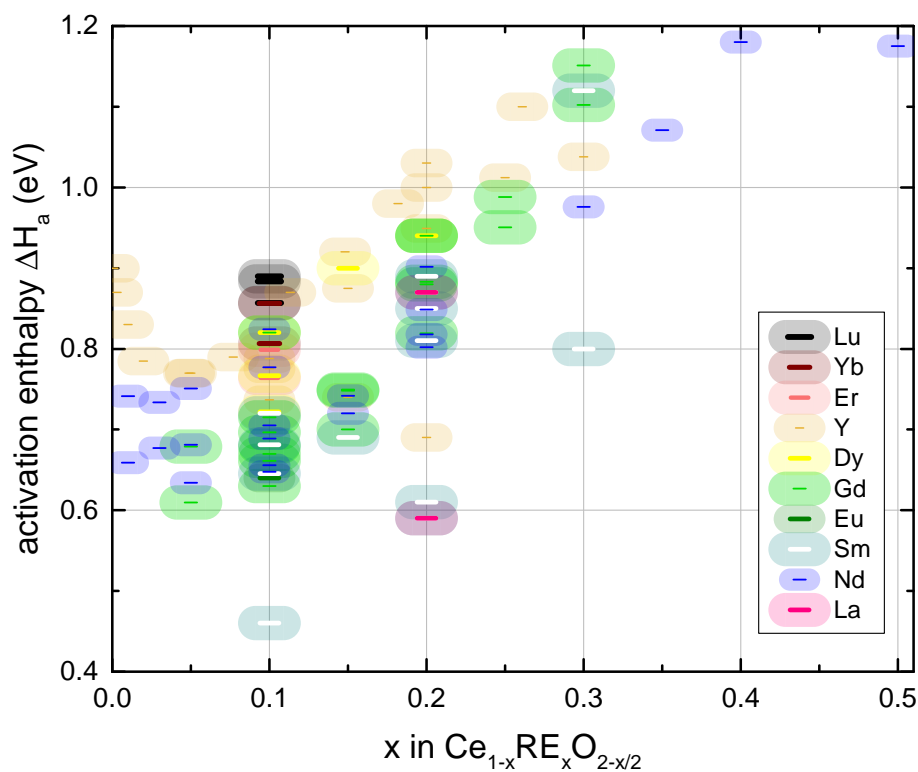


Figure 2.16: Activation enthalpy for the bulk ionic conductivity of doped ceria for various temperature ranges between room temperature and 1000 °C for Lu,<sup>[165,166]</sup> Yb,<sup>[166]</sup> Er,<sup>[166]</sup> Y,<sup>[166–170,180]</sup> Dy,<sup>[69,166]</sup> Gd,<sup>[64,166,168–170,173,174,176]</sup> Eu,<sup>[178]</sup> Sm,<sup>[74,166,170,180,195]</sup> Nd<sup>[76,166,170,182,183]</sup> and La doped ceria.<sup>[169]</sup>

up to about Gd, Eu, Sm, Nd and increases afterwards. For example, Faber *et al.*<sup>[163]</sup> investigated Yb, Y, Gd, Nd and La doped ceria where Nd doped ceria has the lowest activation enthalpy. Omar *et al.*<sup>[166]</sup> investigated Lu, Yb, Er, Y, Dy, Gd, Sm, Nd doped ceria ( $x = 0.1$ ) and found for Sm doped ceria the lowest  $\Delta H_a$ , similar to Zajac<sup>[170]</sup> who investigated Y, Gd, Sm and Nd doped ceria ( $x = 0.15$ ). Pérez-Coll *et al.*<sup>[169]</sup> investigated Y, Gd, Sm and La doped ceria ( $x = 0.2$ ) and also found the lowest  $\Delta H_a$  for Sm doped ceria.

### Activation Enthalpy and Ionic Conductivity

The analysis of the ionic conductivity in Chapter 2.4.2 and 2.4.3 and the activation enthalpy in Chapter 2.4.4 suggests that the curve progression of the activation enthalpy is inverted to the curve progression of the ionic conductivity. This was especially investigated by Wang *et al.*,<sup>[164,167]</sup> who showed for Y doped ceria that the maximum of the conductivity at 182 °C for different dopant fractions occurs at similar compositions as the minimum in activation enthalpy. The same applies to the data of Faber *et al.* (Fig. 2.15)<sup>[163]</sup> with the best dopants Gd and Nd and to the data of Pérez-Coll *et al.*<sup>[169]</sup> with the best dopant Sm. Mori *et al.* reported as well that the activation enthalpy mirrors the maximum in the conductivity for several dopant fractions in Gd doped ceria.<sup>[196]</sup> Deviations from this trend are shown by Omar *et al.*<sup>[166]</sup> and Zajac,<sup>[170]</sup> which might be influenced by sample preparation.

## 2.5 The Influence of Doping

In this chapter, interpretations of the oxygen ion conductivities of doped ceria according to literature are summarized. Therefore, only the bulk domain (Fig. 2.9) is discussed as it represents the inherent property of the doped material largely without influences of the microstructure of the sample.

Ionic conductivities (Chapter 2.4.2),  $x_{\max}$  (Chapter 2.4.3) and activation enthalpies (Chapter 2.4.4) are discussed. The influence of the dopant fraction and the influence of the type of dopant on the conductivity are analyzed.

### 2.5.1 Varying the Dopant Fraction

The oxygen ion conductivity increases steeply with increasing dopant fraction of the trivalent rare-earth dopant to a maximum at about  $x_{\max} = 0.08\text{--}0.2$  and then decreases gently similar to doped  $\text{ZrO}_2$ .<sup>[197]</sup>

The initial rise in oxygen ion conductivity with increasing dopant fraction is caused by the creation of oxygen vacancies according to Eq. 2.1.<sup>[34]</sup> If no further interactions existed, the ionic conductivity would increase to a maximum until half of the oxygen sublattice is unoccupied.<sup>[198]</sup> In experiments, the maximum in conductivity appears at significantly lower dopant fractions. According to literature, the position of the maximum clearly depends on the number of oxygen vacancies,<sup>1</sup> which are created per dopant, as in  $\text{Ca}^{2+}$  or  $\text{Sr}^{2+}$  doped ceria the maximum appears at lower dopant fractions.<sup>[25,199–202]</sup> Reasons given for the decrease in conductivity are the association between oxygen vacancies and dopants, the ordering of oxygen vacancies or a modified jump probability of the oxygen vacancies.

In literature, it is commonly assumed that the maximum in oxygen ion conductivity is caused by the *association* between oxygen vacancies and dopants. The association originates from the opposite charge of both defects and local relaxation of the crystal lattice. The migration energies for jumps away from the associating dopant are higher than in pure ceria, while jumps to the dopant are even more favored. These jump configurations are shown in Fig. 2.17, where the inequality symbols indicate the relation of the corresponding migration energies. In simple terms it is often described that the oxygen vacancies are trapped by the almost immobile dopants, and the concentration of the free vacancies is reduced.<sup>2</sup> Several experiments and calculations support this thesis:

It is assumed that the high-temperature and low-temperature regimes differ in activation enthalpy by the association energy between the migrating oxygen vacancy and the dopant (Chapter 2.4.4). While at low temperature vacancies are trapped or even immobile, at high temperature sufficient energy is available to free the vacancies, which leads to a decrease in activation enthalpy.<sup>[33,74,167]</sup>

---

<sup>1</sup>However, for e.g.  $\text{Ca}^{2+}$  doped ceria the association energy and the jump barriers around  $\text{Ca}^{2+}$  differ significantly compared to most rare-earth dopants, which is rarely discussed in literature.

<sup>2</sup>This picture is an oversimplification as vacancies are not trapped for an infinitely long duration.

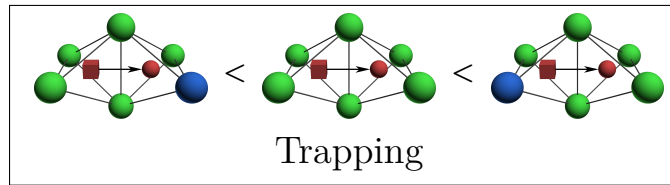


Figure 2.17: The migration energy increases if the oxygen ion jump decreases the association.

However, activation enthalpies at high temperature still depend on the dopant fraction<sup>[74,182]</sup> and type of dopant.<sup>[166]</sup> This indicates that the assumption is restricted to dilute solutions as shown in literature.<sup>[167,203]</sup>

Semi-empirical<sup>[39,40]</sup> and *ab initio*<sup>[44,45]</sup> calculations confirm the association energies found by impedance measurements. Schmalzried used electrostatic interactions, which lead to different probabilities for forward and backward jumps, to describe a relationship between increasing activation energies with increasing dopant fraction.<sup>[35]</sup> Neutron diffraction experiments of yttria-stabilized zirconia (YSZ) show not only sharp Bragg reflections but also a background that is modulated with the scattering vector. This diffuse scattering indicates the presence of not completely ordered atoms such as oxygen ions, which are moved towards the vacancies, or possibly associates.<sup>[204]</sup> Electron spin resonance spectroscopy suggests that charged defect complexes of dopants and an oxygen vacancy  $(\text{RE}'_{\text{Ce}}\text{V}_{\text{O}}^{\bullet\bullet})^{\bullet}$  exist at low dopant fractions.<sup>[205]</sup> Extended X-Ray Absorption Fine Structure (EXAFS) measurements of the coordination numbers of cations and anions confirm the formation of associates.<sup>[206–209]</sup> Finally, Nuclear Magnetic Resonance (NMR) measurements support the formation of associates for  $^{45}\text{Sc}$  doped ceria,<sup>[210]</sup>  $^{89}\text{Y}$  doped ceria,<sup>[210–212]</sup> and  $^{139}\text{La}$  doped ceria.<sup>[213]</sup>

While the formation of associates is commonly accepted, the dopant fraction at which associates appear and influence the conductivity is a topic of discussion. Early approaches assumed that discrete localized clusters separate from the ideal cerium lattice are present, and that their concentration can be described using equilibrium thermodynamics.<sup>[33]</sup> However, this model failed at larger dopant fractions.<sup>[167]</sup>

Besides association, research groups presume the formation of *defect cluster*<sup>[30,174]</sup> or *nano-scale domains*: Especially at high dopant fractions, Tien and Subbarao,<sup>[214]</sup> Nakamura,<sup>[215,216]</sup> Ou *et al.*<sup>[186,217]</sup> and Hooper *et al.*<sup>[218,218]</sup> reported an ordering of the oxygen vacancies leading to reduction of the oxygen ion conductivity.

While the association and ordering of defects can be investigated experimentally, the influence of both phenomena on the oxygen ion migration can only be speculated on. Thus, many investigations show that attractive and repulsive interactions are not sufficient to describe the experimental results without considering *modified jump probabilities* or migration energies.

Murray and Murch calculated the oxygen ion conductivity using Kinetic Monte Carlo (KMC) simulation and explained the maximum in conductivity as a function of dopant fraction.<sup>[41]</sup> For this purpose, they used migration energies for oxygen ion jumps depending on the local environment,

which were calculated using empirical potentials. Here, for high dopant fractions, oxygen vacancies jump mostly in the vicinity of dopants. Therefore, they do not contribute to the oxygen ion transport through the crystal and decrease the ionic conductivity.

Shimojo *et al.* deduced from molecular dynamics simulations of YSZ using empirical potentials that the ionic conductivity is less influenced by the  $\text{Y-V}_{\text{O}}^{\bullet\bullet}$  associates, but rather by lower jump probabilities of oxygen ion around  $\text{Y}^{3+}$  dopants.<sup>[219,219]</sup> Indeed, it is rarely discussed that increasing dopant fractions lead to migration configurations, where oxygen vacancies and dopants have the same distance before and after a jump. These configurations possess a symmetric jump profile: Initial and final states are energetically equivalent. Forward and backward jumps have the same migration energy. For large dopants, the migration is typically hindered, i.e. the oxygen ion is blocked. Migration energies increase for an increasing number of large dopants as illustrated in Fig. 2.18. Meyer and Nicoloso showed using KMC simulations that interactions between nearest neighbors of oxygen vacancies and dopants are not sufficient to calculate the oxygen ion conductivity, but rather a migration energy model is required.<sup>[220]</sup> Martin showed using an analytical model that the combination of nearest neighbor interaction and reduced jump probabilities could explain the experimental findings.<sup>[37]</sup>

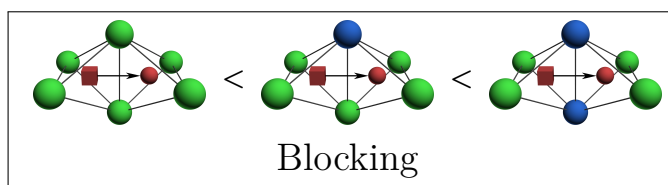


Figure 2.18: The migration energy increases for an increasing number of large dopants at the migration edge.

Migration energies were calculated e.g. by Nakayama and Martin for variously doped ceria using Density Functional Theory (DFT) calculations.<sup>[54]</sup> However, for similar migration configurations, the variation of the type of dopant leads to different trends in literature, which has to be investigated further.<sup>[44,221–225]</sup>

Therefore, the question remains whether immobilized vacancy-dopants associates, an ordering of the vacancies and modified jump probabilities exist separately or even simultaneously and may be mutually dependent.

### 2.5.2 Varying the Type of Dopant

The oxygen ion mobility depends not only on the dopant fraction but also on the type of dopant. First theories postulated that the highest oxygen ion conductivity occurs for dopants, which result into the least *distortion of the crystal lattice*.<sup>[34]</sup> In 1981, Wang *et al.*<sup>[167]</sup> and Gerhardt-Anderson and Nowick<sup>[33]</sup> suggested that the optimal dopant has the ionic radius of the  $\text{Ce}^{4+}$ -cation. However,

in the next 15 years, different dopant radii leading to the least distortion of the crystal lattice were proposed.<sup>[25,30,226–229]</sup>

Alternatively, the influence of different dopants on the ionic conductivity is attributed to the formation of *associates*. In experiments, EXAFS measurements show the formation of oxygen vacancy-dopant associates based on coordination numbers or distances between anions and cations. Here, dopants, which lead to high oxygen ion conductivities like Sm and Gd, involved less formation of associates than other dopants like Y or La.<sup>[208,209,230]</sup> However, few EXAFS measurements deviate from this rule.<sup>[207]</sup> NMR measurements confirm a stronger association between Sc dopants and oxygen vacancies compared to Y dopants and oxygen vacancies.<sup>[210]</sup> Association energies derived from early impedance experiments and calculations using potentials of the Born-Mayer form show that dopants, which lead to high oxygen ion conductivities, possess lower association energies (Fig. 2.14).<sup>[33,39,40]</sup> Here, oxygen vacancies are less trapped by dopants and have a higher mobility. According to previous reports, the strong association for small dopants (e.g. Sc) is based on Coulomb interactions, while large dopants (e.g. La) form associates due to minimal stress in the crystal lattice. This opposed effects should lead to a minimal association energy for Gd doped ceria.

However, subsequent experiments demonstrated that association energies scatter or activation enthalpies are even temperature independent and exhibit no kink (Chapter 2.4.4). Association energies depend on the dopant fraction with a minimum around  $x = 0.03$ . For Sm doped ceria, large association energies are reported despite its high ionic conductivity (Fig. 2.14). Later, empirical<sup>[231]</sup> and *ab initio* calculations<sup>[44,54,55]</sup> showed that the association energy decreases with increasing ionic radius up to La. These and further calculations also show that, for large dopants, oxygen vacancies are no longer in closest possible proximity to the dopants (nearest neighborhood,  $1_{\text{NN}}$ ), but in the next-adjacent location (next nearest neighborhood,  $2_{\text{NN}}$ ).<sup>[232,233]</sup> The latter is in contrast to calorimetric measurements of La doped ceria where vacancies were found to remain predominantly in nearest neighborhood to the trivalent dopant.<sup>[234]</sup> Clearly, the microscopic association between dopants and oxygen vacancies and the macroscopic experimental association energy e.g. derived from impedance experiments are connected. However, microscopic and macroscopic processes are not equivalent. In this work, KMC simulations are used to link both processes.

If the dopant fraction or the type of dopant are varied, experiments suggest a relationship between *conductivity and association energy*. As shown in Chapter 2.4.4, the maximum in conductivity correlates with a minimum in activation enthalpy as a function of dopant fraction and dopant type. Similar to the association energy, microscopic migration energies and macroscopic activation enthalpies are connected. In this work, again KMC simulations are used to link both processes.

In addition to doping with a single dopant, several studies investigate the oxygen ion conductivity of ceria co-doped with more than one type of dopant. It is commonly assumed that in co-doped materials the properties of both dopants are averaged. Ralph *et al.*<sup>[235]</sup> and Li *et al.*<sup>[236]</sup> hoped that the ionic radii of both dopants are averaged, which could lead to an optimal dopant with the least distortion of the crystal lattice. However, the ionic conductivity could not be increased.

Therefore, the authors suggest that local distortions are more important than global deformations of the lattice, and the strong association between oxygen vacancies and dopants is of particular importance. Anderson *et al.*<sup>[44]</sup> could theoretically and Omar *et al.*<sup>[165,237]</sup> experimentally produce better results with a small ionic radius difference. Further examples were shown by Maricle *et al.*<sup>[238]</sup> and Ralph *et al.*<sup>[239,240]</sup> Particularly promising are co-doped ceria, which use widely available and inexpensive starting materials such as calcium and magnesium.<sup>[241]</sup> In this work, Sm-Zr and Gd-Zr co-doped ceria are investigated as Zr impurities are common, especially, if powders are milled using zirconia balls.

# 3 Methods

## 3.1 Experimental Methods

### 3.1.1 Composition

The composition of samples can be investigated using Energy Dispersive X-ray Spectroscopy (EDX) and X-Ray Diffraction (XRD) experiments.<sup>[1]</sup>

For Energy Dispersive X-ray Spectroscopy (EDX) measurements, electrons emitted by a tungsten filament are accelerated using a high voltage (20 kV) in vacuum onto the sample. An incident electron excites an electron in an inner shell, which subsequently is ejected from the sample. The hole is filled by an electron from a higher energy level while the excess energy, which is characteristic for the atom, is being radiated. The emitted X-Ray radiation not only allows a qualitative analysis of the composition, except for elements with low atomic mass, but also a quantitative analysis, after a calibration is performed.

The structure of crystal lattices can be investigated using X-Ray Diffraction (XRD).<sup>[242-244]</sup> Electrons emitted by a hot wire are accelerated using a high voltage (40 kV) in vacuum on e.g. a Cu-anode. The electrons decelerate creating ‘Bremsstrahlung’ or ionize Cu atoms by removing an electron from an inner shell. The latter causes electrons from higher energy levels to fill up the hole leading to an X-ray emission that is characteristic for the ionized element Cu. For example, the transition of an electron from the p-orbital of the second shell (L-shell) to the innermost K-shell leads to  $K_\alpha$  radiation. While most of the wavelength range of the radiation (e.g. Bremsstrahlung) is absorbed using a Ni-filter or deflected using a monochromator, the  $K_\alpha$  emission is directed to the sample and scattered at the electron shells of the atoms. In case the atoms are arranged in a periodic lattice, the reflected waves interfere according to Bragg’s law.<sup>[245]</sup> Depending on the angle between incident and reflected radiation ( $2\theta$ ), constructive or destructive interference occurs caused by the path difference between the diffracted waves ( $2d\sin(\theta)$ ). Here,  $d$  is the spacing between successive crystallographic planes of the crystal lattice. Is the path difference an integer multiple ( $n$ ) of the wavelength  $\lambda$  of the incident radiation, constructive interference appears according to

$$2d\sin(\theta) = n\lambda. \quad (3.1)$$

The resulting X-ray radiation from penetration depths of up to a few  $\mu\text{m}$  is measured as a function of scattering angle using a scintillation counter. The constructive interferences give insights

into the crystal system and the lattice constant. In case the sample composition is known, the diffraction intensity can be simulated and iteratively adjusted to the experiment using the Rietveld refinement.<sup>[246]</sup>

## 3.1.2 Macroscopic Structure

### Density

Since for impedance spectroscopy measurements relative densities above 90 % are desirable,<sup>[184,247–249]</sup> the density  $\rho_s$  is measured using Archimedes' principle.<sup>[1]</sup> Here, the buoyant force raises a body, which is immersed in a fluid, by the weight of the fluid that the body displaces. Therefore, the apparent weight of the body in the fluid  $G'$  and the actual weight in air  $G$  can be compared with the density of the fluid  $\rho_{\text{fluid}}$  and the volume of the body  $V_s$  according to  $G/(G - G') = \rho_s \cdot gV_s/(\rho_{\text{fluid}} \cdot gV_s)$  where  $g$  is the gravitational acceleration. The relative densities can be now obtained as a fraction of the theoretical density, which is given by  $\rho_{\text{theo}} = Z_{\text{cell}} \cdot \frac{M}{N_A} / V_{\text{cell}}$  with the unit cell volume  $V_{\text{cell}}$ , the number of formula units  $Z_{\text{cell}}$ , the molecular mass  $M$  given by  $\text{Ce}_{1-x}\text{RE}_x\text{O}_{2-x/2}$  and the Avogadro constant  $N_A$ . The error of the relative density  $\rho_s/\rho_{\text{theo}}$  is estimated to be  $\pm 1\%$ .

### Scanning Electron Microscope

The surface structure is investigated using a Scanning Electron Microscope (SEM).<sup>[1,250,251]</sup> Electrons emitted by a tungsten filament are accelerated using a high voltage (20 kV) in vacuum onto the sample. The incident electron beam is focused in a raster scan pattern onto the sample where inelastic scattering leads to the emission of secondary electrons with low energy. The latter are collected by a detector at the side of the sample resulting in the impression of a top view of the sample, which is illuminated from the side.

## 3.1.3 Local Structure

Structural and electronic properties can be investigated by X-ray Absorption Spectroscopy (XAS). Here, a sample is radiated with X-rays and the absorption coefficient is measured as a function of energy.

X-Rays are generated by a synchrotron source where charged particles are diverted and accelerated by a magnetic field, which leads to synchrotron radiation tangentially to the circular path. From the broad energy range of the synchrotron radiation, the desired X-Ray energy is selected using a monochromator consisting of a couple of single crystals (Fig. 3.1). The incident X-Ray beam can ionize atoms in the sample when the X-ray energy matches the binding energy of an electron according to the photoelectric effect<sup>[252]</sup> with the transition probability given by Fermi's golden rule.<sup>[253]</sup> Here, electrons from different energy levels (Fig. 3.2) can be excited with energies characteristically for the ionized atom and its valence. This leads to absorption of the X-Ray beam. The

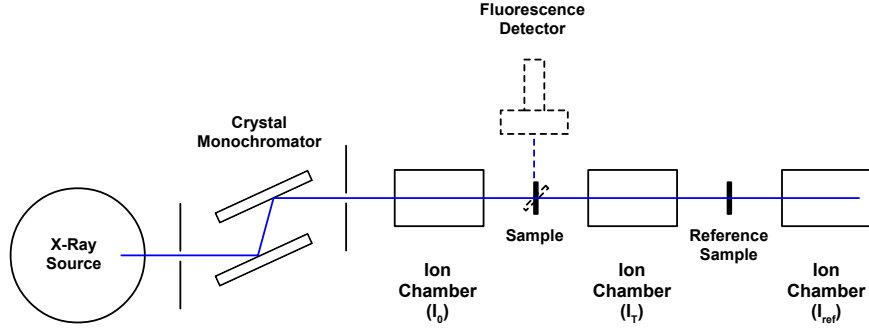


Figure 3.1: Setup of a XAS beamline using both X-Ray absorption and fluorescence.

intensity of the radiation is measured before and after the sample by gas ionization chambers filled with mixtures of  $N_2$ , Ar and Kr. Alternatively, thick samples can be tilted by  $45^\circ$  and the X-Ray fluorescence, caused by electrons from higher energy levels that fall into the created electron hole, can be measured.

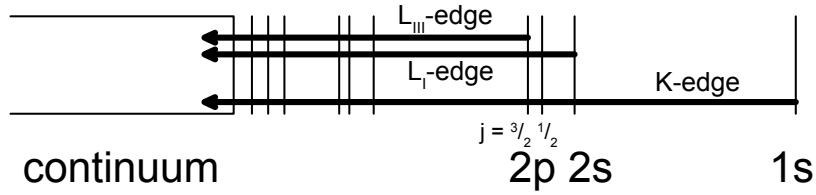


Figure 3.2: Schematic representation of an electronic excitation with an X-ray quantum. Here,  $j$  is the total angular momentum quantum number of the one electron given by the particle's spin and orbital angular momentum.

The X-ray absorption coefficient  $\mu(E)$  can be depicted as a function of energy (Fig. 3.3), where the increase in adsorption caused by absorbed X-Rays is referred to as absorption edge or X-ray Absorption Near-edge Structure (XANES). For solid samples, the higher energy region after the absorption edge contains the Extended X-Ray Absorption Fine Structure (EXAFS).

The Extended X-Ray Absorption Fine Structure (EXAFS) is caused by the transition of an electron from a deep core state to an unoccupied state, which is dipole mediated and therefore influenced by its surrounding. The excited electron can be perceived as expanding spherical wave that is scattered by neighboring atoms creating new spherical waves. The constructive or destructive interference between the waves leads to local maxima or minima in the transition probability and subsequently the absorption coefficient. The resulting sinusoidal oscillation in the absorption coefficient (see Eq. 3.2) is damped by the limited lifetime of the excited photoelectron that is scattered both elastically and inelastically (second exponential term in Eq. 3.2) and the thermal and statistical disorder (first exponential term in Eq. 3.2).

The normalized, wave-vector dependent absorption coefficient  $\chi(k)$  is given by the sum of multiple

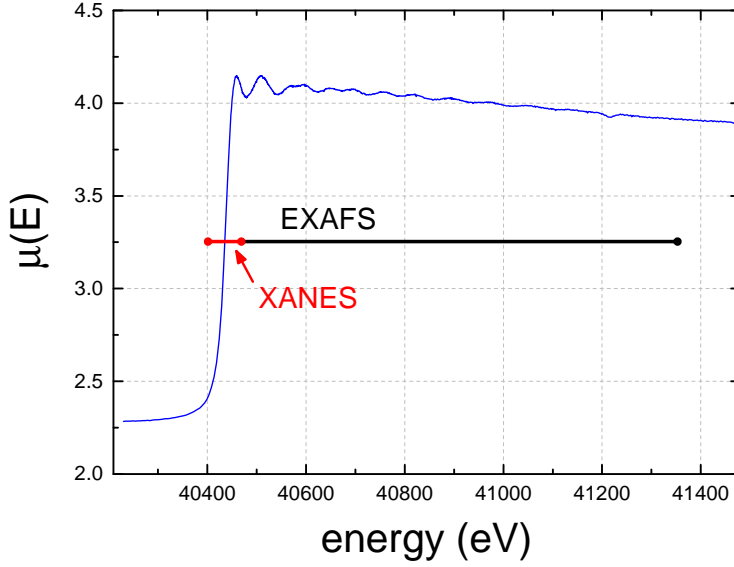


Figure 3.3: X-ray spectrum of an  $\text{Ce}_{0.975}\text{Sm}_{0.025}\text{O}_{1.9875}$  sample, showing the XANES and EXAFS region on the Ce(K)-edge.

scattering paths  $\chi(k) = \sum_i \chi_i(k)$  by the EXAFS equation

$$\chi_i(k) = \frac{N_i S_0^2}{k R_i^2} F_i(k) \sin[2kR_i + \delta_i(k)] e^{-2\sigma_i^2 k^2} e^{-2R_i/\lambda(k)} \quad (3.2)$$

with the absolute value of the wave vector  $k = \sqrt{2m_e E_{\text{kin}}/\hbar^2}$ , the kinetic energy of the electron  $E_{\text{kin}}$ , the degeneracy  $N_i$  of path  $i$ , which corresponds to the coordination number, the many body amplitude or passive electron reduction factor  $S_0^2$ , the distance to the scattering atom  $R_i$ , the effective scattering amplitude  $F_i(k)$ , the effective scattering phase shift  $\delta_i(k)$ , the mean squared displacement  $\sigma_i^2$  and the mean free path  $\lambda(k)$ .<sup>[254]</sup>

The degeneracy of path  $N_i$ , the distance to the scattering atom  $R_i$  and the mean squared displacement  $\sigma_i^2$  reveal information about the local structure of about 10 Å around the probed atom. The degeneracy of path  $N_i$  reveals how many neighboring atoms exist. Therefore, the number of oxygen vacancies near the probed atom can be investigated, which is of special interest in this study.

### 3.1.4 Conductivity and Diffusion

#### Overview of Experimental Methods used in Literature

In literature, the conductivity and diffusion in pure and doped ceria were investigated using both macroscopic and microscopic methods.<sup>[255]</sup> For example, tracer diffusion and conductivity measurements investigate macroscopic long-range diffusion, whereas Nuclear Magnetic Resonance (NMR) and NMR relaxation investigate microscopic properties like oxygen vacancy hopping frequencies or activation energies. All mentioned methods use probe atoms to examine the sample contrary to conductivity measurements.

NMR measurements often investigate Sc doped ceria containing  $^{45}\text{Sc}$ .<sup>[256]</sup> At room temperature and below, magic angle spinning NMR spectra contain two sharp, resolved resonances assigned to  $\text{Sc}^{(7)}$  and  $\text{Sc}^{(8)}$  sites with the Sc-O coordination number 7 or 8, respectively. At 300 °C, a broad peak centered at the weighted average of both peaks appears due to a fast dynamic cross-exchange of a small subpopulation between both sites. The width of this peak decreases monotonically with increasing temperature indicating an increased cross-exchange frequency and can be compared to simulations using a standard two-site random cross-exchange model.

Alternatively, Sc doped ceria was investigated by spin-lattice relaxation where during a saturation recovery pulse sequence the magnetization is rotated by  $90^\circ$  followed by relaxation of the system where the gained energy is dissipated within the lattice. Subbi *et al.* reported vacancy hopping around  $\text{Sc}^{(7)}$  sites with an activation energy of 0.37 eV between 250 K and 550 K.<sup>[257]</sup>

Tracer diffusion experiments in pure and doped ceria use an  $^{18}\text{O}/^{16}\text{O}$  isotope exchange at high temperature, where  $^{18}\text{O}$  from an enriched gas phase diffuses into the sample. For Gas Phase Analysis (GPA) measurements, the decreasing concentration of  $^{18}\text{O}$  in the gas phase during diffusion annealing is measured.<sup>[258–260]</sup> In Secondary Ion Mass Spectrometry (SIMS) measurements, the concentration of  $^{18}\text{O}$  in the solid after diffusion annealing is measured. The sample surface is sputtered with a primary ion beam in ultra high vacuum and ejected secondary ions are analyzed.<sup>[260]</sup> For depth profiles, the surface is gradually eroded away while sequential SIMS measurements are performed. Results are shown in Chapter 6 and 7.

Conductivity measurements of pure and doped ceria investigating the ionic conductivity generally assume that the electronic conductivity can be neglected, which is true for low and intermediate temperatures in air. While direct current measurements only reveal the total conductivity, impedance measurements with alternating current may allow a distinction between the conductivity of the bulk and grain boundary domain.

## Impedance Spectroscopy

In this work, the oxygen ion conductivity is investigated using impedance spectroscopy whereat it is assumed that ions in a solid behave comparably to electrons in an electric circuit. The conductivity is inversely proportional to the resistivity, which is given by the quotient of current and the preset excitation voltage. By using alternating voltage, a shift between current  $I(t)$  and voltage  $U(t)$  arises with the time  $t$ . The shift can be described as a phase angle  $\varphi$  (Eq. 3.3) which is negative in a capacitive circuit ( $-\frac{\pi}{2} < \varphi < 0$ ) and positive for an inductive circuit ( $0 < \varphi < \frac{\pi}{2}$ ). Therefore, the resistance is phase-dependent and referred to as impedance  $Z$  with

$$Z = \frac{U(t)}{I(t)} = \frac{U_0 e^{i\omega t}}{I_0 e^{i(\omega t - \varphi)}} = \frac{U_0}{I_0} e^{i\varphi} = \underbrace{\frac{U_0}{I_0} \cos \varphi}_{Z'} + i \underbrace{\frac{U_0}{I_0} \sin \varphi}_{Z''} \quad (3.3)$$

where  $I_0$  is the amplitude of the current,  $U_0$  the amplitude of the voltage and  $\omega$  the angular frequency.<sup>[1,247]</sup> Using Euler's formula, the impedance can be expressed as real part  $Z'$  and imaginary part  $Z''$ , which are traditionally shown as  $-Z''$  as a function of  $Z'$  in the Nyquist plot.<sup>[261]</sup>

## 3.2 Computational Methods

### 3.2.1 Quantum Mechanical Calculations

Alternatively to experiments, materials can be investigated computationally by solving the time-independent Schrödinger equation:

$$\hat{H}\Psi = E\Psi. \quad (3.4)$$

Here, the Hamilton operator  $\hat{H}$  is applied onto the wave function  $\Psi$ , whose square modulus can be interpreted as the probability density of the particle positions, resulting in the investigated energy eigenvalue  $E$ . The Hamilton operator is given by the (potential) interaction with an external field, the kinetic energy of all particles, the Coulomb attraction between electrons and nuclei as well as the repulsion between electrons or between nuclei. Here, methods using only theoretical principles for the Hamilton operator are called *ab initio* or first principles calculations while methods that use experimental data are referred to as empirical or semi-empirical calculations. For the *ab initio* studies of a solid, several simplifications have to be introduced. <sup>[1,262–264]</sup>

Nuclei have significantly larger masses than electrons and move much slower. Therefore, to study electronic properties approximately, the positions of the nuclei can be fixed and the kinetic energy of the nuclei can be neglected according to the Born-Oppenheimer approximation. <sup>[265]</sup>

### Density Functional Theory

To avoid calculating an electronic wave function with three times as many coordinates as electrons, Thomas and Fermi suggested the direct use of the three-dimensional electron density  $\rho(\mathbf{r})$  and therefore introduced the first density-functional based theory in the year 1927. <sup>[266,267]</sup> As a result, the energy  $E[\rho(\mathbf{r})]$  is a functional of the electron density, which itself is a function of the position. However, Thomas and Fermi approximated the kinetic energy based on a homogeneous electron gas leading to problems like the missing electronic shell structure and the impossibility of bonding in molecules and solids.

These problems can be overcome by the two basic theorems for the Density Functional Theory (DFT) that were formulated by Hohenberg and Kohn in 1964. <sup>[268]</sup> Obviously, the electron density is obtained from the wave function, which obeys the Schrödinger equation. Therefore, the ground-state electron density is a functional of the external potential, which is the Coulomb potential of the nuclei. <sup>[269]</sup> The first Hohenberg-Kohn theorem states the reverse: The ground-state wave function is a unique functional of the electron density since the external potential is a functional of the electron density. The second Hohenberg-Kohn theorem states that the true ground-state energy is given by the ground-state electron density, which leads to the lowest energy according to the variational principle.

How the energy can be calculated from the electron density in practice was given by Kohn and Sham. <sup>[270]</sup> They started from the electron density of a non-interacting electron, which can

be described as the sum of the electronic states, namely  $\rho(\mathbf{r}) = \sum \rho_i(\mathbf{r})$ , where  $\rho_i(\mathbf{r}) = \psi_i^2(\mathbf{r})$  are one-electron orbital probability densities. In this reference system of non-interacting electrons, the kinetic energy can be exactly calculated. The energy of the reference system is solved self-consistently, iteratively using the variational principle for all one-electron Schrödinger-like equations (called Kohn-Sham equations) for the orbitals  $\psi_i(\mathbf{r})$ . The potential, which acts on the electron  $i$ ,

$$V_i(\mathbf{r}) = V_{\text{ext},i}(\mathbf{r}) + V_{H,i}(\mathbf{r}) + V_{x,i}(\mathbf{r}) + V_{c,i}(\mathbf{r}), \quad (3.5)$$

is given by the Coulomb potentials of the nuclei  $V_{\text{ext},i}(\mathbf{r})$  and the electrons  $V_{H,i}(\mathbf{r})$ , the exchange interaction  $V_{x,i}(\mathbf{r})$  and the correlation term  $V_{c,i}(\mathbf{r})$ .<sup>[269]</sup> The exchange and correlation functionals include the Pauli exclusion principle and the dynamical correlation of electrons, respectively. Compared to theories like Hartree-Fock, the electron correlation is included in DFT, but the exchange-correlation-functional is unknown and has to be approximated.

In the Local Density Approximation (LDA), it is assumed that the exchange-correlation energy is equal to that in a homogeneous electron gas of the same electron density similar to Thomas and Fermi. While the exchange part is given analytically, the correlation part can be derived from perturbation theory or quantum Monte-Carlo calculations.<sup>[271]</sup> Additionally, the gradient or derivative of the electron density with respect to the position can be considered in the so-called Generalized Gradient Approximation (GGA).

Both exchange-correlation approximations fail if the electronic correlation becomes dominant like in the case of cerium oxide where the Ce  $4f$ -electrons are localized and the Coulomb repulsion is not described properly. Here, a repulsion parameter  $U$  according to Dudarev *et al.*<sup>[272]</sup> can be introduced for example for GGA

$$E_{\text{GGA}+U} = E_{\text{GGA}} + \frac{U}{2} \sum_{\sigma} \left[ \left( \sum_j \rho_{jj}^{\sigma} \right) - \left( \sum_{j,l} \rho_{jl}^{\sigma} \rho_{lj}^{\sigma} \right) \right], \quad (3.6)$$

where  $\rho_{jl}^{\sigma}$  is the density matrix of the  $f$ -electrons with a given projection of spin  $\sigma$ , which is for an individual ion equal to the occupation number of the respective state.<sup>[273]</sup> The repulsion parameter is often determined empirically by comparing the theoretical results with experimental band gaps, magnetic moments, lattice parameters or by assessment of the localization of electrons.<sup>[56,274,275]</sup>

## Bloch's Theorem and k-Points

Positions in real space are given by the real-space vector

$$\mathbf{R} = n_1 \mathbf{a}_1 + n_2 \mathbf{a}_2 + n_3 \mathbf{a}_3 = \mathbf{a}, \quad (3.7)$$

as linear combination of the real-space basic vectors  $\mathbf{a}_1$ ,  $\mathbf{a}_2$  and  $\mathbf{a}_3$  with the lattice vector  $\mathbf{a}$ , while positions in reciprocal space are given by the reciprocal vector

$$\mathbf{K} = m_1 \mathbf{g}_1 + m_2 \mathbf{g}_2 + m_3 \mathbf{g}_3, \quad (3.8)$$

constructed from the reciprocal basic vectors  $\mathbf{g}_1$ ,  $\mathbf{g}_2$  and  $\mathbf{g}_3$ .

For calculations of solids with a vast number of atoms, the following simplifications have to be introduced. In a perfect crystal, structures appear periodically. As a result, the electronic potential and the wave function are periodic as well according to Bloch.<sup>[276]</sup> Then, the translation symmetry of the wave function by a translation vector  $\mathbf{T}$  is given by a plane wave  $e^{i\mathbf{k}\cdot\mathbf{T}}$  according to

$$\Psi(\mathbf{k}, \mathbf{r} + \mathbf{T}) = e^{i\mathbf{k}\cdot\mathbf{T}} \cdot \Psi(\mathbf{k}, \mathbf{r}) \quad (3.9)$$

where  $\mathbf{r}$  and  $\mathbf{k}$  are the position in real and reciprocal space, respectively. Due to periodicity and Kramer's theorem, all information is given in the first Brillouin zone  $0 \leq |\mathbf{k}| \leq \frac{\pi}{a}$  for a cubic unit cell. For isolators and semiconductors, only a few  $\mathbf{k}$ -points in this region have to be calculated due to small changes in the electronic wave function. These can be selected using the original Monkhorst-Pack scheme<sup>[277]</sup> creating a reciprocal mesh with the dimensions  $N_1 \times N_2 \times N_3$

$$\mathbf{k} = \mathbf{g}_1 \frac{n_1 + \frac{1}{2}}{N_1} + \mathbf{g}_2 \frac{n_2 + \frac{1}{2}}{N_2} + \mathbf{g}_3 \frac{n_3 + \frac{1}{2}}{N_3}, \quad (3.10)$$

with  $n_i = 0, \dots, N_i - 1$ . Here, the reciprocal  $\mathbf{k}$ -point mesh dimensions should be about inversely proportional to the real lattice dimensions.

## Plane Waves

Wave functions can be expressed as a linear combination of exponential functions, naturally following Bloch's Theorem as a basis set, with reciprocal lattice vector  $\mathbf{G}$ .

$$\Psi_n(\mathbf{k}, \mathbf{r}) = e^{i\mathbf{k}\cdot\mathbf{r}} \sum_{\mathbf{G}} c_n(\mathbf{k}, \mathbf{G}) e^{i\mathbf{G}\cdot\mathbf{r}} \quad (3.11)$$

where  $c_n$  is the mixing coefficient. The number of plane waves can be restricted using a cut-off energy  $E_{\text{cut}}$

$$\frac{\hbar^2}{2m} |\mathbf{k} + \mathbf{G}|^2 < E_{\text{cut}} \quad (3.12)$$

where higher cut-off energies increase the number of plane waves with  $E_{\text{cut}}^{\frac{3}{2}}$ . While the flat electronic wave function between atoms can be easily represented with few plane waves, high potential energies near the nuclei lead to strong oscillations (node structure) requiring large amounts of plane waves.

To avoid this problem, the strong Coulomb association between valence electrons and nuclei as well as the Pauli repulsion between valence and core electrons can be described by a weak pseudopotential, which can be calculated for different atoms. More efficient is the Projector Augmented Wave (PAW) method where the plane waves are replaced by augmented plane waves.<sup>[278]</sup>

### 3.2.2 Monte Carlo Simulations

Though any solid can be investigated using quantum mechanical calculations, the size of a periodically repeating supercell, which is shown by the periodic boundary conditions in Eq. 3.9, is computationally limited. Especially molecular dynamics (MD) simulations for the migration of atoms

or ions, where Newton equations are solved starting from the Boltzmann distribution of the atomic velocities for a chosen temperature, are limited in time and size. These restrictions are insufficient for the topics investigated in this study. Here, Monte Carlo Simulations are applicable, which use energy weighted random processes to simulate physical states or processes.

### Metropolis Monte Carlo

The Metropolis Monte Carlo (MMC) method can be used to simulate the thermodynamic equilibrium state of a system like the configuration of ions.<sup>[279]</sup> Generally, an integration over the whole configuration space is necessary to calculate properties of a canonical ensemble in thermodynamic equilibrium, which appear weighted by the Boltzmann probability factor  $p = \exp\left(-\frac{E}{k_{\text{B}}T}\right)$  with the energy of the microstate  $E$ , the temperature  $T$  and the Boltzmann factor  $k_{\text{B}}$ . Instead of sampling the configuration space by choosing configurations randomly and weighting them with the Boltzmann probability, Metropolis *et al.* proposed a modified Monte Carlo integration where configurations are efficiently chosen with the Boltzmann probability and weighted evenly. This importance sampling is realized by a Markov process where each state is constructed from a previous state using a transition probability without any further knowledge of preceding states. A sufficient condition to achieve the equilibrium distribution is a similar transition probability for forward and backward move in the Markov chain, which is called detailed balance.<sup>[280]</sup>

Practically, an ideal three-dimensional fluorite-structured lattice consisting of a cation- and anion sublattice is created and filled randomly according to Eq. 2.1 with cerium or dopant ions and oxygen ions or oxygen vacancies, respectively. The occupants (ion or vacancy) of two randomly chosen lattice sites are permuted, if the resulting energy change  $\Delta E$  is negative or its Boltzmann probability  $p = \exp\left(-\frac{\Delta E}{k_{\text{B}}T}\right)$  is higher than a random number in the interval  $[0,1[$ . The latter is repeated until the average energy is constant.

### Kinetic Monte Carlo

In literature, the oxygen ion conductivity in ceria was calculated using analytical models<sup>[34–38]</sup> and Kinetic Monte Carlo (KMC) simulations.<sup>[41,55,220,224,281–287]</sup>

The KMC method can be used to simulate kinetic processes in a system dynamically from state to state like the oxygen ion migration.<sup>[41,288]</sup> Instead of propagating the classical equations of motions forward in time and simulating atomic vibrations in time steps of about  $10^{-15}$  s, which is done in molecular dynamics (MD), KMC simulations use the knowledge that systems typically evolve with time through diffusive jumps from state to state.<sup>[289]</sup> These occasional jumps shall be limited by an energy barrier  $E_{\text{mig},i,j}$ , which has to be surmounted by the system for each atom  $i$  and each corresponding pathway  $j$ . As the transition rate  $\Gamma_{i,j} = \nu_{0,i,j} \cdot e^{-\frac{E_{\text{mig},i,j}}{k_{\text{B}}T}}$  with the attempt frequency  $\nu_{0,i,j}$  depends only on the initial and transition state according to the transition state theory (see Chapter 2.2), the KMC method is again a Markov process.

Practically, again a three-dimensional lattice is filled similar to the MMC method. An oxygen

vacancy and jump direction is randomly chosen and the jump is performed, if a random number in the interval  $[0,1[$  is smaller than the Boltzmann probability  $p_{i,j} = e^{-\frac{\Delta E_{\text{mig},i,j}}{k_{\text{B}}T}}$ . The latter is repeated until the number of successful jumps reaches a prespecified number of Monte Carlo steps per particle (oxygen ion).<sup>[290]</sup>

The time for each Monte Carlo step  $\Delta t$  is given by the total jump rate  $\Gamma_{\text{total}} = \sum_i \sum_j \Gamma_{i,j}$ , which is the sum of all rates for each vacancy or atom  $i$  and each corresponding pathway  $j$ . Analog to a first-order exponential decay process, the probability a jump has not been performed is given by  $p_{\text{survival}} = e^{-\Gamma_{\text{total}}t}$  and the elapsed time  $\Delta t = -\frac{1}{\Gamma_{\text{total}}} \ln(r)$  can be drawn with a random number  $r$  from the interval  $]0,1[$ .<sup>[289]</sup> For ceria in thermodynamic equilibrium, the average time is

$$\langle \Delta t \rangle = \frac{1}{\langle \Gamma_{\text{total}} \rangle} = \left( \sum_{i=1}^{N_{\text{V}\bullet\bullet}} \sum_{j=1}^6 \langle \Gamma_{i,j} \rangle \right)^{-1} \quad (3.13)$$

with the number of oxygen vacancies  $N_{\text{V}\bullet\bullet}$  and

$$\langle \Gamma_{i,j} \rangle = \langle \nu_{0,\text{base}} \cdot \nu_{0,\text{dev},i,j} \cdot e^{-\frac{\Delta E_{\text{mig},i,j}}{k_{\text{B}}T}} \rangle = \nu_{0,\text{base}} \langle e^{-\frac{\Delta E_{\text{mig},i,j} - k_{\text{B}}T \ln \nu_{0,\text{dev},i,j}}{k_{\text{B}}T}} \rangle = \nu_{0,\text{base}} \frac{MCS}{N} \quad (3.14)$$

with the number of Monte Carlos Steps  $MCS$  and the number of jump attempts  $N$  and where the attempt frequency is factorized in a base identical for all jumps  $\nu_{0,\text{base}}$  and a deviation factor depending on the jump environment  $\nu_{0,\text{dev},i,j}$ . This results in the total physical time span per simulation

$$t = MCS \cdot \langle \Delta t \rangle = \frac{N}{6N_{\text{V}\bullet\bullet}\nu_{0,\text{base}}}. \quad (3.15)$$

Typically numbers of Monte Carlos Steps and total physical time spans are 100 times the number of oxygen ions and  $10^{-6}$  s, respectively. At low temperature, jumps are rarely accepted and the number of jump attempts increases rapidly. In the ‘dynamically scaling’ method, more jumps are accepted to decrease the computation time. Here the jump probability is compared to a random number in the interval  $[0,A[$  for a choose number  $0 < A < 1$  and the total physical time span is divided by  $A$ .

To investigate the conductivity, a small electric field with the strength  $\epsilon_x$  is applied in  $x$ -direction and the oxygen ion conductivity is given by the mean displacement of all oxygen ions  $\langle x \rangle$  in the field direction:<sup>[55,287]</sup>

$$\sigma = \frac{\langle x \rangle}{\epsilon_x t} q n_{\text{V}\bullet\bullet} \quad (3.16)$$

where  $q$  and  $n_{\text{V}\bullet\bullet}$  are the charge and concentration of the oxygen ions, respectively. The electric field strength has to be chosen large enough to induce a significant mean displacement and small enough to ensure a linear relationship between mean displacement and field strength.<sup>[55]</sup> The mean displacement is investigated in thermodynamic equilibrium; therefore, the anion sublattice has to be equilibrated by a previous MMC or KMC simulation. Both Monte Carlo methods yield identical oxygen vacancy distributions as verified in an earlier work.<sup>[55]</sup>

# 4 Experimental and Computational Details

## 4.1 Experimental Details

Polycrystalline samples of the composition  $\text{Ce}_{1-x}\text{RE}_x\text{O}_{2-x/2-\delta}$  with  $\delta \approx 0$  were prepared according to an earlier work.<sup>[1,291]</sup> The rare-earth (RE) cations Sm ( $x = 0, 0.025, 0.05, 0.07, 0.075, 0.1, 0.125, 0.15, 0.2, 0.225$  and  $0.25$ ), Lu ( $x = 0, 0.05, 0.1, 0.15, 0.2$  and  $0.25$ ), Gd ( $x = 0.07, 0.1$  and  $0.2$ ), Y ( $x = 0.2$ ) and Yb ( $x = 0.2$ ) were used. Furthermore, the quaternary oxides  $\text{Ce}_{0.88}\text{Zr}_{0.05}\text{Sm}_{0.07}\text{O}_{1.965}$  and  $\text{Ce}_{0.86}\text{Zr}_{0.08}\text{Sm}_{0.06}\text{O}_{1.97}$  were prepared. In this work, 20% Sm doped ceria refers to  $\text{Ce}_{0.8}\text{Sm}_{0.2}\text{O}_{1.9}$ .

### 4.1.1 Synthesis and Sample Preparation

Ternary and quaternary oxides can be synthesized by a solid state reaction. Alternatively, reactions in gas and liquid phase may lead to a more homogeneous distribution of the cations and use a lower sintering temperature. In this work, the sol-gel method<sup>[292,293]</sup> is applied, which is characterized by low cost and low carbon residue.<sup>[294]</sup> Cerium (III) nitrate hexahydrate ( $\text{Ce}(\text{NO}_3)_3 \cdot 6\text{H}_2\text{O}$ , 99.9% Chempur), rare-earth (III or IV) nitrate hydrate ( $\text{RE}(\text{NO}_3)_z \cdot x\text{H}_2\text{O}$ , 99.9%, with  $z = 3$  for Sm/Yb: Sigma-Aldrich, Lu/Y: Chempur, Gd: Strem Chemicals or  $z = 4$  for Zr: Alfa Aesar) and citric acid (VWR International, 2.5 equivalent) were dissolved in water. While for some rare-earth nitrates the amount of hydration was specified (for Sm/Gd:  $x = 6$ , for Yb:  $x = 5$ ), for other rare-earth nitrates  $x$  was determined by oxidation and gravimetric analysis. Lu doped ceria was synthesized by Gerald Dück.<sup>[295]</sup> During mixing for several hours at 50 °C, the sol-gel transformation occurred. It is assumed that the cations are homogeneously distributed and chelated by the citric acid.<sup>[47]</sup> The temperature was increased to 120–150 °C leading to formation of nitrogen dioxide and subsequently foaming. The foam was dried for three hours at 350 °C, crushed with a glass rod, again dried for 17 hours when necessary and calcined for four hours at 1000 °C with a heating and cooling rate of about 5 °C/min. In contrast,  $\text{Ce}_{0.85}\text{Sm}_{0.15}\text{O}_{1.925}$ , which was synthesized and prepared by Mark Bispinghoff to investigate influences on the macroscopic structure by sintering-variation, was calcined for six hours.

The calcined powder was crushed in a mortar, dry milled for several hours in a planetary or ball mill using a Teflon bowl and zirconia balls. For the milling of  $\text{Ce}_{0.85}\text{Sm}_{0.15}\text{O}_{1.925}$  (for the sintering-

## 4 Experimental and Computational Details

variation),  $\text{Ce}_{0.93}\text{Gd}_{0.07}\text{O}_{1.965}$  and  $\text{Ce}_{0.86}\text{Zr}_{0.08}\text{Sm}_{0.06}\text{O}_{1.97}$ , ethanol was added and removed afterwards by heating at 80 °C for 20 hours.

The powder was uniaxially pressed to pellets with 10 mm diameter of ca. 0.7 g using a force of 25 kN for 25 min. The pellets were sintered in air at 1400 °C for 24 hours with a heating and cooling rate of 200 °C/hour. For the sintering-variation, samples with different sintering temperatures  $T$  and sintering times  $t$  are prepared with a heating and cooling rate of 150 °C/hour. Here, the samples are named according to  $T$ - $t$ , whereat the actual temperatures deviated of about  $-1\%$  (up to 1275 °C) and  $+1\%$  (1350 °C and above) from the nomenclature.

The samples were polished with silicone oil on silicon carbide paper (P600, P800, P1000, P2500 and P4000 with the grain sizes 26, 22, 18, 10 and 5  $\mu\text{m}$  for 1, 1, 2.5, 5 and 10 min).

### 4.1.2 Composition

The compositions were successfully verified using EDX measurements (Oxford INCA, Oxford Instruments, Abingdon, UK). Using XRD measurements ( $\theta/\theta$ -diffractometer, STOE & Cie GmbH, Darmstadt, Germany with secondary monochromator or X'Pert Pro diffractometer, PANalytical, Almelo, Netherlands with Ni-Filter), the phase purity was investigated and the lattice parameter was compared to literature (Fig. 2.3).

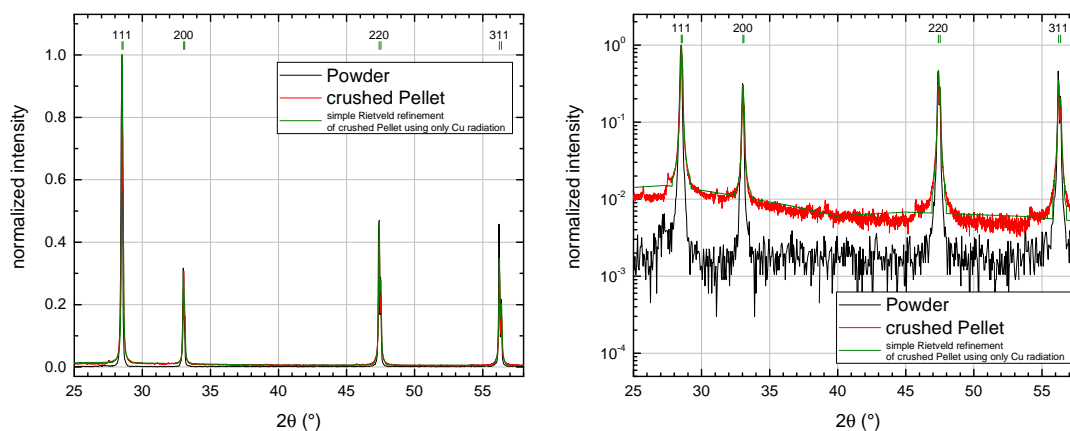


Figure 4.1: X-ray diffractogram of Gd doped ceria ( $\text{Ce}_{0.8}\text{Gd}_{0.2}\text{O}_{1.9}$ ) in linear (left) and logarithmic (right) representation.

However, first XRD measurements for example of  $\text{Ce}_{0.8}\text{Gd}_{0.2}\text{O}_{1.9}$  powder showed several peaks with minor intensity, which could not be assigned according to literature data (see Fig 4.1). These peaks (especially at  $27.25^\circ 2\theta$ ) appeared regularly before the assigned doped ceria peaks. For non-stoichiometric ceria, in fact, a linear increase in the pseudocubic lattice parameter for increasing non-stoichiometry was found.<sup>[25]</sup> Since the powder was calcined in air for four hours at 1000 °C in compliance with literature, non-stoichiometry was not anticipated according to the phase diagram of doped ceria.<sup>[296]</sup> The XRD measurements were repeated<sup>[296]</sup> for crushed pellets in cooperation with

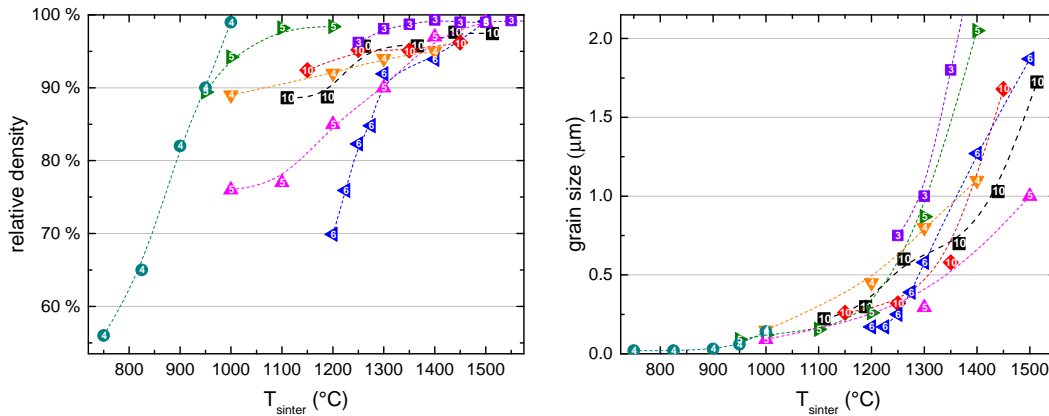
Dr. Lars Peters and Angelika von Berg from the Institute of Crystallography (RWTH Aachen University). As pellets were additionally sintered at 1400 °C for 24 hours, stoichiometric doped ceria was expected. However, again several minor peaks were observed. Figure 4.1 shows a Rietveld refinement of the crushed pellet using Cu radiation and only a simple background function. Further investigations revealed that the minor peaks are caused by impurities in the X-Ray tube rather than being a second phase in the sample. Finally, compositions and phase purity could be verified.

### 4.1.3 Macroscopic Structure:

#### Varying the Sintering Temperature and Duration

##### Density

In literature, the sample density increases with increasing sintering temperatures (see Fig. 4.2). Depending on the sample preparation technique, densities above 90 % can be reached above 1000 °C using nano-sized powder by carbonate coprecipitation<sup>[297]</sup> or 1300 °C using commercial powder.<sup>[298]</sup> A high density is required for precise impedance measurements.<sup>[247]</sup>



reference	doping	synthesis
■	this work	Sm, $x = 0.15$ citric acid - nitrate
④	Li et al. <sup>[299]</sup>	Sm, $x = 0.20$ carbonate coprecipitation
▶	Ding et al. <sup>[297]</sup>	Sm, $x = 0.20$ carbonate coprecipitation
■	Zhang et al. <sup>[300]</sup>	Gd, $x = 0.20$ oxalate coprecipitation
◆	Yan et al. <sup>[301]</sup>	Sm, $x = 0.15$ glycine - nitrate
▼	Zhou et al. <sup>[302]</sup>	Gd, $x = 0.10$ ammonium hydroxide - nitrate
▲	Tian et al. <sup>[303]</sup>	Sm, $x = 0.20$ citric acid - nitrate
◀	Pérez-Coll et al. <sup>[298]</sup>	Gd, $x = 0.10$ commercial powder

Figure 4.2: Density (left) and grain size (right) as a function of sintering temperature in literature. Sintering durations in hours are noted inside the symbols. Lines are a guide to the eye only.

## 4 Experimental and Computational Details

In this work, dense samples could be produced for sintering temperatures above 1260 °C or sintering durations above 24 hours at 1190 °C (see Fig. 4.3, densities have an error of 1 %). For parameters below these values, the density is significantly lower. Increasing either sintering temperature (blue arrow) or sintering durations (red arrow) increases the density according to literature<sup>[69]</sup> though few exceptions are quoted in literature.<sup>[304]</sup> As expected, the influence of temperature is larger than the influence of time, which was shown by varying both parameters while maintaining similar densities (green arrow). Here, for small changes in sintering temperature, large changes in sintering duration are necessary.

Density measurements according to the Archimedes method gave similar results in water and ethylene glycol. Using better grinding techniques, starting from an agate mortar to a ball mill to a planetary mill, as well as faster rotation both increases the density. Varying time and force for the uniaxial pressing as well as additional isostatic pressing barely influences the density.<sup>[1]</sup> Particularly high densities could be achieved for pure (98–99 %) and lightly doped ceria. Densities over 95 % could be reproduced within the measurement error of 1 % using the same sample preparation.

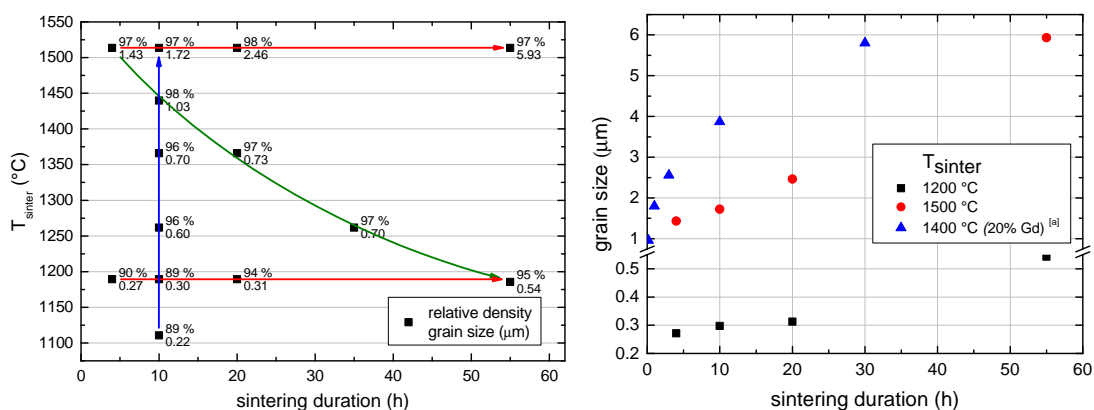


Figure 4.3: Density and grain size as a function of sintering temperature and sintering duration for  $\text{Ce}_{0.85}\text{Sm}_{0.15}\text{O}_{1.925}$  in comparison with [a] literature ( $\text{Ce}_{0.8}\text{Gd}_{0.2}\text{O}_{1.9}$ ).<sup>[300]</sup>

### Scanning Electron Microscope

Grain sizes are investigated by SEM (LEO/Zeiss 1450VP, Carl Zeiss, Oberkochen, Germany). In literature, different methods for image analysis are used.<sup>[305]</sup>

In this work, pellets used for the sintering-variation were chemically etched using 36 % hydrochloric acid for 5–20 min at 20 °C. For samples sintered at 1500 °C, breaking edges were investigated. All other pellets were thermally etched using 1300 °C for 16 h with a heating and cooling rate of 200 °C/h. All samples show dense surfaces with few holes in the μm range (see Fig. 4.4). Grain sizes were determined by a manual trace of 50–300 grains. Since only an undefined cross section of grains is visible, the maximum diameter (Feret diameter) is given (see Fig. 4.3). Grain sizes are in agreement with literature (see Fig. 4.2 and 4.3).<sup>[306]</sup> The width of the distribution of grain sizes is

nearly proportional to the grain size itself leading to a standard deviation in grain size of 30 %.

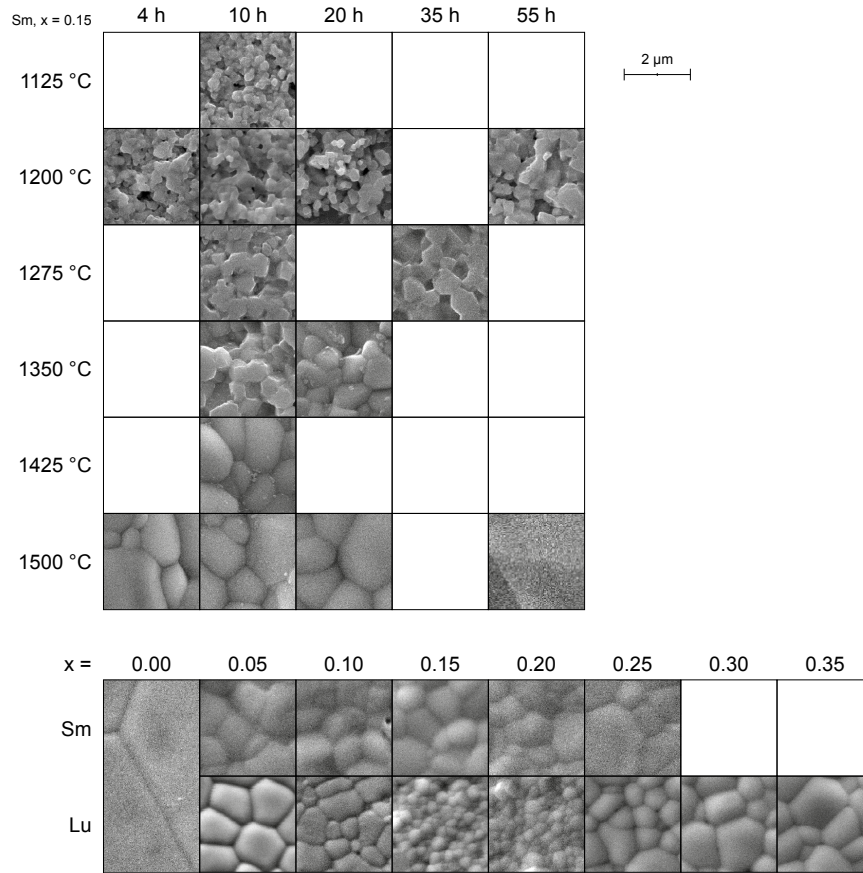


Figure 4.4: SEM measurements of  $\text{Ce}_{0.85}\text{Sm}_{0.15}\text{O}_{1.925}$  for different sintering temperatures and durations as well as  $\text{Ce}_{1-x}\text{RE}_x\text{O}_{2-x/2}$  with RE = Sm, Lu as a function of dopant fraction. Tonal values are adapted.

Grain sizes and density both increase with sintering temperature and sintering duration, which is in agreement with literature (Fig. 4.2).<sup>[69]</sup> However, their ascending slope is quite different. Between 1100–1300 °C, the density increases significantly (e.g. 89–96 % for  $t = 10$  h) while the grain sizes increases only moderately (e.g. 0.22–0.60 μm for  $t = 10$  h). Between 1300–1500 °C the grain sizes increases significantly (e.g. 0.60–1.72 μm for  $t = 10$  h) while the density increases only moderately (e.g. 96–98 % for  $t = 10$  h). Therefore, between 1100–1300 °C the densification dominates while between 1300–1500 °C the grain growth dominates, which is in agreement with literature.<sup>[298]</sup> At higher temperature, the increase in grain sizes for longer sintering durations is significantly larger. If the sintering temperature is decreased, the sintering durations has to be considerably increased to maintain the same grain size, which was not fully accomplished in this work (green arrow in Fig. 4.3).

Grain sizes are similar for variously doped ceria (about 1–2 μm). Only for  $\text{Ce}_{0.85}\text{Lu}_{0.15}\text{O}_{1.925}$  and  $\text{Ce}_{0.8}\text{Lu}_{0.2}\text{O}_{1.9}$  smaller grain sizes were found ( $0.5 \pm 0.1$  μm). Pure ceria has a significantly larger

grain size (10  $\mu\text{m}$ ), which is in agreement with literature.<sup>[64]</sup> Varying the grinding technique barely influences the grain size.

### 4.1.4 Local Structure

#### XAS Setup

X-Rays were generated in the positron storage ring Doris III (DESY, Hamburg, Germany), where positrons were accelerated to an energy of 4.5 GeV. Experiments were performed in HASYLAB at Beamline C. For the monochromator, a Si (111) single crystal couple for the 2.3–22.3 keV energy range or a Si (311) for 4.4–43.4 keV was used. X-Ray fluorescence was measured using a Passivated Implanted Planar Silicon detector (PIPS) with 75 mm diameter.

The investigated samples, the investigated edges and the reference samples are shown in Table 4.1.

Sample	Sample Edge	Reference	Reference Edge
pure and Sm, Gd, Y doped ceria	Ce(K)	CeO <sub>2</sub>	Ce(K)
Sm doped ceria	Sm(L <sub>I</sub> )	Ni	Ni(K)
Gd doped ceria	Gd(L <sub>III</sub> )	Ni	Ni(K)
Y doped ceria	Y(K)	Y	Y(K)

Table 4.1: Samples investigated by EXAFS.

#### XAS Data Processing

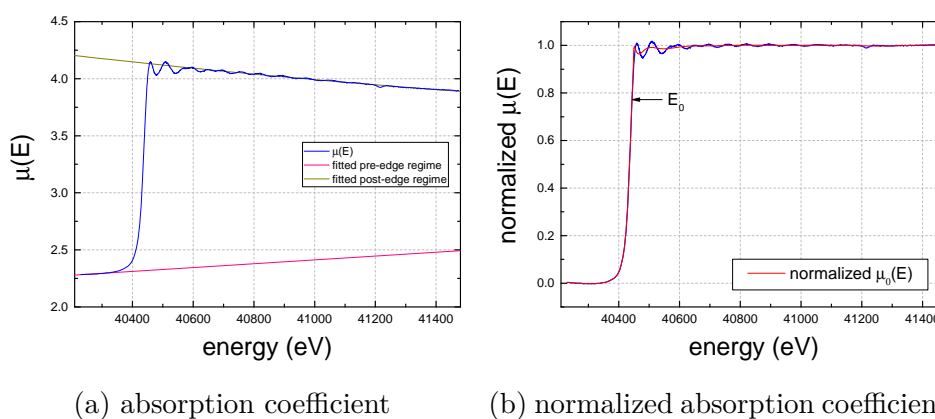


Figure 4.5: Evaluation of an EXAFS measurement of 2.5% Sm doped ceria as a function of the incident X-Ray energy.

The XAS data was processed using the program Athena<sup>[307]</sup> by (a) fitting of the pre- and post-edge

regime, (b) normalization of the absorption coefficient and (c) energy alignment of the absorption edge.

The pre- and post-edge regimes are fitted using a linear function and a second-degree polynomial, respectively (Fig. 4.5a). Afterwards, the absorption coefficient  $\mu(E)$  is normalized by subtracting the fitted pre-edge regime and dividing the result by the difference between fitted post- and pre-edge regime (Fig. 4.5b).

To compare different samples, all energy axis have to be aligned to a point of reference provided by the reference sample (Table 4.1), since energy-shifts between measurements, for example due to the monochromator, are common. For this purpose, the inflection point  $E_0$  is determined. While the energy alignment worked well for the Ce(K)-Edge in Sm doped ceria, other energy alignments may possess larger errors.

Still, even the XANES Ce edge energy fluctuates (Fig. 4.6). As no change in the valence state for the cerium cations at room temperature is assumed (Chapter 2.1.3), which is confirmed in other EXAFS measurements,<sup>[206,207,230]</sup> the deviations may be due to alignment problems with the reference spectrum.

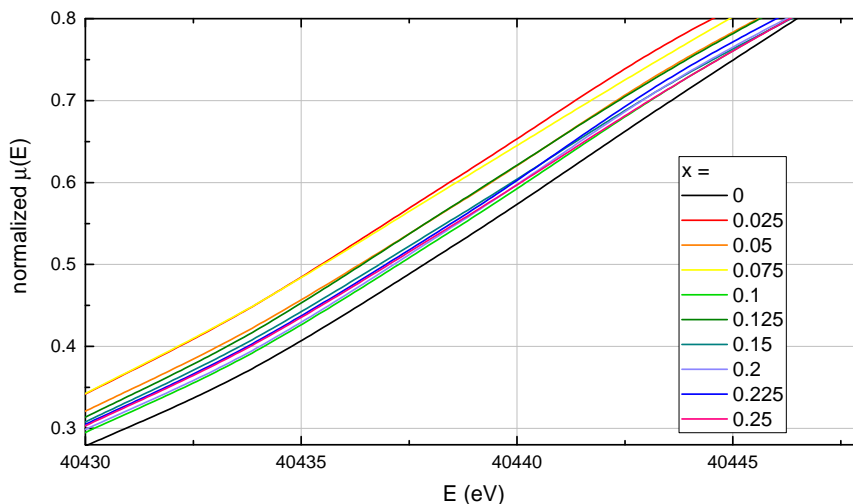


Figure 4.6: Normalized X-Ray Absorption at the Ce(K)-edge (XANES) of  $\text{Ce}_{1-x}\text{Sm}_x\text{O}_{2-x/2}$ .

## EXAFS Data Processing

The local structure can be investigated by transforming the EXAFS region of the absorption coefficient into a modified Radial Distribution Function. Therefore, the following steps have to be performed: (a) A background removal, (b) the transformation from the energy into the wave vector-range and (c) a Forward Fourier transform.

At first, the difference between the absorption coefficient with and without interference has to be calculated. As the absorption coefficient without interference cannot be measured, a spline function  $\mu_0(E)$  is assumed (see Fig. 4.5b).<sup>[308]</sup> By removing the background function, the normalized  $\mu(E)$

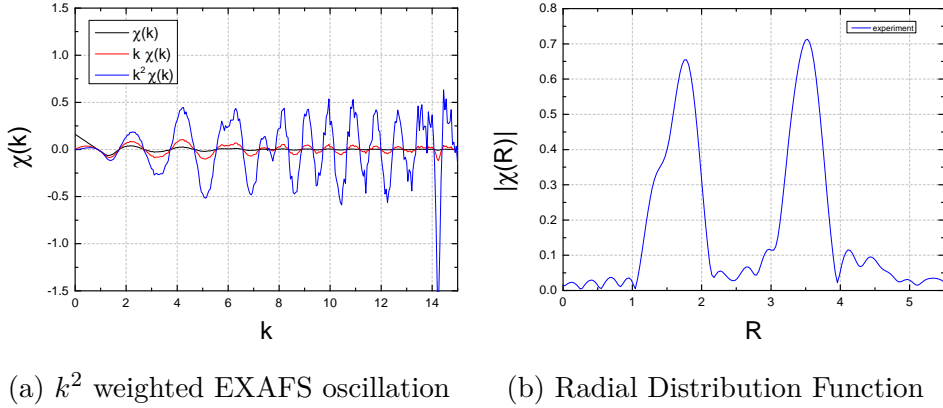


Figure 4.7: Evaluation of an EXAFS measurement of 2.5% Sm doped ceria.

is transformed to the pure EXAFS oscillation  $\chi(E)$  according to

$$\chi(E) = \frac{\mu(E) - \mu_0(E)}{\mu_0(E)} \quad (4.1)$$

Commonly, the EXAFS oscillation  $\chi(E)$  is given as a function of the absolute value of the wave vector  $\chi(k)$  using

$$k = \sqrt{2m_e(E - E_0)/\hbar^2} \quad (4.2)$$

with the electron mass  $m_e$ . For larger energies or wave vectors, the EXAFS oscillation decays. Therefore,  $\chi(k)$  is weighted with  $k^2$  in this work (Fig. 4.7a).

The  $k^n$ -weighted EXAFS oscillations as a function of the wave vector  $k^n\chi(k)$  can be transformed into a pair correlation function or Radial Distribution Function (RDF)<sup>1</sup> in the direct space  $|\chi(R)|$  using a Forward Fourier transform according to Eq. 4.3 (Fig. 4.7b).<sup>[309,310]</sup> For this purpose, only a limited  $k$ -range similar for all samples is selected by applying a window function  $W(k)$  between about 2–11 Å<sup>-1</sup> depending on the signal-to-noise ratio.

$$\chi(R) = \frac{1}{\sqrt{2\pi}} \int_{k_{\min}}^{k_{\max}} k^n \cdot \chi(k) \cdot W(k) \cdot e^{2ikR} dk \quad (4.3)$$

For pure and doped ceria, the Radial Distribution Function around a cation (Fig. 4.7b) shows contributions of oxygen ions or vacancies (first peak) as well as cerium ions or rare-earth dopants (second peak). In this work, the distribution of the oxygen vacancies is investigated. Therefore, the occupation of the first coordination shell is of particular interest and can be investigated by modeling the EXAFS oscillation.

<sup>1</sup>In contrast to a pair correlation function,  $|\chi(R)|$  still possess a phase shift  $\delta_i$  for the different scattering paths, which is corrected by fitting with the EXAFS equation.

## Modeling: The EXAFS Equation

As the structure of the pure and doped ceria is well known,  $\chi(k)$  can be modeled using the EXAFS equation and fitted to the experimental data. The EXAFS oscillation was modeled using the program Artemis<sup>[307]</sup> and IFEFFIT.<sup>[311]</sup> The EXAFS equation calculates  $\chi(k)$  as a sum of multiple scattering paths  $\chi(k) = \sum_i \chi_i(k)$  with

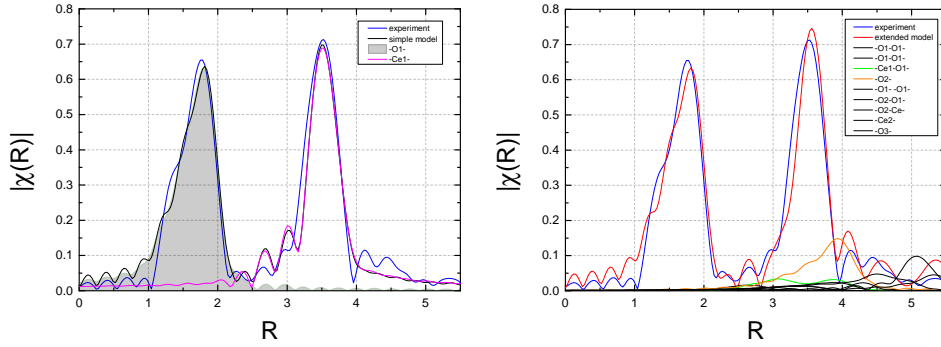
$$\chi_i(k) = \frac{N_i S_0^2}{k R_i^2} F_i(k) \sin[2kR_i + \delta_i(k)] e^{-2\sigma_i^2 k^2} e^{-2R_i/\lambda(k)} \quad (4.4)$$

$$\text{using } N_i S_0^2 = \text{amp}_i \cdot N_0, k = \sqrt{2m_e(E - E_0)}/\hbar \text{ and } R_i = R_0 + \Delta R_i. \quad (4.5)$$

For the crystalline ceria structure, the initial distance to the scattering atom  $R_0$  and the sample-independent degeneracy of path  $N_0$  are given by theory. The effective scattering amplitude  $F_i$ , the effective scattering phase shift  $\delta_i$  and the mean free path  $\lambda(k)$  were calculated using the *ab initio* program code FEFF8.<sup>[312]</sup>

A ceria reference sample can be used to determine the energy shift  $E_0$  and the mean squared displacement  $\sigma_i^2$ .

Therefore, only the amplitude  $\text{amp}_i$  and the change in distance to the scattering atom  $\Delta R_i$  for each path are the fitted parameters for each sample. The local structure is given by  $N_i$  and  $R_i$  which show the number and distance of neighboring atoms.



(a) Simple model with two scattering paths. (b) Minor improvement in an extended model using 11 paths.

Figure 4.8: Modeling an EXAFS measurement of 2.5% Sm doped ceria.

To model the EXAFS oscillation only a limited number of scattering paths, which contribute in the investigated  $R$ -region, is selected. Figure 4.8 shows the Radial Distribution Function of 2.5% Sm doped ceria with (a) two and (b) 11 fitted scattering paths. The simple model in (a) uses only the two scattering paths that possess amplitudes ten times bigger than nearly all other paths in the (b) extended model. As the difference between both models is small, only the two main scattering paths are considered in this work. Results are shown in Chapter 5.2.2.

### 4.1.5 Conductivity

For impedance measurements, top and bottom of the samples were thinly coated with platinum paste. Subsequently, a platinum wire, which was formed into a spiral with three turns, was attached to the sample. After drying on a hot plate, the samples were heated at 1000 °C for 3 hours with a heating rate of 0.5 °C/min and cooling rate of 0.9 °C/min to consolidate the contact and make the platinum paste porous.

Impedance spectroscopy measurements were performed using a Solatron 1260 (Schlumberger) and a 2-point geometry. After heating, the temperature in the furnace is constant ( $\pm 1$  °C) after a waiting time of about 3 hours. It is assumed that at this point the sample is in thermodynamic equilibrium, which could be shown at 270 °C by the synchronous evolution of bulk conductivity with temperature.<sup>[1]</sup> The impedance was measured for frequencies between  $10^7$  and  $7 \cdot 10^{-2}$  Hz using 199 points with equidistant logarithmic spacing. Between  $7 \cdot 10^{-02}$  Hz and 20 Hz, measurements were repeated five times and averaged. Therefore, the impedance measurement for each temperature takes 37 min. Including the waiting time, a total dwell time of 280 min was chosen.

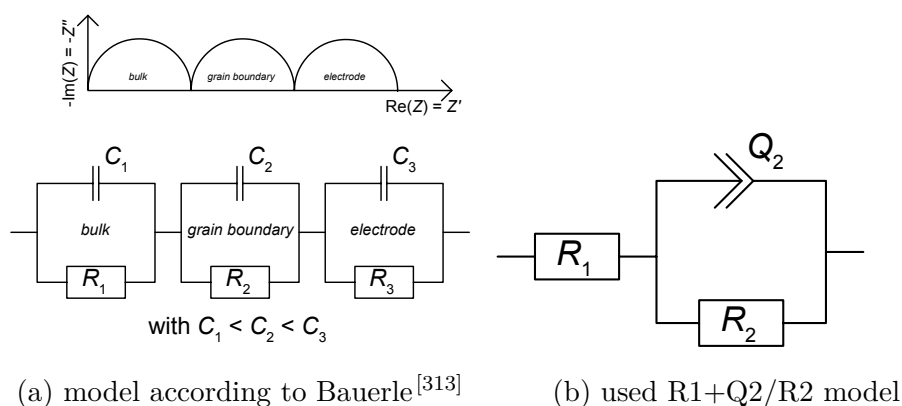


Figure 4.9: Equivalent circuit models.

Impedance measurements are often shown in the Nyquist plot, where the negative imaginary part as a function of the real part is given (see Fig. 4.9a and 4.10). The impedance of the solid electrolyte is compared to an electric circuit, which is then called equivalent circuit. J.E. Bauerle<sup>[313]</sup> proposed in the year 1969 an equivalent circuit for solid electrolytes consisting of a bulk, a grain boundary and an electrode contribution. Though many other equivalent circuits have been proposed,<sup>[171]</sup> a modified variant of Bauerle's equivalent circuit model consisting of three resistor-capacitor circuits (RC circuit) is commonly used. The equivalent circuit is shown in Fig. 4.9a with the resistances  $R_i$  and capacitances  $C_i$ . For pure and doped ceria, the bulk, grain boundary and electrode contribution appear each as a semicircles in the Nyquist plot with decreasing frequency.<sup>[174,176,177,185,297]</sup> For the resulting equivalent circuit, the capacitance increases from bulk to electrode contribution.

Rarely all contributions can be measured at the same time due to the limited frequency range in the experiment. Beyond that, interferences caused by other electric fields and overlapping semicircles

appear. Therefore, in this work, every semicircle is fitted individually using the equivalent circuit model shown in Fig. 4.9b. Fitting semicircles individually may lead to an overestimation of the resistance. For Lu doped ceria, bulk and grain boundary semicircle were fitted both simultaneously and separately. For the fit of individual semicircles, the resistance was overestimated up to 5% for the bulk domain and up to 10% for the grain boundary domain. For Sm doped ceria and dopant fractions above 10%, the separation of the grain boundary and electrode semicircles was challenging leading to a large error on the grain boundary conductivity.

For most measurements, the center of the semicircles was found to be below the x-axis, the semicircles appear flattened. The reason for this is the dispersion of physical properties in the sample. This behavior is especially typical for double-layer regions in the grain boundaries, rough electrode surfaces, non-homogeneous reaction rates at the surface due to different platinum coating and uneven current distribution on the surface. Therefore instead of a capacitor, a constant phase element  $Q$  with the impedance  $1/Z = (i\omega)^n Q$  is used for the equivalent circuit model (Fig. 4.9b).<sup>[69,169,176,178,247]</sup> For  $n = 1$ , the constant phase element is a capacitor. For smaller  $n$ , semicircles appear more flattened. Capacitance  $C$  and  $Q$ -value can be compared in a pseudo-capacitance using a model according to Hsu and Mansfeld:<sup>[314]</sup>

$$C = Q \cdot (\omega_{\max})^{n-1} \quad (4.6)$$

with the angular frequency  $\omega_{\max}$  at the vertex of the semicircle for which the imaginary part is a maximum. The semicircles are assigned according to their capacitance to the bulk and grain boundary domain.<sup>[315]</sup> Few impedance spectra exhibit additional semicircles as discussed in literature.<sup>[74,316]</sup>

Impedance measurements were analyzed using EC-Lab (BioLogic) and a consecutive Randomize (10000 steps) and Simplex-algorithm (5000 steps) with similar results to a Marquardt-Levenberg algorithm. Ceria is investigated between 50 °C and 750 °C in steps of 50 °C (furnace temperature). However, bulk conductivity could only be investigated up to 550 °C (except for pure ceria up to 750 °C) and grain boundary conductivity only above 100 °C (400 °C for pure ceria) due to the limited frequency range.<sup>1</sup> The contributions were assigned based on their pseudo-capacitance according to literature. The capacitance of the bulk domain is in the range of tens of picofarads ( $10^{-11}$  F), which is consistent with the geometric capacitance of the samples according to literature. The capacitance of the grain boundary domain is in the range of tens of nanofarads ( $10^{-8}$  F).<sup>[167,170,315]</sup>

The ionic conductivity is calculated according to

$$\sigma_i = \frac{l}{R_i \cdot A} \quad (4.7)$$

for the bulk and grain boundary domain respectively, where  $R_i$  is the resistance according to the equivalent circuit,  $l$  the thickness of the sample and  $A$  the surface area. The sample dimensions are chosen similarly for bulk and grain boundary domain. Errors arise due to the equivalent circuit

<sup>1</sup>In literature, bulk conductivities are given for higher temperatures. Here the bulk resistance is calculated from the difference of the total resistance and the extrapolated grain boundary resistance.

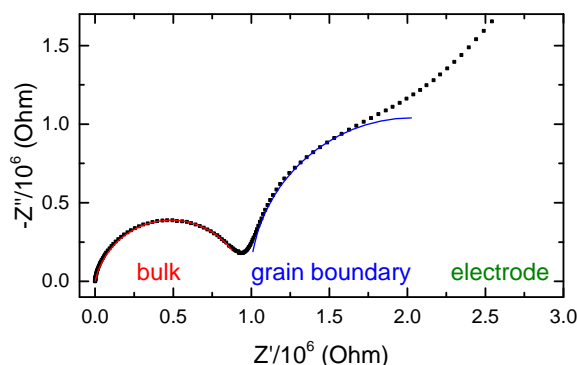


Figure 4.10: Nyquist plot with fitted equivalent circuit model for  $\text{Ce}_{0.75}\text{Sm}_{0.25}\text{O}_{1.875}$  at 200 °C.

fit, the thickness of the sample (about  $\pm 0.02$  mm) and the diameter of the pellets. The resulting error on the conductivity is mostly smaller than the symbol sizes used in this work. The prefactor of diffusion and the activation enthalpy is determined according to Arrhenius (see Chapter 2.2). For selected samples, the conductivity behavior is divided into temperature regions according to literature.<sup>[74,317]</sup>

Impedance spectroscopy measurements could be easily reproduced even with different samples based on the same synthesis and preparation. However, fitting the impedance data according to equivalent circuits can lead to different conductivities if the used equivalent circuit or selected frequency range for fitting is varied. Still, the resulting error in conductivity has only a small impact on the activation enthalpy.

## The Brick Layer Model

The macroscopic grain boundary conductivity  $\sigma_{\text{gb}}^{\text{mac}}$  according to Eq. 4.7 is independent of the sample dimensions. However,  $\sigma_{\text{gb}}^{\text{mac}}$  still depends on the geometry of the grains and its grain boundaries. Several models have been developed to investigate the microscopic grain boundary conductivity  $\sigma_{\text{gb}}^{\text{mic}}$  of the grain boundaries itself. Important classes are the effective medium theory and the brick layer model.<sup>[318–323]</sup>

Effective medium theories based on Maxwell<sup>[324]</sup> describe grains, which are surrounded by an effective medium that has the effective conductivity of a mixture.<sup>[325–327]</sup> Kidner *et al.*<sup>[328,329]</sup> use the Maxwell-Wagner/Hashin-Shtrikman model (MW-HS),<sup>[325,330]</sup> which can be described as a space-filling array of similar coated spheres that have different sizes. Though the MW-HS model is rarely used to describe the microstructure of doped ceria, its bounds can be used to show if other models are physically unrealistic.

The first brick layer model (BLM) is the Bauerle equivalent circuit for the bulk and grain boundary<sup>[313]</sup> consisting of two RC-elements in series. Beekmans and Heyne<sup>[331]</sup> described a model based on this equivalent circuit consisting of grains, which are surrounded by grain boundaries. This model, which was later named brick layer model,<sup>[323,332]</sup> only considers the series path through grain and

grain boundary (see Fig. 4.11a) and is therefore referred to as S-BLM.

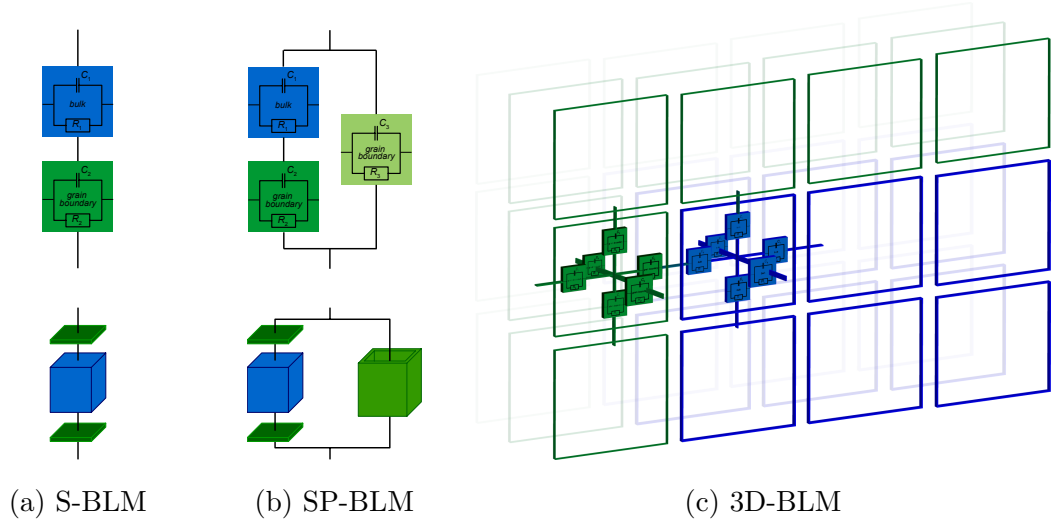


Figure 4.11: Equivalent circuit and schematic representation of the brick layer models.

Other equivalent circuits leading to the same impedance like the blocking zone model<sup>[313]</sup> and the construction model<sup>[171,333]</sup> have been discussed.

Later brick layer models also considered a parallel path, which consists of the grain boundary side-walls and is again represented with a RC-element (Fig. 4.11b). This parallel path can contain either similar (SP-BLM)<sup>[334]</sup> or different grain boundary properties (SP'-BLM)<sup>[328]</sup> than the series path.

Finally, the nested cube model by Kidner *et al.*<sup>[328,329]</sup> builds up a three-dimensional body based on pixels, which are assigned to either grain or grain boundary (3D-BLM, Fig. 4.11c). The pixels are constructed from a finite-difference node at its center from which six RC-elements extend to the next interconnected pixel. System sizes up to  $80^3$  pixels were solved numerically using a finite-difference computer algorithm.

In the limit of thin grain boundaries, the brick layer models are a good approximation for the physical properties of electroceramic microstructures and can describe the conductivity well based on mapping individual impedance semicircles corresponding to bulk and grain boundary. Beyond this limit, e.g. for nanocrystalline materials, only the 3D-BLM can be used. However, as grains have not the form of cubes, deviations are to be expected here and impedance semicircles are now influenced by both bulk and grain boundary. Additionally, with increasing complexity, the solution of brick layer models is mathematically challenging.<sup>[318]</sup>

For effective medium theories, closed-form solutions exist. However, as the Maxwell-Wagner/Hashin-Shtrikman model does not represent electroceramic microstructures directly it is rarely used. Though an equivalent circuit analogy exists,<sup>[335]</sup> impedance arcs are influenced by both bulk and grain boundary.

In this work, grain sizes  $d_g$  are much larger compared to the grain boundary thickness  $\delta_{gb}$  which

allows the use of a brick layer model. Since the grain boundary conductivity is significantly lower than the bulk conductivity, the microscopic behavior is modeled using the S-BLM model (Fig. 4.11a) as the conductivity due to a pure grain boundary path can be neglected.<sup>[176,315]</sup> This allows the investigation of individual impedance semicircles, which have either bulk or grain boundary properties. Therefore, the following relation between microscopic and macroscopic grain boundary conductivity can be established:

$$\sigma_{\text{gb}}^{\text{mic}} = \frac{\delta_{\text{gb}}}{d_{\text{g}}} \sigma_{\text{gb}}^{\text{mac}}. \quad (4.8)$$

Hence, the macroscopic grain boundary conductivity is large for large grain sizes and thin grain boundaries. While grain sizes  $d_{\text{g}}$  can be determined using chemical and thermal etching in combination with SEM, defining and measuring the grain boundary thickness  $\delta_{\text{gb}}$  is difficult. Here, the crystallographic grain boundary, which is the crystallographic mismatch zone observed by Transmission Electron Microscopy (TEM) of about 1 nm, can be distinguished from the electrical grain boundary, which additionally includes adjacent space-charge layers and is often connected with the Debye length.<sup>[336,337]</sup> Therefore, often the capacitance of the bulk  $C_{\text{bulk}}$  and grain boundary domain  $C_{\text{gb}}$  is used:<sup>[318,337–339]</sup>

$$\frac{\delta_{\text{gb}}}{d_{\text{g}}} = \frac{C_{\text{bulk}}}{C_{\text{gb}}} \cdot \frac{\epsilon_{\text{gb}}}{\epsilon_{\text{bulk}}}. \quad (4.9)$$

Commonly it is approximated that  $\epsilon_{\text{bulk}} \approx \epsilon_{\text{gb}}$  resulting in

$$\sigma_{\text{gb}}^{\text{mic}} \approx \frac{C_{\text{bulk}}}{C_{\text{gb}}} \sigma_{\text{gb}}^{\text{mac}}. \quad (4.10)$$

Using this method in yttria-stabilized zirconia (YSZ), grain boundary thicknesses were calculated to be about 5.0 nm,<sup>[339–341]</sup> or 5.4 nm,<sup>[332]</sup> independent of grain size.<sup>[337]</sup> For doped ceria, grain boundary thicknesses between 3–50 nm were reported<sup>[306]</sup> while, in this work,  $\delta_{\text{gb}}$  is about 2–5 nm for pure and Sm doped ceria. For nanocrystalline doped ceria, also smaller grain boundary thicknesses were found.<sup>[338]</sup>

### The Total Conductivity

According to the serial brick layer model (S-BLM), the total resistivity is the sum of the macroscopic resistivities of bulk and grain boundary domain,  $R_{\text{total}} = R_{\text{bulk}} + R_{\text{gb}}$ . Therefore the total conductivity

$$\sigma_{\text{total}} = \frac{l/A}{R_{\text{bulk}} + R_{\text{gb}}} \quad (4.11)$$

is always dominated by the higher resistivity or the lower conductivity according to

$$\sigma_{\text{total}} = \frac{\sigma_{\text{bulk}} \cdot \sigma_{\text{gb}}}{\sigma_{\text{bulk}} + \sigma_{\text{gb}}}. \quad (4.12)$$

## 4.2 Computational Details

### 4.2.1 Quantum Mechanical Calculations

#### General Computational Setup

Quantum mechanical calculations were performed using the Vienna Ab initio Simulation Package (VASP)<sup>[342,343]</sup> calculating geometric parameters and energies at zero temperature. All *ab initio* calculations were carried out within the scope of the Density Functional Theory (DFT) using the Generalized Gradient Approximation (GGA) according to Perdew, Burke and Ernzerhof (PBE)<sup>[344]</sup> and the projector augmented-wave method (PAW).<sup>[278]</sup> Alternative methods like LDA and HSE have been investigated in literature.<sup>[56]</sup> Hafner discusses the advantages of the different exchange-correlation-functionals.<sup>[345]</sup>

For the plane waves, an energy cut-off of 500 eV was chosen. Supercells consisting of between 8 (a multiplication of  $2 \times 2 \times 2$  unit cells in each dimension) and 64 unit cells ( $4 \times 4 \times 4$ ) were employed. A Monkhorst-Pack k-point mesh between  $2 \times 2 \times 2$  for the  $2 \times 2 \times 2$  supercell and  $1 \times 1 \times 1$  for the  $3 \times 3 \times 3$  supercell or larger supercells were investigated.

The  $5s^2 5p^6 6s^2 5d^1 4f^1$  electrons of the cerium atoms were treated as valence electrons. Similarly, the  $5s^2 5p^6 6s^2 5d^1$  electrons of the lanthanum, neodymium and samarium atoms, the  $5p^6 6s^2 5d^1$  electrons of the gadolinium, erbium, thulium and lutetium atoms, the  $5p^6 6s^2$  electrons of the ytterbium atoms, the  $3s^2 3p^6 3d^1 4s^2$  electrons of the scandium atoms, the  $4s^2 4p^6 4d^1 5s^2$  electrons of the yttrium atoms, the  $3p^6 3d^5 4s^2$  electrons of the manganese atoms and the  $2s^2 2p^4$  electrons of the oxygen atoms were treated as valence electrons.

To account for the localization of strongly correlated f-electrons, a Hubbard  $U$  parameter was introduced by the rotational invariant approach.<sup>[272]</sup> A repulsion parameter of  $U = 5$  eV for the 4f-orbitals of cerium was chosen according to earlier studies<sup>[45,218,224,275,346–350]</sup> though also other values have been proposed.<sup>[56,274,351–354]</sup>

The total number of electrons in the cell was adapted for all defective cells to reproduce the actual charge state of the defects according to Eq. 2.1, e.g.  $(\text{Ce}_{108}\text{O}_{215})^{2+}$  for a  $3 \times 3 \times 3$  supercell containing one oxygen vacancy. Though charge-neutral cells containing defects according to Eq. 2.1 without adjustment of the number of electrons would be preferable, in this work interactions between defects shall be limited. Therefore, charge-neutral cells with large distances between defects are virtually divided into oppositely charged cells. Charged cells are calculated by VASP assuming a neutralizing background charge, which is a valid approach as shown in literature.<sup>[355]</sup>

The convergence parameters for electronic and ionic relaxation were set to at least  $10^{-5}$  eV and  $10^{-2}$  eV/Å, respectively, to guarantee a sufficient accuracy of the calculated forces.

A lattice constant of 5.49 Å was calculated for defect-free ceria using the Birch-Murnaghan equation of state, which is larger than the experimental lattice parameter due to the chosen set of parameters,<sup>[356–358]</sup> and applied for all calculations as performed in literature.<sup>[51,359,360]</sup> For all

calculations, the internal atomic positions in the cell were relaxed (changed to minimize the energy of the cell) without changing the lattice parameter. Only for selected constant pressure calculations, the lattice parameter was optimized for zero pressure.

Calculated energy differences between cells in VASP are reproducible (about  $\pm 0.001$  eV) due to high electronic and ionic convergence parameters. Transition state related properties have a lower accuracy (about  $\pm 0.01$  eV) as finding the exact ionic geometry is challenging. The choice of potential and especially supercell size affects calculated energies significantly. Furthermore, deviations from the correct energies might also be introduced by using the DFT with the GGA.

### Association Energies between Defects

The association energy is the energy, which is required to move two defects from an infinite distance towards adjacent lattice sites. Possible defects are oxygen vacancies ( $V_{\text{O}}^{\bullet\bullet}$  or  $V$ ) and dopant cations ( $\text{RE}'_{\text{Ce}}$  or  $\text{RE}$ ). Possible distances between defects are numbered consecutively with  $1_{\text{NN}}$  being the nearest neighbor position and  $2_{\text{NN}}$  the next nearest neighbor position. As an infinite large defect distance in an infinitely large supercell cannot be calculated,<sup>1</sup> association energies are approximated as difference to the largest calculated defect distance. The right choice of the largest calculated defect distance, which is in the following referred to as termination, will be discussed in this work.

Figure 4.12 shows the attractive RE-V association energy for RE doped ceria in a  $2 \times 2 \times 3$  supercell calculated up to a RE-V distance of 9 Å.<sup>[1]</sup> Due to the convergence of the energies, it can be concluded that the assumption of a  $6_{\text{NN}}$  RE-V association energy of zero is a good approximation. The convergence is similar to YSZ according to Eichler.<sup>[361]</sup> In another earlier work from 2014,<sup>[55]</sup> only the  $1_{\text{NN}}$  and  $2_{\text{NN}}$  RE-V association energy was given and all other association energies were assumed to be zero. However, the maximum RE-V distance depending on the supercell size was calculated. In this work, the possibility of using the  $3_{\text{NN}}$  RE-V association energy as a maximum RE-V distance will be discussed.

Figure 4.12 also shows the monotonous increase of the  $1_{\text{NN}}$  RE-V association energy (or decrease of its absolute value) with increasing dopant size, which correlates with the electronegativity. For the  $2_{\text{NN}}$  association energy, a minimum for the absolute value of the Y-V association compared to other dopants appears. An energetically preferred  $1_{\text{NN}}$  association is found for small dopants (e.g. Sc), while for the large dopant La the absolute value of the  $2_{\text{NN}}$  RE-V association energy is larger. For comparison, the Coulomb energy was calculated

$$E_{\text{Coulomb}} = \frac{q_1 \cdot q_2}{4\pi\epsilon_0\epsilon_r r} \quad (4.13)$$

with the charge of the defects compared to an ideal lattice  $q$  according to Eq. 2.1, the dielectric constant for vacuum  $\epsilon_0$ , the relative dielectric constant for pure ceria  $\epsilon_r$  of about 25, which was calculated using DFT and the defect distance  $r$ . The classical Coulomb energy, calculated for an

---

<sup>1</sup>Actually, cells with isolated defects can be used. However, earlier investigations show that this method may introduce major errors.<sup>[54,55]</sup>

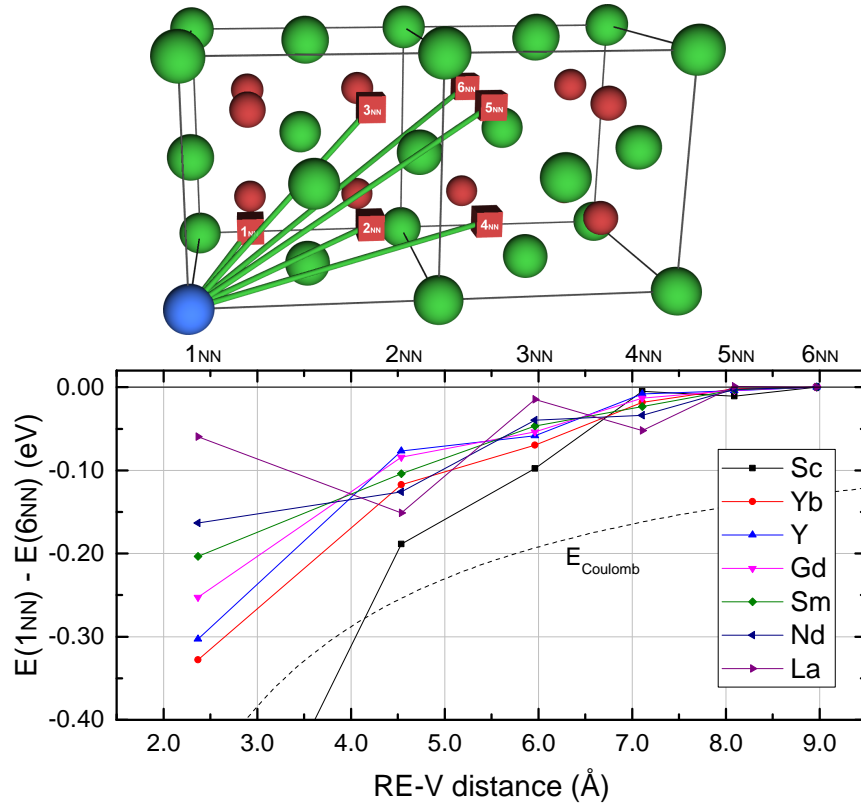


Figure 4.12: Total energy difference between 1<sub>NN</sub> and 6<sub>NN</sub> RE-V and corresponding lattice sites for RE doped ceria in a  $2 \times 2 \times 3$  supercell taken from an earlier work.<sup>[1]</sup> Distances between 1<sub>NN</sub> and 6<sub>NN</sub> RE-V were calculated. The dashed line shows the Coulomb energy. Other Lines are a guide to the eye only. Cerium ions are green spheres, dopants are blue spheres, the oxygen ions are red spheres and the oxygen vacancy is a red cube.

ideal lattice geometry, possesses a larger absolute value compared to the calculated association energies, with the exception of the 1<sub>NN</sub> Sc-V association. Reasons for this deviation are local lattice relaxations and different electron densities. These effects lead to a large difference between the association energies of different dopants as already found in literature.<sup>[44,54]</sup>

### Migration Energies of Oxygen Ion Jumps

The Nudged Elastic Band method (NEB)<sup>[362–364]</sup> was applied to investigate the transition states and the minimum energy pathways. The ionic configuration for the saddle point configuration (‘image’) was interpolated from the initial and final state of the migration process. During the NEB calculations, the atom positions of the interpolated image are relaxed whereat an artificially introduced spring force ( $-5 \text{ eV}/\text{Å}$ ) counteracts deviation of atom positions compared to adjacent images (here: initial and final state).

Tests with more than one intermediate image between the initial and final configuration of the mi-

gration showed no differences in the migration energies. The same is true for tests using the climbing image nudged elastic band method (CI-NEB).<sup>[365]</sup> For the latter, deviations in the lattice geometry of only  $\pm 0.0001$  Å were found. Selected jump configurations were also successfully compared with the improved dimer method.<sup>[366,367]</sup> Only doping with several Sc dopants causes severe problems during the Nudged Elastic Band (NEB) calculation due to the small ionic radius of Sc, which leads to large lattice distortions and a very low solubility of Sc in ceria.

### Diluted Defects and Finite Size Correction

Association and migration energies strongly depend on the finite supercell size due to the interactions of the defects with their image in other cells. Therefore, in literature, generally large supercell sizes are recommended. Alternatively, Freysoldt *et al.* propose a method based on the local electrostatic potential given by VASP to correct electrostatic finite size errors. In this work, the Freysoldt method did not lead to the desired result due to the extended defect clusters.<sup>[368]</sup>

Makov and Payne formulated an analytic expression to correct the electrostatic energy created by periodic boundary conditions in calculations.<sup>[369]</sup> The energy of an isolated defect  $E_{\text{isolated}}$  is given by the calculated energy  $E_{\text{finite}}$  by

$$E_{\text{isolated}} = E_{\text{finite}} + \frac{\alpha \cdot q^2}{2\epsilon L} + \frac{2\pi \cdot qQ}{3\epsilon L^3} + O(L^{-5}) \quad (4.14)$$

with the Madelung constant  $\alpha$  depending on the type of lattice structure, the charge  $q$  and the quadrupole moment of the defect  $Q$ , the linear dimension of the supercell  $L \propto V^{\frac{1}{3}}$  proportional to the third root of the volume of the supercell  $V$ , dielectric constant  $\epsilon$  and unspecified function  $O$  depending on  $L^{-5}$ , which may be neglected for larger supercell sizes.

As both association and migration energies depend only on differences between two cells, the monopole interaction ( $L^{-1}$ ) is neglected. In this work, the dipol interaction ( $L^{-3}$ ) is corrected. Therefore, different supercell sizes are fitted as a function of volume. Equation 4.14 is only valid for cubic supercells. Non-cubic supercells, which were still used in an earlier work from the year 2014 ('model 2014'),<sup>[55]</sup> lead to major deviations as discussed in the following chapters.

In the following, two models are presented. In the model 2014,<sup>[55]</sup> edge energies were only calculated in a  $2 \times 2 \times 2$  supercell while the model 2015 includes edge energies extrapolated from a  $2 \times 2 \times 2$  and a  $3 \times 3 \times 3$  supercell to an infinitely large supercell.

### Phonon Calculations

For phonon calculations, the convergence parameters for electronic and ionic relaxation were increased to  $10^{-8}$  eV and  $10^{-4}$  eV/Å, respectively.

Phonon frequencies at constant volume were calculated using the finite difference method, which was introduced by Parlinski *et al.*,<sup>[370]</sup> implemented in the commercial software MedeA.

The ionic geometries of all investigated structures were relaxed, subsequently displaced by  $\pm 0.005$  Å and the electronic ground state was calculated. Using the Hellmann-Feynman forces

on the ions, a force constant matrix was built and Fourier-transformed. The diagonalization of the dynamical matrix yielded the phonon frequencies at different wave vectors ( $\mathbf{q}$ -points). No longitudinal or transverse optical splitting (LO/TO) was applied.

## 4.2.2 Monte Carlo Simulations

### Metropolis Monte Carlo

MMC simulations were performed in a  $12 \times 12 \times 12$  supercell with 20736 ions or vacancies and periodic boundary conditions. The lattice configuration energy  $E_{\text{conf}}$  was calculated according to a pair interaction model with the number of interactions  $N^i$  and the distance  $i$  based on DFT calculations of the RE-RE, RE-V and V-V association energy  $\Delta E^i$ :

$$E_{\text{conf}} = \sum_i N_{\text{RE-RE}}^i \cdot \Delta E_{\text{RE-RE}}^i + \sum_i N_{\text{RE-V}}^i \cdot \Delta E_{\text{RE-V}}^i + \sum_i N_{\text{V-V}}^i \cdot \Delta E_{\text{V-V}}^i \quad (4.15)$$

where association energies up to 1<sub>NN</sub> RE-RE, 2<sub>NN</sub> RE-V and 4<sub>NN</sub> V-V in the model 2014 (cut-off radius 5.5 Å with neglected 2<sub>NN</sub> RE-RE interaction)<sup>[55]</sup> or 2<sub>NN</sub> RE-RE, 2<sub>NN</sub> RE-V and 4<sub>NN</sub> V-V in the model 2015 (cut-off radius 5.5 Å) are used. The models and used parameters are discussed in Chapter 5.1. Coordination numbers from MMC simulations are averaged over 20 individual simulations each with additional  $5 \cdot 10^5$  Monte Carlo steps after reaching equilibrium.

Three different lattice types are created: In a RND lattice the cation sublattice is randomly ordered (or equilibrated at infinite temperature  $T_1 = \text{inf}$ ) while the anion sublattice is in thermodynamic equilibrium at the investigated temperature  $T_2$ . This type of lattice is commonly used in KMC simulations in literature and this work.<sup>[220,225,281,282,286,287,371–373]</sup> In an EQ lattice, both sublattices are equilibrated at 2/3 of the ceria melting point ( $T_1 = 1500$  K) similar to the sintering process in experiments. At lower temperatures, the cations are frozen due to their low mobility and the anions are equilibrated at  $T_2$ . In a DEG lattice, both sublattices are equilibrated at the final investigated temperature  $T_1 = T_2$ , simulating a degraded lattice, which had a very long time to reach thermodynamic equilibrium.

All MMC simulations were performed by Steffen Grieshammer.<sup>[374]</sup>

### Kinetic Monte Carlo

KMC Simulations were performed using the software iCon developed by Philipp Hein and Benjamin Grope<sup>[287]</sup> according to an earlier work<sup>[55]</sup> in a  $16 \times 16 \times 16$  supercell with 49152 ions or vacancies and periodic boundary conditions.

Random lattice configurations were used. Anion sublattices were at first equilibrated by 100 Monte Carlo Steps per particle. For low temperatures, lattices were employed, which were equilibrated at higher temperature, and subsequently only 10 Monte Carlo Steps per particle for equilibration were used. For the investigation of degradation effects, lattices were equilibrated using MMC simulations.

An electric field strength of  $0.1 k_B$  was used, which had no influence on the thermodynamic equilibrium according to an earlier work.<sup>[55]</sup> Dynamical scaling was activated for temperature below  $500\text{ }^\circ\text{C}$  where up to  $10^{-5}\%$  of the most probable jumps from a sampling size of  $5 \cdot 10^9$  were always accepted. Tests confirm no influence of the dynamical scaling on the ionic conductivity.

Simulations of the ionic conductivity were repeated at least ten times each with 100 Monte Carlo Steps per particle. The standard error on the conductivity results primarily from the use of different starting lattices.

The calculation of the migration energy  $E_{\text{mig}}$  is described in Chapter 7. Two models are presented in which association energies up to  $2_{\text{NN}}$  RE-V and  $3_{\text{NN}}$  V-V in the model 2014 (cut-off radius  $4.7\text{ \AA}$ )<sup>[55]</sup> and  $2_{\text{NN}}$  RE-V and  $4_{\text{NN}}$  V-V in the model 2015 (cut-off radius  $5.5\text{ \AA}$ ) are used.

# 5 Defect Interactions and Local Structures

In this chapter, defect interactions and association energies are calculated for doped ceria. Subsequently, MMC simulations are employed to simulate the local structure. In addition, EXAFS measurements are performed.

## 5.1 Defect Interactions and Association Energies

In DFT calculations, cells with isolated defect clusters as well as cells with experimental defect concentrations were studied. Association energies should be investigated in infinite large cells, while the validity of the pair interaction model can be investigated best at experimental defect concentrations. As the supercell size is limited due to large calculation times, defects interact with their image in other cells. Therefore, association energies are calculated in different supercell sizes and extrapolated to an infinitely large supercell.

### 5.1.1 Diluted Defects

#### RE-V Association Energy

In this work, the attractive  $1_{\text{NN}}$  and  $2_{\text{NN}}$  RE-V association energy was calculated in the  $2 \times 2 \times 2$  and  $3 \times 3 \times 3$  supercell in relation to the  $3_{\text{NN}}$  RE-V association energy (Fig. 5.1), according to  $E_{\text{RE-V}}^1 = E(1_{\text{NN}}) - E(3_{\text{NN}})$  and  $E_{\text{RE-V}}^2 = E(2_{\text{NN}}) - E(3_{\text{NN}})$  where  $E(x_{\text{NN}})$  is the energy of the supercell with a  $x_{\text{NN}}$  RE-V distance. Using the finite size correction according to Makov and Payne (Eq. 4.14), energies for an infinitely large supercell are obtained ('inf'). Ionic radii are given according to Shannon.<sup>[32]</sup>

Figure 5.1 shows a monotonous decrease of the absolute value of the  $1_{\text{NN}}$  RE-V association energy with increasing dopant size (cp. Chapter 4.2.1). For the absolute value of the  $2_{\text{NN}}$  association energy, a minimum for the Lu-V association compared to other dopants appears. Again, an energetically preferred  $1_{\text{NN}}$  association is found for small dopants (e.g. Sc), while for the large dopant La the absolute value of the  $2_{\text{NN}}$  RE-V association energy is larger, in agreement with literature.<sup>[44,54,55,224]</sup> Yb<sup>3+</sup> and Mn<sup>2+</sup> show deviation from this behavior. However, Mn is not a rare-earth element and has

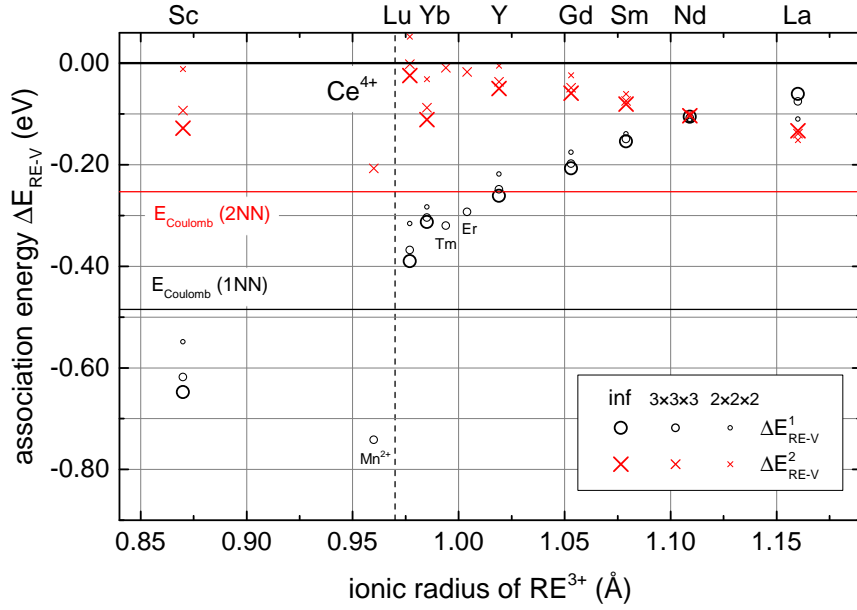


Figure 5.1: RE-V interaction for different supercell sizes and  $\Delta E_{\text{RE-V}}^3 = 0$ .

a different charge state. In addition, the used PAW-GGA-PBE potential for ytterbium is optimized for  $\text{Yb}^{2+}$ .

For small dopants, the absolute value of the association energy decreases for decreasing cubic supercell sizes. Lu dopant and oxygen vacancies even repel each other on next nearest neighbor position (2<sub>NN</sub>) in a  $2 \times 2 \times 2$  supercell. The Nd-V association energy is independent of the supercell size. The absolute value of the La-V interaction energy increases for smaller cubic supercell sizes. All these supercell size depended effects emphasis the need for extrapolation of the association energy to an infinitely large supercell.

$\text{Lu}^{3+}$  and  $\text{Mn}^{2+}$  have a similar ionic radius compared to  $\text{Ce}^{4+}$ . Therefore, it could be assumed that their strong association with oxygen vacancies is not caused by elastic contributions (local distortions) but the Coulomb energy. In fact, for the  $3 \times 3 \times 3$  supercell, the 1<sub>NN</sub> Mn-V association is twice as large as the 1<sub>NN</sub> Lu-V association. The absolute value of the 1<sub>NN</sub> Mn-V association energy is 25% smaller than the absolute value of the calculated Coulomb energy. However, the 2<sub>NN</sub> Lu-V association energy is nearly zero, while the absolute value of the 2<sub>NN</sub> Mn-V association energy is less than half of the absolute value of the calculated Coulomb energy. Therefore, the above-stated assumption fails, and the association energy is influenced by elastic contributions (local distortions). Beyond that, the equivalent radii for  $\text{Ce}^{4+}$  and  $\text{Lu}^{3+}$  affect the association energy as the 2<sub>NN</sub> RE-V association energy has a maximum for Lu.

**Termination and finite size correction** Compared to the work of Nakayama and Martin,<sup>[54]</sup> an own work shown in Chapter 4.2.1 and an improved work in cooperation with Steffen Grieshammer,<sup>[55]</sup> two major changes to the calculation of the association energy were made: termination and finite size correction.

Firstly, the association energy strongly depends on the supercell sizes. As a result, the association energy was extrapolated to an infinitely large supercell to avoid any size dependencies using finite size correction. While Nakayama and Martin used a  $2 \times 2 \times 2$  supercell<sup>[54]</sup> and in Chapter 4.2.1 a  $2 \times 2 \times 3$  supercell was used, an infinitely large supercell was extrapolated in cooperation with Steffen Grieshammer,<sup>[55]</sup> which is referred to in the following as model 2014, as well as in this work, which is referred to in the following as model 2015. It should be noted that the extrapolations in the models 2014 and 2015 are different: In model 2015 the extrapolation was performed using cubic supercells ( $2 \times 2 \times 2$  and  $3 \times 3 \times 3$ ), while for the model 2014 also non-cubic supercells were used, which is not ideal.

The use of finite size correction leads to an almost constant shift in the association energy. This can be seen in comparing the work of Nakayama and Martin<sup>[54]</sup> and Chapter 4.2.1 with the models 2014 and 2015.<sup>[55]</sup>

Secondly, the association energy is defined as the energy that is required to move two defects from an infinite distance towards adjacent lattice sites. On the one hand, infinite distances necessary for the so-called ‘infinite termination’ are difficult to calculate. On the other hand, association energies are usually only calculated for a selected defects distance. Any further interactions are assumed to be zero. Therefore, it seems obvious to use the first interaction, which is assumed to be zero (e.g. at 6 Å RE-V distance), directly as a reference for ‘termination at the first neglected interaction’.

To compare both types of termination, it may be assumed that the association energy is identical to a fictive Coulomb energy according to Eq. 4.13. Adjacent defects, nearby defects and widely separated defects are distinguished. While an adjacent defect is on a nearest neighborhood site ( $1_{\text{NN}}$ ) or in close vicinity up to  $i_{\text{NN}}$ , nearby defects are just outside of the considered interaction radius on  $(i+1)_{\text{NN}}$ . Here, for infinite termination, the energy difference between ionic configurations with adjacent defects and widely separated defects is well defined. However, the energy difference of nearby defects compared to adjacent defects just outside of the considered interaction radius is too large. For a termination at the first neglected interaction, the latter is well defined. However, the energy for widely separated defects is now assumed too low. Instead, their energy is equivalent to adjacent defects.

Thus, both types of terminations keep the ranking of different configurations while for the termination at the first neglected interaction also the energies between defects just outside of the considered interaction radius are well defined. The latter is of significant importance for KMC simulation. As for MMC simulation permutations across the whole lattice are possible, intuitively the infinite termination might be better suited, which coincides with the classical definition of the association energies. Nevertheless, MMC simulation of Y doped ceria using the termination at the

first neglected interaction show a better agreement with experimental literature (see Chapter 5.2.1). Both arguments support the use of the termination at the first neglected interaction in this work.

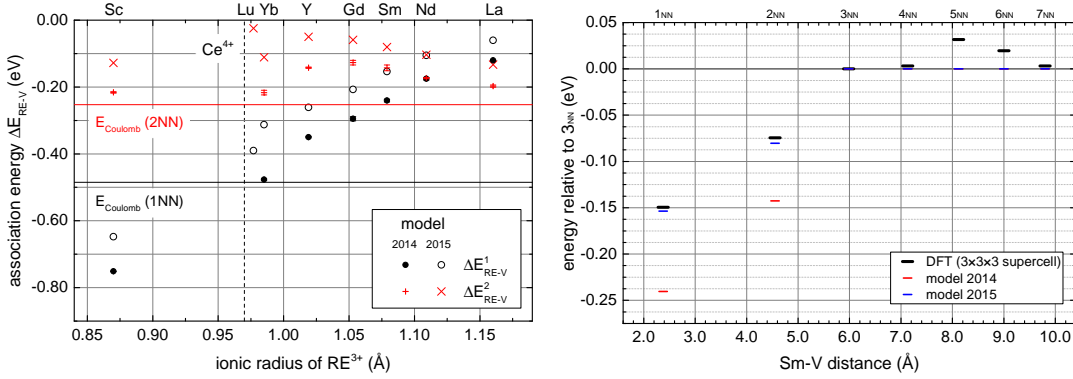


Figure 5.2: RE-V interaction for the infinitely large supercell (left and right) or the  $3 \times 3 \times 3$  supercell (right). For the former, association energies are extrapolated for either  $2 \times 2 \times 2$  and  $3 \times 3 \times 3$  supercells (model 2015) or variable supercell sizes (model 2014).<sup>[55]</sup> The RE-V interaction is calculated relative to  $3_{NN}$  (model 2015) or infinite distances (model 2014).

The use of infinite termination or termination at the first neglected interaction leads to an almost constant shift of 0.1 eV as shown in Fig. 5.2 (left). Here, the model 2014,<sup>[55]</sup> which uses the infinite termination, and model 2015, which uses the termination at the first neglected interaction, are compared.

In addition, Steffen Grieshammer calculated association energies by DFT calculations with experimental dopant concentrations and found for Y and Sm doped ceria similar RE-V association energies as for the model 2015.<sup>[374]</sup>

Figure 5.2 (right) illustrates the difference between both models as a function of defect distance. The energy difference between  $1_{NN}$  and  $2_{NN}$  is similar for both models, while all other energy differences deviate. In the further course of this work, the model 2015, which is based on a limited amount of extrapolated energies, is compared to DFT calculations in the  $3 \times 3 \times 3$  supercell for each individual configuration, as larger supercells are computationally too expensive. Surprisingly, the association energy of Sm doped ceria does not behave monotonously like the Coulomb energy. The agreement between DFT energies and the model 2015 supports the use of the termination at the first neglected interaction.

Comparisons with other theoretical studies show a strong influence of used method, supercell size and termination on the association energy.<sup>[39,40,44,223,224,231,275,350]</sup> As a result, both positive and negative RE-V association energies were calculated, and the transition between energy-favorable  $1_{NN}$  or  $2_{NN}$  appears at different dopant radii. For example, Dholabhai *et al.* predicted an energy-favorable  $2_{NN}$  Pr-V interaction,<sup>[224,275,350]</sup> while Andersson *et al.* already found similar association energies for  $1_{NN}$  and  $2_{NN}$  Pm-V (Fig. 5.3).<sup>[44]</sup>

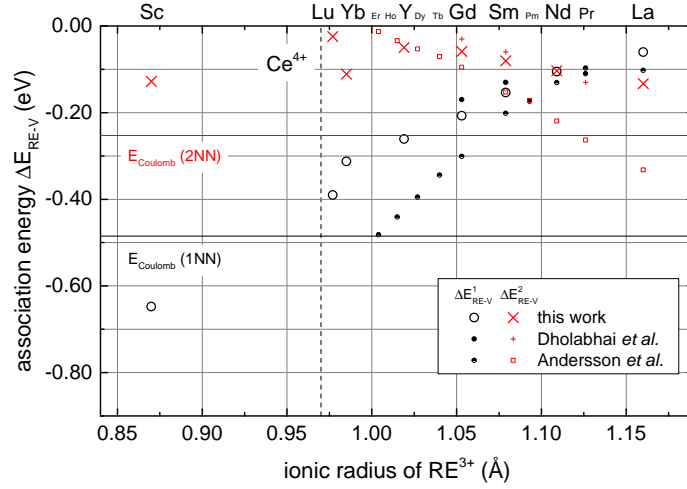


Figure 5.3: RE-V association energy in comparison with other theoretical studies. [44,224,275,350] For Dholabhai *et al.* a termination at 3<sub>NN</sub> is assumed.

**Experimental values** The large absolute value of the association energy for Sc is in agreement with its low experimental solubility. [66,207] MMC calculations confirm phase separations for larger dopant fractions caused by strong association. [55]

The experimental values as discussed in Chapter 2.5.2 are defined as positive values and confirm a strong association of Sc doped ceria. Likewise, a stronger association of Y compared to Gd or Y compared to La is measured. The range of experimental and calculated association energies is similar. However, the smallest association is measured for Gd, in contrast to the calculated 1<sub>NN</sub> association energies.

Though the experimental values scatter, and earlier considerations also consider the possibility of extrapolating experimental values to infinite low concentrations, [55] a significant difference between calculated 1<sub>NN</sub> association energies and experimental association energies is found. Consequently, a direct comparison of calculated 1<sub>NN</sub> association energies with experiments might not be possible as e.g. for La doped ceria, oxygen vacancies are also trapped in the 2<sub>NN</sub> position. The resulting influence of several RE-V and additional V-V association energies can be properly compared with impedance experiments by calculating the temperature-dependent ionic conductivity using KMC simulations. Results will be presented in Chapter 6, 7 and 8.

## V-V Association Energy

For the repulsive interaction of two oxygen vacancies (Fig. 5.4), a fast decrease in the positive association energy is found between the  $1_{\text{NN}}$  and  $2_{\text{NN}}$  interaction (Fig. 5.5). Further interactions are similar up to the  $5_{\text{NN}}$  V-V interaction, which is considerably small and will, therefore, be neglected in the following. For the  $3_{\text{NN}}$  V-V interaction, there are two possible geometries, one without ( $3_{\text{NNA}}$ ) and one with a cation between the oxygen vacancies ( $3_{\text{NNB}}$ ). Both show significantly different association energies, though this difference decreases with increasing supercell size.

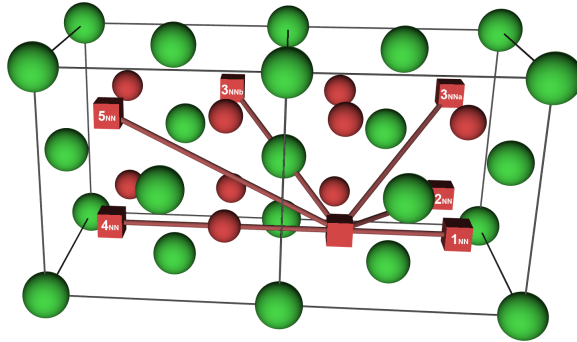


Figure 5.4: V-V interaction lattice sites. Cerium ions are green spheres, oxygen ions are red spheres and oxygen vacancies are red cubes.

The  $1_{\text{NN}}$  V-V interaction energy is independent of the supercell size. For other V-V distances, increasing the supercell sizes leads to both lower and higher association energies, probably due to different shielding effects of the surrounding cations.

Nakayama and Martin<sup>[54]</sup> found a smaller  $1_{\text{NN}}$  V-V association energy (0.77 eV), not because of the missing finite-size correction as suggested earlier,<sup>[55]</sup> but because of the missing Hubbard  $U$  parameter and the different termination.

Compared to the model 2014, which was calculated similar as described for the RE-V interaction above, a nearly constant energy shift of 0.05–0.1 eV to lower energies for the model 2015 was found. Again, the main reason is the termination at the first neglected interaction additionally to the new extrapolation method (Fig. 5.6).<sup>[55]</sup>

Steffen Grieshammer calculated association energies based on DFT calculations with experimental dopant concentrations and found for Y and Sm doped ceria similar V-V association energies as for the model 2015 with the exception of the  $3_{\text{NN}}$  V-V configuration with an intermediary cation.<sup>[374]</sup>

Furthermore, the results are in agreement with Ismail *et al.*, who also found a rapid decrease in the V-V repulsion after the first shell, similar energies for  $2_{\text{NN}}$  to  $4_{\text{NN}}$  and a negligible  $5_{\text{NN}}$  V-V interaction.<sup>[375]</sup>

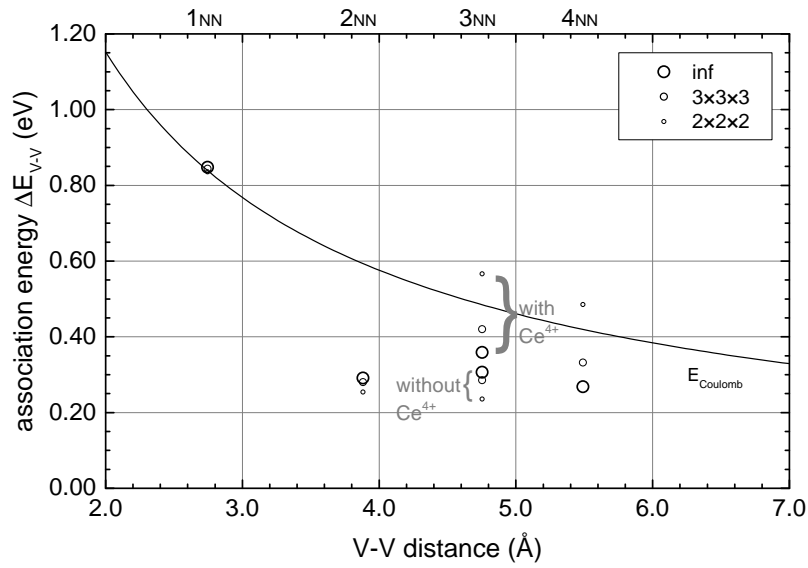


Figure 5.5: V-V interaction for different supercell sizes.

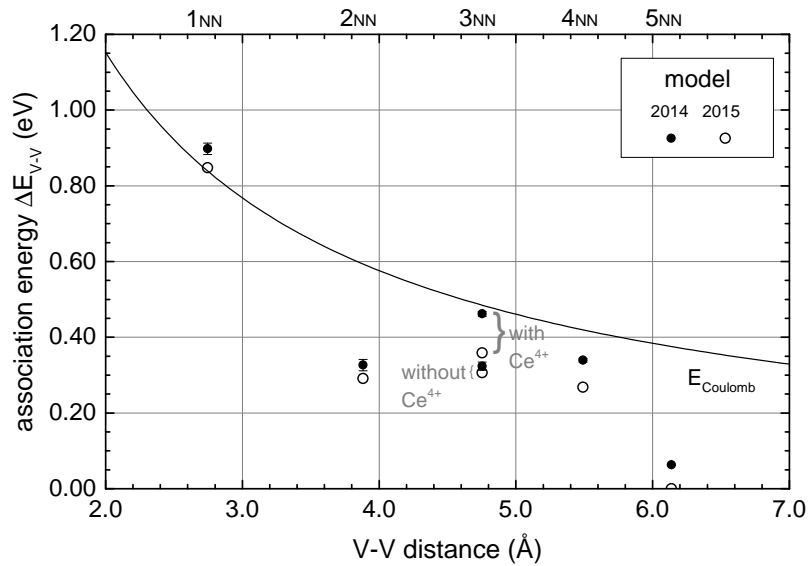


Figure 5.6: V-V interaction extrapolated for  $2 \times 2 \times 2$  and  $3 \times 3 \times 3$  supercells (model 2015) or variable supercell sizes (model 2014).<sup>[55]</sup> The V-V interaction is calculated relative to  $5_{NN}$  (model 2015) or infinite distances (model 2014).

### 5.1.2 High Defect Concentrations

Until now, only the association of two defects was investigated. The association energy models are pair interaction models where energies of multiple defects are just summed up and therefore linearly scaled.

For three defects, DFT calculations of a  $3 \times 3 \times 3$  supercell with two Sm dopants and one oxygen vacancy (Fig. 5.7), in accordance with Eq. 2.1, confirm the validity of the pair interaction model as already found by Nakayama and Martin.<sup>[54]</sup> The energy differences between 1<sub>NN</sub> and either 2<sub>NN</sub>, 4<sub>NN</sub> or 5<sub>NN</sub> Sm-V interaction nearly doubles for an additional Sm dopant with deviations less than 0.005 eV. Therefore, the introduction of triplet interactions can be dispensed.

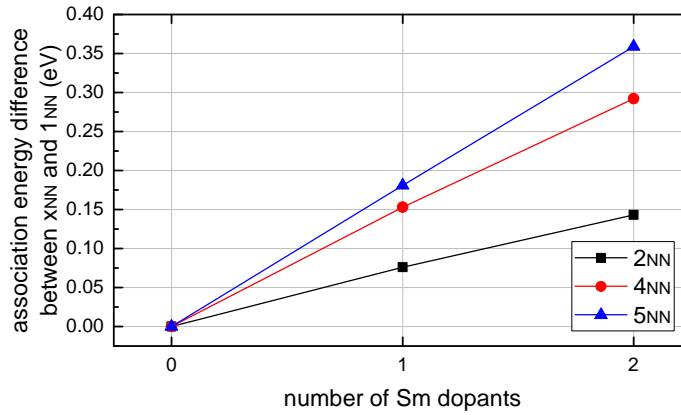


Figure 5.7: Sm-V association energy difference between  $x_{NN}$  and 1<sub>NN</sub> for one oxygen vacancy and either one or two Sm dopants.

For higher defect concentration similar to experimentally used materials, MMC simulations in a  $3 \times 3 \times 3$  supercell were performed by Steffen Grieshammer for this work to determine typical ionic configurations for  $\text{Ce}_{1-x}\text{Sm}_x\text{O}_{2-x/2}$  with  $x = 0.05, 0.1$  and  $0.15$ . Subsequently, in this work, the energy of the supercell was determined using DFT calculations. Typical jump configurations were identified, and jumps were performed using again DFT calculations. The difference between initial and final state of an oxygen ion jump gives an association energy difference, which is crucial to investigating diffusion in doped ceria. Comparing the DFT association energy differences with a pair interaction model with the above-calculated energies for dilute defects, helps to validate the use of both an additive model with linear scaling (pair interaction model) and the used association energies.

In total, 450 association energy differences were investigated. Figure 5.8 shows a good agreement between model and DFT association energy differences, especially for low defect concentrations. With increasing dopant fractions, the standard deviation  $\sigma_s$  increases with 0.09, 0.12 and 0.15 for  $x = 0.05, 0.1$  and  $0.15$ , respectively. For all dopant fractions  $\sigma_s$  is totally 0.13. The good agreement validates that a pair interaction model with non-interacting cation and anion sublattice can be used.

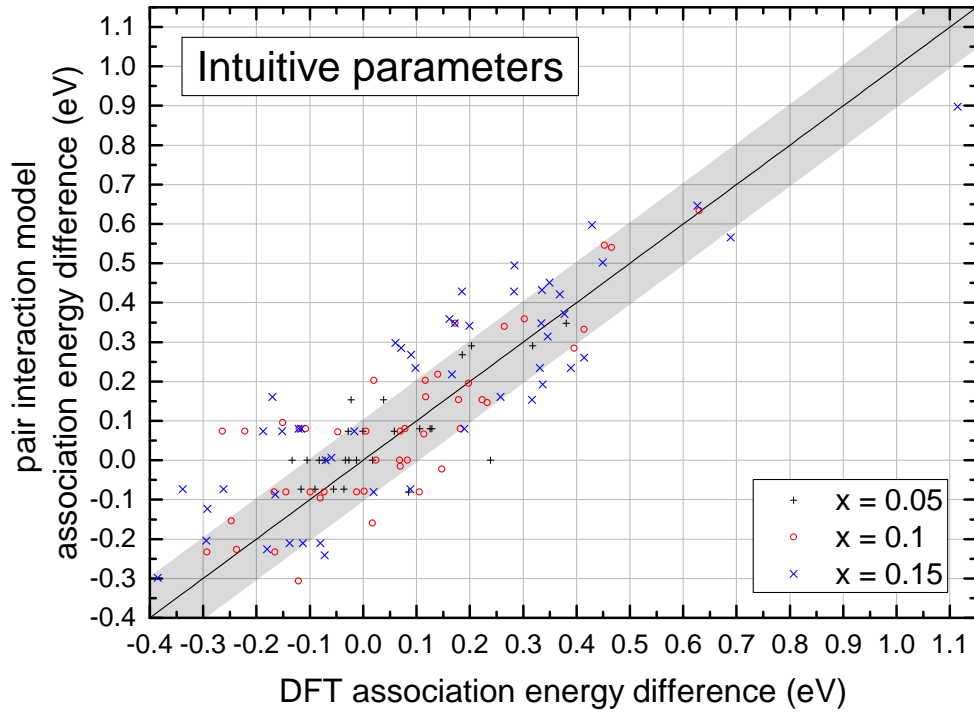


Figure 5.8: Model and DFT association energies with intuitive parameters. The jumping oxygen vacancy interacts with both dopants and vacancies. Both sublattices interact. Association energies around the moving oxygen vacancy up to  $2_{\text{NN}}$  RE-V and  $4_{\text{NN}}$  V-V ( $5.41 \text{ \AA}$ ) are added up. Intuitive parameters are chosen for the extrapolated supercell according to Chapter 7.2 with the termination  $E_{\text{ass}}(3_{\text{NN}} \text{ RE-V}) = 0$  and  $E_{\text{ass}}(5_{\text{NN}} \text{ V-V}) = 0$ . Sm doped ceria in  $3 \times 3 \times 3$  supercell.

## 5.2 Local Structure

The calculated association energies can be used to simulate the local structure in doped ceria using MMC simulations. The results are compared with EXAFS measurements of the coordination numbers of the cations in Y, Gd and Sm doped ceria.

### 5.2.1 Metropolis Monte Carlo Simulations

MMC simulations were performed with association energies according to the models 2014<sup>[55]</sup> and 2015. For the model 2015, a similar RE-RE interaction for all dopants based on 1<sub>NN</sub> and 2<sub>NN</sub> Sm-Sm was assumed for all dopants. MMC simulations were performed by Steffen Grieshammer using a randomly distributed cation sublattice. While generally in this work the standard deviation is used as an error, for the MMC simulations the standard error of the mean is shown as an error, which is the standard deviation divided by the square root of the numbers of independent simulations.

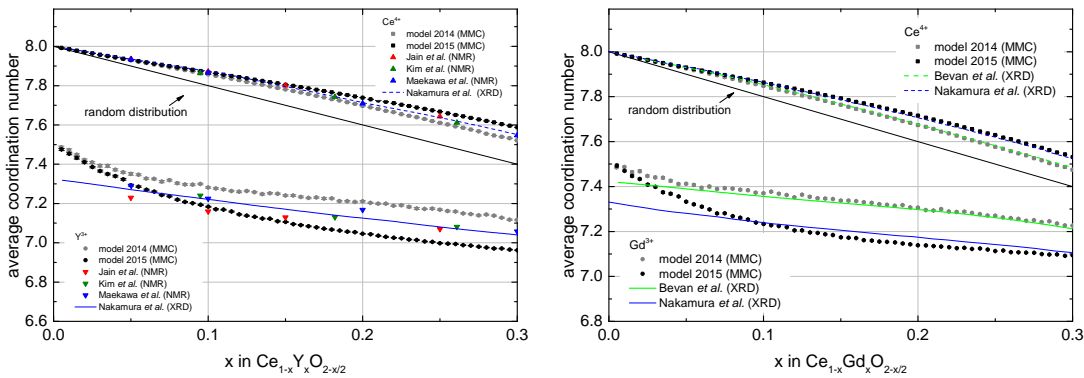


Figure 5.9: Coordination numbers according to NMR<sup>[210–212]</sup> and XRD experiments<sup>[376]</sup> for Y doped ceria (left) and according to XRD experiments<sup>[377,378]</sup> for Gd doped ceria (right). For Gd doped ceria, Bevan *et al.* sintered the samples at 1600 °C and Nakamura *et al.* at 1450 °C. Additionally, MMC simulations according to the models 2014<sup>[55]</sup> and 2015 are shown.

For a random distribution of defects, the (average) coordination number is  $CN = 8 - 2 \cdot x$ . The oxygen vacancy concentration increases for increasing dopant fractions leading to a lower coordination number for the first shell of both the Ce<sup>4+</sup> and RE<sup>3+</sup> ions. The coordination number is identical for both cations. A random distribution will emerge at very high temperatures.

For Y, Gd and Sm doped ceria at room temperature (Fig. 5.9 and 5.10) all Ce<sup>4+</sup> coordination numbers are larger and all RE<sup>3+</sup> coordination numbers are smaller than those in a random distribution. This indicates an association of oxygen vacancies with rare-earth dopants.

As the absolute value of the 1<sub>NN</sub> RE-V association energy decreases with increasing ionic radius of the dopant, the MMC simulations show a decreased association with increasing ionic radius (Fig. 5.10).

Coordination numbers for the model 2015 are larger ( $\text{Ce}^{4+}$ ) or smaller ( $\text{RE}^{3+}$ ) than for the model 2014, which suggests a stronger association of oxygen vacancies with dopants in the model 2015. Exceptions to this behavior can be found for very small dopant concentrations. The stronger association for the model 2015 is surprising, as the RE-V association energies are less negative suggesting a decline in association.

Possible reasons for the stronger association are the smaller  $1_{\text{NN}}$  RE-RE association ( $0.1 \rightarrow 0.04$  eV), the introduction of a  $2_{\text{NN}}$  RE-RE association ( $0 \rightarrow 0.02$  eV) or a by  $0.05\text{--}0.1$  eV smaller V-V association.

Due to the decreasing  $1_{\text{NN}}$  RE-RE repulsion from the model 2014 to 2015, about 10% more configurations with dopants in  $1_{\text{NN}}$  position appear. For these  $1_{\text{NN}}$  RE-RE pairs, an oxygen vacancy probably appears in  $1_{\text{NN}}$  position to both dopants due to the combined attraction of both dopants. This leads to a significant decrease in the RE-O coordination number and an increase in the Ce-O coordination number. This strong effect is surprising, as the RE-RE repulsion is only considered at 1500 K, where the high temperature favors the entropic influence of the number of possible lattices sites rather than the RE-RE repulsion energy, while the lattice is relaxed afterwards at 300 K using only the RE-V and V-V association.

The V-V repulsion decreases from model 2014 to 2015, however, less than the RE-V association. The number of V-V pairs (in  $2_{\text{NN}}$ ,  $3_{\text{NN}}$  and  $4_{\text{NN}}$ ) for the model 2015 is smaller than those according to the model 2014. This suggests a stronger V-V repulsion in the model 2015. Generally, it is assumed that a strong V-V repulsion prevents two oxygen vacancies to approach a single dopant in nearest neighborhood. In case the V-V repulsion is neglected in MMC simulations, a very strong RE-V association is found.<sup>[374]</sup> However, also a strong V-V repulsion might increase the association: In case of the above-described (RE-V-RE) triplet, a strong V-V repulsion repels a second oxygen vacancy, which subsequently might search for another dopant pair in  $1_{\text{NN}}$  position. This might decrease the RE-O coordination number and increase the Ce-O coordination number.

For low dopant fractions, coordination numbers according to the model 2014 indicate a stronger RE-V association than the model 2015, especially for Sm doped ceria. However, for lightly doped ceria, even more  $1_{\text{NN}}$  Sm-Sm pairs exist in the model 2015 (more than twice as much) than in the model 2014. Due to the low oxygen vacancy concentration, nearly no V-V pairs exist. Therefore, for low dopant fractions, the above-described interpretation fails. It may be noted that the strong deviations between both models for Sm doped ceria are a result of the low Sm-V association. Additionally, the coordination numbers of lightly Sm doped ceria show significantly lower RE-V association than Y and Gd doped ceria though the deviation in RE-V association energy is similar between Y and Gd or Gd and Sm. This clearly shows competing effects between the RE-V association and the V-V or RE-RE repulsion, which do not lead to soft transitions between coordination numbers.

Steffen Grieshammer calculated association energies based on DFT calculations with experimental dopant concentrations and found for Y and Sm doped ceria similar MMC coordination numbers as for the model 2015.<sup>[374]</sup>

For Y doped ceria (Fig. 5.9), coordination number according to NMR<sup>[210–212]</sup> and XRD experiments<sup>[376]</sup> are in agreement with both MMC models.

For Sm doped ceria (Fig. 5.10), XRD experiments<sup>[376]</sup> are in better agreement with the MMC simulations for the model 2014 rather than for the model 2015.

For Gd doped ceria (Fig. 5.9), coordination numbers were extracted from XRD experiments by Bevan *et al.* and Nakamura *et al.*<sup>[377,378]</sup> According to Nakamura, the main difference between both experimental investigations is the sintering temperature. Bevan *et al.* sintered their samples at 1600 °C and Nakamura *et al.* at 1450 °C. Surprisingly, the MMC simulations according to the model 2014 fit well to the values of Bevan *et al.*, while the model 2015 fits to the values of Nakamura *et al.* For this reason, there is experimental evidence for both models.

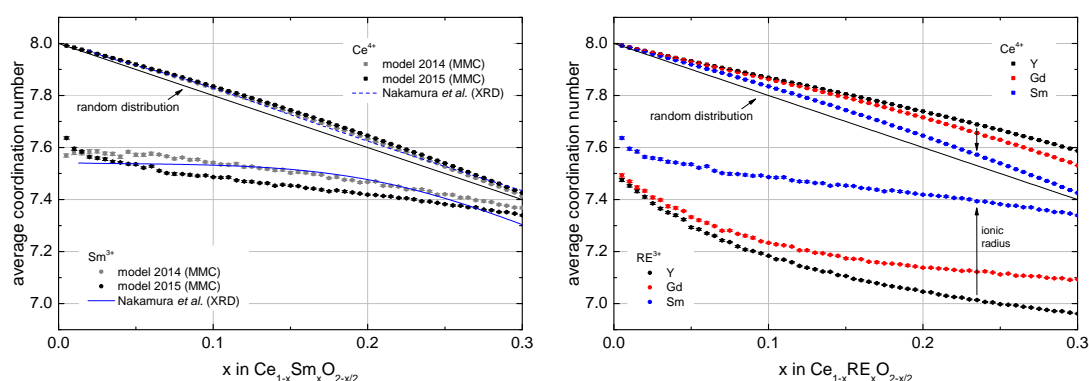


Figure 5.10: Coordination numbers for Sm doped ceria (left) according to XRD experiments<sup>[376]</sup> and MMC simulations for the models 2014<sup>[55]</sup> and 2015 are shown. Additionally, MMC simulations for Y, Gd and Sm doped ceria according to the model 2015 are compared (right).

## 5.2.2 Coordination Numbers in EXAFS Experiments

Experimentally, the local structure was investigated in this work using EXAFS. In literature, doped ceria has already been studied using XANES<sup>[379]</sup> and EXAFS<sup>[206–209,230,380–383]</sup>. Y doped ceria has been investigated for dopant fractions of  $x = 0, 0.05, 0.1, 0.15, 0.2, 0.25$  and  $0.3$ . However, Sm doped ceria, which possesses a significantly higher conductivity, has only been investigated for dopant fractions of  $x = 0.1, 0.2,$  and  $0.3$ . In this work, significantly smaller doping increments are used ( $0.025$ ), and the method of calculating the coordination number has been improved.

### Sm doped ceria, Ce-edge

As shown in Chapter 4.1.4, a Radial Distribution Function can be extracted from the EXAFS oscillation. For the Ce-edge in Sm doped ceria, the extracted Radial Distribution Function before phase-shift correction is shown in Fig. 5.11.

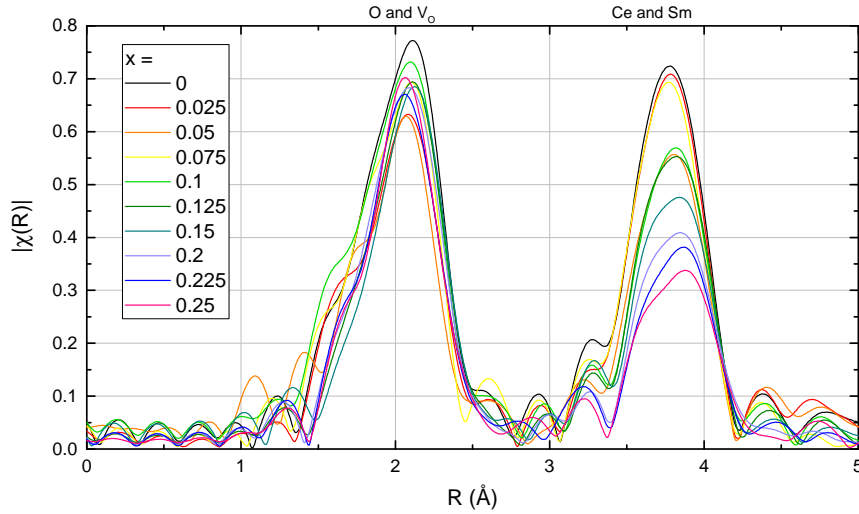


Figure 5.11: Radial Distribution Function at Ce(K)-edge of  $\text{Ce}_{1-x}\text{Sm}_x\text{O}_{2-x/2}$ .

The Radial Distribution Function shows contributions of oxygen ions or vacancies (first peak) as well as cerium ions or Sm dopants (second peak). The amplitude fluctuates for the first coordination shell. For the second coordination shell, the amplitude decreases with increasing dopant fraction and changes its shape. Similar observations were made previously.<sup>[230,236,382,383]</sup> For Y, Gd and La doped ceria, even a decrease for the amplitude of the first peak with increasing dopant fraction up to  $x = 0.25$  was found.<sup>[206,207,209]</sup>

Compared to pure ceria, doping with Sm leads to smaller amplitudes due to a decrease in coordination number and an increase in structural disorder. For the first peak, especially a decrease in coordination number is expected. In this work, however, only a fluctuation of the amplitude can be observed. For the second peak, an increasing amount of Sm dopants clearly leads to a lower backscattering. The Debye-Waller factor decreases due to the disorder of the cation sublattice caused by the cation substitution. The increasing disorder also contributes to the broadening of the second peak.

Additionally, differences in interatomic distance can be observed. The maximum of the first coordination peak (oxygen ions and vacancies) moves to lower  $R$  values for higher dopant fractions. The second peak broadens and rather moves to larger  $R$  values for higher dopant fractions. Similar observations were made up to  $x = 0.2$  in literature, though the position of the second peak varies.<sup>[206,207,209,230,236,382,383]</sup> An exception is the result of Yamazaki *et al.*<sup>[207]</sup> They show in the Radial Distribution Function for the maximum of the first peak an increasing  $R$  value with increasing dopant fraction, though they report decreasing Ce-O distances.<sup>[207]</sup> The reason for this deviation is the missing phase-shift correction for the shown Radial Distribution Function. This emphasizes the importance of modeling according to the EXAFS equation.

Decreasing Ce-O distances correlate with the expected decrease in coordination number. In other words, oxygen ions near cations relax towards adjacent vacancies leading to decreasing cation-anion distances. Especially the position of the second peak is influenced by the change in lattice parameter

(Fig. 2.3). As the distances between Ce-Ce and Ce-RE differ, a broadening of the second peak is observed as shown by Deguchi *et al.*<sup>[209]</sup>

Afterwards, the Radial Distribution Function is modeled using the EXAFS equation (Chapter 4.1.4). The results are shown in Table 9.1 in the appendix. To investigate the local structure, the first coordination shell around a cation was chosen. Here, oxygen ions or vacancies are present. The occupation of the first coordination shell or the coordination number of cations shows the formation of Ce-V or Sm-V associates in nearest neighborhood.

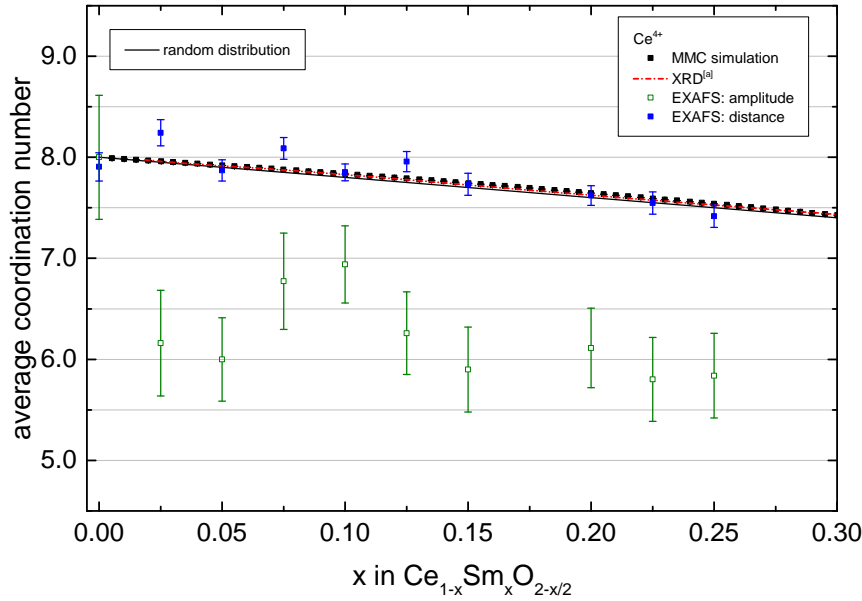


Figure 5.12: Coordination number of Ce-O for Sm doped ceria. XRD experiments according to Nakamura.<sup>[376]</sup> MMC simulations according to an earlier work.<sup>[55]</sup>

The coordination number can directly be extracted from the EXAFS equation from the amplitude. For the amplitude, the coordination number is  $CN_i = 8 \cdot \frac{amp_i}{amp(CeO_2)}$ .

The coordination number is equivalent to the number of neighboring atoms  $N$ , which is fitted here with the amplitude. However, the amplitude depends strongly on the EXAFS Data Processing and has a great error, which can be seen in Fig. 5.12.

Alternatively, the determination of the coordination number can be improved by using the distance to the neighboring atoms  $R$ . Shannon has shown that the ionic radius depends on the coordination number.<sup>[32]</sup> According to Shannon, the distance between cation and anion lattice sites decreases for an increasing number of vacant anion lattice sites (or for a lower coordination number). Therefore, a coordination number can be calculated from the distance to the neighboring atom (Fig. 5.12).

For the distance, the coordination number is  $CN_i = 6 + 2 \cdot \frac{r_i - r^{CN=8}}{r^{CN=8} - r^{CN=6}}$ , with the distances  $r^{CN=6}$  and  $r^{CN=8}$  given by Shannon,<sup>[32]</sup> which are shifted to the Ce-O distance according to XRD measurements in pure ceria.<sup>[25]</sup> For the latter,  $CN = 6$  is the only investigated

coordination number smaller than  $CN = 8$ . In this simple model, a mixture of the two isotropic coordination states is assumed. The error of the coordination number based on the distances is significantly smaller than for the amplitude. Comparing both types of coordination numbers suggests that the error based on the EXAFS fitting procedure is smaller than the actual systematic error of the data, especially for the amplitude data.

Using the amplitude in the EXAFS equation leads to a very bad approximation of the Ce-O coordination number: The error of the coordination numbers is large. Ce-O coordination numbers are significantly lower than predicted by a random cation distribution. This would mean that oxygen vacancies do not associate with rare-earth dopants but appear near cerium ions. While this might be a reason for further investigations, in fact, the Ce-O coordination numbers are lower than even physically possible as determined by the oxygen vacancy concentration. Using the distance leads to a significantly better coordination number in the range of both random distribution and MMC simulation. The Ce-O coordination number generally decreases with increasing dopant fraction as shown previously.<sup>[206,207,209]</sup> However, the error is still much larger than the difference between random distribution and MMC simulation, suggesting that EXAFS may be not the best method to determine coordination numbers for different samples.

### Sm doped ceria, Sm-edge

For the Sm(L<sub>I</sub>)-edge in Sm doped ceria (Fig. 5.13), the signal-to-noise ratio of the normalized absorption coefficient is not as good as shown for the Ce-edge. The reason for the comparably bad signal-to-noise ratio is the smaller dopant concentration at similar measuring times. Obviously, this results in a Radial Distribution Function with strong scattering (see Fig. 5.14).

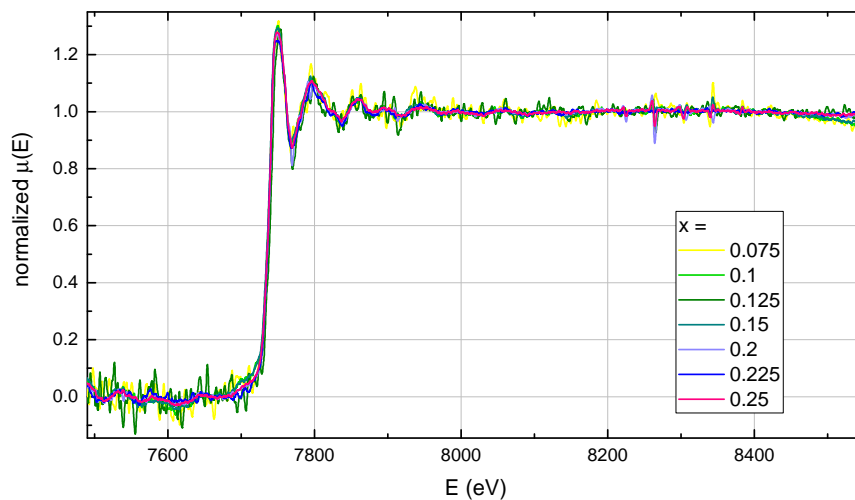


Figure 5.13: Normalized X-Ray Absorption near the Sm(K)-edge (XANES) of  $Ce_{1-x}Sm_xO_{2-x/2}$ .

For the extracted Radial Distribution Function, again the position of the first coordination peak, which represents oxygen ions and vacancies, moves to lower  $R$  values for higher dopant fractions.

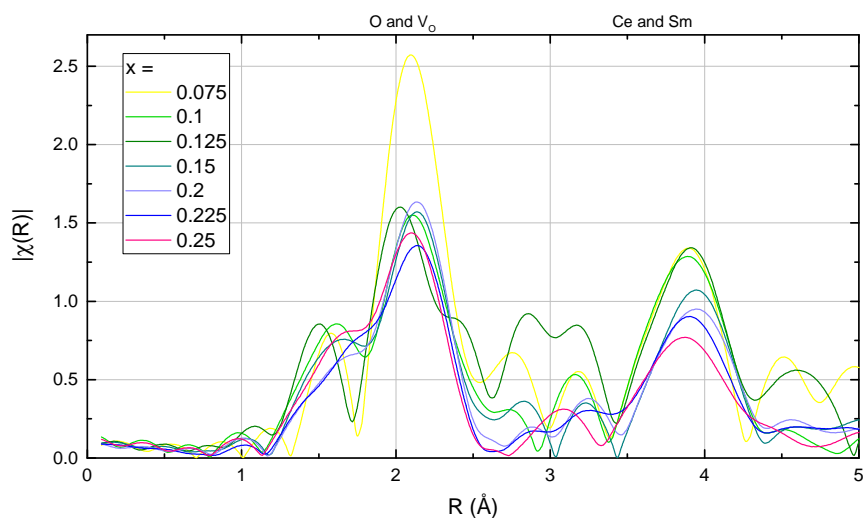


Figure 5.14: Radial Distribution Function at Sm(K)-edge of  $\text{Ce}_{1-x}\text{Sm}_x\text{O}_{2-x/2}$ .

Here, an exception is found for  $x = 0.125$ . The amplitude of the Radial Distribution Function  $\chi(R)$  varies.

The coordination number based on the EXAFS equation shows strong scattering for both the amplitude and distance method (Fig. 5.15). The coordination numbers according to the distance method are significantly lower compared to XRD results, random distribution and Metropolis Monte Carlo (MMC) simulations and are therefore probably not valid.

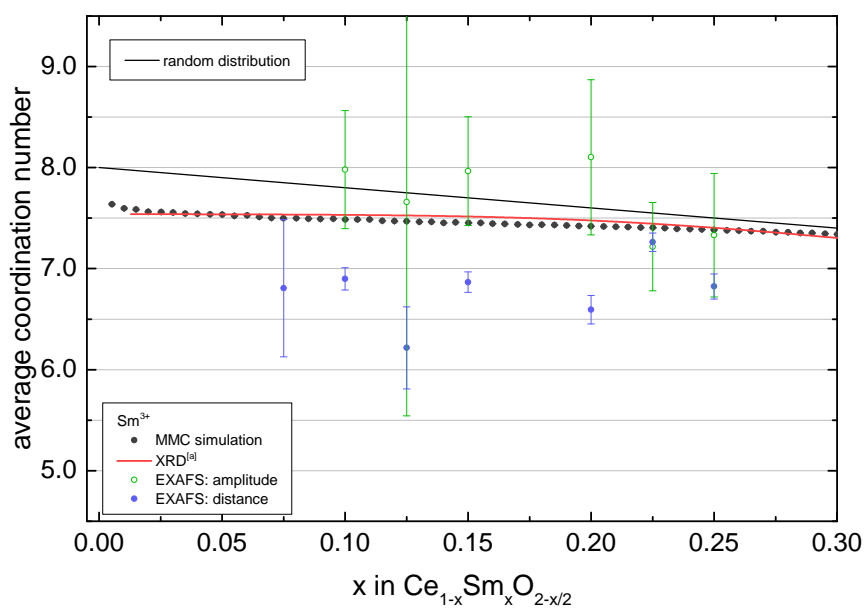


Figure 5.15: Coordination number of Sm-O for Sm doped ceria. XRD experiments according to Nakamura.<sup>[376]</sup> MMC simulations according to an earlier work.<sup>[55]</sup>

## RE doped ceria

For 20 mol% Y, Gd and Sm doped ceria, MMC simulations predict a decrease in the Ce-O coordination number and an increase in the RE-O coordination number with increasing ionic radii (Fig. 5.10). The reason for this is the decreasing association between dopants and oxygen vacancies mainly due to the decreasing absolute value of the  $1_{NN}$  RE-V association energy. In experiments, this would lead to a decreasing amplitude or decreasing interatomic distance for the Ce-edge in the series Y, Gd and Sm doped ceria. For the RE-edge, the opposite is expected.

In literature, this behavior of association was found,<sup>[208]</sup> although disagreeing results exist where large dopants lead either to weaker<sup>[207]</sup> or stronger<sup>[209,230]</sup> associations. Yoshida *et al.* even propose to use the difference of the Ce-O and RE-O coordination numbers.<sup>[230]</sup>

In this work, again the data quality was not sufficient. For the Ce-edge, the first peak, which is influenced by oxygen ions and vacancies, is nearly independent of the dopant ion (see Fig. 9.2 in appendix).

For the RE-edge, an increase in the amplitude of the first peak in the series Y, Gd and Sm doped ceria due to decreasing association is found as expected (see Fig. 9.3 in appendix). However, the large difference in amplitude and an unexpected behavior of the interatomic distance indicate problems with the data quality. These problems manifest even more clearly in the second peak.

## Conclusion

The coordination numbers were successfully simulated in agreement with XRD measurements. While the accuracy of the coordination numbers from EXAFS experiments especially for the Ce-edge in Sm doped ceria was improved compared to studies considering only the amplitude of the Radial Distribution Function, measurements of the Sm-edge or other rare-earth dopants did not provide the desired quality of data. The Sm-V association was verified for the Ce-edge in Sm doped ceria.



## 6 Attempt Frequency

The ionic conductivity can be simulated from the microscopic attempt frequencies and migration energies for the distribution of different ionic configurations. The *ab initio* calculation of attempt frequencies is described in this chapter, the calculation of the migration energies is described in Chapter 7 and ionic conductivities are discussed in Chapter 8.

The attempt frequency for an oxygen ion jump was calculated from first principles combining DFT+*U*, NEB, phonon calculations and the transition state theory. Convergence checks of the phonon mesh reveal that the common reduction to the Gamma point is not sufficient to calculate the attempt frequency. Calculations of Sm doped ceria revealed an increase of the prefactor, while smaller dopants lead to a decrease of the prefactor. The attempt frequency for the constant pressure case in quasi-harmonic approximation is larger than the attempt frequency at constant volume in harmonic approximation.

While *ab initio* calculations generally investigate microscopic properties, at the same time the macroscopic conductivity can be fitted to an Arrhenius equation (Eqs. 2.3 and 2.4) to extract an experimental attempt frequency and activation enthalpy. These properties can be directly compared between simulations and experiments. The relation between microscopic and macroscopic properties is investigated in this chapter. The calculated electronic energies, enthalpies and entropies of migration are in agreement with experimental diffusion coefficients and activation energies.

The ionic conductivity in ceria can be simulated by means of molecular dynamics (MD) using pair potentials<sup>[384–389]</sup> or by Kinetic Monte Carlo simulations using empirical<sup>[41]</sup> or *ab initio* data<sup>[50,54,225,371,372]</sup> for the activation barrier (migration energy) for each occurring jump. In all these KMC studies ‘a typical value’ (mostly  $10^{13} \text{ s}^{-1}$ ) for the attempt frequency for all ionic configurations was applied. For praseodymium doped ceria, Dholabhai *et al.* calculated the attempt frequency by means of DFT with a Hubbard *U* parameter (DFT+*U*) resulting in  $5 \cdot 10^{12} \text{ s}^{-1}$  for one of many possible ionic configurations.<sup>[284]</sup> However, a Vineyard approximation was applied considering only the Gamma point phonons. As mentioned before, it was assumed that the attempt frequency is constant for different configurations. Attempt frequencies for different ionic configurations are rarely calculated. Tarancón *et al.* used classical molecular dynamics (MD) to indirectly calculate attempt frequencies for  $\text{Ce}_{0.92}\text{Gd}_{0.08}\text{O}_{1.96}$  resulting in  $(5.4 \pm 0.3) \cdot 10^{12} \text{ s}^{-1}$  for jumps through an edge formed either by two host cations (Ce-Ce edge, see Fig. 6.1) or one dopant and one host cation (Ce-Gd edge).<sup>[387]</sup>

In this work, the migration of oxygen vacancies in fluorite-structured ceria is considered between adjacent tetrahedral oxygen sites<sup>[54]</sup> in (100) direction with the experimental jump distance  $l = 2.7055 \text{ \AA}$  given by half of the unit cell length at room temperature.<sup>[25]</sup> Along this migration pathway, two cations form a ‘migration edge’. In pure  $\text{CeO}_2$ , only cerium ions are at the migration edge, while doping with samarium oxide leads to configurations with one or two Sm ions at the migration edge (see Fig. 6.1). Jumps through a Ce-Ce, Ce-Sm or Sm-Sm edge were explicitly calculated in this work. For KMC simulations, the migration energies and the attempt frequencies must be known for all occurring configurations containing multiple Sm dopants and oxygen vacancies at various positions. The migration energies of all possible configurations can be calculated combining three explicit migration edge energies with association energies between the migrating oxygen vacancy and the other adjacent defects according to a pair interaction model proposed earlier.<sup>[55]</sup> The attempt frequencies of the three edge configurations are assumed to be representative for all possible migration configurations.

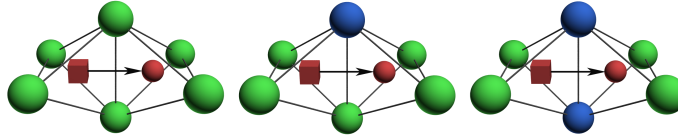


Figure 6.1: Possible migration edge configurations in samarium doped ceria. Ce-Ce edge (left), Ce-Sm edge (middle) and Sm-Sm edge (right). Cerium ions (green), samarium ions (blue), oxygen ions (red spheres) and oxygen vacancies (red boxes).

## 6.1 Calculation of the Attempt Frequency:

### Doping at the Migration Edge

Phonon dispersions for the initial and the transition state of the migration (see Eq. 2.9) showed minor contributions of imaginary frequencies at some  $\mathbf{q}$ -points (cp. Chapter 2.3.4) in the vicinity of the Gamma point that had to be taken into account (see Fig. 6.2, imaginary frequencies are shown as negative frequencies). The number of imaginary acoustic branches, which often depend on the chosen exchange-correlation-functional and the supercell size, varies between initial and transition state. For this reason, occurring imaginary parts were disregarded symmetrically in initial and transition state as the resulting error is assumed to be small. In general, imaginary frequencies suggest an unstable structure leading to deformations along the associated phonon wave vectors. However, for some  $\mathbf{q}$ -point samplings the occurring imaginary frequencies may be caused by non-cubic supercells, or, as shown by Grabowski *et al.*,<sup>[147,390]</sup> not fully converged parameters. The latter can probably be neglected since the results by Grabowski *et al.* suggest that the k-point mesh and supercell size are converged in this work.<sup>[147,345]</sup> Furthermore, the supercell volume was doubled compared to

previous phonon calculations. [50]

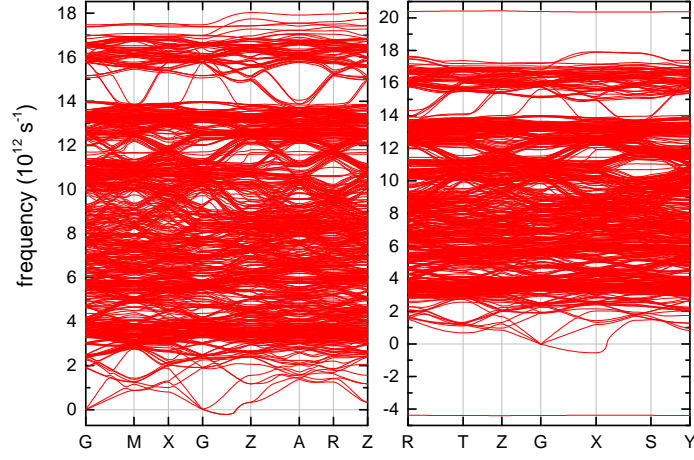


Figure 6.2: Phonon dispersions of the initial state  $V_{O1}^{\bullet\bullet} - O_{O2}^{\times}$  (left, space group  $P\bar{4}m2$ ) and the transition state  $V_{O1}^{\bullet\bullet} - O_{TS}'' - V_{O2}^{\bullet\bullet}$  (right, space group  $Pmmm$ ) in ceria according to Eq. 2.9.

Figure 6.3 shows the vibrational free energy difference  $\Delta F_{\text{vib}}$  (Eq. 2.19) and its components, the vibrational energy difference  $\Delta E_{\text{vib}}$  and entropy difference of initial and transition state  $\Delta S_{\text{vib}}$ , according to Eq. 2.11 in ceria in harmonic approximation for a  $6 \times 6 \times 6$  phonon mesh. As previously mentioned, the vibrational energy difference is similar to  $-k_{\text{B}}T$  as it differs less than 5% for temperatures above 900 K.

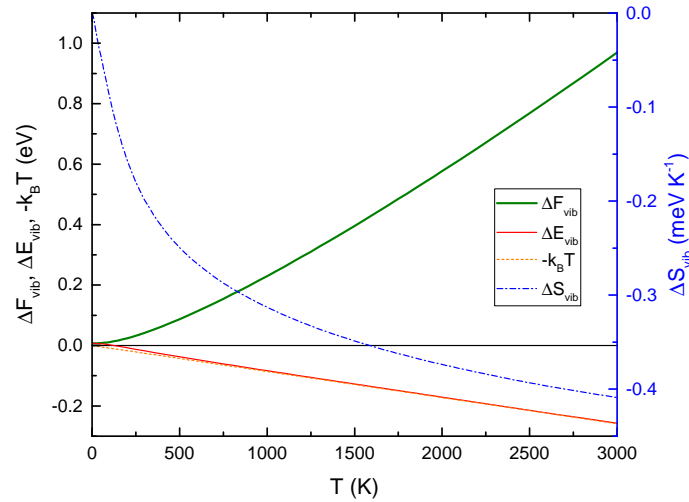


Figure 6.3: Vibrational free energy difference  $\Delta F_{\text{vib}}$ , vibrational energy difference  $\Delta E_{\text{vib}}$  and entropy difference  $\Delta S_{\text{vib}}$  of initial and transition state in ceria in harmonic approximation for a  $6 \times 6 \times 6$  phonon mesh. For comparison  $-k_{\text{B}}T$  is shown, which is similar to  $\Delta E_{\text{vib}}$ .

### 6.1.1 Pure Ceria: Influence of the Phonon Mesh

The attempt frequency was calculated using the Eyring method<sup>[109]</sup> (Eq. 2.10) with Eq. 2.19 and the in this work presented generalized Vineyard<sup>[110]</sup> method (Eq. 2.22) with different  $\mathbf{q}$ -point mesh sizes. The attempt frequency rises to a plateau with increasing temperature (Fig. 6.4). Above 600 K, both the Eyring and the generalized Vineyard method lead to similar attempt frequencies as predicted by theory. At 0 K the free vibrational energy difference between initial and transition state is 0.007 eV. Some authors move this zero point energy contribution of the attempt frequency (ZPE) to the migration energy leading to another definition of the attempt frequency, which is larger especially at low temperatures.<sup>[103,154,391,392]</sup> For the calculation of the phonon dispersion, an equidistantly spaced  $\mathbf{q}$ -point mesh of dimensions between  $1 \times 1 \times 1$  and  $6 \times 6 \times 6$  was applied to sample the phonon dispersion, since the number of all possible discrete wave vectors is too large (Eq. 2.18). It can be clearly seen that the common reduction to the Gamma point ( $1 \times 1 \times 1$ ) is not sufficient to calculate the attempt frequency. The convergence of the phonon mesh is reached only above 64  $\mathbf{q}$ -points corresponding to a  $4 \times 4 \times 4$  grid. The resulting attempt frequency in pure ceria  $1.5 \cdot 10^{12} \text{ s}^{-1}$  is in the range of the usually assumed values ( $10^{12} - 10^{13} \text{ s}^{-1}$ ).

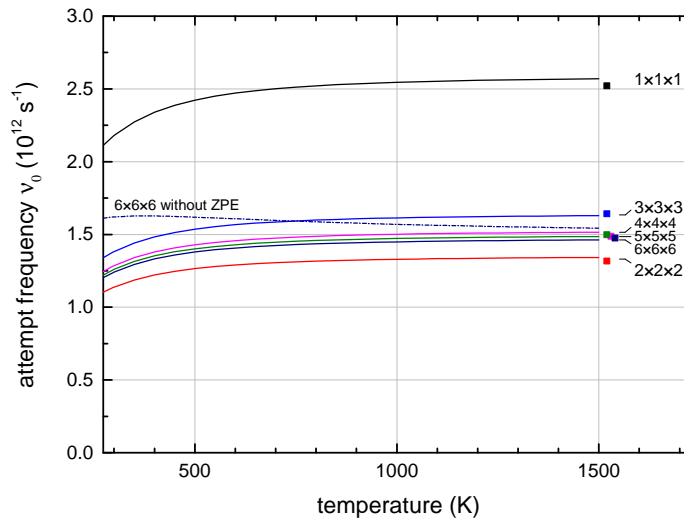


Figure 6.4: Oxygen vacancy attempt frequency  $\nu_0$  in ceria in harmonic approximation for different phonon mesh sizes. Lines are calculated using the Eyring method, squares are the results of the generalized Vineyard formula (Eq. 2.22). The dashed line shows the result according to the Eyring method without zero point energy (ZPE).

### 6.1.2 Sm Doped Ceria

The influence of doping with Sm on the attempt frequency was investigated. Therefore, one or two samarium dopants were introduced at the migration edge (see Fig. 6.1) between two edge-sharing tetrahedra. A convergence of the resulting attempt frequencies as a function of the used phonon

mesh was observed, similar to pure ceria, while the approximation of the attempt frequency based on Gamma point calculations was even worse. All further results correspond to the  $6 \times 6 \times 6$  phonon mesh. The results are shown in Table 6.1. The following can be observed:

One samarium dopant does not influence the attempt frequency. Two samarium dopants increase the attempt frequency by a factor of three.

The increase in attempt frequency for the Sm-Sm edge compared to pure ceria is expected due to the higher activation barrier and steeper electronic energy curvature. For the Ce-Sm edge, the migrating oxygen ion deviates from the direct, straight path found for the Ce-Ce and the Sm-Sm edge between initial and final position. The migrating oxygen ion follows a curved path by avoiding the steeper electronic energy curvature and a high attempt frequency. Surprisingly, this leads to similar attempt frequencies for one Sm dopant and pure ceria. The resulting attempt frequencies for the Ce-Ce and Ce-Sm edge are in agreement with literature in which a constant attempt frequency for different configurations is either assumed<sup>[284]</sup> or calculated for both the Ce-Ce and Ce-Gd edge.<sup>[387]</sup> Here, Tarancón *et al.* did not consider the Gd-Gd edge due to “the negligible impact on the final diffusion properties”.

A key property for the interaction between the edge cations and the migrating oxygen ion are the distances of the edge cations in the transition state  $d_{\text{TS}}$  and the initial state  $d_{\text{IS}}$  (see Table 6.1). The migration energies  $\Delta E_{\text{el}}^0$  of the different edge configurations depend linearly on the difference of the distances of the edge cations between transition and initial state,  $d_{\text{TS}} - d_{\text{IS}}$ . Simply described, the cations at the edge must be pushed apart during an oxygen ion jump. This leads to a linear relationship between the widening of the edge cations and the migration energy. Likewise, the attempt frequency is majorly influenced by the edge cation distance in the transition state  $d_{\text{TS}}$ . For the Ce-Ce and Ce-Sm edge  $\nu_0$  and  $d_{\text{TS}}$  are similar, respectively. Both values increase significantly for the Sm-Sm edge.

migration edge	$d_{\text{IS}}$ (Å)	$d_{\text{TS}}$ (Å)	$d_{\text{TS}} - d_{\text{IS}}$ (Å)	$\Delta E_{\text{el}}^0(V,T)$ (eV)	$\nu_0(V,T)$ (s <sup>-1</sup> )
Ce-Ce	4.148	4.267	0.119	0.587	$1.47 \cdot 10^{12}$
Ce-Sm	4.142	4.268	0.126	0.759	$1.49 \cdot 10^{12}$
Sm-Sm	4.141	4.280	0.139	1.166	$4.30 \cdot 10^{12}$

Table 6.1: Electronic migration energies for different migration configurations (Eq. 2.10), distances of the edge cations in the initial and the transition state and oxygen vacancy attempt frequencies  $\nu_0(V,T)$  (Vineyard, Eq. 2.22) at constant volume ( $V = \text{const.}$ )

For further investigation and in consideration of the very time-consuming phonon calculations, the attempt frequency could be described in a simple approximation by displacing the migrating oxygen ion in the initial state. Using the classical harmonic oscillator with the displacement  $x$  and the electronic energy  $E_{\text{el}}^0 = \frac{1}{2}kx^2 + E_{\text{el},x=0}^0$  the attempt frequency can be calculated according to

$\nu_0 = \frac{\sqrt{k/m}}{2\pi}$  with the mass  $m$  of the migrating oxygen ion. In this simplified case, it is assumed that all neighboring atoms are frozen similar to the Einstein model (one body problem), a classical model can be used and only the initial state has an influence on the attempt frequency. This simple static displacement model leads to similar attempt frequencies for all three edge configurations (Fig. 6.1) with a slight increase for more Sm dopants from  $8.42 \cdot 10^{12}$  to  $9.74 \cdot 10^{12} \text{ s}^{-1}$  (see Fig. 6.7). Analogous bulk calculations without any oxygen vacancy lead to a frequency of  $11 \cdot 10^{12} \text{ s}^{-1}$ . The attempt frequencies according to the static displacement model are higher than the values from the phonon calculations indicating a hard potential around the initial state. As described, the phonon calculations revealed an exceptionally high attempt frequency for the Sm-Sm edge. This deviation from the static displacement result indicates a strong influence of the neighboring atoms for the Sm-Sm edge as established above.

### 6.1.3 Gd and Yb Doped Ceria

For Gd and Yb doped ceria, the attempt frequency was calculated as a function of dopants at the migration edge. While for Sm doped ceria the attempt frequency increases linear with the distance of the edge cations in the transition state, this simple relationship between geometry and attempt frequency fails for other dopants. Table 6.2, Fig. 6.5 and 6.6 show that smaller dopant radii lead to lower attempt frequencies. This leads even to a decrease in attempt frequency for increasing number of Yb dopants at the migration edge. Especially the decrease in attempt frequency (e.g. Ce-Yb, Yb-Yb, Ce-Gd compared to Ce-Ce) for configurations with higher migration energies are contrary to the assumption that higher barriers lead to steep potential energies landscapes in the initial state and therefore to higher attempt frequencies.

migration edge	$d_{\text{IS}}$ (Å)	$d_{\text{TS}}$ (Å)	$d_{\text{TS}} - d_{\text{IS}}$ (Å)	$\Delta E_{\text{el}}^0(V,T)$ (eV)	$\nu_0(V,T)$ (s <sup>-1</sup> )
Ce-Ce	4.148	4.267	0.119	0.587	$1.47 \cdot 10^{12}$
Ce-Gd	4.145	4.253	0.108	0.694	$1.28 \cdot 10^{12}$
Gd-Gd	4.148	4.244	0.096	1.015	$2.31 \cdot 10^{12}$
Ce-Yb	4.125	4.256	0.131	0.694	$1.14 \cdot 10^{12}$
Yb-Yb	4.235	4.473	0.238	0.705	$0.97 \cdot 10^{12}$

Table 6.2: Electronic migration energies for different migration configurations, distances of the edge cations in the initial and the transition state and oxygen vacancy attempt frequencies  $\nu_0(V,T)$  (Vineyard) at constant volume ( $V = \text{const.}$ )

For different dopants at the migration edge, the correlation between attempt frequencies and distances of edge cations in the transition state is quite bad. The same is true for the migration energy as a function of widening of the edge cations from initial to transition state. For Yb doped



Large dopants lead to an increase and small dopants to a decrease in attempt frequency.

### 6.1.4 Attempt Frequency at Constant Pressure

All phonon calculations were performed isochoric, i.e. for a constant volume that was derived for bulk ceria at the absolute zero. This follows the harmonic approximation in which all calculations are performed at a fixed equilibrium volume. To investigate the isobaric behavior, i.e. the constant pressure case ( $p = 0$ ), the quasi-harmonic approximation can be applied in which the minimum of the free energy for different volumes is determined at given temperatures. Therefore, all properties like the migration energy should be calculated at constant pressure (Eq. 2.15). The influence of the change between constant volume and constant pressure case on the electronic migration energy at zero temperature  $\Delta E_{\text{el}}^0$  is small ( $\pm 0.015$  eV), and the exponential factor varies below  $\pm 20\%$  at 900 K (compare Table 6.1 and 6.3). As phonon calculations are computationally demanding it is commonly assumed that the change in vibrational entropy with changing volume,  $\left(\frac{\partial S_{\text{vib}}}{\partial V}\right)_T$ , is similar in defect-free bulk, the defective cell in the initial state and in the transition state.<sup>[393,394]</sup> Starting from the equilibrium volume  $V_0$ , the entropy of migration for  $p = 0$  is given according to Grieshammer *et al.*<sup>[50]</sup>

$$\begin{aligned}\Delta S_{\text{vib}}(p,T) &= \Delta S_{\text{vib}}(V(p,T),T) \\ &= \Delta S_{\text{vib}}(V_0,T) + \int_{V_{\text{IS}}(p,T)}^{V_{\text{IS}}(p,T)+\Delta V} \left(\frac{\partial S_{\text{vib}}}{\partial V}\right)_T^{\text{bulk}} dV \\ &= \Delta S_{\text{vib}}(V_0,T) + \alpha_V B_T \cdot \Delta V,\end{aligned}\tag{6.1}$$

with the change in volume between transition state and initial state at constant pressure  $\Delta V = V_{\text{TS}}(p=0,T) - V_{\text{IS}}(p=0,T)$  which is assumed to be independent of temperature. Alternatively, the change in pressure between transition state and initial state at constant volume  $\Delta p$  can be used (see Eq. 6.2). The volumetric thermal expansion coefficient  $\alpha_V$  and the bulk modulus  $B_T$  for bulk ceria were already determined by Grieshammer *et al.*<sup>[50]</sup> The free vibrational energy of migration  $\Delta F_{\text{vib}}$  is defined by the vibrational energy  $\Delta E_{\text{vib}}$  and entropy  $\Delta S_{\text{vib}}$  (see Eq. 2.11). The free vibrational energy of migration at zero pressure can then be written as

$$\begin{aligned}\Delta F_{\text{vib}}(p,T) &= \Delta F_{\text{vib}}(V_0,T) - T \cdot \alpha_V B_T \cdot \Delta V \\ &= \Delta F_{\text{vib}}(V_0,T) + T \cdot \alpha_V V \cdot \Delta p.\end{aligned}\tag{6.2}$$

Therewith the generalized Vineyard result (Eq. 2.22) can be modified:<sup>[395]</sup>

$$\nu_0(p) = \frac{\prod_{q,i} \nu_{q,i}^{\frac{1}{M}}}{\prod_{m,j} \nu_{m,j}^{\frac{1}{M}}} \exp\left(\frac{\alpha_V B_T \Delta V}{k_B}\right).\tag{6.3}$$

The same modification applies to the Eyring formula (Eq. 2.10):

$$\nu_0(p, T) = \frac{k_B T}{h} \exp\left(\frac{-\Delta F_{\text{vib}}(V_0, T)}{k_B T}\right) \times \exp\left(\frac{\alpha_V B_T \Delta V}{k_B}\right). \quad (6.4)$$

migration edge	$\Delta E_{\text{el}}^0(p, T)$ (eV)	$\Delta V$ ( $\text{\AA}^3$ )	$\nu_0(p, T)$ ( $\text{s}^{-1}$ )
Ce-Ce	0.602	3.06	$7.67 \cdot 10^{12}$
Ce-Sm	0.769	3.01	$7.52 \cdot 10^{12}$
Sm-Sm	1.162	2.64	$1.79 \cdot 10^{13}$

Table 6.3: Electronic migration energies for different migration configurations, changes in volume between transition state and initial state  $\Delta V$  and oxygen vacancy attempt frequencies  $\nu_0(p, T)$  (Vineyard) at constant pressure ( $p = 0$ ) and 900 K

In Fig. 6.7 and 6.8, the attempt frequencies in samarium doped ceria for the relaxed cell volume ( $p = 0$ ) are shown. Now, the constant volume case can be compared with the constant pressure case: The hydrostatic pressure for the constant volume case ( $V_0$ ) results in a volume compression for the Ce-Ce, Ce-Sm edge and an expansion for the Sm-Sm edge for the constant pressure case for both initial state  $[V_{\text{IS}}(p, T)]$  and transition state  $[V_{\text{TS}}(p, T)]$ . In the constant pressure case, the change in volume between transition state and initial state  $\Delta V$  is similar for the Ce-Ce and Ce-Sm edge and slightly smaller for the Sm-Sm edge (see Table 6.3). The influence of  $\alpha_V B_T \Delta V$  in Eq. 6.1 on the attempt frequency is significant. Minor errors in  $\alpha_V B_T$  are propagated exponentially in the attempt frequency. Thus, the error of the attempt frequency is larger than 10% above 1500 K. The attempt frequency at constant pressure increases compared to the constant volume case by a factor of about five for the Ce-Ce and Ce-Sm edge and four for the Sm-Sm edge at 900 K.

### The attempt frequency at constant pressure increases compared to the constant volume case.

The resulting attempt frequencies are roughly in the range of the usually assumed values ( $10^{12} - 10^{13} \text{ s}^{-1}$ ) and similar to experimental Debye frequencies in ceria, which are between  $8 \cdot 10^{12}$  and  $10 \cdot 10^{12} \text{ s}^{-1}$  according to ultrasonic pulse, specific heat and thermal expansion coefficient measurements.<sup>[396-399]</sup> The experimental Debye frequencies  $\nu_D$  were calculated from the Debye temperature  $\theta_D$  according to  $\theta_D = (h/k_B) \nu_D = (2ha/\pi k_B) (D/2\mu)^{1/2}$  with the inverse width of the Morse potential and the reduced mass of the oscillator  $\mu$ .<sup>[399]</sup> For ceria, a rough estimate for the Debye temperature is  $\theta_D = 410 \text{ K}$ <sup>[396]</sup> or  $480 \text{ K}$ <sup>[397]</sup>. Doped ceria  $\text{Ce}_{1-x}\text{RE}_x\text{O}_{2-x/2}$  (RE = Yb, Dy, Sm, La) has Debye temperatures around 467 K ( $x = 0.1$ ) or 453 K ( $x = 0.2$ ).<sup>[397]</sup>

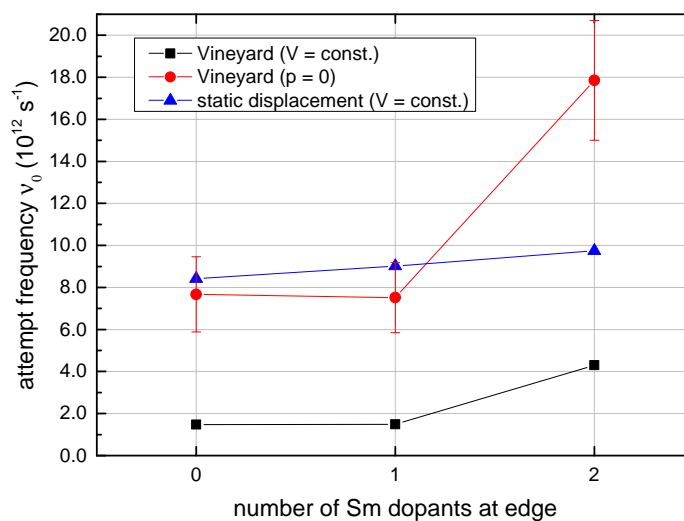


Figure 6.7: Oxygen vacancy attempt frequency  $\nu_0$  in harmonic (squares) and quasi-harmonic approximation (circles) in samarium doped ceria with different number of dopants at the migration edge, using the generalized Vineyard method at a temperature of 900 K. For comparison also the results of the simple displacement approximation (triangles) are shown.

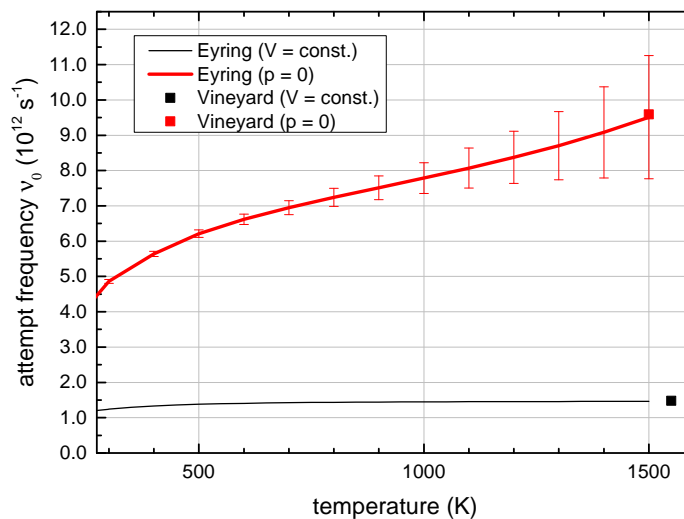


Figure 6.8: Oxygen vacancy attempt frequency  $\nu_0$  in pure ceria in harmonic and quasi-harmonic approximation calculated using the Eyring (lines) and generalized Vineyard (squares) method at a temperature of 900 K at constant volume ( $V = \text{const.}$ ) and constant pressure ( $p = 0$ ).

## 6.1 Calculation of the Attempt Frequency: Doping at the Migration Edge

---

For Gd and Yb doped ceria in constant pressure case, the change in volume between transition state and initial state  $\Delta V$  is smaller than in Sm doped ceria (Table 6.4). In fact, a decrease in  $\Delta V$  with decreasing ionic radius is found. Smaller dopants lead to smaller volume expansions during the migration. As a result, the attempt frequency at constant pressure increases compared to the constant volume case by a factor of about four/two for the Ce-Gd/Ce-Yb edge and three for the Gd-Gd/Yb-Yb edge at 900 K. Again, the change in electronic migration energies is small.

migration edge	$\Delta E_{\text{el}}^0(p,T)$ (eV)	$\Delta V$ ( $\text{\AA}^3$ )	$\nu_0(p,T)$ ( $\text{s}^{-1}$ )
Ce-Ce	0.602	3.06	$7.67 \cdot 10^{12}$
Ce-Gd	0.724	2.67	$5.40 \cdot 10^{12}$
Gd-Gd	1.026	2.20	$7.55 \cdot 10^{12}$
Ce-Yb	0.732	1.59	$2.70 \cdot 10^{12}$
Yb-Yb	0.723	1.75	$2.48 \cdot 10^{12}$

Table 6.4: Electronic migration energies for different migration configurations, changes in volume between transition state and initial state  $\Delta V$  and oxygen vacancy attempt frequencies  $\nu_0(p,T)$  (Vineyard) at constant pressure ( $p = 0$ ) and 900 K

## 6.2 Calculation of the Attempt Frequency: Doping in Nearest Neighborhood

Alternatively to doping at the migration edge, dopants can appear in nearest neighborhood to the start position of the migrating oxygen vacancy (Fig. 6.9).

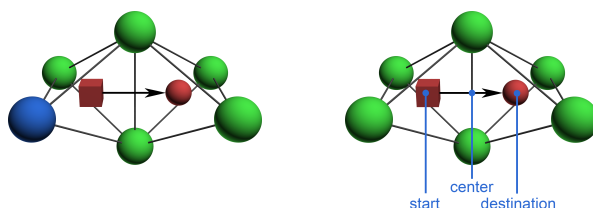


Figure 6.9: Jump environment with a dopant in nearest neighborhood to the start position of the migrating oxygen vacancy (left). Cerium ions are green spheres, dopants are blue spheres, the oxygen ion is a red sphere and the oxygen vacancy is a red cube. On the right, the positions of the migrating oxygen vacancies are labeled start (s), center (c) and destination (d).

For the constant volume case, similar to doping at the migration edge, doping in nearest neighborhood to the start position of the migrating oxygen vacancy also leads to an increase in attempt frequency for more Sm dopants (Fig. 6.10, Table 6.5). However, a maximum in attempt frequency is found for a single Sm dopant in nearest neighborhood to the start position.

Doping with Sm in nearest neighborhood to the start position of the migrating oxygen vacancy increases the attempt frequency.

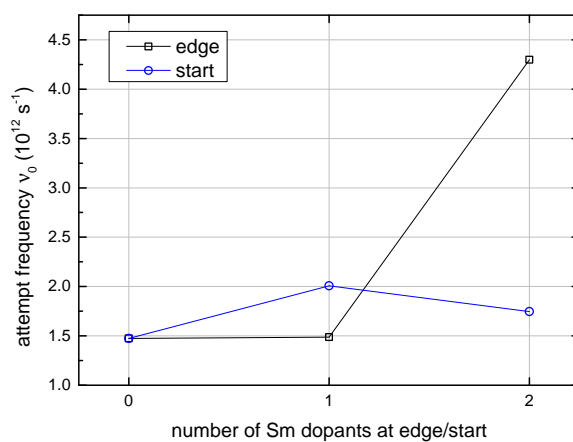


Figure 6.10: Attempt frequencies for Sm doped ceria with dopants at migration edge and in nearest neighborhood to the start position of the migrating oxygen vacancy.

## 6.2 Calculation of the Attempt Frequency: Doping in Nearest Neighborhood

cations at start	$d_{\text{IS}}$ (Å)	$d_{\text{TS}}$ (Å)	$d_{\text{TS}} - d_{\text{IS}}$ (Å)	$\Delta E_{\text{el}}^0(V,T)$ (eV)	$\nu_0(V,T)$ (s <sup>-1</sup> )
Ce, Ce	4.148	4.267	0.119	0.587	$1.47 \cdot 10^{12}$
Ce, Sm	4.153	4.270	0.118	0.562	$2.01 \cdot 10^{12}$
Sm, Sm	4.156	4.272	0.116	0.531	$1.75 \cdot 10^{12}$

Table 6.5: Electronic migration energies for different migration configurations, distances of the edge cations in the initial and the transition state and oxygen vacancy attempt frequencies  $\nu_0(V,T)$  (Vineyard) at constant volume ( $V = \text{const.}$ )

For the constant pressure case, the attempt frequency increases monotonously with an increasing amount of Sm dopants in nearest neighborhood to the start position of the migrating oxygen vacancy (Table 6.6). This is surprising, as for doping at the migration edge the trend for the constant volume and constant pressure case was similar.

For an increasing number of Sm dopants at the edge, the migration volume decreases. For an increasing number of Sm dopants in nearest neighborhood to the start position, the migration volume increases. While the volume of the supercell in the initial state is similar for dopants at the edge and the start position, the volume expansion is stronger for dopants at the start position especially perpendicular to the direction of migration. This is surprising, as the widening of the edge cation distance increases with doping at the edge while it decreases with doping at the start position. The volume expansion is therefore caused by long-range distortion.

cations at start	$\Delta E_{\text{el}}^0(p,T)$ (eV)	$\Delta V$ (Å <sup>3</sup> )	$\nu_0(p,T)$ (s <sup>-1</sup> )
Ce, Ce	0.602	3.06	$7.67 \cdot 10^{12}$
Ce, Sm	0.593	3.26	$1.16 \cdot 10^{13}$
Sm, Sm	0.525	3.82	$1.37 \cdot 10^{13}$

Table 6.6: Electronic migration energies for different migration configurations, changes in volume between transition state and initial state  $\Delta V$  and oxygen vacancy attempt frequencies  $\nu_0(p,T)$  (Vineyard) at constant pressure ( $p = 0$ )

## 6.3 Experimental Attempt Frequencies

### 6.3.1 Experimental Values for Pure Ceria

Although the Vineyard method directly uses the normal mode frequencies in the initial and transition state (see Chapter 2.3), their resulting ratio defines a frequency that differs from any existing frequency in the real lattice.<sup>[112]</sup> However, the attempt frequency of oxygen ion jumps can be extracted as an average macroscopic property based on the temperature dependence of the oxygen ion conductivity or the oxygen diffusion coefficient. Common experiments to examine the experimental attempt frequency are therefore direct current measurements (DC), impedance spectroscopy (AC), Secondary Ion Mass Spectrometry (SIMS) and Gas Phase Analysis (GPA). Experimental attempt frequencies and oxygen vacancy diffusion coefficients are shown in Table 6.7 and Fig. 6.11.

source	crystallinity	method	domain	$T$ ( $^{\circ}\text{C}$ )	$\bar{\nu}_{\text{exp},V_{\text{O}}^{\bullet\bullet}}$ ( $\text{s}^{-1}$ )
this work	poly	AC	bulk	227–733	$(9 \pm 2) \cdot 10^{14}$
Wang <i>et al.</i> <sup>[315]</sup>	poly <sup>hp</sup>	AC	bulk	237–352	$(9 \pm 4) \cdot 10^{13}$
Wang <i>et al.</i> <sup>[315]</sup>	poly <sup>lp</sup>	AC	bulk	237–596	$(8 \pm 1) \cdot 10^{13}$
Floyd <sup>[258]</sup>	sc	GPA	bulk	836–1151	$(2 \pm 3) \cdot 10^{15}$
Brugner <i>et al.</i> <sup>[248]</sup>	sc, poly	DC	bulk, total	1200–1500	$(6.7 \pm 0.8) \cdot 10^{19}$
Wang <i>et al.</i> <sup>[315]</sup>	poly <sup>hp</sup>	AC, DC	total	621–847	$5.2 \cdot 10^{21}$
Wang <i>et al.</i> <sup>[315]</sup>	poly <sup>lp</sup>	AC, DC	total	507–891	$4.9 \cdot 10^{17}$
Kamiya <i>et al.</i> <sup>[260]</sup>	poly	SIMS	total	1095–1297	$(1.6 \pm 0.9) \cdot 10^{20}$
Kamiya <i>et al.</i> <sup>[260]</sup>	poly	SIMS	total	797–895	$(3 \pm 5) \cdot 10^{14}$
Kamiya <i>et al.</i> <sup>[259]</sup>	poly	GPA	total	1094–1296	$(3 \pm 2) \cdot 10^{22}$
Tuller <i>et al.</i> <sup>[83]</sup>	sc <sup>[a]</sup>	AC, DC	bulk	200–1150	$2.3 \cdot 10^{13}$
Naik <i>et al.</i> <sup>[84]</sup>	poly <sup>[b]</sup>	DC	total	1030–1330	$(1.1 \pm 0.2) \cdot 10^{13}$

Table 6.7: Experimental oxygen vacancy attempt frequency  $\bar{\nu}_{\text{exp},V_{\text{O}}^{\bullet\bullet}}$  of pure ceria for polycrystalline samples (poly) and single crystals (sc) calculated based on impedance spectroscopy (AC), direct current (DC), Secondary Ion Mass Spectrometry (SIMS) and Gas Phase Analysis (GPA) measurements. The number of charge carriers is based on the purity (hp = high, lp = low) of the starting material or the non-stoichiometry for [a]  $\text{CeO}_{1.992}$  and [b]  $\text{CeO}_{1.96}$ . The error of the attempt frequency is given according to the linear regression.

SIMS and GPA experiments were used by Floyd<sup>[258]</sup> and Kamiya *et al.*<sup>[259,260]</sup> to investigate the oxygen tracer diffusion coefficient  $D_{\text{O}^{2-}}^*$ . The oxygen tracer diffusion coefficient is related to the oxygen self-diffusion coefficient  $D_{\text{O}^{2-}}$  by a correlation factor  $f_{\text{O}^{2-}}$  according to  $D_{\text{O}^{2-}}^* = f_{\text{O}^{2-}} D_{\text{O}^{2-}}$ . In contrast to the jumps of an oxygen vacancy, the jumps of a tracer ion are correlated, leading to a smaller mean square displacement for the tracer and a correlation factor below unity. For vacancy diffusion in a simple cubic lattice the correlation factor is 0.65 at very low defect concentrations. Be-

yond that, the tracer correlation factor is a function of the defect concentration: Increasing vacancy concentrations decrease the probability of ‘return jumps’ for a tracer atom, the tracer correlation decreases and  $f_{\text{O}^{2-}}$  increases. In addition, for increasing defect concentration the ion-vacancy interaction increases and the distribution of conducting ions influences the tracer correlation factor.<sup>[102]</sup> Therefore, the here used correlation factor ( $f_{\text{O}^{2-}} = 0.65$ ) is an approximation.

The oxygen self-diffusion coefficient  $D_{\text{O}^{2-}}$  is related to the oxygen vacancy self-diffusion coefficient  $D_{\text{V}_{\text{O}}^{\bullet\bullet}}$  according to Eq. 2.5 using the charge carrier concentration. For pure ceria at oxidizing conditions, the determination of the concentration is quite difficult as oxygen vacancies exist due to (extrinsic) impurities, reduction and intrinsic disorder. However, many studies point out a high impurity concentration compared to the intrinsic- (anti-Frenkel) or reduction-dominated oxygen vacancy concentration at  $p(\text{O}_2) = 0.2$  bar for temperatures below 800 °C.<sup>[50–53]</sup> At higher temperatures, the oxygen vacancy concentration increases especially due to reduction, though it could only be roughly estimated for experimental samples with unknown impurities. Therefore, in this work, the charge carrier concentration for all temperatures was derived from the purity of the starting materials according to literature assuming trivalent impurities<sup>[258–260,315]</sup> or, for one sample, from mass spectrographic analysis.<sup>[199,248]</sup> The approximated oxygen vacancy concentration varies over two orders of magnitude for stoichiometric ceria ( $10^{17} - 10^{19} \text{ cm}^{-3}$ ) and is a reason for scattering of the extracted oxygen vacancy self-diffusion coefficient (see Fig. 6.11a).

In literature, direct current measurements and impedance spectroscopy experiments were used to measure the oxygen ion conductivity.<sup>[83,84,248,315]</sup> In this work, additional impedance spectroscopy experiments were performed (see appendix). Using the charge carrier concentration, the conductivity can be converted into the ‘conductivity’ diffusion coefficient or charge diffusion coefficient of the oxygen ions  $D_{\sigma, \text{O}^{2-}}$ , which is defined according to the classical Nernst-Einstein equation (Eq. 2.3). It should be noted that  $D_{\sigma, \text{O}^{2-}}$  has the dimensions of a diffusion coefficient but is not defined by Fick’s first law. Conductivity and tracer diffusion coefficients can be compared using the Haven Ratio  $H_{\text{R}} = D_{\text{O}^{2-}}^* / D_{\sigma, \text{O}^{2-}}$ .<sup>[102,400]</sup> Only for non-interacting defects the Haven Ratio is equal to the tracer correlation factor. Otherwise, a thermodynamic factor has to be considered, which was neglected in this work. Based on this assumption, the conductivity diffusion coefficient  $D_{\sigma, \text{O}^{2-}}$  can be converted in the oxygen vacancy self-diffusion coefficient  $D_{\text{V}_{\text{O}}^{\bullet\bullet}}$  according to Eq. 2.5 using again the charge carrier concentration.

Experimental attempt frequencies  $\bar{\nu}_{\text{exp}, \text{V}_{\text{O}}^{\bullet\bullet}}$  and activation enthalpies  $\Delta H_{\text{a}}$  can be extracted as an average macroscopic property from the Arrhenius behavior of the oxygen vacancy self-diffusion coefficient  $D_{\text{V}_{\text{O}}^{\bullet\bullet}}$  according to Eq. 2.4 for a known jump distance and geometrical factor (Eq. 2.3). The results are shown in Table 6.7.

Surprisingly, the experimental attempt frequency for pure ceria varies vastly between  $10^{13} - 10^{22} \text{ s}^{-1}$ .

In the following section, it will be explained that all experiments are probably based on the same elemental frequency for a jump process.

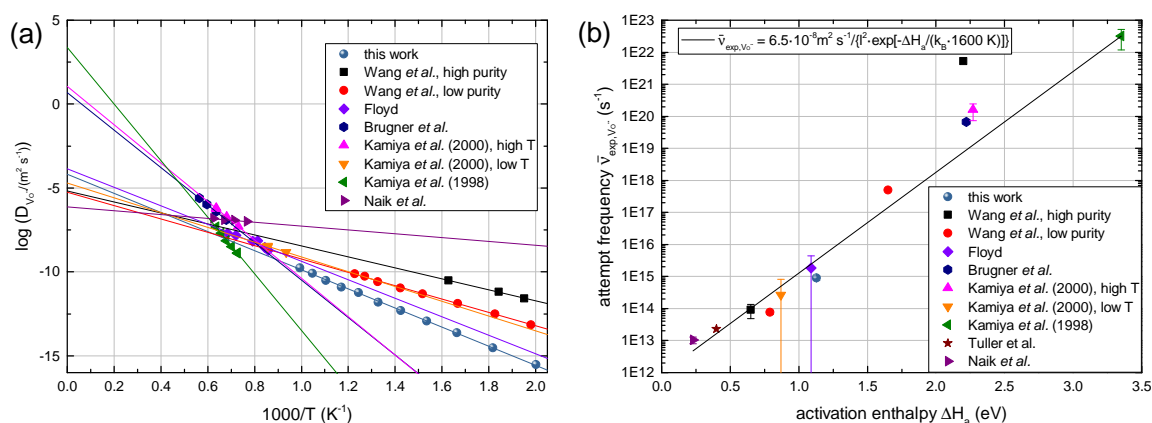


Figure 6.11: Experimental (a) oxygen vacancy diffusion coefficients and (b) resulting attempt frequencies of pure ceria using bulk<sup>[315]</sup> and total<sup>[83,84,248,258–260]</sup> domain. Though experimental attempt frequencies vary over several orders of magnitude, all experiments are probably based on the same elemental frequency for a jump process.

### 6.3.2 Reasons for Scattering

The vast scattering of the experimental attempt frequency is caused by measurement technique, sample properties and temperature range.

Minor influences of the *measurement technique* include measuring inaccuracies, different experimental methods for either tracer diffusion or conductivity and the conversion of  $D_{O^{2-}}^*$  and  $D_{\sigma, O^{2-}}$  to the oxygen vacancy self-diffusion coefficient. Measuring inaccuracies are assumed to be small, especially since the experimental attempt frequency is extrapolated from measurements at several temperatures. Oxygen tracer diffusion coefficients and conductivities from different experiments differ due to diverse oxygen vacancy concentrations: The oxygen tracer diffusion coefficients of SIMS and GPA measurements for pure ceria vary about one order of magnitude.<sup>[258–260]</sup> The ionic conductivities measured in the present work and literature vary up to two orders of magnitude.<sup>[84,248,315]</sup> However, similar results for one sample are expected using different experimental methods. For example, Tuller *et al.*<sup>[83]</sup> observed the same ionic conductivity for single crystals using impedance spectroscopy and direct current measurements. To compare the different experiments the charge carrier concentration has to be approximated, which is a reason for scattering of the oxygen vacancy self-diffusion coefficient. Furthermore,  $D_{O^{2-}}^*$  and  $D_{\sigma, O^{2-}}$  are compared, thereby approximating values for the tracer correlation factor and the thermodynamic factor. For Gd doped ceria single crystals, where the charge carrier concentration is well defined, Ruiz-Trejo *et al.*<sup>[175]</sup> reported a tracer diffusion coefficient based on SIMS measurements one order of magnitude smaller than the conductivity diffusion coefficient. In the related fluorite structure, 9.5 mol% single crystal yttria-stabilized zirconia (YSZ), Manning *et al.*<sup>[401]</sup> reported a Haven Ratio of 0.33 for low and 0.48 for high temperature. Both examples give a lower product of tracer correlation factor and thermodynamic factor than assumed in this work, though this is expected for high defect concentrations. For small

defects concentrations as in pure ceria, the tracer correlation factor of 0.65 may be a good choice. Therefore, the conversion of  $D_{\text{O}_2^-}^*$  and  $D_{\sigma, \text{O}_2^-}$  to the oxygen vacancy self-diffusion coefficient has probably only a minor impact on the scattering of the experimental attempt frequency.

To validate the different macroscopic experimental techniques, the diffusion coefficients can be compared to microscopic Nuclear Magnetic Resonance (NMR) measurements. Avila-Paredes *et al.*<sup>[210,256]</sup> measured the oxygen transport in  $\text{Ce}_{0.95}\text{Sc}_{0.05}\text{O}_{1.975}$  using the bulk conductivity relaxation frequency from impedance spectroscopy measurements as well as the temperature dependence of  $^{45}\text{Sc}$  magic-angle-spinning NMR line shapes. The resulting prefactors from the extrapolation of the oxygen vacancy hopping frequencies are similar for both impedance with  $(4.6 \pm 0.1) \cdot 10^{13} \text{ s}^{-1}$  and NMR measurements with  $(4.3 \pm 1.1) \cdot 10^{13} \text{ s}^{-1}$ . Fuda *et al.*<sup>[402]</sup> examined lightly Y doped ceria (0.02 – 0.6 mol%  $\text{Y}_2\text{O}_3$ ) using NMR. They found the correlation times of the vacancy motion to be essentially independent of dopant fraction. The resulting prefactor from the extrapolation of the oxygen vacancy hopping frequency is  $(2.8 \pm 0.3) \cdot 10^{12} \text{ s}^{-1}$ . The nanocrystalline samples that are examined by Fuda *et al.*<sup>[402]</sup> feature a large grain boundary effect, while NMR measurements can give bulk properties for polycrystalline samples due to the low grain boundary volume as in the case of Avila-Paredes *et al.*<sup>[210,256]</sup> Both NMR results fit well with the calculated attempt frequencies for pure ceria.

A major influence on the macroscopic experimental attempt frequency are *sample properties* which include the mentioned diverse oxygen vacancy concentrations, the macroscopic structure composed of bulk and grain boundaries and different impurities. In this work, all calculations were performed in the bulk domain. In order to allow a better comparison of the calculated attempt frequency with experimental values, single crystals should be used or bulk properties from polycrystalline samples should be extracted. Otherwise, the total conductivity or diffusion could result from the contribution of the bulk (grain, lattice) and the grain boundary domain. Impedance spectroscopy is an important tool to separate both contributions and has been extensively used on pure<sup>[83,315]</sup> and samarium doped ceria.<sup>[74,156,158,180,403,404]</sup> However, only a few authors specify the bulk ionic conductivity separately. Well known is the relation between bulk and grain boundary conductivity for rare-earth doped ceria: Zhan *et al.*<sup>[74]</sup> and Bellino *et al.*<sup>[180]</sup> separated the bulk, grain boundary and total conductivity of Sm and Y doped ceria showing a bulk conductivity that is larger than both grain boundary and total conductivity. The resulting experimental attempt frequency for the bulk is however only a fraction (0.8–0.005) compared to the experimental attempt frequency of the total domain caused by higher activation enthalpies for the total domain. For pure ceria, Wang *et al.*<sup>[315]</sup> measured bulk conductivities orders of magnitude larger than the total conductivity with an activation enthalpy lower than for the total domain. In fact, Figure 6.11 and Table 6.7 show, for most stoichiometric ceria measurements, higher  $\Delta H_a$  and higher  $\bar{\nu}_{\text{exp}, \text{V}\bullet\bullet}$  for the total domain compared to the bulk. While the experimental attempt frequencies for the bulk domain fit well with the calculated attempt frequencies for pure ceria, the attempt frequencies for the total domain are significantly higher. However, Brugner *et al.*<sup>[248]</sup> reported the same conductivity for polycrystalline

samples and single crystals resulting in the same experimental attempt frequency though compared to other bulk measurements  $\bar{\nu}_{\text{exp},V_{\text{O}}^{\bullet\bullet}}$  is very large here. Furthermore, it has been shown that the contribution from the grain boundaries to the total resistivity diminishes at high temperature.<sup>[187]</sup> Therefore, also attempt frequencies for the total domain are shown included in Fig. 6.11.

Beyond the macroscopic structure, even small amounts of impurities that associate with oxygen vacancies, e.g. small rare-earth cations, can increase the activation enthalpy. While the impact on the oxygen vacancy self-diffusion coefficient at intermediate temperatures might be small, different impurities may lead to different activation enthalpies, which would significantly influence the experimental attempt frequency. Therefore, Kinetic Monte Carlo simulations were performed similarly to an earlier work<sup>[55]</sup> between 500 and 800 °C without considering changes in the jump attempt frequency or the existence of polarons. For all jumps the calculated jump attempt frequency ( $1.47 \cdot 10^{12} \text{ s}^{-1}$ ) was applied and in pure ceria a migration energy of 0.47 eV was used. Subsequently, the conductivity was fitted according to Eq. 2.4. In contrast to  $\text{CeO}_{1.99995}$ , where  $\Delta H_a$  and  $\bar{\nu}_{\text{exp},V_{\text{O}}^{\bullet\bullet}}$  are similar to the input values, for  $\text{Ce}_{0.999}\text{Sc}_{0.001}\text{O}_{1.9995}$  the apparent activation enthalpy (1 eV) and attempt frequency ( $1.54 \cdot 10^{14} \text{ s}^{-1}$ ) increase significantly, while the oxygen vacancy self-diffusion coefficient decreases up to two orders of magnitude. This effect can only be observed for dopants with strong association between dopant and oxygen vacancy. For lightly Sm or La doped ceria, no significant influence on oxygen vacancy self-diffusion coefficient, activation enthalpy and attempt frequency can be observed. Therefore, different impurities can significantly influence the experimental attempt frequency. Experimentally, this can be seen e.g. in the conductivity measurements by Wang *et al.*<sup>[315]</sup>

Finally, the macroscopic experimental attempt frequency is influenced by the measured *temperature range* due to the above-discussed influences. While the conductivity and the oxygen tracer diffusion coefficient are continuous with temperature, the activation enthalpy may change for different temperature regimes. This leads to kinks in the oxygen vacancy self-diffusion coefficient and jumps in the experimental attempt frequency if a constant charge carrier concentration is assumed as discussed in Chapter 2.4.4. Two types of kinks are well known in literature: For a change from a low temperature region dominated by impurities to a high temperature region dominated by reduction, the activation enthalpy increases abruptly for higher temperatures. As the number of oxygen vacancies created by reduction (or intrinsic disorder) increases with temperature, their concentration may exceed the number of defects created by impurities. Defects created by reduction and intrinsic defects have to be formed leading to an increase in activation enthalpy.<sup>[26,260]</sup> Actually, Kamiya *et al.*<sup>[260]</sup> reported for low temperature an experimental attempt frequency orders of magnitude lower than for high temperature indicating a change from an impurity- to a reduction-dominated regime. It shall be mentioned that Kamiya *et al.* measured penetration depths for low temperature similar to the grain size of pure ceria, which might lead to bulk dominated properties while at high temperatures the penetration depths are orders of magnitude higher.<sup>[405]</sup> Ideally, for investigating reduction-dominated regions, the change in the charge carrier concentration should be

included in the oxygen vacancy self-diffusion coefficient, which might lead to similar experimental attempt frequencies at both temperature regimes.

The second type of kink is a decrease in activation enthalpy for higher temperatures caused by a change in the diffusion behavior for different temperatures, especially for non-stoichiometric or doped ceria.<sup>[174,180,185,187,406]</sup> Zhan *et al.*<sup>[74]</sup> described a critical curvature temperature  $T_b$  for Sm doped ceria. Below this temperature, oxygen vacancies are trapped by samarium ions  $[\text{Sm}'_{\text{Ce}} - \text{V}_{\text{O}}^{\bullet\bullet}]$ . Therefore,  $\Delta H_a$  is the sum of the ‘migration enthalpy’ of the oxygen ions and the association enthalpy of  $[\text{Sm}'_{\text{Ce}} - \text{V}_{\text{O}}^{\bullet\bullet}]$  while at higher temperature  $\Delta H_a$  is equivalent to the ‘migration enthalpy’ of the oxygen ions. This causes a kink in the ionic conductivity in the Arrhenius plot leading to lower activation enthalpies and prefactors at high temperatures. This kink can be reproduced using Kinetic Monte Carlo simulation although further influences on the activation enthalpy are given.<sup>[55,287]</sup> For another perspective on this effect, Zhan *et al.* assume that the concentration of the oxygen vacancies depends on the association enthalpy of the forming  $[\text{Sm}'_{\text{Ce}} - \text{V}_{\text{O}}^{\bullet\bullet}]$  defect complexes at low temperature while at  $T > T_b$  the concentration of oxygen vacancies is set by the dopant fraction, as all oxygen vacancies are free. Taking into consideration that the association reduces the oxygen vacancy concentration, this could lead to the same attempt frequencies at low and high temperatures. Therefore, the experimental attempt frequency can only be extracted above the critical curvature temperature if the degree of association is unknown. This effect was examined using Kinetic Monte Carlo simulations similar to an earlier work<sup>[55]</sup> without considering changes in the jump attempt frequency. Although Zhan *et al.* investigate highly doped ceria, the Kinetic Monte Carlo simulations show this effect for Sc doped ceria for dopant fractions as low as  $\text{Ce}_{0.99998}\text{Sc}_{0.00002}\text{O}_{1.99999}$  around  $T_b = 800$  °C (Fig. 9.4 in appendix). For the above-mentioned  $\text{Ce}_{0.999}\text{Sc}_{0.001}\text{O}_{1.9995}$ , apparent activation enthalpy (0.67 eV) and attempt frequency ( $4.65 \cdot 10^{12} \text{ s}^{-1}$ ) decrease again for conductivities fitted between 1100 and 1300 °C. However, impedance measurements of the bulk domain in pure ceria are commonly limited to low temperatures due to a restricted frequency range.

Obviously, measurements of non-stoichiometric ceria might lead to different results as the presence of polarons changes the diffusion behavior. In fact, the smallest activation enthalpies in this work are the ones measured by Tuller *et al.*<sup>[83]</sup> and Naik *et al.*<sup>[84]</sup> [see Fig. 6.11(b)].

In summary, differences in measurement technique, sample properties or investigated temperature range change the oxygen self-diffusion coefficient by about two orders of magnitude at intermediate temperature (see Fig. 6.11a).

The vast scattering of the experimental attempt frequency  
in the range of nine orders of magnitude is caused  
by a change in activation enthalpy.

Especially different contributions of bulk and grain boundary domain to the total conductivity or diffusion, different impurities, a change from an impurity- to a reduction-dominated regime and a change in the diffusion behavior can lead to significant changes in the activation enthalpy. A closer

examination shows a clear dependence of the experimental attempt frequency on the activation enthalpy [Fig. 6.11(b)]. As diffusion coefficients are extrapolated to infinite temperature to obtain experimental attempt frequencies, larger activation enthalpies lead obviously to larger attempt frequencies. If now the oxygen tracer diffusion coefficient is identical for all measurements at a specific temperature, the relation between experimental attempt frequency and activation enthalpy is given by

$$D_{V_{\bullet\bullet}} = l^2 \cdot \bar{\nu}_{\text{exp}, V_{\bullet\bullet}} \cdot \exp\left(-\frac{\Delta H_a}{k_B T}\right). \quad (6.5)$$

All oxygen vacancy diffusion coefficients were fitted according to Arrhenius (Eq. 2.4). Using the resulting activation enthalpies and experimental attempt frequencies, an average oxygen vacancy diffusion coefficient at 1600 K was fitted (Eq. 6.5). Here, 1600 K showed the best agreement for all measurements. Figure 6.11a already shows that all  $D_{V_{\bullet\bullet}}$  can be described as a function of  $\bar{\nu}_{\text{exp}, V_{\bullet\bullet}}$  and  $\Delta H_a$  using an average oxygen vacancy diffusion coefficient at 1600 K. This is even true for non-stoichiometric ceria. The good regression of Eq. 6.5 in Fig. 6.11(b) verifies that all measurements can be linked:

The experimental attempt frequency can be described  
as a function of the activation enthalpy for all measurements.

Therefore, it is assumed that all experiments are based on the same elemental frequency for a jump process, which is similar to the calculated attempt frequency.

The main influences that are causing the vast scattering of the experimental attempt frequency are recapitulated in the following:

Samples of low purity exhibit a smaller experimental bulk attempt frequency than predicted by the fit (Eq. 6.5). This indicates that the charge carrier concentration may be overestimated for these samples.

The total domain indeed has similar oxygen vacancy self-diffusion coefficients compared to bulk measurements; however, most experiments show a higher activation enthalpy leading to higher experimental attempt frequencies obviously due to the grain boundary contribution.<sup>[315]</sup>

High concentrations of impurities that associate with the oxygen vacancies lead to a significant increase in activation enthalpy and experimental attempt frequency especially at low temperatures where dopants and oxygen vacancies possibly associate. This can be seen by comparing measurements from this work with the bulk domain of Wang *et al.*<sup>[315]</sup>

With increasing temperature the charge carrier concentration increases, one example is given by Kamiya *et al.*<sup>[260]</sup> whose low temperature regime might show bulk dominated properties indicated by the low experimental attempt frequency. Brugner *et al.*<sup>[248]</sup> show similar high  $\bar{\nu}_{\text{exp}, V_{\bullet\bullet}}$  and  $\Delta H_a$  at high temperature for both single crystals and polycrystalline samples indicating that at high temperatures a reduction-dominated region exists. In this work, a constant charge carrier concentration was used, leading for a reduction-dominated region to an overestimated increase in oxygen vacancy self-diffusion coefficient. Consequently, the resulting experimental attempt frequency is too high.

The example of pure ceria emphasizes the difficulties in measuring the experimental attempt frequency. While calculations are often performed in defect-poor (or periodic) materials, creating these materials experimentally is challenging. Here, the experimental bulk attempt frequencies for stoichiometric ceria are the best values for comparison and indeed agree with the calculated attempt frequency.

### 6.3.3 Experimental Values for Doped Ceria

For the bulk of Sm and Y doped ceria,<sup>[74,167,180,407]</sup> a similar fit of the macroscopic, experimental attempt frequencies using Eqs. 2.3 and 2.4 would lead to an increase in the experimental attempt frequency with increasing dopant fraction. Here, overestimated attempt frequencies for small dopant fractions<sup>[167,407]</sup> were neglected due to an unknown number of charge carriers because of additional impurities.

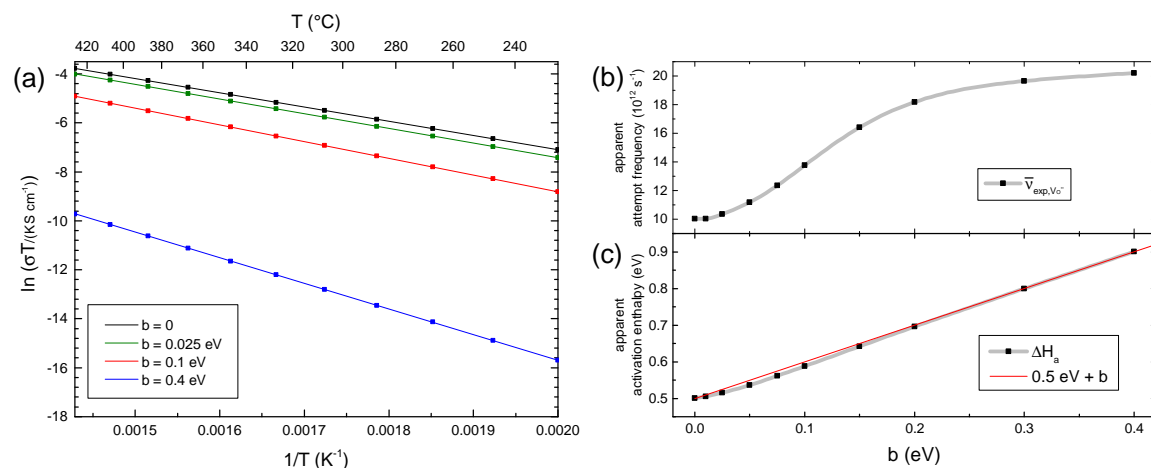


Figure 6.12: The (a) ionic conductivity for the simple model and regression according to Eqs. 2.3 and 2.4. The fit parameters are the (b) apparent oxygen vacancy attempt frequency and (c) the apparent activation enthalpy.

However, despite the considerations above, comparing the attempt frequency for doped ceria is more difficult, since the classical Einstein equation cannot be used (Eq. 2.3) as there are many defects, which will interact. Moreover, in doped ceria, a variety of possible defect configurations exists leading to a distribution of different jump environments with a distribution of migration energies and possibly different local attempt frequencies. In contrast, in experiments, the linear interpolation of the conductivity with temperature in the Arrhenius plot gives only a single value for the attempt frequency and for the activation enthalpy. Comparing a single fit value with the actually present distribution is not trivial. Beyond that, the apparent value of the attempt frequency obtained by fitting is directly influenced by the distribution of migration energies.

This dependency can be shown in a simple model: A highly ordered, fluorite-structured crystal is considered, half of the migration energies are 0.5 eV and the other half is larger by a value  $b$ . Both

jump environments appear alternating. Now, a single oxygen vacancy jumps through the crystal. Each jump has the same attempt frequency. To simulate the ionic conductivity Kinetic Monte Carlo simulations can be used according to previous calculations.<sup>[55,287]</sup> In Fig. 6.12a, the oxygen ion conductivity for the simple model was calculated between 500 and 700 K for different  $b$ -values. All linear regressions of the simulated conductivities, naively based on Eqs. 2.3 and 2.4, show a good fit.

The fit parameters are the apparent attempt frequency and the apparent activation enthalpy shown in Fig. 6.12(b,c). The resulting activation enthalpy is about  $0.5 \text{ eV} + b$ . Therefore, the activation enthalpy is strongly influenced by the higher migration energy. Although always the same attempt frequency in the Kinetic Monte Carlo simulations is used, the apparent attempt frequency increases for higher migration energies. For high  $b$ -values only the higher migration energy determines the ionic conductivity and the lower migration barrier is passed in a considerably small amount of time. Therefore, the covered distance is doubled, which appears here in the doubled attempt frequency.

The effect is already mentioned in literature. Wang *et al.*<sup>[315]</sup> explains the increase in pre-exponential factor for high dopant fractions with the migration distance after each rate-controlling jump, which increases beyond the lattice jump distance of the oxygen vacancy.

This simple example shows that the experimental attempt frequency is strongly influenced by the distribution of migration energies.

This effect depends strongly on the chosen temperature range. For infinite large temperature, only the attempt frequency determines the ionic conductivity and the experimental attempt frequency is independent of the distribution of migration energies. This is shown in Fig. 6.13, where conductivities at infinite large temperature were chosen according to the limit of Eq. 2.4.

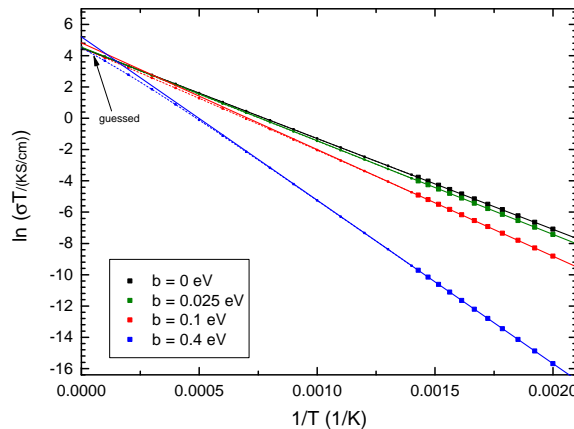


Figure 6.13: The ionic conductivity for the simple model and regression (lines) according to Eqs. 2.3 and 2.4 between 500 and 700 K. The values for infinite temperatures were chosen according to an educated guess.

Therefore, Kinetic Monte Carlo simulations have to be performed, which include different attempt frequencies for different ionic configurations, to compare calculated attempt frequencies with experimental attempt frequencies for doped ceria.

#### **Conclusion**

The attempt frequency for an oxygen ion jump in pure and Sm doped ceria was calculated. The convergence of the phonon mesh was shown pointing out that the common reduction to the Gamma point is not sufficient to calculate the attempt frequency. The resulting attempt frequency for the constant volume case in harmonic approximation ( $1.47 \cdot 10^{12} \text{ s}^{-1}$ ) and constant pressure case in quasi-harmonic approximation ( $7.67 \cdot 10^{12} \text{ s}^{-1}$ ) for pure ceria at 900 K is in agreement with common literature estimates and experiments. Experimental attempt frequencies scatter within several orders of magnitude while they are probably based on the same elemental frequency for a jump process. The calculated attempt frequency is unaffected by doping with a single Sm ion at the migration edge while a Sm-Sm edge exhibits a significantly larger attempt frequency. Smaller dopants lead to a decrease in attempt frequency. Doping with Sm at the start position also increases the attempt frequency. Calculated attempt frequencies of doped ceria should only be compared with experimental attempt frequencies by performing Kinetic Monte Carlo simulations.

## 6.4 KMC Simulations with Varying Attempt Frequencies

KMC simulations were performed with four different sets of attempt frequencies to investigate the influence of varying attempt frequencies on the ionic conductivity. The used `c1+sd [ds]` model with an interaction radius of 5.41 Å will be introduced in Chapter 7.2. At first, fixed similar attempt frequencies for all configurations with  $\nu_0(V,T)$  from the pure ceria case were employed. Alternatively, for the three edge configurations different attempt frequencies according to the constant volume case were used. The last two sets of attempt frequencies consider further varying attempt frequencies: Additionally, varying attempt frequencies were introduced for dopants at the start position (Fig. 6.9) based on the case for a single dopant. Finally, also varying attempt frequencies were introduced for dopants at the end position, for which the same change compared to the start position was assumed.

Figure 6.14 shows the very small influence of variations in the migration edge attempt frequency as the curves are close to each other. The reason for the small influence is the high migration energy for doped edges. Only at high temperature and high dopant fraction a significant influence can be found since in this case many doped edges exist and sufficient thermal energy is available for jumps through doped edges.

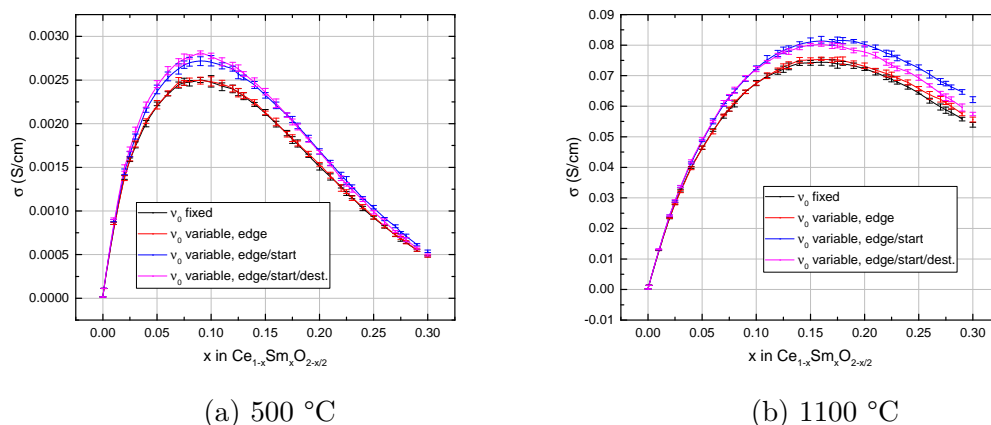


Figure 6.14: KMC simulations of the ionic conductivity for Sm doped ceria with fixed and varying attempt frequencies. Lines are a guide to the eye only.

Varying the attempt frequency of the start position has a significant influence, which starts at low temperature and intermediate dopant fractions. Jumps away from dopants in nearest neighborhood position, which free trapped vacancies and feature a large attempt frequency, appear often. Therefore, the ionic conductivity is increased.

If the same change in attempt frequency is assumed for jumps with dopants in the destination position, the ionic conductivity increases at intermediate dopant fractions and decreases at high dopant fractions for 500 °C. For 1100 °C, the ionic conductivity decreases at high dopant fractions. As an increase in attempt frequency for the destination position leads to an increase in trapping, a

decrease in ionic conductivity can be expected. The trapping increases at low temperature, as less thermal energy is available. Therefore, the above-described increase in conductivity is surprising. This implicates that at intermediate dopant fractions for 500 °C common diffusion paths cross dopant sites. Increasing the frequency of trapping processes, therefore, increases the conductivity. For increasing dopant fractions, more Sm-Sm edges appear and block the migrating oxygen vacancies. At 1100 °C, considerably more thermal energy is available to cross trapping barriers so that the change in ionic conductivity is negligible. The conductivity is obviously strongly influenced by trapping, especially at low and intermediate dopant fractions, and blocking, especially at high dopant fractions.

The optimal dopant concentration is determined by an interplay of trapping and blocking.

Fig. 6.15 shows the comparison between experimental ionic conductivities of the bulk domain and the result of the KMC simulations. The experimental conductivities scatter significantly as discussed in Chapter 6.3.2. Further reasons for the scattering will be investigated in Chapter 8.1. The trends of experimental and theoretical results are in agreement. However, the scattering in experimental values is significantly larger than changes in the simulated conductivity between the different variations in attempt frequency. Therefore, a clear preference cannot be determined.

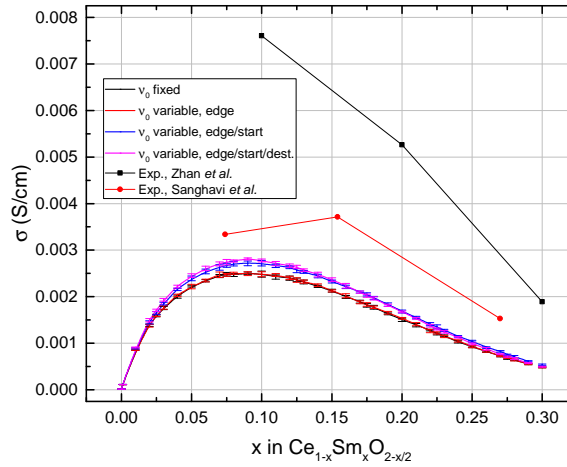


Figure 6.15: KMC simulations of the ionic conductivity for Sm doped ceria at 500 °C with fixed and varying attempt frequencies. Experimental values according to Zhan *et al.*<sup>[74]</sup> and Sanghavi *et al.*<sup>[179]</sup> Lines are a guide to the eye only.

The temperature dependence of the ionic conductivity (Fig. 6.14) can be investigated by applying the Arrhenius equation (Eqs. 2.3 and 2.4) between 500 °C and 1100 °C. The result is shown in Fig. 9.5 in the appendix. The behavior for all four cases is similar: The activation enthalpy  $\Delta H_a$  increases from 0.47 to 0.81 eV nearly linearly with increasing dopant fraction. The experimental attempt frequency  $\bar{\nu}_{\text{exp}, \text{V}\bullet\text{O}}$  increases with increasing dopant fraction except for a plateau between  $x = 0.04$  and 0.12. The activation enthalpy is similar for fixed and variable attempt frequency. For an increase

in microscopic attempt frequency (from the fixed, to the edge-variable to the edge/start-variable case), an increase in experimental attempt frequency  $\bar{\nu}_{\text{exp},V\bullet\bullet}$  can be found. Compared to the fixed attempt frequency case, including attempt frequencies for the three edge configurations increases  $\bar{\nu}_{\text{exp},V\bullet\bullet}$  up to 7% and additionally including attempt frequencies for dopants at the start position increases  $\bar{\nu}_{\text{exp},V\bullet\bullet}$  up to 20%.

The microscopic increase in local attempt frequency leads to a macroscopic increase in experimental attempt frequency.

In contrast, the activation enthalpy is similar. The microscopic increase in local attempt frequency does not influence the activation enthalpy. This result can be combined with the previous observations: Doping with very small amounts of Sc leads to an increase in both experimental attempt frequency and activation enthalpy at low and intermediate temperatures. The simple model study above (Fig. 6.12) shows that the activation enthalpy is strongly influenced by the higher migration energy and the attempt frequency is strongly influenced by the distribution of migration energies. This may be summarized as follows:

The distribution of microscopic migration energies influences both macroscopic attempt frequency and activation enthalpy. The distribution of microscopic attempt frequencies influences the macroscopic attempt frequency but has only a small influence on the activation enthalpy. Correlations between the macroscopic  $\bar{\nu}_{\text{exp},V\bullet\bullet}$  and  $\Delta H_a$  as discussed in literature (see Chapter 2.4.4)<sup>[163,164,167,169,196]</sup> are therefore caused by a change in the microscopic distribution of migration energies.

# 7 Activation Energy

In experiments, the macroscopic dependence of the diffusion coefficient on temperature is called *activation* energy or enthalpy  $\Delta H_a$  (see Chapter 2.2). However, in a solid electrolyte several defects and therefore a large number of ionic configurations exists. Each of these microscopic jump environments has an own *migration* energy  $E_{\text{mig}}$ . In this chapter, the *ab initio* calculation of migration energies and the creation of a migration energy model, which can predict migration energies for all possible jump environments, are described.

First, the calculation of the migration energy using DFT is discussed with focus on the influence of the supercell size. Deviations in the migration energy of  $\pm 0.01$  eV, given by the accuracy of Nudged Elastic Band (NEB) calculations within a set of parameters, change the probability of a jump about  $\pm 11\%$  at 1000 K or about  $\pm 22\%$  at 500 K. Thus, deviations in the migration energy have a great impact on the ionic conductivity. For pure ceria, the calculated migration energy is briefly compared with experimental activation enthalpies.

In the following, an introduction to the mathematical foundations for the creation of linear and additive models as well as an evaluation method is introduced. The modeling is presented separately for the cation and the anion sublattice and the interaction of both sublattices is checked.

Finally, KMC simulations for different migration energy models are performed to investigate the influence of the chosen model on the ionic conductivity. Further ionic conductivities are discussed in Chapter 8.

## 7.1 Calculating the Migration Energy

In this work, oxygen ion jumps are labeled with all interactions of the migrating oxygen vacancy before and after the jump. For this purpose, the interaction distances of either the cation or anion sublattice are numbered consecutively according to Chapter 4.2.1 (e.g.  $1_{\text{NN}}$ ,  $2_{\text{NN}}$ ).

As a first example, only the six nearest cation sites around a jump are presented, the ‘6-cation environment’ (see Fig. 7.1). The two cation sites on the plane crossing the transition state position perpendicular to the jump direction are called ‘migration edge’. They have the same distance to initial and final position of the jump ( $1_{\text{NN}} \leftrightarrow 1_{\text{NN}}$  RE-V) and are nearest to the transition state position of the migrating oxygen. This type of dopant position is called geometrically symmetric. An undoped migration edge is called Ce-Ce edge. If rare-earth dopants (RE) are present, the labels Ce-RE edge or RE-RE edge are used. The other two cation site pairs are near to either the initial ( $1_{\text{NN}} \rightarrow 2_{\text{NN}}$  RE-V)

or final position ( $2_{NN} \rightarrow 1_{NN}$  RE-V). This type of dopant position is called geometrically asymmetric.

In a simplified nomenclature for the six cations, the number of dopant at each of the three cation sites is enumerated. The format  $xyz$  is used with  $x$  standing for dopants near the initial position,  $y$  for dopants at the migration edge and  $z$  for dopants near the final position of the migrating oxygen vacancy. The number of dopants is labeled with Z for zero, O for one and T for two dopants. O\*O configurations, where each dopant is on the same side along to the jump direction, are marked with 'e' for even. Other O\*O configurations are marked with 'c' for cross. Examples are shown on page 139.

For Sm doped ceria, these six nearest cation sites around a jump can be occupied by either a Ce ion or a Sm dopant. The resulting number of possible jump configurations is  $2^6 = 64$  and can be reduced by symmetry to 30 unique jump environments. A few examples are shown in Fig. 7.1.

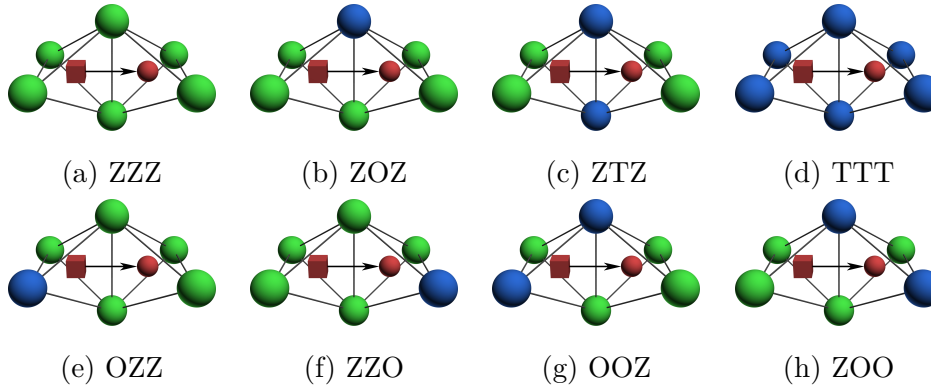


Figure 7.1: Examples of migration configurations including only the six nearest cation sites around a jump (6-cation environment). Cerium ions are green spheres, dopants are blue spheres, the oxygen ion is a red sphere and the oxygen vacancy is a red cube.

### 7.1.1 Widening of the Edges Cation Distance

In Table 7.1, the migration energies for Sm doped ceria in the  $2 \times 2 \times 2$  supercell according to an earlier work are shown.<sup>[1]</sup> The migration energy in pure ceria (ZZZ) increases for one Sm dopant at the edge (ZOZ) and even more for two Sm dopants at the edge (ZTZ). The different change in migration energy for either one or two dopants is caused by the local lattice distortion around the two cations at the migration edge. As described before (Chapter 6.1), the migration energies of the edge configurations are proportional to the widening of the edge cations. The widening is the difference of distances of the edge cations in transition state ( $d_{TS}$ ) and initial state ( $d_{IS}$ ). Simply described, this means that the cations at the edge must be pushed apart during the jump.

Sm dopants at the edge lead to a decrease of the edge cation distance in the initial state compared to pure ceria, because  $\text{Sm}^{3+}$  dopants have a lower charge than  $\text{Ce}^{4+}$ . In the transition state, Sm dopants at the edge lead to an increase of the edge cation distance, because  $\text{Sm}^{3+}$  dopants have a

migration configuration	$d_{\text{IS}}$ (Å)	$d_{\text{TS}}$ (Å)	$d_{\text{TS}} - d_{\text{IS}}$ (Å)	$\Delta E_{\text{el}}^0(V,T)$ (eV)
ZZZ	4.153	4.266	0.113	0.518
ZOZ	4.146	4.266	0.120	0.692
ZTZ	4.142	4.277	0.135	1.091
OZZ	4.161	4.272	0.110	0.506
ZZO	4.147	4.272	0.125	0.427

Table 7.1: Electronic migration energies for different migration configurations and distances of the edge cations in the initial and the transition state for the  $2 \times 2 \times 2$  supercell at constant volume.

larger ionic radius than  $\text{Ce}^{4+}$  and, therefore, must be pushed apart further. This strong widening leads to an increase in the migration energy.

Sm dopants in the OZZ, ZZO or related jump configurations also result in an increase of the edge cation distance in the transition state. However, in the initial state, an even stronger increase (OZZ) or decrease (ZZO) of the edge cation distance takes place. For the OZZ jump configuration, the therefore smaller widening of the edge cation distance leads to a decrease of the migration energy. The decrease in migration energy is even more pronounced with increasing number of Sm dopants at the edge since the effect scales with the increasing migration energy. Surprising is the ZZO configuration, where a larger widening of the edge cation distance also leads to a decrease of the migration energy. In general, for all jump configurations of the 6-cation environment, a correlation between widening and the migration energy can be found.

The migration energy correlates with the difference of distances of the edge cations in transition and initial state for each rare-earth dopant.

For Sm and Nd doped ceria, the migration energy generally increases for a larger widening of the edge cation distance. However, a strong scattering can be found. For Y doped ceria the migration energy decreases for a larger widening of the edge cation distance. In Fig. 7.2, the migration energy as a function of widening of the edge cation distance is shown for all jump configurations of the 6-cation environment. Jump configurations like ZOT, OOT and TOT (\*OT) lead to smaller migration energies than suggested by the linear fit. Jump configurations like ZTZ, OTZ and TTZ (\*TZ) lead to larger migration energies than suggested by the linear fit. Therefore, for selected configurations a systematic deviation from the linear relation between migration energy and widening due to local relaxation effects can be found. The 95%-confidence regions of the linear fits show a strong correlation for Y doped ceria in the  $2 \times 2 \times 2$  supercell. For Y doped ceria in the  $3 \times 3 \times 3$  supercell, a similar correlation can be found. For Sm doped ceria in the  $3 \times 3 \times 3$  supercell, results are similar to the  $2 \times 2 \times 2$  supercell (Table 7.2).

In Fig. 7.3, the proportionality between widening and migration energy for different dopants is

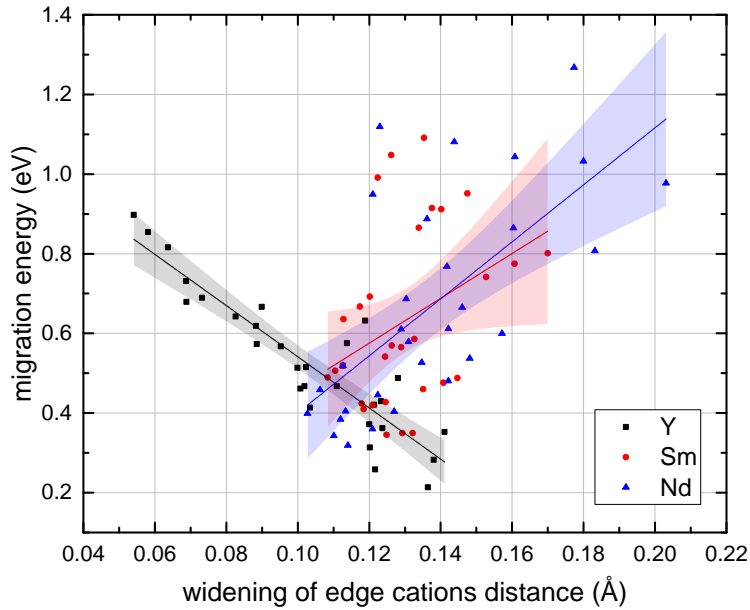


Figure 7.2: Migration energy and widening of the edges cation distance for all jump configurations in the 6-cation environment. The widening is the difference of distances of the edges cations in transition and initial state. Confidence region (95 %) is shown. Y, Sm and Nd doped ceria,  $2 \times 2 \times 2$  supercell.

investigated further in the  $3 \times 3 \times 3$  supercell. For each selected jump configuration, ionic radius and migration energy correlate. The dependence of the migration energy on the widening, however, clearly differs between jump environments. The RE-RE edge leads to a large range of widenings. For the ZZO jump configuration, the widening is similar for different dopants. While for all selected jump configurations the distance of the edge cations increases for larger ionic radii in the transition state, in the initial state the distance both increases (for OZZ, ZOO) and decreases (for ZOZ, ZTZ). Therefore, the widening is similar for different dopants in the OZZ and ZZO jump configuration. Still, for OZZ, the migration energy decreases with increasing ionic radius similar to the widening. For ZZO, the migration energy increases with increasing ionic radius while the widening slightly decreases.

If different dopants are compared, the following conclusion can be made: For small dopants, which lead to widenings smaller than in pure ceria, the migration energy decreases with increasing widening. For large dopants, which lead to widenings larger than in pure ceria, the migration energy increases with increasing widening.

Doping with Gd and Sm leads to similar widenings as in pure ceria. Though Shannon suggests larger ionic radii for both dopants compared to  $\text{Ce}^{4+}$ ,<sup>[32]</sup>  $\text{Gd}^{3+}$  and  $\text{Sm}^{3+}$  appear to be optimal dopants that cause a low lattice distortion. As both dopants lead to large ionic conductivities in experiments, a relationship between lattice distortion and large ionic conductivity might exist as suggested in experimental literature (Chapter 2.5.2).

migration configuration	$d_{\text{IS}}$ (Å)	$d_{\text{TS}}$ (Å)	$d_{\text{TS}} - d_{\text{IS}}$ (Å)	$\Delta E_{\text{el}}^0(V, T)$ (eV)
ZZZ	4.163	4.274	0.111	0.482
ZOZ	4.154	4.274	0.120	0.649
ZTZ	4.153	4.284	0.131	1.049
OZZ	4.167	4.276	0.109	0.488
ZZO	4.156	4.276	0.120	0.413

Table 7.2: Electronic migration energies for different migration configurations and distances of the edge cations in the initial and the transition state for the  $3 \times 3 \times 3$  supercell at constant volume.

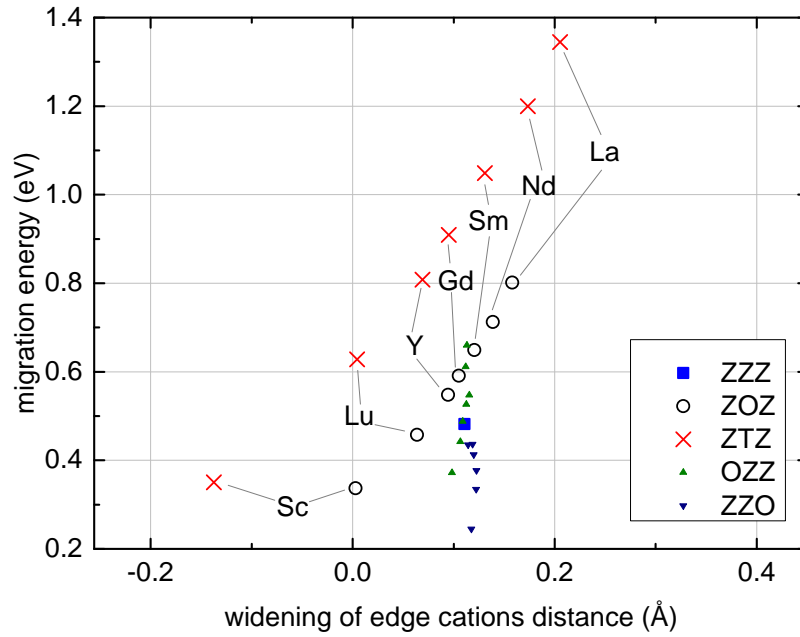


Figure 7.3: Migration energy and widening of the edges cation distance for different jump configurations in the  $3 \times 3 \times 3$  supercell. The widening is the difference of distances of the edges cations in transition and initial state.

## 7.1.2 Supercell Size

### Pure Ceria

The migration energy in pure ceria is calculated by introducing a single migrating oxygen vacancy in  $\text{CeO}_2$ . The calculation of migration energies depends strongly on the following choices: (a) The computation method, which may include the use of empirical, interionic potentials or *ab initio* calculations using DFT. (b) The computational details, in the case of DFT calculation e.g. the choice of the charged state of the defects, the choice between LDA and GGA, the use of an Hubbard  $U$  parameter as well as the choice of the used potential itself. Further influences are (c) the lattice parameter and (d) the supercell size. Table 7.3 shows these influences on the calculated migration energy of pure ceria according to literature, resulting in a range of 0.46–0.95 eV.<sup>[350]</sup>

$E_{\text{mig}}$ (eV)	computational method	reference
0.53	interionic potential	Butler <i>et al.</i> <sup>[39]</sup>
0.47	interionic potential	Conesa <i>et al.</i> <sup>[408]</sup>
0.74	interionic potential	Pryde <i>et al.</i> <sup>[409]</sup>
0.63	interionic potential	Balducci <i>et al.</i> <sup>[410,411]</sup>
0.95	interionic potential	Bulgakov <i>et al.</i> <sup>[412]</sup>
0.70	GGA, PBE	Geerlings <i>et al.</i> <sup>[413]</sup>
0.48	GGA, PBE	Nakayama and Martin <sup>[54]</sup>
0.46	GGA, PW91	Andersson <i>et al.</i> <sup>[44]</sup>
0.53	GGA+ $U$ , PW91 <sup>a</sup>	Nolan <i>et al.</i> <sup>[346]</sup>

Table 7.3: Calculated migration energy in pure ceria according to literature.

<sup>a</sup>Nolan *et al.* used different electron configurations compared to this work. They investigated  $(\text{Ce}_{32}\text{O}_{63})^0$  instead of  $(\text{Ce}_{32}\text{O}_{63})^{2+}$  and two cerium ions neighbored to the oxygen vacancy are reduced to  $\text{Ce}_{\text{Ce}}$ .

In this work, only a few parameters were exemplarily varied (see Fig. 7.4). The use of the 2000 and the revised 2003 potential for the cerium ions (b) leads to a change in migration energy of 0.03 eV.<sup>[343]</sup> The lattice parameter (c) can be chosen according to experimental values at room temperature (5.411 Å) or even temperature-dependent with the linear thermal lattice expansion coefficient of ceria ( $\alpha = 1.10 \cdot 10^{-5} \text{ K}^{-1}$ ).<sup>[57,184,398,414,415]</sup> Alternatively, the defect-free material can be calculated and its volume can be relaxed until the sum of all forces on the ions is zero. The variation of the lattice parameter leads here to a difference of up to 0.2 eV in the migration energy for a change in the lattice parameter of 0.1 Å. The electronic migration energy decreases linearly with increasing lattice parameter. In contrast, metadynamics simulations in cooperation with P. C. Schmidt and T. Bucko suggest that the free migration energy is independent of temperature although thermally

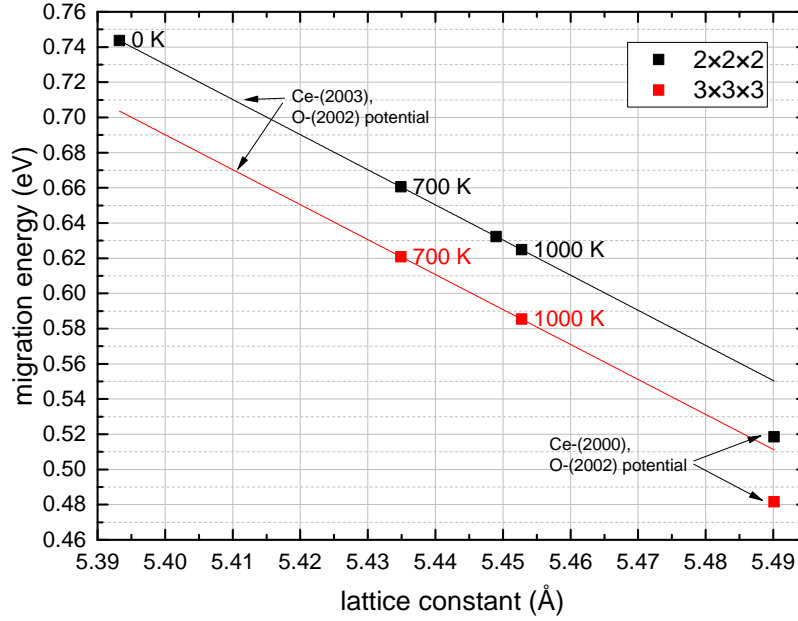


Figure 7.4: Migration energy of a single oxygen vacancy in pure ceria as a function of used potential, lattice parameter and supercell size. The electronic energy difference at absolute zero is shown. Calculations are labeled with the used temperature-dependent experimental lattice parameters.

corrected experimental lattice constants are used for the simulations.<sup>[416]</sup> Though electronic and free energy differ in the vibrational contributions, the change in lattice parameter with temperature possibly may be neglected. Finally, increasing the supercell size from  $2 \times 2 \times 2$  to  $3 \times 3 \times 3$  (d) leads to both a decrease in oxygen vacancy concentration and a decrease in the image Coulomb interactions between the defects. Independent of the lattice constant, the difference in migration energy between the  $2 \times 2 \times 2$  and  $3 \times 3 \times 3$  supercell is 0.04 eV in pure ceria with a single oxygen vacancy.

The right choice of these parameters is still a topic of discussion. In the following, the Ce-(2000) potential<sup>[343]</sup> and a lattice constant of 5.49 Å based on a relaxed defect-free cell is used.<sup>[1]</sup> The resulting migration energies for pure ceria are shown in Table 7.4. The influence of the supercell size is further investigated in the following.

supercell size	$E_{\text{mig}}$ (eV)
inf	0.466
$4 \times 4 \times 4$	0.471
$3 \times 3 \times 3$	0.482
$2 \times 2 \times 2$	0.518

Table 7.4: Calculated migration energy in pure ceria. The supercell extrapolated to infinite volume is called ‘inf’.

The here calculated migration energies are in agreement with the calculated literature data. In addition, experimental activation energies in pure ceria are similar, which are about 0.65 eV according to ionic conductivity<sup>[315]</sup> and dielectric relaxation measurements<sup>[417]</sup> or 0.49 eV according to <sup>17</sup>O-NMR lattice relaxation measurements.<sup>[402,418]</sup> An overview of experimental activation enthalpies is given in the next section.

## Experimental Activation Enthalpy

In experiments, activation enthalpies for pure ceria were found to be between 0.23–3.35 eV (Table 7.5). Reasons for the scattering were already discussed in Chapter 6.3. Especially different contributions of bulk and grain boundary domain to the total conductivity or diffusion, different impurities, a change from an impurity- to a reduction-dominated regime and a change in the diffusion behavior can lead to significant changes in the activation enthalpy. Furthermore, a correlation between the experimental activation enthalpy and experimental attempt frequency were found in experiments (Fig. 6.11b) and simulations (Fig. 6.14).

source	crystallinity	method	domain	$T$ (°C)	$\Delta H_a$ (eV)
this work	poly	AC	bulk	227–733	1.13
Wang <i>et al.</i> <sup>[315]</sup>	poly <sup>hp</sup>	AC	bulk	237–352	0.65
Wang <i>et al.</i> <sup>[315]</sup>	poly <sup>lp</sup>	AC	bulk	237–596	0.79
Floyd <sup>[258]</sup>	sc	GPA	bulk	836–1151	1.09
Brugner <i>et al.</i> <sup>[248]</sup>	sc, poly	DC	bulk, total	1200–1500	2.22
Wang <i>et al.</i> <sup>[315]</sup>	poly <sup>hp</sup>	AC, DC	total	621–847	2.2
Wang <i>et al.</i> <sup>[315]</sup>	poly <sup>lp</sup>	AC, DC	total	507–891	1.65
Kamiya <i>et al.</i> <sup>[260]</sup>	poly	SIMS	total	1095–1297	2.27
Kamiya <i>et al.</i> <sup>[260]</sup>	poly	SIMS	total	797–895	0.87
Kamiya <i>et al.</i> <sup>[259]</sup>	poly	GPA	total	1094–1296	3.35
Tuller <i>et al.</i> <sup>[83]</sup>	sc <sup>[a]</sup>	AC, DC	bulk	200–1150	0.4
Naik <i>et al.</i> <sup>[84]</sup>	poly <sup>[b]</sup>	DC	total	1030–1330	0.23

Table 7.5: Experimental activation enthalpy  $\Delta H_a$  of pure ceria for polycrystalline samples (poly) and single crystals (sc) calculated based on impedance spectroscopy (AC), direct current (DC), Secondary Ion Mass Spectrometry (SIMS) and Gas Phase Analysis (GPA) measurements. The number of charge carriers is chosen constant for all temperatures as discussed in Chapter 6.3. Samples differ in purity (hp = high, lp = low) or non-stoichiometry with [a] CeO<sub>1.992</sub> and [b] CeO<sub>1.96</sub>.

For lightly Y doped ceria, where impurities and reduction have a smaller influence, the scattering of the migration energy is smaller (0.49–0.9 eV see Table 7.6). As dopant fractions are rather low,

the migration energies for lightly Y doped ceria might still be a good approximation for pure ceria. Both experimental activation enthalpies for pure and lightly Y doped ceria especially for the bulk domain are in agreement with the calculated migration energies in pure ceria.

source	material	method	$\Delta H_a$ (eV)
Fuda <sup>[402]</sup>	0.02 % $Y_2O_3$	$^{17}O$ -NMR lattice relaxation	0.49
Adler <i>et al.</i> <sup>[418]</sup>	0–0.6 % $Y_2O_3$	$^{17}O$ -NMR lattice relaxation	0.49
Wang and Nowick <sup>[417]</sup>	0.5 % $Y_2O_3$	dielectric relaxation	0.64
Tian <i>et al.</i> <sup>[407]</sup>	0.58 % $Y_2O_3$	AC	0.84
Wang <i>et al.</i> <sup>[167]</sup>	0.05 % $Y_2O_3$	AC	0.90

Table 7.6: Experimental activation enthalpy  $\Delta H_a$  of lightly Y doped ceria for the bulk of polycrystalline samples calculated based on  $^{17}O$ -NMR lattice relaxation, dielectric relaxation and impedance spectroscopy (AC) measurements.

## Jumps in Doped Ceria

In doped ceria, dopants and additional oxygen vacancies are introduced and a vast amount of possible ionic configurations around an oxygen ion jump exists. In this section, only the influence of dopants on the migrating oxygen vacancy is investigated.

In this work, a model is developed to predict all related migration energies for these jump configurations using cells with only a few defects and the assumption that the influence of the cation and anion sublattice on the migrating oxygen can be separated. As few defects as possible are used to calculate parameters for the model since long-range Coulomb interactions lead to the repulsion of the defects and their copies due to the periodic boundary conditions. Energies are even extrapolated to an infinitely large supercell to minimize interactions and dependencies on the supercell size. The model is tested versus defect-rich cells and cells with experimental defect concentrations.

Figure 7.5 shows the migration energy in pure and Sm doped ceria at different supercell sizes ( $x \times y \times z$ ) at constant volume, given by the relaxed defect-free material.<sup>1</sup> The supercell size determines the distance between the migrating oxygen vacancy and its mirror image. Increasing the supercell in  $x$ - or  $y$ -direction changes the interaction of the oxygen ions perpendicular to the jump direction. Increasing the supercell in  $z$ -direction changes the interaction of the migrating oxygen with its periodic copies.

In pure ceria (ZZZ), extending the distance between the diffusing oxygen ions in the diffusion direction decreases the migration energy significantly, while the migration energy slightly increases with the extension of the perpendicular distance to the diffusion direction.

<sup>1</sup>Relaxing the volume of supercells containing defects would lead to different lattice parameters.

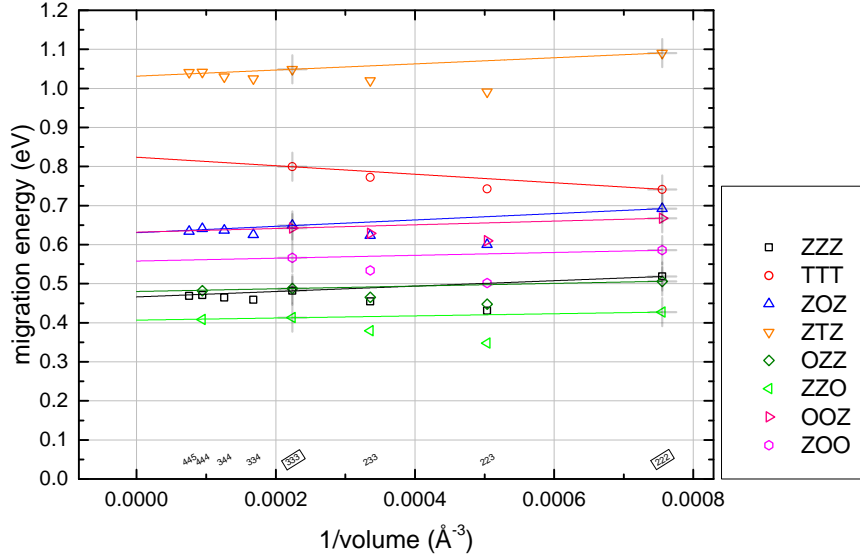


Figure 7.5: Migration energy in Sm doped ceria at different supercell sizes at constant volume.

For Sm doped ceria, different jump configurations are shown in Fig 7.5. The migration energy of the Ce-RE and RE-RE edge as a function of supercell size is shown for different dopants in Fig 9.6 and 9.7 in the appendix. For the selected jump configurations, the migration energy depends similar on the supercell size as in pure ceria. Exceptions are the TTT configurations due to the large number of dopants and the Lu-Lu and Sc-Sc edge due to the small ionic radius of the dopants. Figure 7.6 shows the change in migration energy with supercell size as a function of ionic radius. The change in migration energy with increasing cubic supercell size is strongly negative for large dopants (e.g. La), positive for small dopants (Sc) and negligible for Lu.

Increasing the distance between migrating oxygen ions by increasing the volume cubically or just the  $z$ -direction decreases the migration energy in most cases since periodic interactions decrease. However, decreasing interactions perpendicular to the migration direction mostly increases the migration energy. Here, the smaller supercell size restricts the moving oxygen vacancy leading to a preferred direction. Exceptions are caused by defect cluster or small dopants. Large defect clusters already restrict the moving oxygen vacancy. Small dopants lead to low migration energies and small or even negative widenings of the edge cation distance (Fig. 7.3). The association energies of small dopants (Fig. 5.1) already show a strong supercell size dependence, which indicates that the energy change has components derived from both initial and transition state. While the above-discussed widening of the edges cation distance correlates with the migration energy both in the  $2 \times 2 \times 2$  and  $3 \times 3 \times 3$  supercell for Y doped ceria, no correlation between the changes of both parameters between both supercell sizes can be found.

According to Makov and Payne (Chapter 4.2.1), the migration energy for an infinitely large supercell ('inf') was calculated using the  $2 \times 2 \times 2$  and  $3 \times 3 \times 3$  supercell. The result is similar to an extrapolation using the  $2 \times 2 \times 2$ ,  $3 \times 3 \times 3$  and  $4 \times 4 \times 4$  supercell.

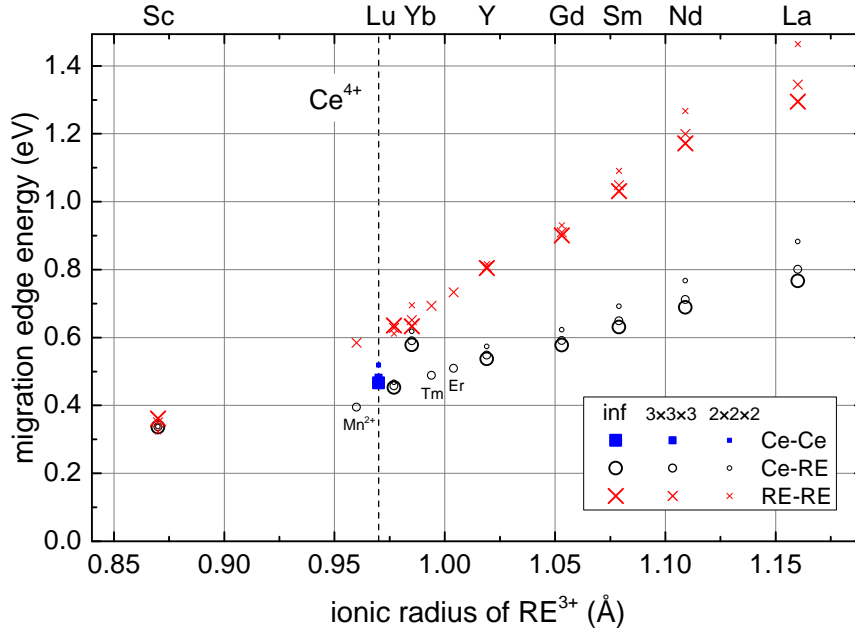


Figure 7.6: Migration energy of Ce-Ce, Ce-RE and RE-RE edge as a function of ionic radius.

In Fig. 7.6, the dopants  $\text{Mn}^{2+}$ ,  $\text{Tm}^{3+}$  and  $\text{Er}^{3+}$  are shown as they have migration energies similar to pure ceria.  $\text{Mn}^{2+}$  shows a similar behavior of the migration edge energy as a function of ionic radius though it has a different charge state. This is contrary to the behavior of the association energy (see Fig. 5.1). This suggests that the migration energy is rather a function of the widening of the edge cation while the association energy is a Coulomb energy dominated property.

Comparing the supercell size dependence of the migration energy (Fig. 7.6) and the association energy (Fig. 5.1) is surprising. For La doped ceria, the migration energy decreases with increasing cubic supercell size while the association energy increases. As both energies feature an opposite sign, the effect decreases with increasing cubic supercell size for La doped ceria. Both migration and association energy show a change between increasing energy and decreasing energy with increasing cubic supercell size as a function of dopant type. For the migration energy, the Ce-Lu and Lu-Lu edge is independent of supercell size. For the association energy, Nd doped ceria is independent of supercell size. Therefore, both energies feature similarities in their supercell size dependence.

Alternatively to a constant volume during migration, which is calculated in a defect-free material, calculations can be performed with a constant pressure and a volume that is relaxed during the migration. This leads to a change in volume of both initial and transition state as described in Chapter 6.1.4.

The supercell dependence of the migration energy for the constant volume case can also be found for the constant pressure case (Fig. 7.7). The migration energies change with a constant shift between  $-0.02$  eV and  $0.04$  eV. Positive shifts compared to the constant volume case can be found for single dopants (ZOZ, OZZ, ZZO) and negative shifts for multiple dopants (ZTZ, OZZ, ZOO). Migration energies for the infinitive large supercell differ accordingly. Therefore, the supercell dependence of the

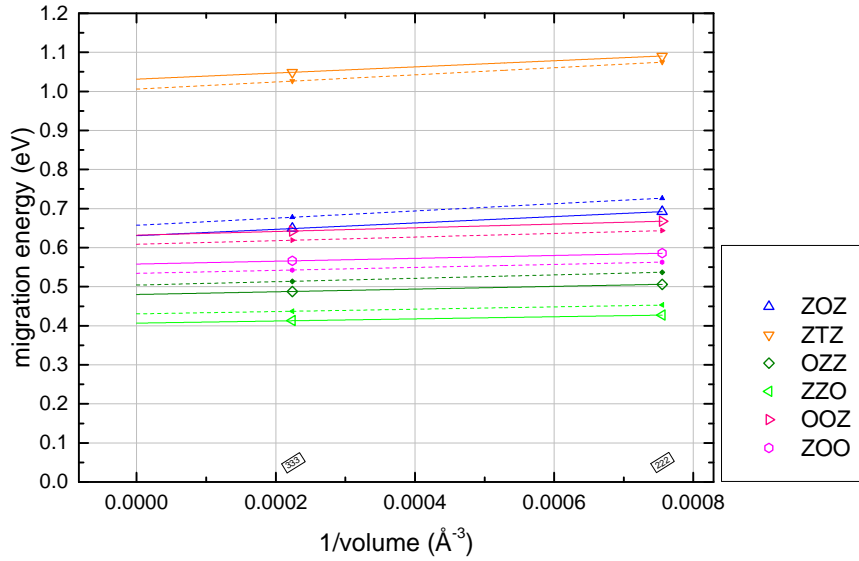


Figure 7.7: Migration energy in Sm doped ceria at different supercell sizes at constant volume (lines) and pressure (dashed lines).

migration energy is not diminished by the relaxation of the cell volume. Interactions of defects and their copies due to periodic boundary conditions still dominate the migration energy. The change in volume during the jump of the oxygen ion is limited as atomic displacements in a solid proceed with the speed of sound.<sup>[123–125]</sup> Therefore, calculations of the constant volume case are used in the following.

### Jumps with Adjacent Vacancies

Similar to the influence of dopants on the migrating oxygen vacancy, the influence of additional oxygen vacancies can be investigated. In Fig. 7.8, the migration energy in a supercell containing two oxygen vacancies is shown at different supercell sizes. According to Makov and Payne (Chapter 4.2.1), the migration energy for an infinitely large supercell was calculated. The V-V distance before and after the jump is noted.

The supercell size dependence is similar to the cation sublattice: Increasing the distance between migrating oxygen ions by increasing the volume cubically or just the  $z$ -direction decreases the migration energy in most cases since periodic interactions decrease. However, decreasing interactions perpendicular to the migration direction increase mostly the migration energy. An exception is the  $4_{NN} \rightarrow 1_{NN}$  V-V configuration. Here, the vector between the defects and migration direction is aligned. Increasing the  $z$ -direction therefore increases the migration energy. Again, the  $4_{NN}$  V-V association energy (Fig. 5.5) already shows a strong supercell size dependence, which indicates that the energy change has components derived from both initial and transition state.

As expected according to the association energies (Fig. 5.5), jumps separating the vacancies possess lower migration energies than jumps in the direction of an additional vacancy. An overview

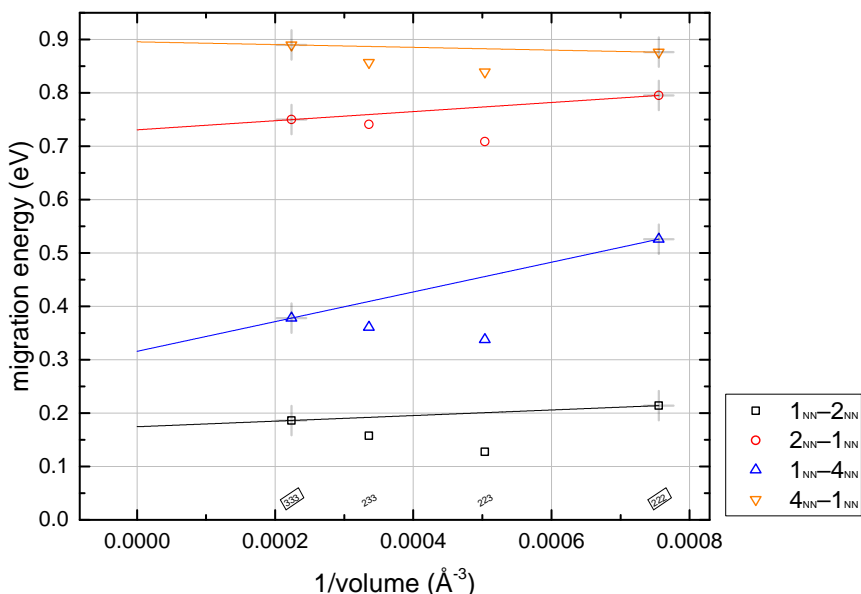


Figure 7.8: Migration energy with two oxygen vacancies at different supercell sizes.

of migration energies with the average distance between the oxygen vacancies before and after the jump is shown in Fig. 7.9. An overview of all jump profiles is shown in Fig. 7.10.

It becomes obvious that the supercell size dependence differs significantly between different configurations. The difference in migration energy between approach and detachment of the additional vacancy generally decreases with increasing distance between the vacancies. The general trend suggests that both migration energies converge to the migration energy for no additional vacancy, which is given by a red line in Fig. 7.9.

The difference in migration energy between the jump for the approach and detachment of the additional vacancy is given by the V-V association energy difference between both sites and can be seen in Fig. 7.11 for an infinitely large supercell. Here, it is assumed that vacancies with a 5<sub>NN</sub> or large distance do not interact and that, therefore, the association energy  $E_{\text{ass}}(5_{\text{NN}} \text{ V-V})$  is zero. Black arrows show exact DFT energies differences, while blue arrows are constructed from the black arrows using the termination  $E_{\text{ass}}(5_{\text{NN}} \text{ V-V}) = 0$ .

The V-V association energy differences (arrows) show large asymmetries for 1<sub>NN</sub>↔2<sub>NN</sub> and 1<sub>NN</sub>↔4<sub>NN</sub>, medium asymmetries for 2<sub>NN</sub>↔5<sub>NN</sub>, 4<sub>NN</sub>↔5<sub>NN</sub>, 3<sub>NN</sub>↔6<sub>NN</sub> and 4<sub>NN</sub>↔8<sub>NN</sub> and small asymmetries for all other jumps. The choice of a termination at  $E_{\text{ass}}(5_{\text{NN}} \text{ V-V}) = 0$  in Fig. 7.11 can be verified by comparing the blue arrows with the difference in migration energy between approach and detachment of the additional vacancy in Fig. 7.9 for an average defect distance of 5.7 Å or more. Both energy differences are in agreement for the 3<sub>NN</sub>↔6<sub>NN</sub>, 4<sub>NN</sub>↔8<sub>NN</sub> (small value in 2 × 2 × 2 supercell) and 5<sub>NN</sub>↔7<sub>NN</sub> jump. The extrapolated difference for 6<sub>NN</sub>↔8<sub>NN</sub> with 0.09 eV is too large, since the migration energy for the 3 × 3 × 3 supercell is already very small. The good agreement confirms a termination of  $E_{\text{ass}}(5_{\text{NN}} \text{ V-V}) = 0$ , which was already discussed in an earlier work.<sup>[55]</sup>

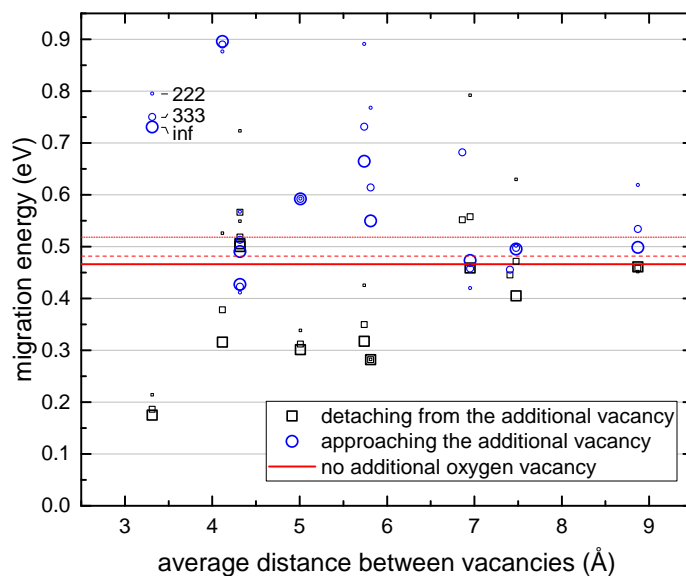


Figure 7.9: Migration energies of an oxygen vacancy jump with an additional vacancy present. The repulsion between vacancies leads to low  $E_{\text{mig}}$ 's for the detachment from the additional vacancy and high  $E_{\text{mig}}$ 's if the additional vacancy is approached. For large distances the migration energy without an additional vacancy is approached, especially for larger supercell sizes.

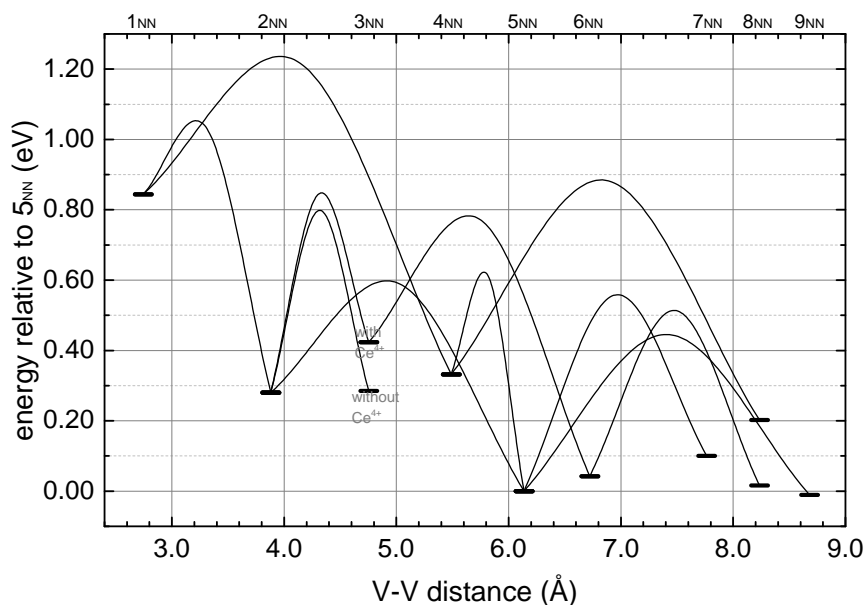


Figure 7.10: DFT migration energies in  $3 \times 3 \times 3$  supercell of ceria including two oxygen vacancies.

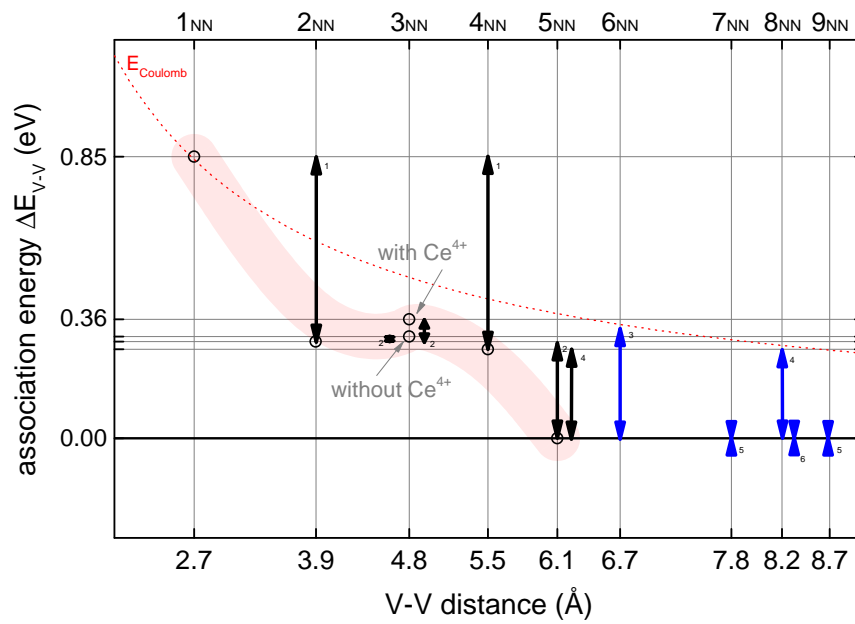


Figure 7.11: V-V association energy as a function of oxygen vacancy distance for an infinitely large supercell. Arrows show the differences between the jump for the approach and detachment of the additional vacancy. Black arrows are exact values, blue arrows are constructed by the termination  $E_{\text{ass}}(5_{\text{NN}} \text{V-V}) = 0$ . The V-V distances are based on the DFT lattice parameter.

## 7.2 Modeling the Migration Energy

### 7.2.1 Mathematics: Linear and Additive Models

The migration energies  $y_i$ , which are observed from DFT calculations for each configuration  $i$ , can be fitted to an model, which can be used to calculate the migration energy  $E(y_i)$  for every possible ionic configuration. Migration energies can be modeled using *multiple linear* and *additive* models.<sup>[419]</sup>

In a *multiple linear model*, the observables  $y_i$  are metric, their expected values  $E(y_i)$  and predicted values  $\eta_i$  are equal and possess an error  $\varepsilon_i$ :

$$y_i = \eta_i + \varepsilon_i, \quad i = 1, \dots, n. \quad (7.1)$$

$$E(y_i) = \eta_i = \beta_0 + \beta_1 x_{i1} + \dots + \beta_k x_{ik} = \eta_i^{\text{lin}} \quad (7.2)$$

with the variables  $x_i$  and the parameters  $\beta_i$ . The errors are independent and identically distributed with an expected value of zero  $E(\varepsilon_i) = 0$  and a constant variance for all observations  $\text{Var}(\varepsilon_i) = \sigma^2$  with the standard deviation  $\sigma$ .

In an *additive model*, observations and errors are similar to a linear model, whereas both the expected and linearly predicted values  $\eta_i^{\text{lin}}$  differ in the use of functions  $f$  depending on the variables  $z_i$

$$E(y_i) = \eta_i = \eta_i^{\text{lin}} + f_1(z_{i1}) + \dots + f_q(z_{iq}) = \eta_i^{\text{add}}. \quad (7.3)$$

In the linear model, the following decisive assumptions are made:

- The function  $f(x_1, \dots, x_k)$  is a linear combination of variables  $x_i$  and parameters  $\beta_i$  (see Eq. 7.2).
- The variables are independent.
- For confidence intervals and hypothesis tests the errors are often assumed to be normally distributed, therefore a *classical* linear regression model is used. If errors increase with a variable (heteroscedastic variance), variances of regression parameters are poorly estimated and the classical linear regression model should be extended.<sup>[419]</sup>

In an additive model, additionally non-linear parameters can be included.

Models are developed by separating the (modeled) systematical compounds  $\eta_i$  and the statistical errors  $\varepsilon_i$ , which are presumably caused by statistical errors in the DFT calculations. The regression parameters are estimated using the method of least squares. The resulting estimated errors are called residua. The modeling can be assessed by omitting single model parameters and obtaining partial residua.

## Categorical Variables

Possible variables for the migration energy model ( $x_i$  or  $z_i$ ) are the occupation of individual lattice sites or the number of defects in a group of several lattice sites. The latter is employed in this work. Both types of variables are discrete.<sup>1</sup>

If observations (migration energies) show no linear trend regarding  $x_i$ , i.e.  $\eta_i \neq \beta_0 + \beta_1 x_i$ , the discrete variables  $x_i \in \{0; 1; 2\}$  can be interpreted as categorical. Therefore, a dummy variable in binary form (zero/one) is defined for each category:

$$d_{i,1} = \begin{cases} 1, & \text{if } x_i = 0 \\ 0, & \text{else} \end{cases}, \quad d_{i,2} = \begin{cases} 1, & \text{if } x_i = 1 \\ 0, & \text{else} \end{cases}, \quad d_{i,3} = \begin{cases} 1, & \text{if } x_i = 2 \\ 0, & \text{else} \end{cases} \quad (7.4)$$

However, if a linear model with a constant value is applied (Eq. 7.5), the identifiability problem occurs.

$$\eta_i = \beta_0 + \beta_1 d_{i,1} + \beta_2 d_{i,2} + \beta_3 d_{i,3} \quad (7.5)$$

Any value can be added to  $\beta_0$  that was subtracted from  $\beta_1$ ,  $\beta_2$  and  $\beta_3$ . Possible solutions are the withdrawal of the constant value  $\beta_0$  or the withdrawal of one dummy variable. In this work, a dummy variable is omitted and integrated into the constant  $\beta_0$ .

## Interactions between Variables

A goal in this work is the identification of independent variables. In contrast, interactions between variables exist if the effect of a variable on the expected value depends on the value of another variable. A simple example is shown in the following.

$$\eta_i = \beta_0 + \beta_1 x_i + \beta_2 z_i + \beta_3 x_i z_i \quad (7.6)$$

---

<sup>1</sup>A continuous variable can take on any of the infinite number of values in a certain range, while a discrete variable can only take on a finite number of values.

## 7.2.2 Evaluation of Models

In case, several statistical models are available and data can be fitted to each model, a property that indicates the goodness of fit is required. Here, the coefficient of determination  $R^2$ , the adjusted  $\bar{R}^2$  and residual standard error  $\sigma_{\text{residual}}$  are introduced.

The variance of  $y$  can be divided into the variance of residuals, which is not explained by the model variation, and the variance of dependent variable, which is explained by the model variation.

$$\underbrace{\sum_{i=1}^n (y_i - \bar{y})^2}_{\substack{\text{n-variance of } y \\ \text{total sum of squares} \\ SS_{\text{tot}}}} = \underbrace{\sum_{i=1}^n (y_i - f_i)^2}_{\substack{\text{n-variance of residuals} \\ \text{residual sum of squares} \\ SS_{\text{res}}}} + \underbrace{\sum_{i=1}^n (f_i - \bar{y})^2}_{\substack{\text{n-variance of dependent variable} \\ \text{regression sum of squares} \\ SS_{\text{reg}}}} \quad (7.7)$$

where  $\bar{y}$  is the average value of  $y$  and  $f_i$  is the value according to the given model.

Then, the coefficient of determination  $R^2$  is defined as ratio of variances between estimated residuals and dependent variable according to<sup>[420]</sup>

$$R^2 = 1 - \frac{\text{Var}_{\text{res}}}{\text{Var}_{\text{tot}}} = 1 - \frac{SS_{\text{res}}/n}{SS_{\text{tot}}/n} = 1 - \frac{\sum_{i=1}^n (y_i - f_i)^2/n}{\sum_{i=1}^n (y_i - \bar{y})^2/n} \quad (7.8)$$

where  $\text{Var}_{\text{res}}$  is the sample variance of the estimated residuals and  $\text{Var}_{\text{tot}}$  is the sample variances of the dependent variable  $y$ . Here,  $n$  is the sample size. The coefficient of determination compares the fit of the regression with the data compared to the fit of the simple average.  $R^2$  automatically increases when additional variables are added to the model.

The adjusted  $R^2$  also includes the number of regressors in the linear model, which are the explanatory, i.e. assumable independent, variables.<sup>[421]</sup>

$$\bar{R}^2 = 1 - \frac{SS_{\text{res}}/df_e}{SS_{\text{tot}}/df_t} = 1 - \frac{\sum_{i=1}^n (y_i - f_i)^2/(n - p - 1)}{\sum_{i=1}^n (y_i - \bar{y})^2/(n - 1)} = \bar{R}^2 = 1 - \frac{\frac{\sum_{i=1}^n (y_i - f_i)^2}{n - p - 1}}{\frac{\sum_{i=1}^n (y_i - \bar{y})^2}{n - 1}} \quad (7.9)$$

with the degrees of freedom  $df_e = n - p - 1$  of the estimate of the underlying population error variance and  $df_t = n - 1$  of the estimate of the population variance of the dependent variable, where  $p$  is the total number of regressors in the linear model without counting the constant term and  $n$  is the sample size.<sup>[422]</sup>

While  $R^2$  can have values between 0 and 1,  $\bar{R}^2$  has a similar or smaller value and can even be negative. Accordingly, the coefficient of determination  $R^2$  is a measure of fit where a value of zero means no linear relationship while for  $R^2 = 1$  a perfect linear relationship exists. However, low values can still be ‘good’ if scattering is generally very high. On the other hand, high values can still be ‘bad’ if the residuals reveal a neglected functional relationship.  $\bar{R}^2$  can be used to compare the suitability of alternative sets of explanatory variables, even if the number of explanatory terms varies. This means, in contrast to  $R^2$ ,  $\bar{R}^2$  tells us if an additional variable leads to a better fit.

The residual standard error  $\sigma_{\text{residual}}$  is

$$\sigma_{\text{residual}} = \sqrt{\frac{1}{n-p} \sum_{i=1}^n (y_i - f_i)^2}. \quad (7.10)$$

Here, the residual sum of squares is compared with the total number of regressors and the sample size without comparing to the sample variances of the dependent variable. Therefore, the residual standard error is a least square variance estimator similar to a standard deviation that includes the number of regressors and shows the absolute scattering of the values.

The standard deviation according to the  $n-1$  method is commonly used to estimate the standard deviation for a sample and does not include the number of regressors in the linear model. It is typically referred to as corrected sample standard deviation

$$\sigma_s = \sqrt{\frac{1}{n-1} \sum_{i=1}^n (y_i - f_i)^2}. \quad (7.11)$$

Is, however, the full population known, the standard deviation is given according to

$$\sigma_n = \sqrt{\frac{1}{n} \sum_{i=1}^n (y_i - f_i)^2}. \quad (7.12)$$

### 7.2.3 Choice of Model and Parameters

In doped ceria, numerous arrangements of cerium ions, dopants, oxygen ions and oxygen vacancies are possible. The activation energies of oxygen migration in these numerous ionic configurations can be predicted by creating a model for the migration energy. In this regard, the lattice sites, whose occupation influences the migration energy, have to be identified and their influence has to be quantified.

#### a) Centers of Interaction

According to Coulomb's law, forces between charged particles depend on their distance. Therefore, lattice sites in a sphere around the migrating oxygen ion are tested for their influence on the migration energy. Since the migrating oxygen ion changes its position during a jump, the interaction sphere can be expanded around the oxygen ion in the initial state, the transition state and the final state. As defects are easier to track, interactions are labeled in accordance to the position of the migrating oxygen vacancy in the start (s), center (c) or destination position (d) as shown in Fig. 7.12.

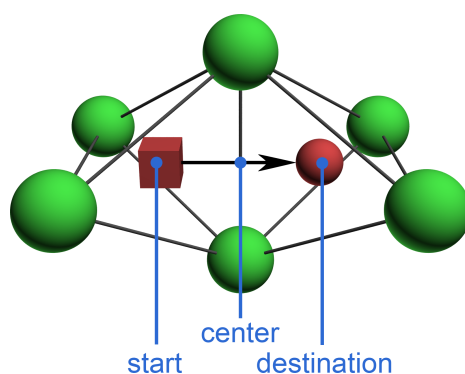


Figure 7.12: Centers of Interaction: start (s), center (c) and destination (d)

The energy of the initial and final state is obviously influenced by the distances of defects to the migrating oxygen vacancy as shown by the association energy in Chapter 5.1. Since the migration energy is calculated as the energy difference between transition and initial state, one might assume that spheres have to be expanded only around the start and center position (**sc**) as done in literature.<sup>[37,54,287]</sup> Other models in literature feature only interactions around the center position (**c**).<sup>[220,225]</sup>

However, the destination position may still be important: The ionic configuration of the whole lattice in equilibrium can be calculated using Metropolis Monte Carlo simulations, which are based on interactions around the start and destination position (cp. Chapter 4.2.2). According to theory, Kinetic Monte Carlo simulations have to lead to the same ionic configuration of the whole lattice in equilibrium. Although a **sc** model is sufficient to build an equivalent model, the resulting radius of the sphere around the center position has to be larger than the radius of the sphere around

the destination position. This highlights the benefit of the use of the destination position in the migration energy model.

In fact, migration energies are calculated in literature using only the interactions around the start and destination position (**sd**).<sup>[220,281]</sup> Other models feature interactions around all three positions (**scd**).<sup>[55,224,284–286]</sup> In this work, models are compared featuring all three centers of interactions.

## b) Grouping the Ions, Scaling their Influence

When all lattice sites, whose occupation influences the migration energy, have been identified, their influence has to be quantified.

On each lattice site of rare-earth (RE) doped ceria either a host ion (Ce, O) or a defect (RE, V) is positioned. For each additional lattice position, which is considered for the calculation, the number of jump configurations multiplies by 2 leading to a total number of  $2^n$  jump configurations for  $n$  influenced positions.

However, not every configuration is unique. For the 6-cation environment, the six nearest cation sites around a jump can be occupied by either a Ce ion or a Sm dopant. The resulting number of possible jump configurations is  $2^6 = 64$ , which can be reduced to 30 unique jump environments by using rotational symmetry around the jump axis.

First, the number of possible arrangements can be reduced  
if configurations are symmetrically equivalent  
and can be converted into each other.

Beyond that, several jump configurations (e.g. stereochemical configurations, see p. 139) are not equivalent but similar in both geometry and migration energy. Still, the reduction of the number of jump environments is limited. Including the next cation shell around start and destination position already leads to about  $10^6$  jump configurations after symmetry considerations, which cannot be calculated using DFT due to the vast computational demand.

If not every configuration should be calculated, it could be assumed that the influence of every lattice site is independent of all other lattice sites. Therefore, for every lattice site a change in migration energy could be quantified in case a dopant is present. This follows a pair interaction model. Lattice sites featuring the same change in migration energy could be grouped. As a result, the change in migration energy  $E_{\text{shell},i}$  changes linearly with increasing number of defects on lattices sites of the group  $N_{\text{shell}}^i$ :

$$E_{\text{shell},i} = N_{\text{shell}}^i \cdot E_{\text{shell}}^i \quad (7.13)$$

This is called *linear* scaling.

If all ions are fixed at the positions of the ideal lattice, Coulomb's law suggest that all lattice sites with the same distance to the migrating oxygen ion can be grouped with linear scaling. Only the distance to the start and destination position needs to be given to identify lattice sites of a group.

The resulting groups for the cation sublattice are shown in Fig. 7.13 using different colors. Figure 7.14 shows groups in both cation (green) and anion sublattice (red) as a function of distance to the migrating oxygen vacancy. Labels refer to the nearest neighborhood position before and after a jump (e.g.  $1_{NN} \rightarrow 2_{NN}$ ). The distance axis position refers to the initial (start and destination) and transition state (center) in an ideal lattice with experimental lattice parameter at room temperature.

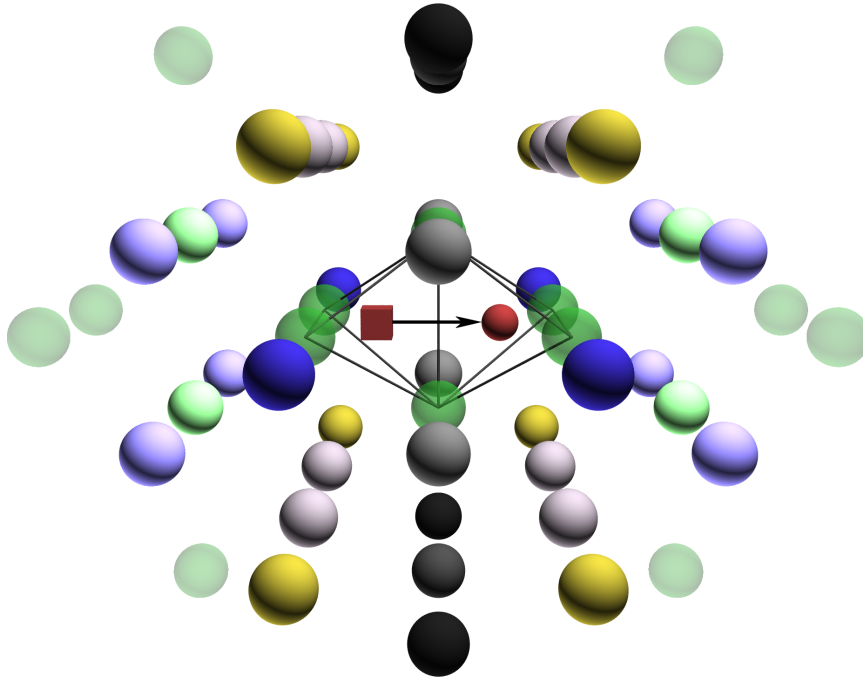


Figure 7.13: Cation sublattice around an oxygen ion jump. Oxygen ion (red sphere), oxygen vacancy (red box) and Cerium ions (all other spheres). Non-transparent ions with the same color possess the same distance to the migrating oxygen ion in either the initial or final state.

Alternatively to the nearest neighborhood nomenclature, shells are consecutively numbered for three spheres expanding around the initial and final position of the oxygen vacancy (start and destination position) and the jump center. For this purpose, only either cation or anion interaction are considered (cation or anion shell). If both sublattices are included, the total shell is given. Figure 7.14 shows that the 1<sup>st</sup> cation shell ( $1_{NN} \rightarrow 1_{NN}$  RE-V, 1<sup>st</sup> total shell) is centered at the jump center, while the 1<sup>st</sup> cation shell ( $1_{NN} \rightarrow 2,4_{NN}$  V-V, 3<sup>rd</sup> total shell) is centered at the start and destination position. It should be noted that all jump configurations according to the nearest neighborhood nomenclature appear at least twice, as they can be centered at the start and destination position as well as the jump center.<sup>1</sup>

<sup>1</sup>Jump configurations with different distances between the defect and the migrating oxygen vacancy in the initial and the final state appear three times in Fig. 7.14 as the shell around the start and destination position can be either left or reached during the jump. For the migration energy model in this work, both references are merged in the first appearance.

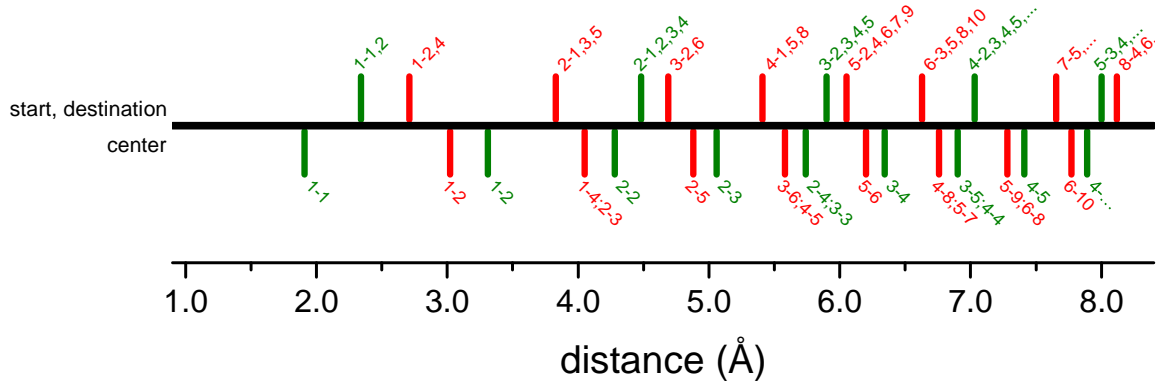


Figure 7.14: RE-V (green) and V-V interactions (red) that are considered, if spheres are expanded around the start, destination (up) or center position (down). All interactions are labeled according to their distance to the oxygen vacancy before and after the jump. For example, “1-1,2” refers to  $1_{\text{NN}} \rightarrow 1_{\text{NN}}$  and  $1_{\text{NN}} \rightarrow 2_{\text{NN}}$  jumps, while “1-4;2-3” refers to  $1_{\text{NN}} \rightarrow 4_{\text{NN}}$  and  $2_{\text{NN}} \rightarrow 3_{\text{NN}}$  jumps.

However, in reality, a displacement of ions takes place, which is called relaxation. Therefore, the influence of lattice sites can depend on other lattice sites. This is, for example, the case when multiple defects form a cluster, which influences the migration energy differently than the separate defects. Nevertheless, the migration energy can still be modeled if lattice sites can be grouped and the change in migration energy depends on the total number of defects in the group. The change is not proportional to the number of defects but for every number of defects a change in migration energy is defined, e.g. for a group with two lattice sites the migration energy contribution is

$$E_{\text{shell},i}^* = \begin{cases} E_{\text{shell},i}^0 & \text{for 0 defects} \\ E_{\text{shell},i}^1 & \text{for 1 defect} \\ E_{\text{shell},i}^2 & \text{for 2 defects} \end{cases} . \quad (7.14)$$

This is called *categorical* scaling.

Lattice positions can be possibly grouped if they have the same distance to the start, center or destination position.

### c) Calculating the Migration Energy based on Groups

If the influence of each group on the migration energy is known, these influences have to be added up to calculate the migration energy. The migration energy is then given by the migration energy in the pure material and the sum of the migration energy changes caused by the different groups.

For a better understanding, the migration energy changes can be classified as symmetric and asymmetric contributions (Fig. 7.15). *Symmetric* influences are characterized by changes in the migration energy, which are independent of the jump direction. Typically, configurations, which are geometrically symmetric around the jump center, feature symmetric influences.

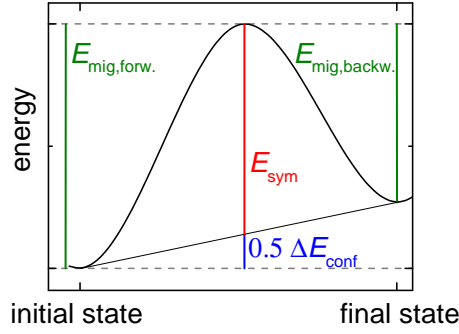


Figure 7.15: Migration energy model.

*Asymmetric* influences define the difference in migration energy between a forward and backward jump. The difference between forward and backward jump  $E_{\text{mig,forw.}} - E_{\text{mig,backw.}} = \Delta E_{\text{conf}}$  is given by the configurational energy difference between final and initial state, which can be modeled according to Eq. 4.15. Therefore, the difference of influences between start and destination position could be used according to

$$E_{\Delta\text{shell},i} = (N_{\text{shell,destination}}^i - N_{\text{shell,start}}^i) \cdot E_{\Delta\text{shell}}^i \quad (7.15)$$

where the energy parameter for linear scaling groups near the start and destination position have equal value with opposite sign. Here, a linear interpolation between the energies of the initial and final state is assumed, which is common in literature.<sup>[423,424]</sup> Alternatively, a polynomial function for a better emulation of the assumed Coulomb potential between defects or sinusoidal shaped migration barriers can be introduced.<sup>[373]</sup>

While geometrically symmetric configurations generally feature symmetric influences, geometrically asymmetric configurations can be influenced by both asymmetric and symmetric contributions.

The migration energy is then given by the sum of symmetric and asymmetric contributions. The interpretation of both contributions is straightforward: Positive symmetric contributions increase the migration energy for both forward and backward jump. While the equilibrium defect distribution is independent of these symmetric contributions, oxygen vacancies are kinetically hindered and therefore blocked (*Blocking*). Positive asymmetric contributions lead to large migration barrier for the forward jump but small migration barrier for the backward jump. The defect distribution is significantly influenced. Vacancies appear more often in nearest neighborhood to the defect because they are trapped (*Trapping*). Both effects are used to describe the experimental ionic conductivity as discussed in Chapter 2.5.1.

In this work, energy parameters are derived from a fit of a model to a large number of configurations to estimate the quality of the model. Subsequently, intuitive energy parameters are derived from as few jump configurations as possible. In this way, not only the quality of the model but also its capability of prediction is investigated.

Furthermore, correlations of asymmetric contributions with the configurational energy are investigated. Therefore, the question of termination (see Chapter 5.1.1) is again discussed.

### d) Interaction Radius

A model for the migration energy should predict the migration energies accurately with as few parameters as possible. Therefore, the interaction radius of the spheres around start and destination position as well as the sphere around the center position should be reduced to a minimum.

An increasing number of parameters in a regression leads to a better fit of the data. However, if this estimated function is used to predict new data, an improvement or a deterioration of adaptation is revealed. If the model is too complex, the prediction of new data is poor. In addition, small improvements of the fit can be *waived* if thereby substantial computational “costs” can be saved. Furthermore, a low number of parameters eases the understanding of the migration energy model.

The interaction radius determines which lattice sites are investigated for their occupation before and after a jump. Interactions are introduced successively according to Fig. 7.14. In case of a sphere around the start position with an interaction radius of 2.34 Å, four cation lattice sites ( $1_{NN}$  RE-V) are taken into consideration for the migration energy. Two of these cations have the same distance to the oxygen vacancy after the jump ( $1_{NN} \leftrightarrow 1_{NN}$ ), while the other two ( $1_{NN} \leftrightarrow 2_{NN}$ ) are on the next nearest neighbor cation position to the oxygen vacancy destination (4.48 Å,  $2_{NN}$  RE-V). If an interaction radius of 2.34 Å around the start position is used, both of these interactions are treated equally: For example, before the oxygen jump, a  $1_{NN}$  RE-V interaction might be detected. After the jump, no interactions are considered. Using an additional interaction sphere of 2.34 Å around the destination position detects the  $1_{NN} \leftrightarrow 1_{NN}$  cation position, while the  $1_{NN} \leftrightarrow 2_{NN}$  cation position cannot be distinguished from any other  $1_{NN} \leftrightarrow X_{NN}$  interaction. Since in the fluorite structure only these jump configurations starting from  $1_{NN}$  exist, all interactions are separated. In contrast, for an interaction radius of 4.48 Å around start and destination position,  $2_{NN} \leftrightarrow 3_{NN}$  and  $2_{NN} \leftrightarrow 4_{NN}$  RE-V jumps cannot be distinguished.

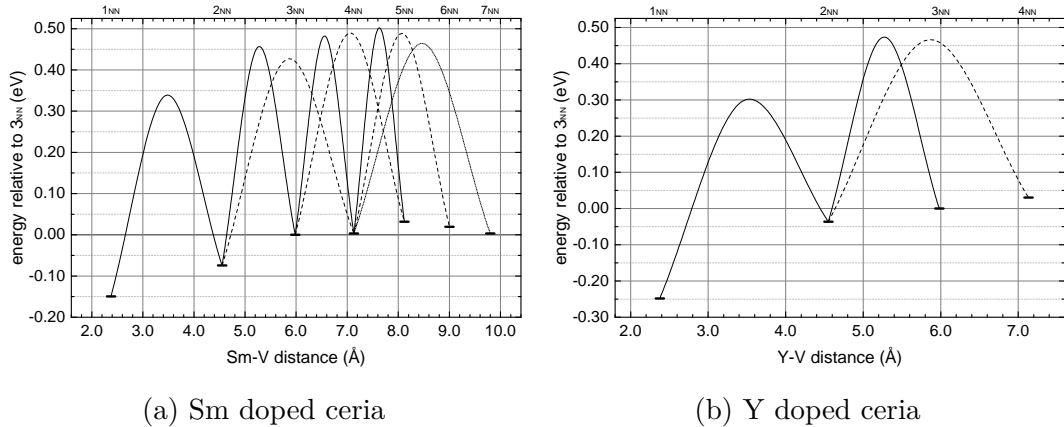


Figure 7.16: Migration energies in a  $3 \times 3 \times 3$  supercell with a dopant and a migrating oxygen vacancy.

The interaction radius should be chosen so that defects placed outside of the interaction range have a negligible influence on the migration energy. As a first approximation, the association energy

can be used (Chapter 4.2.1 and 5.1). Another argument is shown in Fig. 7.16, where the migration energies in a  $3 \times 3 \times 3$  supercell with a dopant and a migrating oxygen vacancy are shown. As the oxygen vacancy jumps away from the defect, the migration energy approaches the migration energy in pure ceria.

The above-described approach to model the migration energy is in literature often referred to as cluster expansion.<sup>[373,423–426]</sup> Similar to this work, groups are formed according to space group symmetry of the crystal (asymmetric contributions for the configurational energy) and the highest coherent point group that maps the cluster onto itself (local cluster expansion). Often, groups scale linearly and the possibility of categorical scaling is neglected. Parameters are called effective cluster interactions and are often determined by a fit of several ionic configurations with several defects. Therefore, the scaling is not systematically verified and insights into the significance of the parameters are limited.

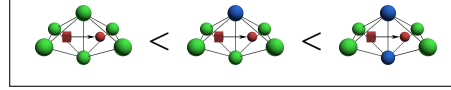
In the following, the scaling of various groups and possible models are investigated. At first, only the influence of rare-earth dopants on the migration energy is examined. Then, the influence of oxygen vacancies on the migrating oxygen ion is discussed. Finally, migration energies of supercells containing defects in both sublattices are presented in order to verify that influences of both sublattices can be calculated separately.

Migration energies were calculated in different supercell sizes. The migration energy depends strongly on the supercell size due to elastic effects and interaction of the migrating oxygen ion with itself as discussed above. Since not all jump configurations were calculated in different supercell sizes, all given migration energies belong to a  $3 \times 3 \times 3$  supercell, unless otherwise denoted.

## 7.2.4 Influence of Dopants on a Jump

### $1_{NN} \leftrightarrow 1_{NN}$ Scaling: Ce-Ce, Ce-RE or RE-RE Edge?

For three spheres expanding around the initial and final position of the oxygen vacancy (start and destination position) and the jump center, the first interaction in the



cation sublattice includes two dopants near the jump center. This 1<sup>st</sup> shell has a  $1_{NN} \leftrightarrow 1_{NN}$  interaction to both initial and final position of the oxygen vacancy and could, therefore, be grouped as  $1_{NN} \leftrightarrow 1_{NN}$  RE-V jump configuration centered at the jump center.

As mentioned before, doping the 1<sup>st</sup> shell leads to the three edge configurations. While the Ce-Ce edge has a migration edge energy of 0.482 eV for the  $3 \times 3 \times 3$  supercell, the migration energy increases to 0.649 eV (+0.17 eV/dopant) for the Ce-Sm edge and 1.049 eV for the Sm-Sm edge, which is an increase of 0.40 eV compared to the Ce-Sm edge (Fig. 7.17). For Y doped ceria, the increase is smaller with +0.07 for the first and +0.26 eV for the second dopant. The increase in migration energy per dopant is not constant. Therefore, all three edge configurations have to be calculated. The 1<sup>st</sup> shell group scales *categorical*.

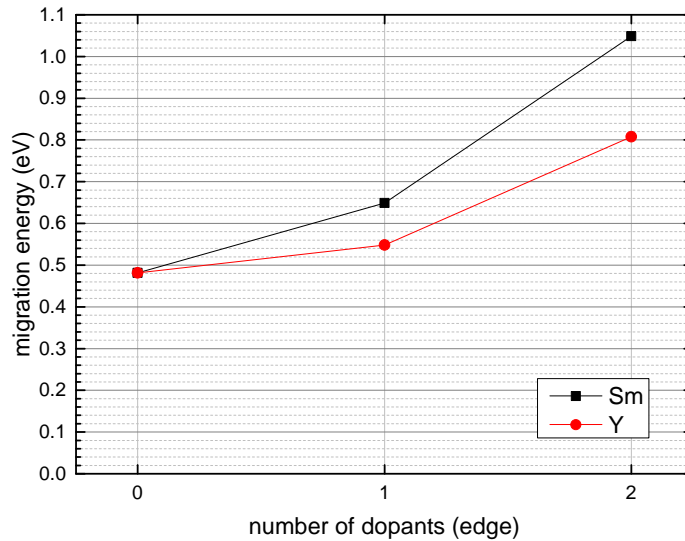


Figure 7.17: Migration energy for different number of dopants at the migration edge. Beside the migrating oxygen vacancy, no other defect is present. Sm and Y doped ceria in  $3 \times 3 \times 3$  supercell.

For different rare-earth dopants, the migration edge energies increase nearly linearly with increasing ionic radius of the dopant as already shown in Fig. 7.6.

For a valid grouping, all jump configurations containing one or two dopants at the migration edge (1<sup>st</sup> shell) have to increase with the same value independent of the occupation of the 2<sup>nd</sup> shell. Figure 7.18 shows the increase in migration energy is similar for all configurations of the 6-cation environment.

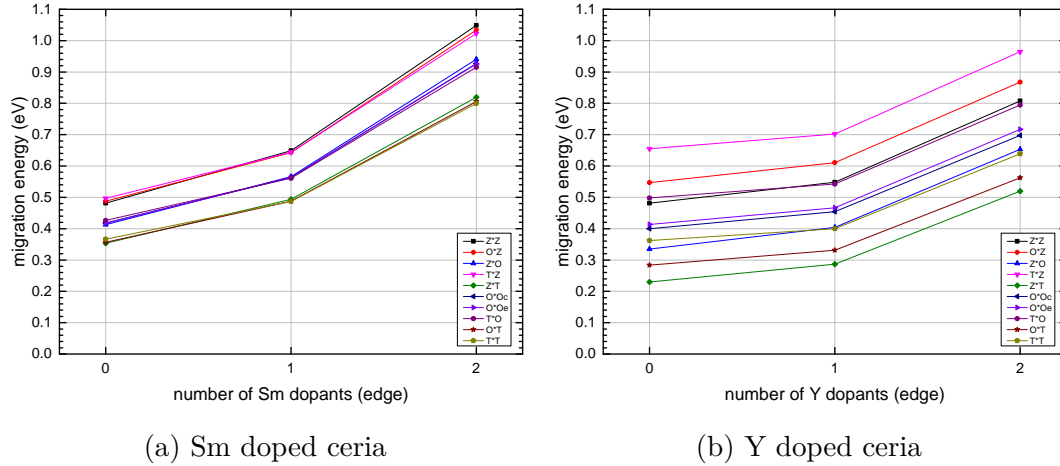


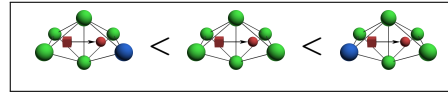
Figure 7.18: Migration energy for different numbers of dopants at the migration edge with varying dopants in the 2<sup>nd</sup> shell.  $3 \times 3 \times 3$  supercell.

For Sm doped ceria, the migration energy increases for 0 to 1 dopants by 0.14(1) eV and for 1 to 2 dopants by 0.36(3) eV. For Y doped ceria, the migration energy increases for 0 to 1 dopants by 0.05(1) eV and for 1 to 2 dopants by 0.25(1) eV. Therefore, the average increase in migration energy is small compared to the edge configurations for Sm doped ceria while the increase is comparable in Y doped ceria. Still, grouping the  $1_{NN} \leftrightarrow 1_{NN}$  RE-V jump configuration is a valid approach.

The migration energy increases categorically with increasing number of dopants at the migration edge.

### $1_{NN} \leftrightarrow 2_{NN}$ Scaling: Jumping to or from a Dopant?

For three spheres expanding around the start and destination position and the jump center, the second cation interaction shell includes four dopants near the start and four dopants near the destination position. Two dopants each have the same distance to the start and destination position and correspond to the 1<sup>st</sup> shell for the cation sublattice ( $1_{NN} \leftrightarrow 1_{NN}$ ).



The other two dopants near the start position could be grouped as  $1_{NN} \rightarrow 2_{NN}$ . The other two dopants near the destination position could be grouped as  $2_{NN} \rightarrow 1_{NN}$ . Contrary to the 1<sup>st</sup> shell, the 2<sup>nd</sup> shell is centered at the start and destination position. If jumps are labeled using shells instead of nearest neighbor interactions, jumps occur between the 2<sup>nd</sup>  $\leftrightarrow$  5<sup>th</sup> cation shell around start and destination position or the 2<sup>nd</sup>  $\leftrightarrow$  9<sup>th</sup> total shell if both sublattices are included.

Including interactions up to the 2<sup>nd</sup> shell already includes all  $1_{NN} \leftrightarrow 2_{NN}$  jump configurations since no other jumps starting from  $1_{NN}$  besides  $1_{NN} \leftrightarrow 1_{NN}$  are possible due to symmetry reasons.

In contrast to the edge configurations, the migration energy of the  $1_{NN} \leftrightarrow 2_{NN}$  jump configuration increases nearly linearly with increasing number of dopants at the start position and decreases

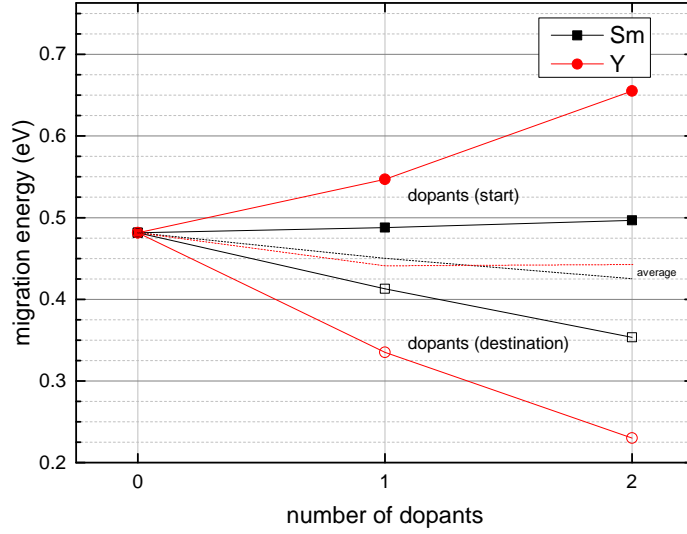


Figure 7.19: Migration energy for different numbers of dopants near the start ( $1_{NN} \leftrightarrow 2_{NN}$ ) or destination position ( $2_{NN} \leftrightarrow 1_{NN}$ ) of the migrating oxygen. No other defect is present. Sm and Y doped ceria in  $3 \times 3 \times 3$  supercell.

linearly with increasing number of dopants at the destination position (Fig. 7.19).

For Sm doped ceria, the migration energy increases by  $0.007(1)$  eV or decreases by  $-0.066(2)$  eV per dopant. For Y doped ceria, the migration energy increases by  $0.08(1)$  eV or decreases by  $-0.14(1)$  eV per dopant. Instead of considering the migration energy change per dopant at either start or destination position, the difference between both migration energy changes can be calculated. This energy difference of the change in migration energy is equivalent to the difference in migration energy between forward and backward jump per dopant. Generally, the difference in migration energy between forward and backward jump is equivalent to the difference in total energy of the initial and final state, which is, of course, the difference in  $2_{NN}$  and  $1_{NN}$  association energy. The difference between increase and decrease in migration energy is  $0.073(2)$  eV for Sm doped ceria and  $0.2122(3)$  eV for Y doped ceria. For Y doped ceria, this average association energy difference scatters less than the average increase or decrease in migration energy. For the  $3 \times 3 \times 3$  supercell and a single dopant, Fig. 5.1 gives  $\Delta E_{\text{conf}}$  with  $0.075$  eV for Sm doped ceria and  $0.2119$  eV for Y doped ceria. For the infinitely large supercell, the values are similar. The good agreement validates the use of a pair interaction model for the configurational energies. Because of the agreement between asymmetric contribution and association energy difference, for small dopants the migration energies are larger for  $1_{NN} \rightarrow 2_{NN}$  than  $2_{NN} \rightarrow 1_{NN}$ , similar for Nd doped ceria and smaller for  $1_{NN} \rightarrow 2_{NN}$  than  $2_{NN} \rightarrow 1_{NN}$  for La doped ceria.

Again, for a valid grouping, all jump configurations containing one or two dopants at  $1_{NN} \leftrightarrow 2_{NN}$  have to change with the same value. In the following, again different ionic configurations from the 6-cation environment are compared with varying occupation of other lattice sites.

Dopants at the start position (Fig. 7.20a and 7.20b) lead to both an in- and decrease in migration

## 7 Activation Energy

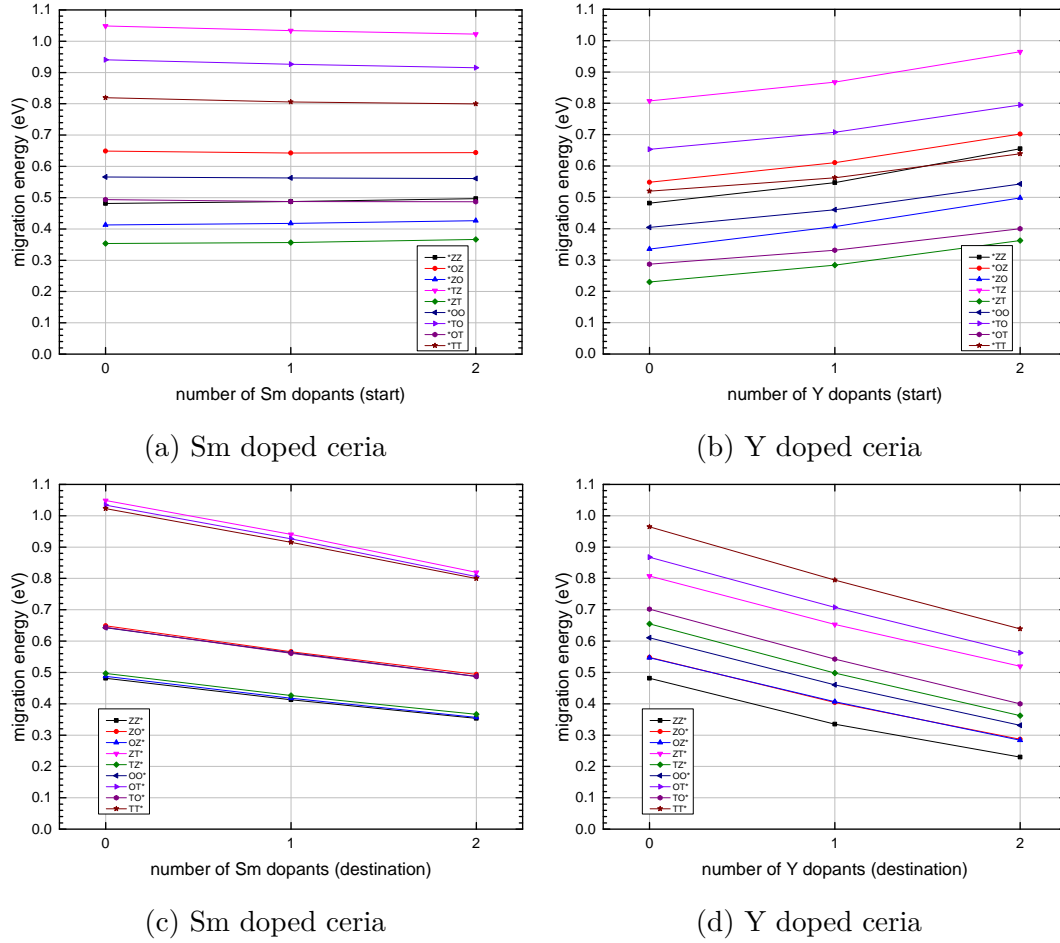


Figure 7.20: Migration energy for different numbers of dopants near the *start* (upper row,  $1_{NN} \leftrightarrow 2_{NN}$ ) and the *destination* position (lower row,  $2_{NN} \leftrightarrow 1_{NN}$ ) of the migrating oxygen. Other defects are present.  $3 \times 3 \times 3$  supercell.

energy for additional dopants in Sm doped ceria ( $-0.003(8)$  eV) and only increase in migration energy for Y doped ceria ( $0.07(2)$  eV). The reason for this different behavior is based on the symmetric influence of the  $2^{\text{nd}} \leftrightarrow 5^{\text{th}}$  cation shell ( $1_{NN} \leftrightarrow 2_{NN}$  RE-V), which is investigated further below. If this symmetric influence is considered, the migration energy increases linearly with increasing number of dopants at the start position for both Sm and Y doped ceria.

Dopants at the destination position (Fig. 7.20c and 7.20d) lead clearly to a decrease in migration energy for additional dopants in both Sm ( $-0.09(2)$  eV) and Y doped ceria ( $-0.14(2)$  eV). The contributions are larger for Y doped ceria due to the higher association between dopant and vacancies. For both Sm and Y doped ceria, the average change in migration energy is again small compared to the configurations containing only defects at  $1_{NN} \leftrightarrow 2_{NN}$ .

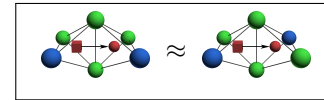
The migration energy increases linearly  
with increasing number of dopants at the start position and  
decreases linearly with increasing number of dopants  
at the destination position.

Therefore the  $1_{NN} \leftrightarrow 1_{NN}$  and  $1_{NN} \leftrightarrow 2_{NN}$  groups scale differently: The edge group scales categorical: All different numbers of dopants have to be calculated. The  $1_{NN} \leftrightarrow 2_{NN}$  group, on the other hand, scales linearly: Calculating a single dopant at the start and destination position reveals the change of migration energy for more dopants. For both groups, the influence of single dopants differs slightly from the average change in migration energy.

In literature, the  $1_{NN} \leftrightarrow 2_{NN}$  group is linked to trapping effects. In this work, both asymmetric and symmetric contributions were found. Therefore, the  $1_{NN} \leftrightarrow 2_{NN}$  group causes both trapping and blocking behavior. The latter is for Sm doped ceria negative.

### $1_{NN} \leftrightarrow 2_{NN}$ Stereochemistry

If dopants are grouped according to  $1_{NN} \leftrightarrow 2_{NN}$ , only the numbers of dopants at start and destination position are registered. If both at start and destination position one dopant is present, two geometri-



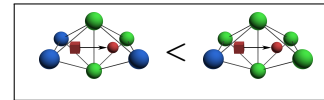
cally possible jump configurations still exist. For a valid grouping, both jump configurations should have the same migration energy.

In this work, configurations like this are called stereochemical. Here, the same number of dopants is present in different groups, but the configurations cannot be transformed into one another using symmetry operations. For the 6-cation environment, the stereochemical configurations are OZO, OOO and OTO.

The deviation in migration energy between stereochemical configurations is small, e.g. for Sm doped ceria 0.001 eV and for Y doped ceria 0.015 eV. Therefore, grouping according to  $1_{NN} \leftrightarrow 2_{NN}$  is possible since the deviations are negligible.

### $1_{NN} \leftrightarrow 2_{NN}$ : Asymmetric Dopant Configurations and their Symmetric Influence

The  $1_{NN} \leftrightarrow 2_{NN}$  jump can be interpreted as a jump between the  $2^{\text{nd}} \leftrightarrow 5^{\text{th}}$  cation shell around the start or the destination position (Fig. 7.21). Alternatively, all four cation sites also add up to the  $3^{\text{rd}}$  cation shell or  $5^{\text{th}}$  total shell, if both sublattices are included. The  $3^{\text{rd}}$  cation shell is centered at the jump center.



Therefore, the four cation sites can be considered both as an asymmetric and symmetric influence. In this work, (energetically) *asymmetric* influences are characterized by changes in the migration energy with a similar amount for dopants near the start and destination position but with a different sign. A configuration would be purely asymmetric if a dopant in  $1_{NN} \rightarrow 2_{NN}$  increases the migration

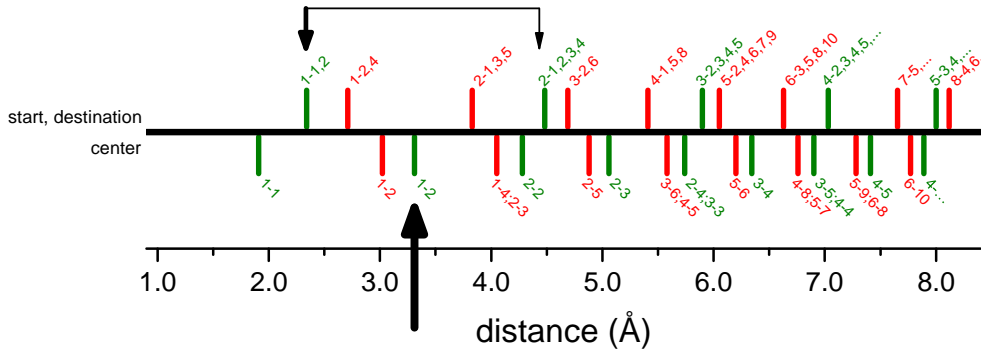


Figure 7.21: RE-V (green) and V-V interactions (red). The asymmetric and symmetric influence of the  $1_{\text{NN}} \leftrightarrow 2_{\text{NN}}$  jump is marked.

energy by 0.01 eV and a dopant in  $2_{\text{NN}} \rightarrow 1_{\text{NN}}$  decreases the migration energy by  $-0.01$  eV. *Symmetric* influences are characterized by changes in the migration energy, which are independent of the jump direction. Typically, configurations, which are geometrically symmetric around the jump center, feature also symmetric influences. For doped ceria, e.g. the  $1_{\text{NN}} \leftrightarrow 1_{\text{NN}}$  configuration is symmetric.

While geometrically symmetric configurations generally feature symmetric influences, geometrically asymmetric configurations can be influenced by both asymmetric and symmetric contributions. As discussed, the  $1_{\text{NN}} \leftrightarrow 2_{\text{NN}}$  configuration in doped ceria features both asymmetric and symmetric contributions. This can be seen in Fig. 7.19 by investigating the average migration energy of two jump configurations with a similar number of dopants at start and destination position, respectively. Purely asymmetric configurations should show a constant average. As this is not the case for Fig. 7.19, the average shows the symmetrical contributions. For Sm doped ceria, the average decreases linearly with  $-0.03$  eV per dopant. For Y doped ceria, the average is constant at  $-0.04$  eV for both one and two dopants.

The symmetric influence can be investigated by projecting the energy for an oxygen ion jump relative to the transition state (TS) as shown in Fig. 7.22.

Comparing the contributions from different edge configurations in of Fig. 7.22, the following becomes evident: For Sm doped ceria in a  $3 \times 3 \times 3$  supercell, the migration energy difference between the forward and backward jump is about  $-0.07$  eV for the Ce-Ce edge,  $-0.08$  eV for the Ce-Sm edge and between  $-0.09$  eV and  $-0.11$  eV for the Sm-Sm edge per dopant difference between start and destination. For Y doped ceria in a  $3 \times 3 \times 3$  supercell, the difference is about  $-0.21$  eV for the Ce-Ce and Ce-Y edge and between  $-0.21$  eV and  $-0.23$  eV for the Y-Y edge per dopant difference between start and destination. Thus, the difference between the forward and backward jump is smaller for Sm than for Y, caused by their different association energies, and the difference increases with more dopants at the migration edge, similar to the migration energy of the edge configurations itself.

Comparing the different configurations within one edge configuration, the following becomes evident: The connecting lines between initial and final state appear in a strict sequence at the

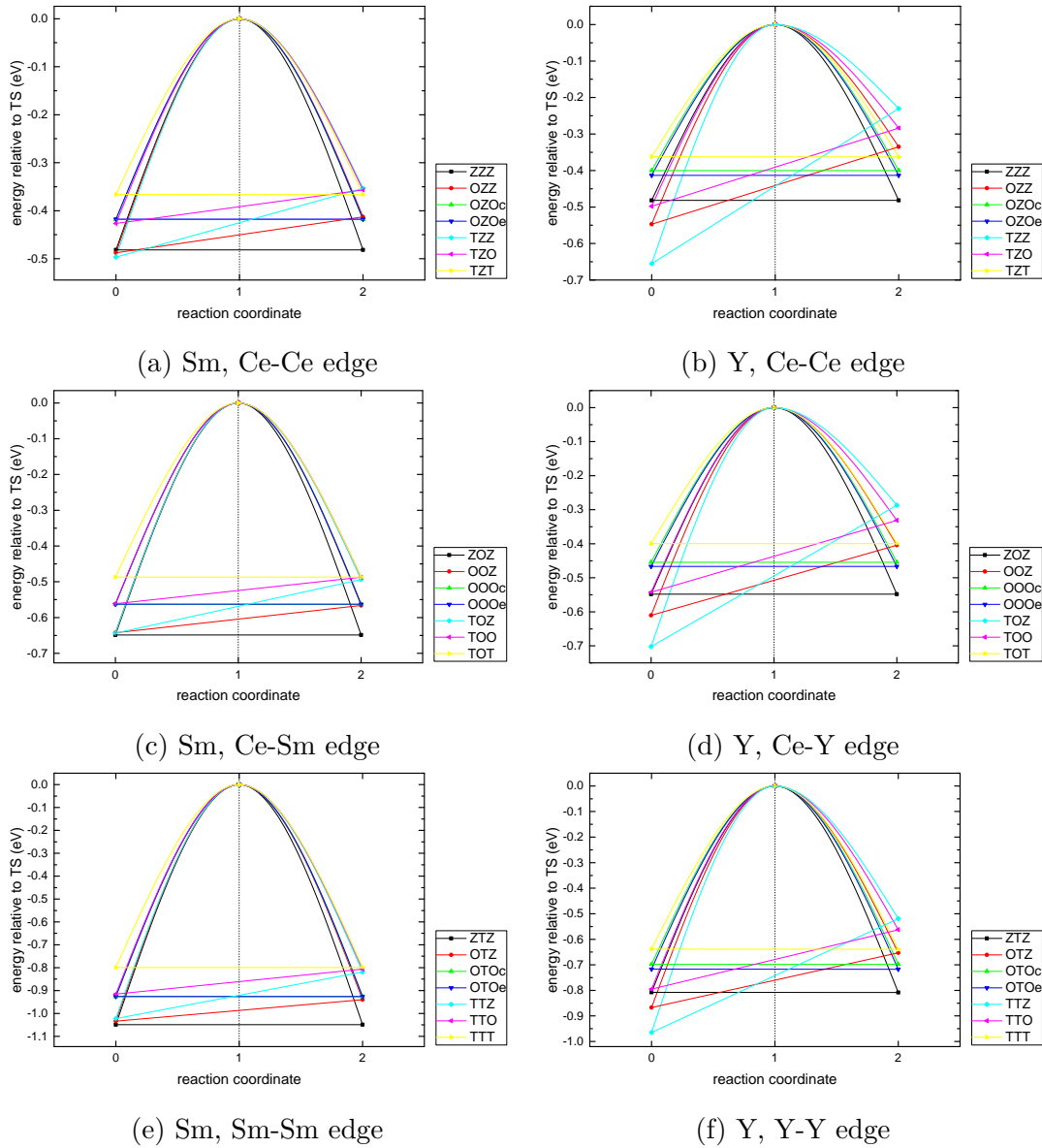
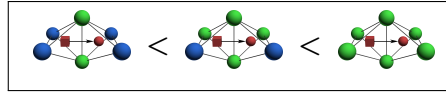


Figure 7.22: Initial and final state energy for an oxygen ion jump relative to the transition state energy. Sm (left) and Y doped ceria (right) in  $3 \times 3 \times 3$  supercell. If only the difference between dopants near start and destination of the oxygen vacancy is relevant, all lines connecting initial and final state should intersect at TS. Lines are a guide to the eye only.

transition state. Their value increases with the number of dopants at either start or destination. This means Z\*Z has the largest migration energies for forward and backward jump followed by O\*Z, the configurations T\*Z and O\*O which are often similar, T\*O and finally T\*T. The only exception is the Ce-Ce edge for Y doped ceria where OZZ and TZZ are similar. The same sequence can be found in the  $2 \times 2 \times 2$  supercell. Therefore, it is obvious:

The migration energy decreases with increasing number of dopants  
at both the start and destination position.

The decreases in migration energy can clearly be seen in Fig. 7.23, where similar migration configurations are grouped and shown with increasing numbers of dopants



near both start and destination position. Again, the influences increase with increasing number of dopants at the migration edge similar the edge energy itself. For Sm doped ceria, the migration energy decreases by  $-0.06 \text{ eV} \pm 0.005 \text{ eV}$  for the Ce-Ce edge, by  $-0.08 \text{ eV} \pm 0.004 \text{ eV}$  for the Ce-Sm edge and by  $-0.13 \text{ eV} \pm 0.01 \text{ eV}$  for the Sm-Sm edge. For Y doped ceria, the migration energy decreases by  $-0.05(1) \text{ eV}$  for the Ce-Ce edge, by  $-0.07(1) \text{ eV}$  for the Ce-Y edge and by  $-0.08(1) \text{ eV}$  for the Y-Y edge.

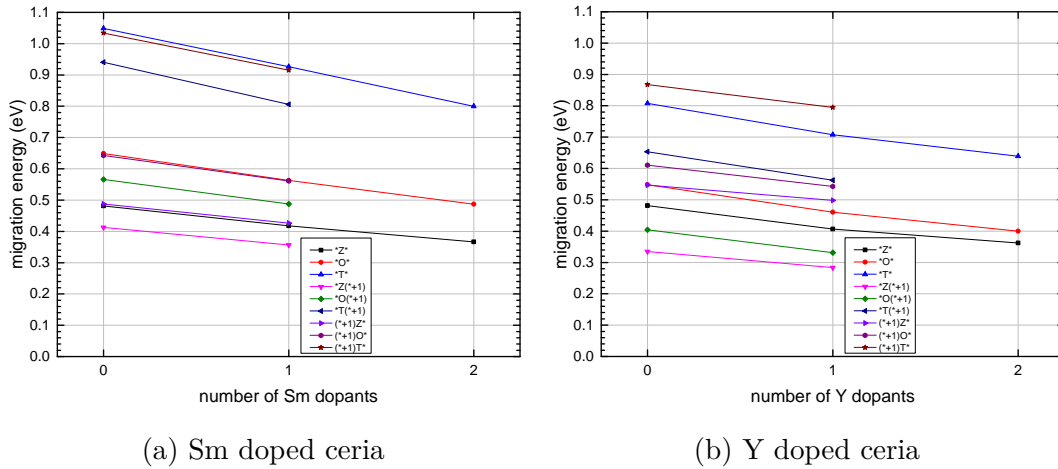


Figure 7.23: Migration energy for different numbers of dopants near *both* start and destination position ( $1_{NN} \leftrightarrow 2_{NN}$  and  $2_{NN} \leftrightarrow 1_{NN}$ ) of the migrating oxygen. Other defects are present.  $3 \times 3 \times 3$  supercell.

If the change in migration energy with increasing number of dopants scales linearly for start and destination position and their average, *asymmetric and symmetric influences scale linearly* as well. This is the case for the  $1_{NN} \leftrightarrow 2_{NN}$  configuration. The average decreases by  $-0.030(2) \text{ eV}$  for Sm and  $-0.03(1) \text{ eV}$  per dopant for Y doped ceria.

### $1_{\text{NN}} \leftrightarrow 1, 2_{\text{NN}}$ : Modeling & Determining Model Parameters using Fitting and an Educated Guess

As a next step, a model for the migration energy is constructed. Instead of using all 30 possible configurations for the 6-cation environment, a migration energy model should be calculated as a function of the number of dopants in the groups and add up their influences. For the 6-cation environment, the 1<sup>st</sup>, 2<sup>nd</sup>  $\leftrightarrow$  5<sup>th</sup> and 3<sup>rd</sup> cation shell were already introduced as possible groups and their scaling has been classified as categorically or linearly above. On this basis, three possible models are introduced in the following. Model and DFT migration energies are shown in Fig. 7.24. The left and right graph use identical models with different parameter values. While the left graph indicates the quality of the model, the right graph illustrates how well the model can predict migration energies using only a few calculations.

**Introducing the models** As a first try, the three possible migration edge configurations of the 1<sup>st</sup> shell and their categorical scaling can be used. The resulting model features 3 parameters:

$$E_{\text{mig}} = E_{\text{shell}, 1}^* = \begin{cases} E_{\text{shell}}^{1, \text{Ce-Ce}} & \text{for } N_{\text{shell}}^1 = 0 \\ E_{\text{shell}}^{1, \text{Ce-RE}} & \text{for } N_{\text{shell}}^1 = 1 \\ E_{\text{shell}}^{1, \text{RE-RE}} & \text{for } N_{\text{shell}}^1 = 2 \end{cases}$$

where  $E_{\text{shell}, 1}^*$  is the migration energy of the edge configuration, which is defined categorical for the number of dopants  $N_{\text{shell}}^i$  in the  $i^{\text{th}}$  total shell. A model that uses the 1<sup>st</sup> total shell, which is centered at the jump center, is called ‘‘c1’’. Fig. 7.24 shows that a variety of DFT migration energies is labeled with the Ce-Ce, Ce-Sm or Sm-Sm edge. A model that uses only the 1<sup>st</sup> total shell is therefore not a sufficient model.

The model can be improved by increasing the interaction radius. The next shell includes the jump configuration 2<sup>nd</sup>  $\leftrightarrow$  5<sup>th</sup> cation shell, which increases or decreases the migration energy linearly for dopants near the start or destination position. As both positions affect the migration energy, a model based on equal interaction radii for start and destination is used. There are two possibilities to include the 2<sup>nd</sup>  $\leftrightarrow$  5<sup>th</sup> cation shell.

On the one hand, the difference between the number of dopants on the 2<sup>nd</sup>  $\rightarrow$  5<sup>th</sup> and 5<sup>th</sup>  $\rightarrow$  2<sup>nd</sup> cation shell can be used. Here only asymmetric contributions for the 2<sup>nd</sup>  $\leftrightarrow$  5<sup>th</sup> cation shell are considered. The resulting model features 4 parameters.

$$E_{\text{mig}} = E_{\text{shell}, 1}^* + E_{\Delta\text{shell}, 2} = \begin{cases} E_{\text{shell}}^{1, \text{Ce-Ce}} & \text{for } N_{\text{shell}}^1 = 0 \\ E_{\text{shell}}^{1, \text{Ce-RE}} & \text{for } N_{\text{shell}}^1 = 1 \\ E_{\text{shell}}^{1, \text{RE-RE}} & \text{for } N_{\text{shell}}^1 = 2 \end{cases} + (N_{\text{shell}, \text{destination}}^2 - N_{\text{shell}, \text{start}}^2) \cdot E_{\Delta\text{shell}}^2$$

with the linear energy-contribution of the  $i^{\text{th}}$  total shell as difference between backward and forward contribution  $E_{\Delta\text{shell}, i}$  defined by the number of dopants  $N_{\text{shell}, j}^i$  in the  $i^{\text{th}}$  total shell near the  $j$ -

position (start or destination) and the energy parameter per dopant difference between destination and start position  $E_{\Delta\text{shell}}^i$ .<sup>1</sup> Energy contributions using the difference between the number of dopants between destination and start position are called “sd [ds]”. From Fig. 7.15 it is obvious that these asymmetric contributions are connected with half of the change in energy between initial and final state, which can be described as association energy difference. Figure 7.24 suggests an acceptable difference between model and DFT migration energies. Therewith, the migration energies for the 6-cation environment could be modeled using the 4 parameters model.

On the other hand, the number of dopants on the 2<sup>nd</sup>→5<sup>th</sup> cation shell and the 5<sup>th</sup>→2<sup>nd</sup> cation shell can be used separately with the linear energy-contributions  $E_{\text{shell}, 2(\text{start})}$  and  $E_{\text{shell}, 2(\text{destination})}$ . A mathematical equivalent description for this is the following: Not only the difference between the number of dopants on the 2<sup>nd</sup>→5<sup>th</sup> and 5<sup>th</sup>→2<sup>nd</sup> cation shell is considered (asymmetric contribution) but also the total number of dopants near start and destination position (symmetric contribution). The resulting model features 5 parameters.

$$E_{\text{mig}} = E_{\text{shell}, 1}^* + E_{\Delta\text{shell}, 2} + E_{\text{shell}, 5(\text{center})}$$

$$= \begin{cases} E_{\text{shell}}^{1, \text{Ce-Ce}} & \text{for } N_{\text{shell}}^1 = 0 \\ E_{\text{shell}}^{1, \text{Ce-RE}} & \text{for } N_{\text{shell}}^1 = 1 \\ E_{\text{shell}}^{1, \text{RE-RE}} & \text{for } N_{\text{shell}}^1 = 2 \end{cases} + (N_{\text{shell}, \text{destination}}^2 - N_{\text{shell}, \text{start}}^2) \cdot E_{\Delta\text{shell}}^2 + N_{\text{shell}}^5 \cdot E_{\text{shell}}^5$$

with the linear energy-contribution of the  $i^{\text{th}}$  total shell around the  $j$ -position  $E_{\text{shell}, i(j)}$  determined by the number of dopants  $N_{\text{shell}}^i$  in the  $i^{\text{th}}$  total shell and the energy parameter per dopant  $E_{\text{shell}}^i$ . Energy contributions using the number of dopants in the 5<sup>th</sup> total shell, which is centered at the jump center, are called “c5”. Energy contributions using the number of dopants near the destination position and near the start position separately are called “sd [s, d]”. Compared to the 4 parameters model, the differences between model and DFT migration energies are significantly reduced for the 5 parameters model (Fig. 7.24). For a large number of defects, the model predicts larger migration energies than found by the DFT calculations. Here, local relaxations of the lattice positions of the ions can decrease the activation barrier.

An overview of the models is shown in Table 7.7.

number of parameters	$E_{\text{mig}} =$
3	$E_{\text{shell}, 1}^*$
4	$E_{\text{shell}, 1}^* + E_{\Delta\text{shell}, 2}$
5 [ds]	$E_{\text{shell}, 1}^* + E_{\Delta\text{shell}, 2} + E_{\text{shell}, 5(\text{center})}$
5 [s, d]	$E_{\text{shell}, 1}^* + E_{\text{shell}, 2(\text{start})} + E_{\text{shell}, 2(\text{destination})}$

Table 7.7: Migration energy models for 6-cation environment including start and destination equally.

---

<sup>1</sup>Instead of a model based on linear interpolation of the site energies, sinusoidal shaped migration barriers can be introduced.<sup>[373]</sup>

While the number of parameters is useful to distinguish the different models here, in general the type of the model and its interaction radius is specified. The *type of the model* denominates the positions around which spheres are expanded for the model, i.e. start (s), center (c) and destination (d). If only specific spheres around the center are used, they can be denominated separately, e.g. c1 or c1+c5. For spheres around start and destination position, again [ds] refers to the difference between the number of dopants near the start and destination position while [s,d] uses the number of dopants separately. The *interaction radius* determines how large the expanded spheres are or whether specific spheres are activated. A comparison between the general nomenclature and the number of parameters is shown in Table 7.8.

RE-V interaction radius	c1+sd [ds]	scd [ds]	scd [s,d]	c1+sd [s,d]
1.91 Å	3	3	3	3
2.34 Å	4	4	5 [s,d]	5 [s,d]
3.31 Å	4	5 [ds]		5 [s,d]

Table 7.8: Number of parameters of migration energy models for 6-cation environment.

Table 7.8 illustrates that all models are similar for a  $1_{\text{NN}}$  RE-V interaction radius of 1.91 Å. The c1+sd [ds] and scd [ds] model differ at a  $3_{\text{NN}}$  RE-V interaction radius of 3.31 Å since the c5 interaction is not included in both models. The scd [s,d] model could have 6 parameters at a  $3_{\text{NN}}$  RE-V interaction radius. However, the additional parameter is not defined because of singularities (see Chapter 7.2.1). The number of parameters increases differently in the models, especially [s,d] models gain parameters more quickly than [ds] models.

**Validating the models** The models may be applied if they reflect the behavior of the DFT energies. The models can be fitted to the DFT energies in order to achieve the lowest possible differences between model and DFT migration energies. This reveals the quality of the models.

The fits are shown in Fig. 7.24 (left). The results of the fit are evaluated using the adjusted  $\bar{R}^2$  and residual standard error  $\sigma_{\text{residual}}$  according to Chapter 7.2.2. For the 6-cation environment, both are shown in Fig. 7.25.

For 30 parameters, the migration energy of every configuration is specified in the model leading to a perfect fit between model and DFT calculations, which is shown in Fig. 7.24 (left) by a line that bisects the x- and y-axis. However, a reduced number of parameters is desirable.

The 4-parameters model shows a good regression result. The residual standard error and  $\sigma_n$  is below 0.06 (see Fig. 7.25); model and DFT migration energies are similar. Including the 3<sup>rd</sup> cation shell (5 parameters model) leads to an even better fit, the residual standard error and  $\sigma_n$  is below 0.02 and  $\bar{R}^2$  improves significantly.

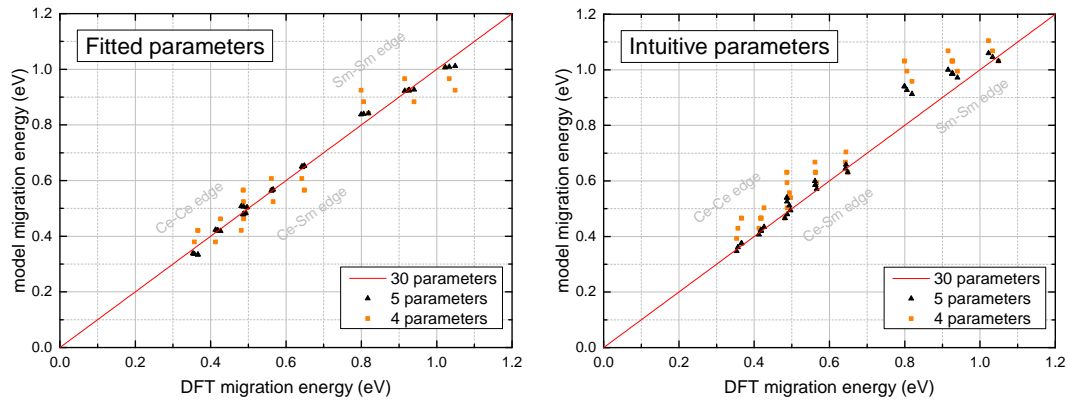


Figure 7.24: Model (see Table 7.7) and DFT migration energies for 6-cation environment with fitted (left) and intuitive parameters (right). The left and right graph use identical models with different parameter values. While the left graph indicates the quality of the model, the right graph illustrates how well the model can predict migration energies using only a few calculations. Intuitive parameters for the infinite supercell. DFT energies for Sm doped ceria in  $3 \times 3 \times 3$  supercell.

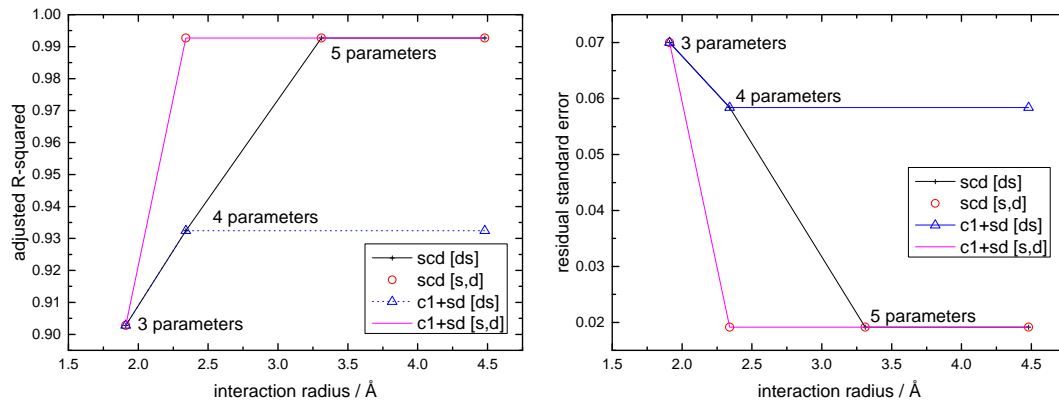


Figure 7.25:  $\bar{R}^2$  and standard derivation for different models in 6-cation environment. Sm doped ceria in  $3 \times 3 \times 3$  supercell.

**Determining model parameters** To gain deeper insight into the migration energy, a 4 or 5 parameters model can be fitted to the 30 DFT migration energies. As a result, influences on the migration energy are revealed and can be further studied by varying few parameters. However, for a larger number of possible configurations, not every configuration can be calculated. Therefore, it is desirable to determine parameter using only a few calculations. An educated guess allows the use of intuitive parameters, which identify the influences on the migration energy.

It is assumed that isolated defects from configurations with only a few dopants in the infinitely large supercell can be used to predict the parameters of the models. According to the investigations of possible groups above, this approach is valid: For dopants in the  $1_{\text{NN}} \leftrightarrow 1_{\text{NN}}$  group, the general increase in the 6-cation environment was 0.14 and 0.36 eV for 0 to 1 and 1 to 2 dopants, which

is similar to the increase in the infinitely large supercell with 0.164 and 0.401 eV as shown in Fig. 7.6. For dopants in the  $1_{\text{NN}} \leftrightarrow 2_{\text{NN}}$  group, the general difference between in- and decrease in the 6-cation environment was 0.073 eV, which is equal to the difference of the  $1_{\text{NN}}$  and  $2_{\text{NN}}$  RE-V association energy in the infinitely large supercell as shown in Fig. 5.1. Therewith, the following intuitive parameters are chosen.

$$E_{\text{shell}}^{1, \text{Ce-Ce}} = E_{\text{mig}}(\text{ZZZ}), \quad E_{\text{shell}}^{1, \text{Ce-RE}} = E_{\text{mig}}(\text{ZOZ}), \quad E_{\text{shell}}^{1, \text{RE-RE}} = E_{\text{mig}}(\text{ZTZ}),$$

$$E_{\Delta\text{shell}}^2 = \frac{E_{\text{mig}}(\text{OZZ}) - E_{\text{mig}}(\text{ZZO})}{2} \text{ and}$$

$$E_{\text{shell}}^5 = E_{\text{mig}}(\text{OZZ}) - \frac{E_{\text{mig}}(\text{ZZO}) - E_{\text{mig}}(\text{OZZ})}{2} - E_{\text{mig}}(\text{ZZZ}).$$

For  $E_{\text{shell}, 1}^*$  intuitive parameters are shown in Fig. 7.6. It may be noted that for asymmetric contributions  $E_{\Delta\text{shell}}^i$  directly half the association energy difference is used (Fig. 5.1 and 5.5) as shown in Fig. 7.15. The resulting migration energies are shown in Fig. 7.24 (right). The models use intuitive parameters from the infinitely large supercell ( $\sigma_{\text{n}} = 0.061$  and  $0.041$  for 4 and 5 parameters model, respectively) though values are compared with the DFT energies for Sm doped ceria in a  $3 \times 3 \times 3$  supercell. Intuitive parameters from the infinitely large supercell are used as it is assumed that isolated defects are best for a multiple linear scaling of the migration energy. The DFT energies in a  $3 \times 3 \times 3$  supercell are used, as experimental defect concentrations are high. The  $3 \times 3 \times 3$  supercell provides the best balance between reasonable concentrations and a limited amount of interactions of the defects and their copies due to periodic boundary conditions. For comparison, Fig. 9.8 in the appendix shows the model using intuitive parameters from the  $3 \times 3 \times 3$  supercell ( $\sigma_{\text{n}} = 0.062$  and  $0.036$  for 4 and 5 parameters model, respectively).

The prediction for both the 4 and 5 parameters model are acceptable. Therefore, the intuitive parameters from about 4–5 calculations can be successfully used to estimate the fitted parameters.

Using the existing 3 and 4 parameters model with intuitive parameters for the infinitely large supercell, the ionic conductivity for Sm doped ceria can already be simulated (see Chapter 7.3).

**Y doped ceria** For Y doped ceria, the results are similar (Fig. 7.26). The quality of the models is high as the adjusted  $\bar{R}^2$  and standard derivation show a good regression (Fig. 7.27). The residual standard error and  $\sigma_{\text{n}}$  is below 0.05 and 0.02 for 4 and 5 parameters model, respectively.<sup>1</sup> Both values are lower than the residual standard errors for Sm doped ceria. Therefore, the quality of the models for the migration energy is better for Y than Sm doped ceria.

For intuitive parameters from the infinitely large supercell, the  $\sigma_{\text{n}}$  is 0.047 and 0.020 for 4 and 5 parameters model, respectively. For intuitive parameters from the  $3 \times 3 \times 3$  supercell, the residual standard error is  $\sigma_{\text{n}} = 0.046$  and  $0.018$  for 4 and 5 parameters model, respectively. Again, all

<sup>1</sup> $\sigma_{\text{n}} = 0.045$  and  $0.014$  for 4 and 5 parameters model, respectively.

## 7 Activation Energy

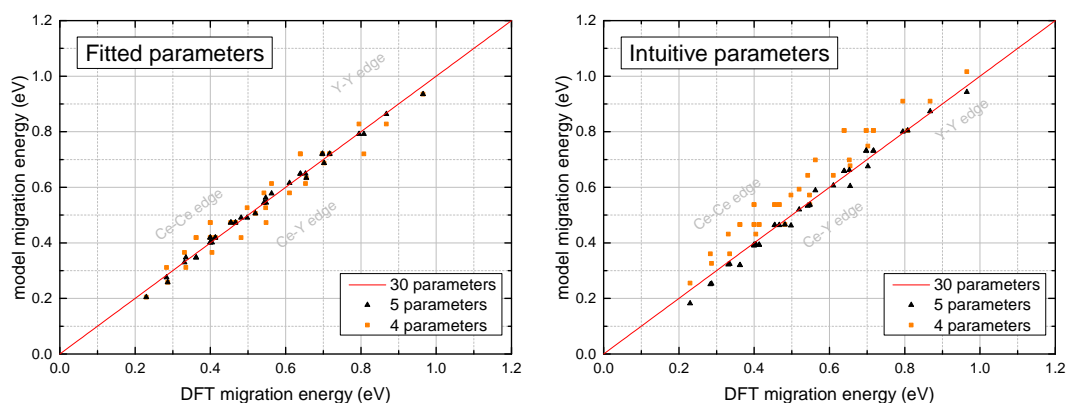


Figure 7.26: Model (see Table 7.7) and DFT migration energies for 6-cation environment with fitted (left) and intuitive parameters (right). Intuitive parameters for the infinite supercell. DFT energies for Y doped ceria in  $3 \times 3 \times 3$  supercell.

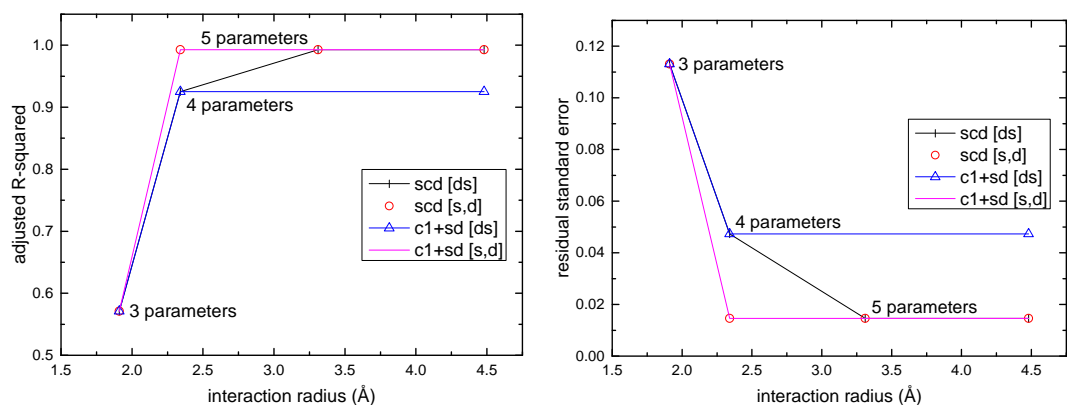


Figure 7.27:  $\bar{R}^2$  and standard derivation for different models in 6-cation environment. Y doped ceria in  $3 \times 3 \times 3$  supercell.

residual standard error for the intuitive parameter are low compared to Sm doped ceria. Therefore, the prediction of migration energies is better for Y than Sm doped ceria.

This is surprising, as the standard derivation for the linearly scaling in Y doped ceria was high compared to Sm doped ceria. The quality of the linear scaling is therefore only partly responsible for the quality of the models. The summation of additive influences for complex ionic configurations with several defects leads obviously to better results for Y doped ceria for the 6-cation environment.

### $1_{NN} \leftrightarrow 1,2_{NN}$ : The Models for Different Supercell Sizes

Up to now, it has been assumed that isolated defects from the infinitely large supercell are best to predict the parameters of the models. However, in the last section lower values for  $\sigma_n$  could be achieved by using intuitive parameters from the  $3 \times 3 \times 3$  supercell. Therefore, the question arises which supercell size should be used.

**Intuitive parameters from infinitely large supercells** Following the latter argument, intuitive parameters would be chosen best from their own supercell size. Figure 7.28 shows DFT and model migration energies. Points are labeled with both the supercell size for DFT calculations and the supercell size, which the intuitive parameters are chosen from.

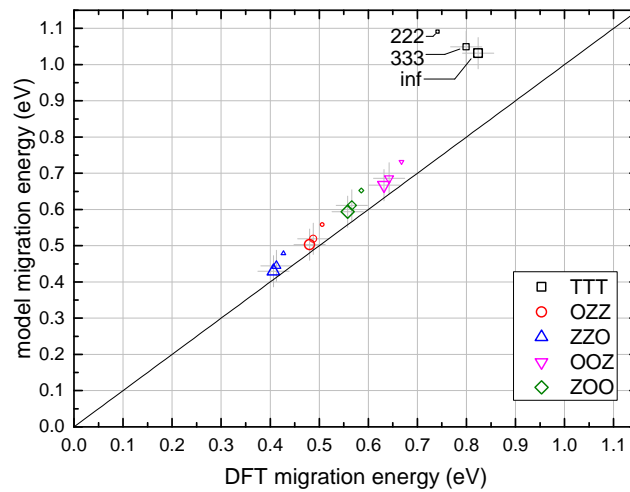


Figure 7.28: 4 parameters model ( $c1+sd$  [ds] up to  $2_{NN}$  RE-V) for 6-cation environment. DFT migration energies in Sm doped ceria for the infinite large,  $3 \times 3 \times 3$  and  $2 \times 2 \times 2$  supercell as well as intuitive parameters chosen from the corresponding supercell size as described in the last section.

The goodness of fit is quite different here for different supercell sizes. With increasing supercell size  $\sigma_n$  decreases from 0.116 to 0.085 and 0.072. More importantly, for infinitely large supercells the best intuitive parameters are chosen from the infinitely large supercell. Using intuitive parameters from the  $3 \times 3 \times 3$  supercell, e.g. by horizontal displacement of the points labeled with  $3 \times 3 \times 3$ , would lead to larger differences between model and DFT migration energies.

A migration energy model is desired that is best suited for the infinitely large supercell. In a real solid, no interactions of defects and their copies due to periodic boundary conditions take place, which is best represented by the DFT calculation from the infinitely large supercell.

Therefore, it is valid to choose intuitive parameters from the infinitely large supercell. If in the last section the difference between DFT migration energies from the infinitely large supercell and model migration energies with intuitive parameters from the infinitely large supercell had been compared, all  $\sigma_n$  values would have been lower. DFT migration energies from the  $3 \times 3 \times 3$  supercell are used

so that a large number of ionic configurations even at experimental defect concentrations can be compared.

**Models most valid for infinitely large supercells** This investigation also suggests that DFT migration energies from the infinitely large supercell can be better fitted to the proposed models. Indeed, while the adjusted  $\bar{R}^2$  for the fit of  $3 \times 3 \times 3$  supercell calculations is 0.9028, 0.9324 and 0.9927 for the 3, 4 and 5 parameters model, respectively, it is 0.9233, 0.9543 and 0.9941 for DFT migration energies from the infinitely large supercell.

Especially the symmetric contribution for the 3<sup>rd</sup> cation shell increases for the  $2 \times 2 \times 2$  supercell, obviously caused by the interactions due to the periodic boundary conditions. By implication, the symmetric contribution for the 3<sup>rd</sup> cation shell is low for the infinitely large supercell. For the fit of the 5 parameters model to the infinitely large supercell,  $E_{\text{shell}}^5$  is  $-0.036$  eV for Sm and  $-0.029$  eV for Y doped ceria. This also validates the use of the 4 parameters model.

**Nd, Sc, Gd and La doped ceria** In the  $2 \times 2 \times 2$  supercell, also Nd and Sc doped ceria<sup>1</sup> have been investigated in an earlier work<sup>[1]</sup> and migration energies for Gd and La doped ceria were calculated by Rachid Touzani. The residual standard error for the models fitted to the  $2 \times 2 \times 2$  DFT calculations indicated a quality for the models for Nd and Gd doped ceria similar to Sm doped ceria. La doped ceria can only be described well using the 5 parameters model. The change in sign for  $E_{\Delta\text{shell}}^2$ , which was already anticipated in Chapter 5.1.1, is obviously not the only change in behavior for La doped ceria due to its large ionic radius. For Sc doped ceria, the residual standard error is above 0.12 for all models. As the solubility of Sc doped ceria is low, this deviation is expected.

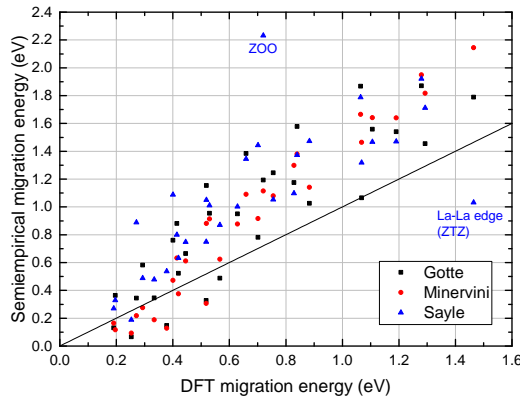


Figure 7.29: Semiempirical<sup>[282,283]</sup> and DFT migration energies in La doped ceria for the  $4 \times 4 \times 4$  and  $2 \times 2 \times 2$  supercell, respectively. The three selected interatomic potentials are labeled.<sup>[232,386,427]</sup>

<sup>1</sup>For Sc doped ceria, the NEB method with three intermediary images has been used. Not all configurations in the 6-cation environment could be calculated successfully.

**Comparison to semiempirical migration energies** For La doped ceria, Oaks *et al.*<sup>[282,283]</sup> have calculated all possible migration configurations in the 6-cation environment using semiempirical calculations with three selected interatomic potentials.<sup>[232,386,427]</sup> The migration energies strongly depend on the interatomic potentials. Correspondingly, the correlation between DFT and semiempirical migration energies is quite bad (Fig. 7.29). Especially, the jump configurations ZOO and ZTZ (La-La edge) deviate significantly from general trend between semiempirical and DFT migration energies.

An interesting historical side note is the comparison of the here calculated DFT migration energies with the semiempirical migration energies from Murray,<sup>[41]</sup> which are the first migration energies calculated for every possible configuration in the 6-cation environment. The results are compared for Y doped ceria in  $2 \times 2 \times 2$  supercell in Fig. 7.30 (left).

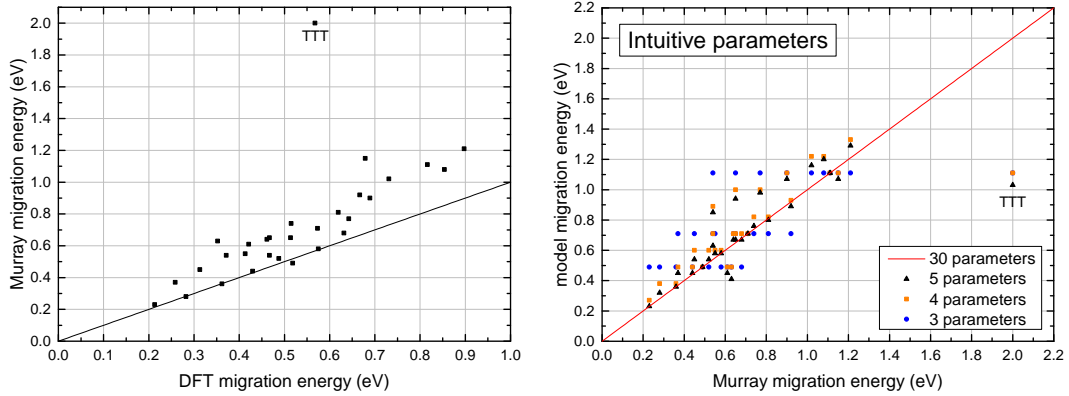
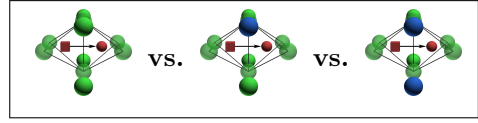


Figure 7.30: Migration energies according to Murray,<sup>[41]</sup> DFT and model migration energies. The models are based on intuitive parameters from the Murray migration energies in the 6-cation environment. Y doped ceria in  $2 \times 2 \times 2$  supercell.

The correlation between DFT and semiempirical migration energies is good. Murray overestimated the migration energies for most configurations. Especially, the jump configuration TTT deviates significantly from general trend between semiempirical and DFT migration energies. Figure 7.30 (right) indicates where the proposed models can also predict the semiempirical migration energies from Murray using intuitive parameters from the semiempirical calculations. If the TTT configuration is excluded,  $\sigma_n$  is 0.189, 0.112 and 0.110 for the 3, 4 and 5 parameters models, respectively. These values are significantly higher than for the DFT calculations in the  $2 \times 2 \times 2$  supercell with intuitive parameters from the same supercell. Here are the values for all configurations,  $\sigma_n = 0.129$ , 0.060 and 0.019 for the 3, 4 and 5 parameters models, respectively. As the correlation between both calculations is good, this difference in model quality can be interpreted as a sign for the high quality of the DFT calculations.

$2_{NN} \leftrightarrow 2_{NN}$

For three spheres expanding around the initial and final position of the oxygen vacancy (start and destination position) and the jump center, the fourth cation interaction shell includes again two dopants near the jump center.



This 4<sup>th</sup> shell for the cation sublattice (8<sup>th</sup> total shell) has a  $2_{NN}$  interaction to both initial and final position of the oxygen vacancy and could, therefore, be grouped as  $2_{NN} \leftrightarrow 2_{NN}$  RE-V jump configuration centered at the jump center.

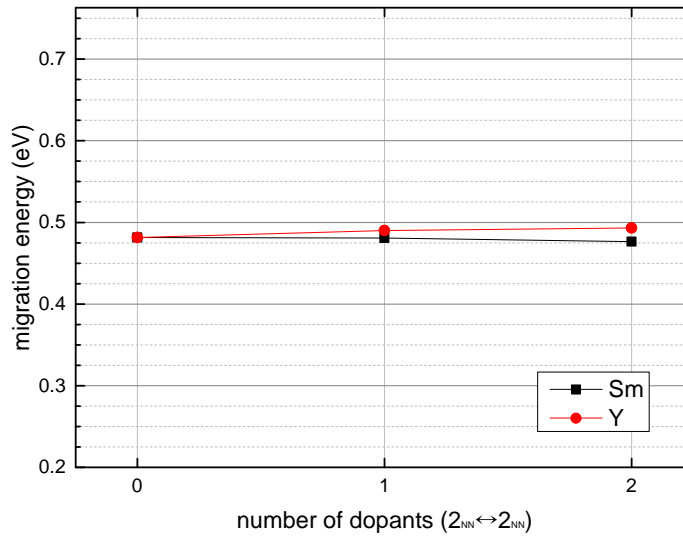


Figure 7.31: Migration energy for different numbers of dopants at the next nearest edge position ( $2_{NN} \leftrightarrow 2_{NN}$ ). Beside the migrating oxygen vacancy, no other defect is present. Sm and Y doped ceria in  $3 \times 3 \times 3$  supercell.

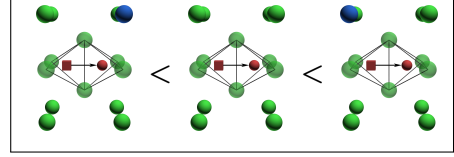
The influence of dopants on the  $2_{NN} \leftrightarrow 2_{NN}$  position is small (Fig. 7.31). For Sm doped ceria, the migration energy decreases slightly with increasing number of dopants. While in pure ceria the barrier height is 0.482 eV, for one Sm dopant a similar (0.481 eV) and for two Sm dopants a lower migration energy (0.476 eV) is found. For Y doped ceria, an increase in migration energy for one (0.490 eV) and two dopants (0.493 eV) can be found. Therefore, doping the  $2_{NN} \leftrightarrow 2_{NN}$  position decreases or increases the migration energy with 0.01 eV for two Sm dopant or Y dopants, respectively. The scaling is categorical. However, the influence on the migration energy is small and can be neglected.

$2_{NN} \leftrightarrow 3,4_{NN}$

For three spheres expanding around the start and destination position and the jump center, the fifth cation interaction shell includes six dopants near the start and six dopants near the destination position. During an oxygen ion jump, four cations each can be grouped as  $2_{NN} \leftrightarrow 3_{NN}$ , while two

dopants each can be grouped as  $2_{\text{NN}} \leftrightarrow 4_{\text{NN}}$ . For the cation sublattice, these are jumps between the  $5^{\text{th}} \leftrightarrow 8, 11^{\text{th}}$  cation shell and for the both sublattices between the  $9^{\text{th}} \leftrightarrow 16, 23^{\text{th}}$  total shell. In Fig. 7.32, the migration energy is again shown as a function of the number of dopants.

**$2_{\text{NN}} \leftrightarrow 3_{\text{NN}}$**  For  $2_{\text{NN}} \leftrightarrow 3_{\text{NN}}$  RE-V jumps in Sm doped ceria, the migration energy increases by 0.0489(1) eV per dopant at the start position or decreases by  $-0.0252(2)$  eV per dopant at the destination position. For Y doped ceria, the migration energy increases by 0.02792(4) eV or decreases



by  $-0.0082(2)$  eV per dopant. The difference between decrease and increase by 0.0741(3) eV for Sm doped ceria and 0.0362(2) eV for Y doped ceria is of course again the difference in  $3_{\text{NN}}$  and  $2_{\text{NN}}$  association energy. The average increases by 0.01 eV per dopant each for Sm and Y doped ceria. The scaling for asymmetric and symmetric contribution is linear.

The influence of the  $2_{\text{NN}} \leftrightarrow 3_{\text{NN}}$  position for Sm doped ceria is very large. The asymmetric influence is similar to the  $1_{\text{NN}} \leftrightarrow 2_{\text{NN}}$  configuration as shown by the difference between decrease and increase in migration energy per dopant. The symmetric influence is smaller as shown by the average. For Y doped ceria, the symmetric influences are equivalent to Sm doped ceria while the asymmetric influence is much smaller than in the  $1_{\text{NN}} \leftrightarrow 2_{\text{NN}}$ . It may be noted that Sm/Y dopants in  $1_{\text{NN}} \leftrightarrow 2_{\text{NN}}$  position in average decrease the migration energy while Sm/Y dopants in  $2_{\text{NN}} \leftrightarrow 3_{\text{NN}}$  position increase the migration energy.

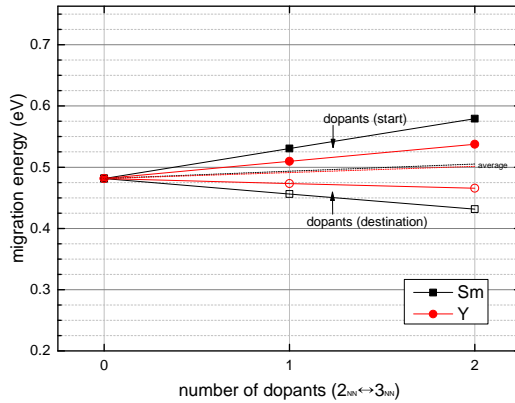
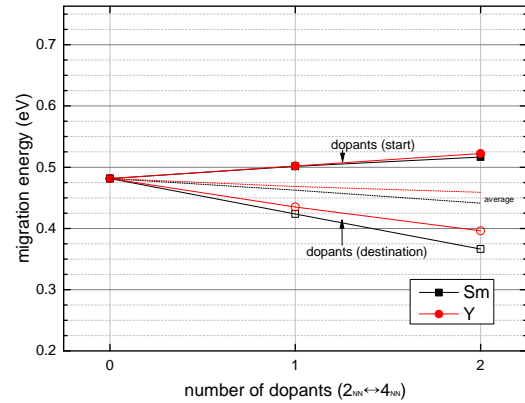
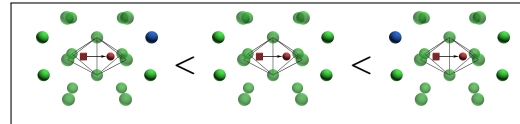
(a)  $2_{\text{NN}} \leftrightarrow 3_{\text{NN}}$ (b)  $2_{\text{NN}} \leftrightarrow 4_{\text{NN}}$ 

Figure 7.32: Migration energy for different numbers of dopants at the  $2_{\text{NN}} \leftrightarrow 3_{\text{NN}}$  and  $2_{\text{NN}} \leftrightarrow 4_{\text{NN}}$  position. Beside the migrating oxygen vacancy, no other defect is present. Sm and Y doped ceria in  $3 \times 3 \times 3$  supercell.

**$2_{\text{NN}} \leftrightarrow 4_{\text{NN}}$**  For  $2_{\text{NN}} \leftrightarrow 4_{\text{NN}}$  RE-V jumps in Sm doped ceria, the migration energy increases by 0.019(1) eV or decreases by  $-0.0578(1)$  eV per



dopant. For Y doped ceria, the migration energy increases by 0.0204(1) eV or decreases by  $-0.045(2)$  eV per dopant. The difference between decrease and increase by 0.076(1) eV for Sm doped ceria and 0.065(2) eV for Y doped ceria is of course again the difference in  $4_{\text{NN}}$  and  $2_{\text{NN}}$  association energy. The average decreases by  $-0.020(1)$  eV for Sm and  $-0.012(1)$  eV per dopant for Y doped ceria. The scaling for asymmetric and symmetric contribution is linear.

The influence of the  $2_{\text{NN}} \leftrightarrow 4_{\text{NN}}$  position for Sm doped ceria is asymmetrically similar to the  $1_{\text{NN}} \leftrightarrow 2_{\text{NN}}$  and  $2_{\text{NN}} \leftrightarrow 3_{\text{NN}}$  position, while its symmetric contribution lies in-between both configurations. For Y doped ceria, the symmetric influences are again similar to Sm doped ceria while the asymmetric influence is much smaller than in  $1_{\text{NN}} \leftrightarrow 2_{\text{NN}}$  but larger than in the  $2_{\text{NN}} \leftrightarrow 4_{\text{NN}}$  position. It may be noted that Sm/Y dopants in  $2_{\text{NN}} \leftrightarrow 4_{\text{NN}}$  position in average decrease the migration energy.

### 1,2<sub>NN</sub> ↔ 1,2,3,4<sub>NN</sub>: Comparing Model and DFT Energies – Termination

Similar to the 6-cation environment, configurations with dopants in the 1<sup>st</sup>, 2<sup>nd</sup> ↔ 5<sup>th</sup>, 3<sup>rd</sup>, 4<sup>th</sup>, 5<sup>th</sup> ↔ 8, 11<sup>th</sup> cation shell can be modeled.

Compared to the 6-cation environment, further jumps should be included into the model. Including the next shell around start and destination position and therefore all interactions up to 4.48 Å helps to distinguish jumps between  $1_{\text{NN}} \leftrightarrow 1_{\text{NN}}$  and  $1_{\text{NN}} \leftrightarrow 2_{\text{NN}}$  RE-V, while jumps between  $2_{\text{NN}} \leftrightarrow 3_{\text{NN}}$  and  $2_{\text{NN}} \leftrightarrow 4_{\text{NN}}$  RE-V cannot be distinguished and lead to the same migration energy. The difference between the increase and decrease in migration energy per dopants near start and destination position, respectively, is somehow similar for the  $2_{\text{NN}} \leftrightarrow 3_{\text{NN}}$  and  $2_{\text{NN}} \leftrightarrow 4_{\text{NN}}$  RE-V jump environment. Therefore, an interactions radius of 4.48 Å might be a good balance between the number of parameters and the quality of the model.

For this interaction radius, the termination and finite size correction becomes crucial for the migration energy, as discussed in Chapter 5.1.1. Intuitive **sd** [**ds**] parameters are chosen for an infinitely large supercell, which is calculated using a  $2 \times 2 \times 2$  and  $3 \times 3 \times 3$  supercell (model 2015) or a variable number of supercell sizes (model 2014). Intuitive **sd** [**ds**] parameters are chosen for a  $3_{\text{NN}}$  RE-V interaction of zero (model 2015) or for a RE-V interaction that is zero for infinite distances (model 2014). While up to now already the finite size correction according to the model 2015 has been used, both influences will be compared again in this section.

The DFT migration energies for an oxygen vacancy jumping away and towards a Sm dopant are shown in Fig. 7.33. According to the model 2014, migration barriers for jumps away from a dopant are overestimated. Migration barriers for jumps towards a dopant are mostly underestimated. The sum of differences between the model 2015 and DFT migration energies and  $\sigma_n$  is smaller. Main reason is the overestimated  $2_{\text{NN}} \leftrightarrow 3_{\text{NN}}$  RE-V association energy differences in the model 2014.

The smaller differences between individual parameters from the model 2015 compared to the model 2014 can also be shown for all selected ionic configurations for 1,2<sub>NN</sub> ↔ 1,2,3,4<sub>NN</sub> cation shell jumps (Fig. 7.34). While a fit of the **c1+sd** [**ds**] and **c1+c5+sd** [**ds**] models with 4.48 Å RE-V in-

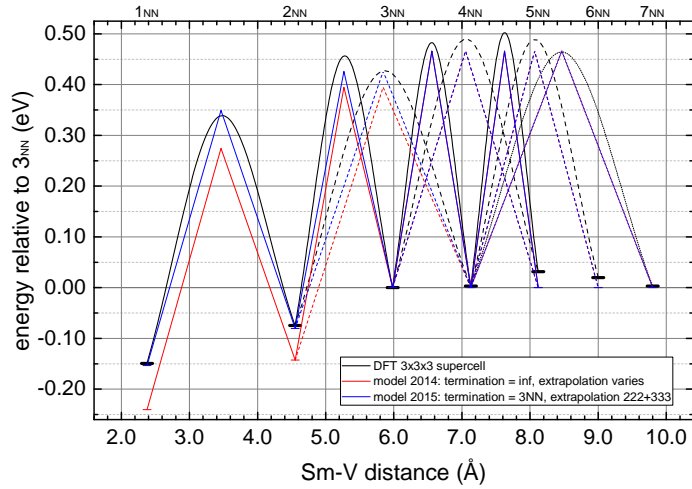


Figure 7.33: DFT and model migration energies. Intuitive parameters are chosen according to the model 2014 and 2015 as discussed above. Sm doped ceria in  $3 \times 3 \times 3$  supercell.

teraction radius lead to a  $\sigma_n$  of 0.048 and 0.026, the intuitive parameters according to the model 2015 lead to 0.065 and 0.047 and according to the model 2014 to 0.075 and 0.061, respectively. This verifies the use of the model 2015.

Figure 7.34 also shows that the use of the  $c1+sd$  [ds] model with 4.48 Å RE-V interaction radius is sufficient to fit or predict migration energies in the  $1,2_{NN} \leftrightarrow 1,2,3,4_{NN}$  cation shells if a low number of parameters is desired.

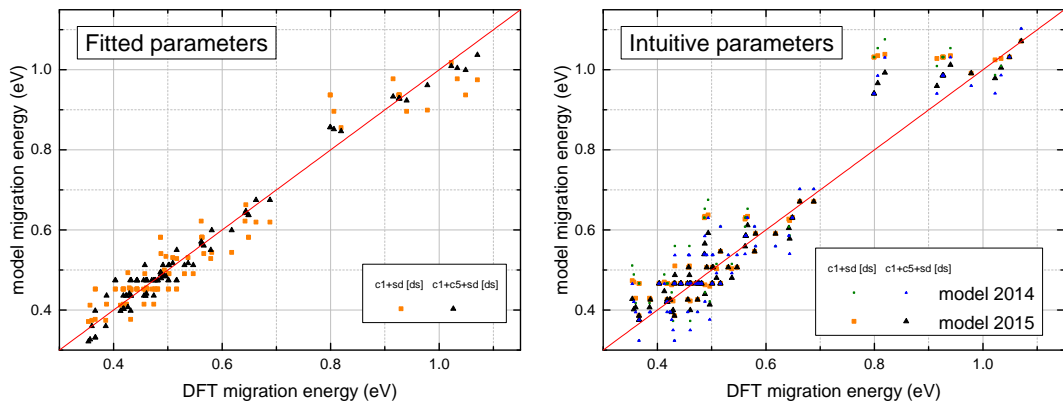


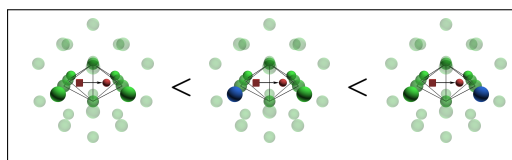
Figure 7.34: Model and DFT migration energies for jumps between  $1,2_{NN} \leftrightarrow 1,2,3,4_{NN}$  cation shells with fitted (left) and intuitive parameters (right). Models  $c1+sd$  [ds] and  $c1+c5+sd$  [ds] with 4.48 Å RE-V interaction radius. Intuitive parameters for the infinite supercell according to model 2014 and 2015. DFT energies for Sm doped ceria in  $3 \times 3 \times 3$  supercell.

## More RE-V Shells

Further investigated shells include jumps between  $3,4_{NN} \leftrightarrow 3,4,5_{NN}$  or the  $8,11^{\text{th}} \leftrightarrow 8,11,14^{\text{th}}$  shell for the cation sublattice. These jumps will be compared with configurations that extend the limitations of Fig. 7.13 using the example of  $4_{NN} \leftrightarrow 6,7_{NN}$ .

**$3_{NN} \leftrightarrow 3_{NN}$**  For the  $3_{NN} \leftrightarrow 3_{NN}$  RE-V jumps, the influence is small. For one Sm dopant, an increase from pure ceria 0.482 to 0.489 eV is found.

**$3_{NN} \leftrightarrow 4_{NN}$**  For the  $3_{NN} \leftrightarrow 4_{NN}$  and  $3_{NN} \leftrightarrow 5_{NN}$  RE-V jumps, the migration energy is shown in Fig. 7.35. For  $3_{NN} \leftrightarrow 4_{NN}$  RE-V jumps in Sm doped ceria, the migration energy increases by 0.0007 eV each or 0.0079(1) eV per dopant at start and destination position, respectively. The difference between changes in start and destination position per dopant is  $-0.0071(1)$  eV. The average increases by 0.0043 eV per dopant each. The scaling for asymmetric and symmetric contribution is linear.



The influence of the  $3_{NN} \leftrightarrow 4_{NN}$  position is asymmetrically about factor 10 smaller compared to the  $1_{NN} \leftrightarrow 2_{NN}$  and  $2_{NN} \leftrightarrow 3,4_{NN}$  position. Surprisingly dopants in  $3_{NN} \rightarrow 4_{NN}$  increase and dopants in  $4_{NN} \rightarrow 3_{NN}$  decrease the migration energy. The symmetric contribution is very small.

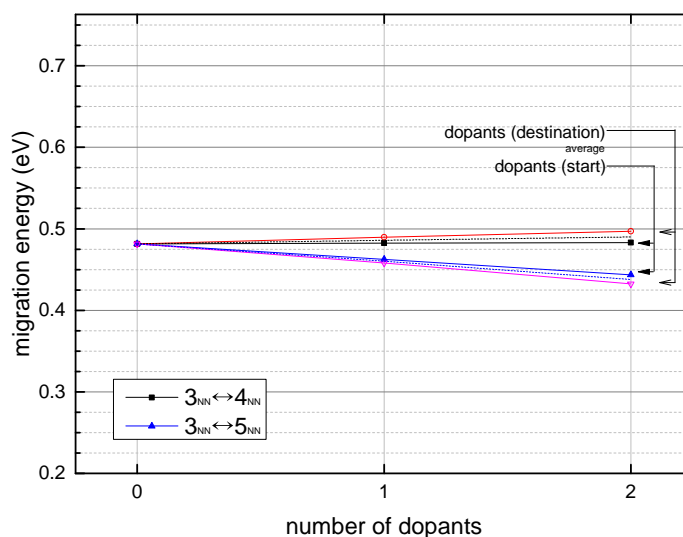
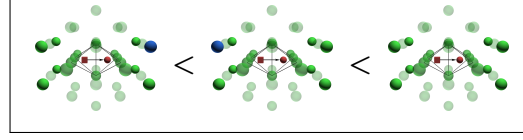


Figure 7.35: Migration energy for different numbers of dopants at the  $3_{NN} \leftrightarrow 4_{NN}$  and  $3_{NN} \leftrightarrow 5_{NN}$  position. Beside the migrating oxygen vacancy, no other defect is present. Sm doped ceria in  $3 \times 3 \times 3$  supercell.

**$3_{\text{NN}} \leftrightarrow 5_{\text{NN}}$**  For  $3_{\text{NN}} \leftrightarrow 5_{\text{NN}}$  RE-V jumps in Sm doped ceria, the migration energy decreases by  $-0.0191(1)$  eV or  $-0.0242(5)$  eV per dopant at start and destination position, respectively. The difference between changes in start and destination position per dopant is  $0.005(1)$  eV. The average decreases by  $-0.0216(2)$  eV per dopant. The scaling for asymmetric and symmetric contribution is linear.



The influence of the  $3_{\text{NN}} \leftrightarrow 5_{\text{NN}}$  position is asymmetrically similar to the  $3_{\text{NN}} \leftrightarrow 4_{\text{NN}}$  position with a changed sign. The symmetric contribution is surprisingly larger than the asymmetric contribution and similar to the  $2_{\text{NN}} \leftrightarrow 4_{\text{NN}}$  position.

**$4_{\text{NN}} \leftrightarrow 4_{\text{NN}}$**  For the  $4_{\text{NN}} \leftrightarrow 4_{\text{NN}}$  RE-V jumps, from pure ceria ( $0.482$  eV) a similar increase of  $0.0151$  eV each for one ( $0.497$  eV) and two dopants ( $0.512$  eV) is found.

**$4_{\text{NN}} \leftrightarrow 5_{\text{NN}}$**  For  $4_{\text{NN}} \leftrightarrow 5_{\text{NN}}$  RE-V jumps in Sm doped ceria, the migration energy increases by  $0.0168(4)$  eV or decreases by  $-0.0115$  eV each per dopant at start and destination position, respectively. The difference between changes in start and destination position per dopant is  $0.0283(4)$  eV. The average increases by  $0.0027(2)$  eV per dopant each. The scaling for asymmetric and symmetric contribution is linear.

The influence of the  $4_{\text{NN}} \leftrightarrow 5_{\text{NN}}$  position is small compared to the earlier positions.

**$4_{\text{NN}} \leftrightarrow 6_{\text{NN}}$**  As the difference in association energy between  $5_{\text{NN}}$ ,  $6_{\text{NN}}$  and  $7_{\text{NN}}$  is assumed to be small (Chapter 4.2.1), jumps between  $4_{\text{NN}} \leftrightarrow 5_{\text{NN}}$  and further shells (e.g.  $4_{\text{NN}} \leftrightarrow 6,7_{\text{NN}}$ ) are assumed to be similar. For the  $4_{\text{NN}} \leftrightarrow 6_{\text{NN}}$  RE-V jumps, compared to pure ceria ( $0.482$  eV), the migration energy increases for one Sm dopant by  $0.004$  eV ( $0.486$  eV) at the start position or decreases by  $-0.01$  eV ( $0.469$  eV) at the destination position. The influence of the  $4_{\text{NN}} \leftrightarrow 6_{\text{NN}}$  position is small.

**$4_{\text{NN}} \leftrightarrow 7_{\text{NN}}$**  For  $4_{\text{NN}} \leftrightarrow 7_{\text{NN}}$  RE-V in Sm doped ceria, the migration energy decreases by  $-0.022(2)$  eV per dopant both at start and destination position. This would suggest a purely symmetric contribution, which scales linearly. However, due to the large defect distance of nearly  $10 \text{ \AA}$  in a  $3 \times 3 \times 3$  supercell, the distance between the defects and their copies due to periodic boundary conditions is only slightly larger than the defect distance itself. Therefore, lattice relaxations may propagate periodically leading to false migration energies. Overall, the contribution is small.

## Conclusion

While the influence of dopants on  $1,2_{NN} \leftrightarrow 2,3,4_{NN}$  positions is large, dopants with larger distances to the migrating oxygen ion show significantly lower asymmetric and (with the exception of the  $3_{NN} \leftrightarrow 5_{NN}$  configuration) symmetric contributions. Interesting is the regular change between in- and decrease in migration energy for dopants at the start position in the sequence of jump configurations (cp. Fig. 7.36). This change in sign for the asymmetric contributions suggests alternating shielding effects for successive jump shells.

Geometric symmetric configurations often feature categorical scaling while geometrically asymmetric configuration can be described well using asymmetric and symmetric contributions.

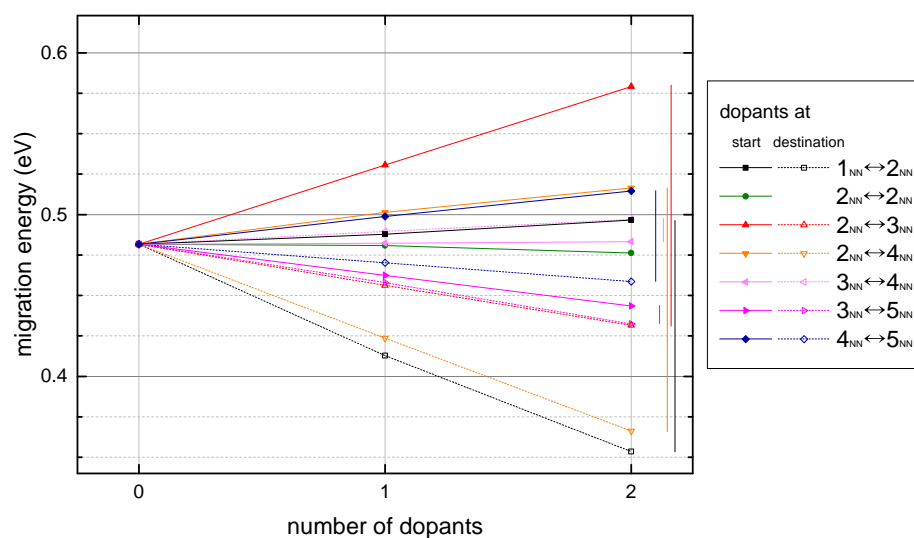


Figure 7.36: Migration energy for different numbers of dopants. Beside the migrating oxygen vacancy, no other defect is present. Sm doped ceria in  $3 \times 3 \times 3$  supercell. The range of the migration energy is marked on the right side.

### 7.2.5 Influence of Vacancies on a Jump

The V-V association energy is positive and decreases with increasing distance between both oxygen vacancies. An exception is the  $2_{NN} \rightarrow 3_{NN}$  configuration (see Chapter 5.1.1).

This trend can also be seen in the migration energies, which are shown as a function of the number of oxygen vacancies in Fig. 7.37. Here, the sum of migrating oxygen vacancy and additional vacancies is given. Jumps are labeled for distances in the anion sublattice similar as described above for the cation sublattice. The  $2_{NN} \leftrightarrow 3^{o,m}_{NN}$  configuration contains jumps to both  $3^{o}_{NN}$  and  $3^m_{NN}$ . A jump of an oxygen vacancy in the direction of another oxygen vacancy is impeded. A jump in the direction of several oxygen vacancies possesses even higher migration energies. Similar to the association energy, the  $2_{NN} \rightarrow 3_{NN}$  jump is an exception.

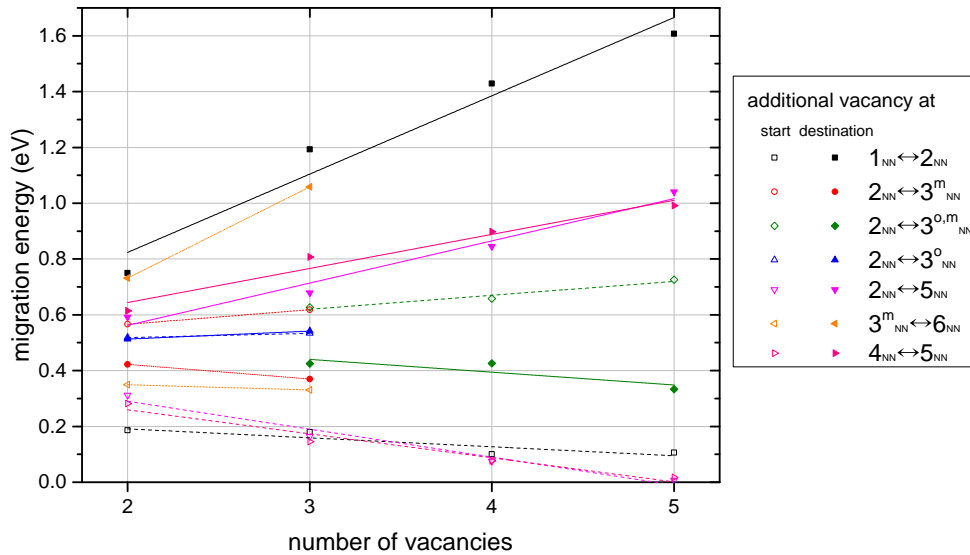


Figure 7.37: Migration energy for different numbers of oxygen vacancies. The moving vacancy is included in the number of vacancies. No other defect is present. Lines show a linear fit.  $3 \times 3 \times 3$  supercell.

Surprising is the  $2_{NN} \leftrightarrow 3^{o}_{NN}$  configuration, where additional oxygen vacancies near both the start and destination position lead to slightly larger migration energies due to a positive symmetric contribution. This is probably caused by the missing shielding of an interjacent cerium-ion causing all configurations with additional vacancies to an increase in migration energy.

Again, the difference and the average between forward and backward jump can be calculated. The difference between both jumps per additional vacancy decreases with increasing number of additional vacancies, e.g. for  $1_{NN} \leftrightarrow 2_{NN}$  from 0.56 to 0.38 eV or for  $2_{NN} \leftrightarrow 5_{NN}$  from 0.28 to 0.26 eV. This is caused by local relaxations, which lead to energetically more similar configurations even if a large number of defects is present. The absolute average between both jumps per additional vacancy is 0.03 eV or below for all configurations except for  $1_{NN} \leftrightarrow 2_{NN}$  and  $3^m_{NN} \leftrightarrow 6_{NN}$ . For the  $1_{NN} \leftrightarrow 2_{NN}$  configuration, one additional vacancy approximately leads to a purely asymmetric configuration

## 7 Activation Energy

while for more vacancies the average migration energy increases by 0.1 eV per addition vacancy. This is obviously caused by the strong repulsion between vacancies and the already low migration energy for one additional vacancy. For the  $3^m_{NN} \leftrightarrow 6_{NN}$  configuration, the effect is similar and starts already for one additional vacancy.

Therefore, the scaling can be approximated as linear, even the sole use of asymmetric contributions is a good approximation. A comparison for a corresponding model (lines) and DFT migration energies (points) is shown in Fig. 7.38.

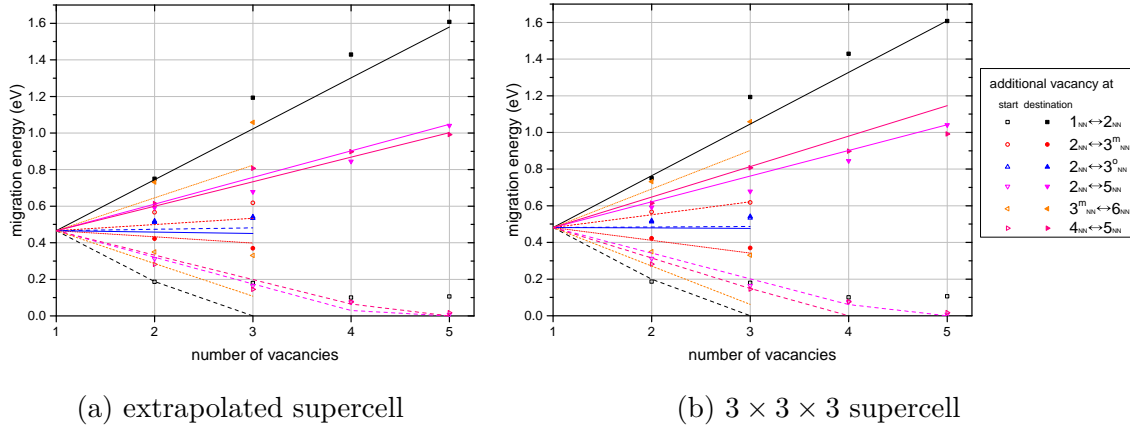


Figure 7.38: Migration energy for different numbers of oxygen vacancies. The moving vacancy is included in the number of vacancies. No other defect is present. Points show DFT results for the  $3 \times 3 \times 3$  supercell. Lines show model migration energies for linear scaling using the association energy from the extrapolated (left) and  $3 \times 3 \times 3$  supercell (right).

The migration energy can again be modeled using the association energies from the extrapolated or  $3 \times 3 \times 3$  supercell. Both cases show a good approximation of the migration energy if only a low number of parameters is desired. The model could be improved by considering a symmetric contribution for the  $3^m_{NN} \leftrightarrow 6_{NN}$  configuration.

## 7.2.6 Comparing Model and DFT Energies

Up to now, models have only been fitted to jump configurations with a single oxygen vacancy. In this chapter, the influence of additional vacancies on a jump is investigated. However, RE-V and V-V interactions are still only investigated separately. Here, jumps configurations contain either additional dopants or vacancies. The interaction between both sublattices is investigated in the next section.

Similar to earlier proposed models, only the  $1_{\text{NN}} \leftrightarrow 1_{\text{NN}}$  RE-V jump configuration is considered to scale categorically, while for simplicity all other jump configurations are considered to scale linearly. Up to now, models based on equal interaction radii for start and destination were used, as the investigation of the groups revealed that both positions affect the migration energy. In this chapter, this assumption will be verified by considering only groups around the start, the center or the destination position.

Besides the question of centering the influences on the migration barrier, a model with sufficient quality but with a low number of parameters is desired. Therefore, the number of parameters is reduced and the interaction radius limited.

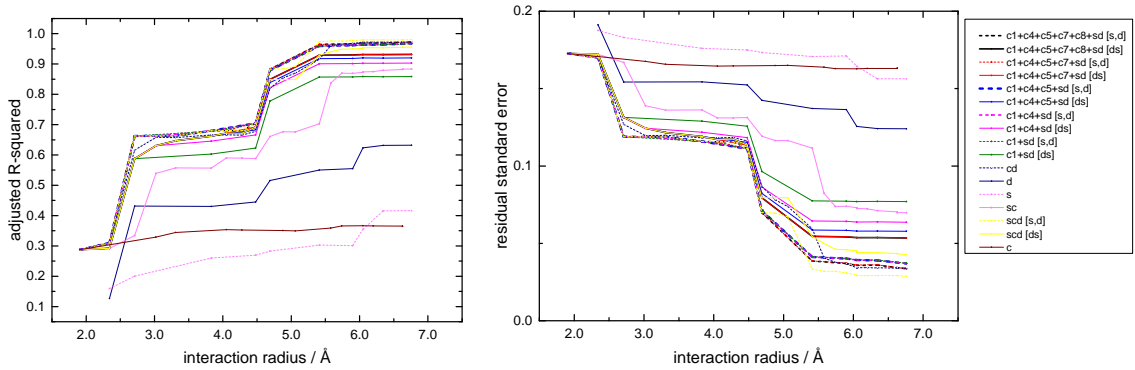


Figure 7.39:  $\bar{R}^2$  and standard derivation for different models (c1 is categorical). The jumping oxygen vacancy interacts with either dopants or vacancies. Jumps up to the 23<sup>th</sup> shell (6.76 Å) are included. Sm doped ceria in  $3 \times 3 \times 3$  supercell.

In Fig. 7.39, the adjusted  $\bar{R}^2$  and standard derivation for different models is shown for Sm doped ceria. An extract of the data is shown in Fig. 7.40 for simplicity.

Clearly, models using only spheres around either the start (s), the center (c) or the destination position (d) are not sufficient to describe the migration energy. Even a combination of spheres at start and center (sc), which is similar to the approach of the transition state theory, could only be used at large interaction radii. However, a combination of spheres at destination and center (cd) gives even better results at low interaction radii than spheres at all three position using the difference of the number of dopants between start and destination position (scd [ds]). Obviously, for Sm doped ceria, influences around the destination position are strong as seen by the scaling of e.g. the  $1_{\text{NN}} \leftrightarrow 2_{\text{NN}}$  and  $2_{\text{NN}} \leftrightarrow 4_{\text{NN}}$  RE-V jumps.

A migration energy model should include interactions  
of the migrating oxygen vacancy with defects  
around its position in initial, transition and final state.

Using the largest number of parameters, as in the `scd [s,d]` model, not always leads to the largest adjusted  $\bar{R}^2$  as the same regression quality can be reached with a fewer number of parameters. At 6.76 Å, the `scd [s,d]` model reaches the highest adjusted  $\bar{R}^2$  value for all models of 0.9804. Here, 36 parameters are used. As the number of parameters is very high, a reduction of parameter is desirable. Without decreasing the quality of the model too much, the number of parameter can be decreased to 10 parameters in the model `c1+sd [ds]` with an interaction radius of 5.41 Å (Fig. 7.40,  $\bar{R}^2 = 0.86$ ). Especially influences near the jump center can be reduced and therefore symmetric contributions neglected. As seen before, these are in most cases small compared to the asymmetric contribution. A comparison between DFT and model energies for the model `c1+sd [ds]` is shown in the appendix in Fig. 9.9. An interaction radius of 5.41 Å corresponds exactly to the length of the unit cell or the lattice parameter. This is not surprising as the length of the unit cell correlates with the translation symmetry in the solid.

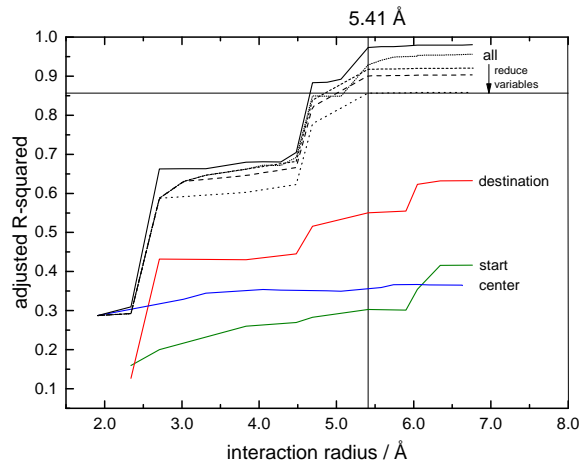


Figure 7.40:  $\bar{R}^2$  for selected models (c1 is categorical). The jumping oxygen vacancy interacts with either dopants or vacancies. Jumps up to the 23<sup>th</sup> shell (6.76 Å) are included. If a minimal number of parameters is desired, a model with a single symmetrical influence (c1) and an interaction radius of 5.41 Å is sufficient. Sm doped ceria in  $3 \times 3 \times 3$  supercell.

### 7.2.7 Jumps at Experimental Defect Concentrations

Previously it was assumed for simplicity that cation and anion sublattice do not interact. In this section, a comparison is performed between migration energies from the model and the DFT calculations at dopant concentrations, which are often used in experiments ( $\text{Ce}_{1-x}\text{Sm}_x\text{O}_{2-x/2}$  with  $x = 0.05, 0.1$  and  $0.15$ ), using probable jump configurations.

A fit of different models to the DFT migration energies is shown in Fig. 7.41.

Again, the **c1+sd [ds]** model with an interaction radius of 5.41 Å has a sufficient quality to describe the migration energies. The adjusted  $\bar{R}^2 = 0.80$  is slightly lower compared to the separate investigation of the sublattices above. This is caused by the interaction of the sublattices and the larger defect concentration. The decrease in  $\bar{R}^2$  is small, which indicates the following:

The interaction between both sublattices is small and even  
migration energies at large defect concentration  
can be fitted using the proposed model.

A comparison with the fitted model and the DFT migration energies is shown in Fig. 7.42 (left). For the fitted parameters  $\sigma_s$  is 0.089 totally.

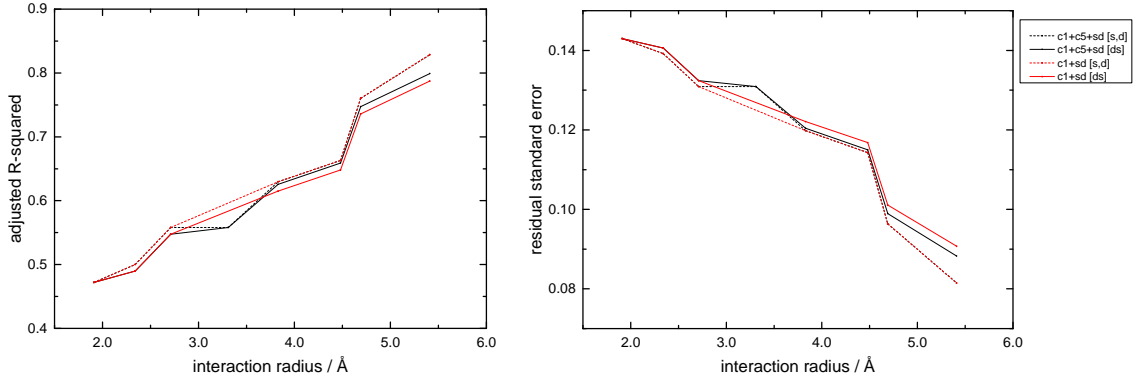


Figure 7.41:  $\bar{R}^2$  and standard derivation for different models (c1 is categorical). The jumping oxygen vacancy interacts with both dopants and vacancies. Both sublattices interact. Interactions up to the 13<sup>th</sup> shell (5.41 Å) are included in the model. Sm doped ceria in  $3 \times 3 \times 3$  supercell.

The ability of the model **c1+sd [ds]** to predict migration energies using intuitive parameters from the infinitely large supercell is shown in Fig. 7.42 (right).<sup>1</sup> With increasing dopant fractions, the standard deviation increases. For the intuitive parameters  $\sigma_s$  is 0.06, 0.09 and 0.11 for  $x = 0.05$ , 0.1 and 0.15, receptively. For all dopant fractions  $\sigma_s$  is totally 0.093. The deviation to the regression of the fitted parameters is small. Therefore, the chosen intuitive parameters are well suited for experimental defect concentrations.

<sup>1</sup>For different interaction radii of the model **c1+sd [ds]**, compare Fig. 9.10 in the appendix.

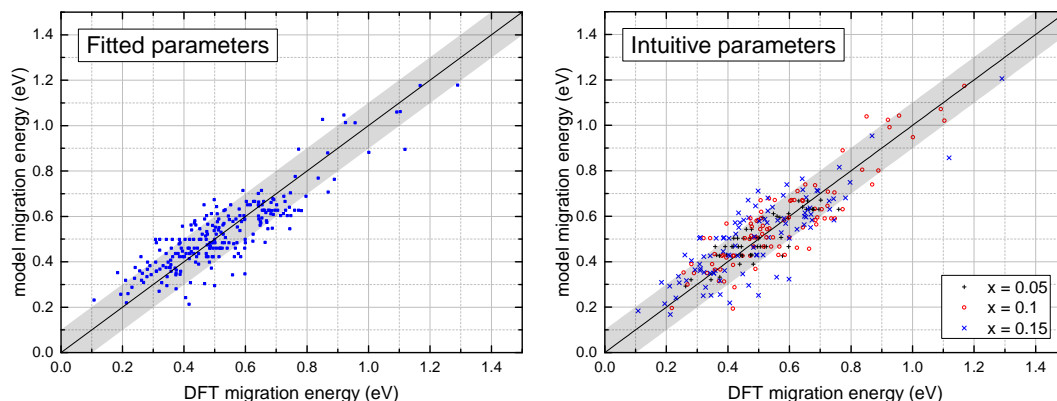


Figure 7.42: Model and DFT migration energies with fitted and intuitive parameters. The jumping oxygen vacancy interacts with both dopants and vacancies. Both sublattices interact. The model `c1+sd [ds]` up to the 13<sup>th</sup> shell (5.41 Å) is used. Intuitive parameters are chosen for the infinite supercell as discussed above with the termination  $E_{\text{ass}}(3_{\text{NN}} \text{ RE-V}) = 0$  and  $E_{\text{ass}}(5_{\text{NN}} \text{ V-V}) = 0$ . A proportional behavior with a deviation of 0.1 eV is marked. Sm doped ceria in  $3 \times 3 \times 3$  supercell.

## 7.2.8 Comparison with Models in Literature

Several models have been proposed in literature to predict the migration energies in doped ceria or yttria-stabilized zirconia. Main differences are the interaction radius, the centers of interactions and the number of chosen parameters. Using the vast amount of configurations calculated in this work, the quality of the proposed models can be estimated.

Krishnamurthy *et al.*<sup>[225]</sup> simulated the ionic conductivity in yttria-stabilized zirconia using an interaction radius of only 1.91 Å. They calculated the three edge configurations of `c1` categorically: Zr-Zr, Zr-Y and Y-Y. Though yttria-stabilized zirconia was not investigated in this work, the reduction of all possible migration energies to three values might be a bad approximation.

Meyer and Nicoloso<sup>[220]</sup> included for fluorite-type oxides only the RE-V interaction and neglected any V-V repulsion. Separate models were created considering either trapping (`sd [ds]` with an interaction radius of 2.34 Å) or blocking (`c1` with  $E_{\text{shell}}^{\text{1, Ce-RE}} = E_{\text{shell}}^{\text{1, RE-RE}}$ ). As trapping and blocking are only considered separately, `c1` is badly approximated and no V-V is considered, several effects are missing that are assumed in this work to be essential to understand the ionic conductivity.

Adler and Smith<sup>[281]</sup> simulated the ionic conductivity in Y doped ceria. For the RE-V and V-V interaction, a modified Coulomb potential is used that contains an empirical scaling term that adjust the range of the interaction. The range of interaction is varied between  $1_{\text{NN}}$  for RE-V and V-V and infinity. The migration barrier that is added to this association energy difference is assumed to be independent of the ionic environment according to spin-lattice measurements.<sup>[418]</sup> This leads to a `sd [ds]` model with an interaction radius between 2.71 Å and infinity. While the linearly scaling

for  $\mathbf{sd}$  [ $\mathbf{ds}$ ] is a good approximation as confirmed in this work, the neglected categorically scaling of the  $\mathbf{c1}$  leads to strong deviations compared to calculated migration energies.

Martin<sup>[37]</sup> and Grope *et al.*<sup>[287]</sup> used  $\mathbf{c1}$  categorically. Martin added the first RE-V interaction around the start position using a linear scaling. In the second paper, they also considered the first V-V interaction for Y and Sm doped ceria. The resulting  $\mathbf{c1+s}$  model with an interaction radius of 2.34–2.71 Å allows a clear separation of blocking and trapping effects. However, the model quality is limited as shown in Fig. 7.39.

Nakayama and Martin<sup>[54]</sup> propose a  $\mathbf{c1+s}$  model considering only the cation sublattice with categorical  $\mathbf{c1}$  and otherwise linear scaling with an interaction radius of 4.48 Å. As shown in this work is the destination position crucial to model the migration energy. Furthermore, no V-V interactions are considered.

All configurations of the 6-cation environment were calculated by Murray,<sup>[41]</sup> and Oaks *et al.*<sup>[282,283]</sup> for Y and La doped ceria, respectively, and by Pornprasertsuk *et al.*<sup>[371]</sup> for yttria-stabilized zirconia. The latter is also investigated by Shimojo and Okazaki<sup>[428]</sup> by extracting the jump configurations of performed jumps from MD simulations. The resulting 30 parameters model ( $\mathbf{scd}$  without grouping and scaling) with an interaction radius of 2.34 Å is an acceptable approximation for the RE-V interaction of the migrating oxygen vacancy. However, no V-V repulsion was considered leading to unphysical results for high dopant fractions. In a later model, Pornprasertsuk *et al.*<sup>[372]</sup> increased the interaction radius to include  $2_{\text{NN}}$  RE-V and V-V interactions using the association energy.

A larger interaction radius was considered by Dholabhai *et al.*<sup>[224,284–286]</sup> for Pr, Gd and Sm doped and Gd-Pr co-doped ceria. For the RE-V interactions, migration energies with a single dopant up to a  $3_{\text{NN}}$  RE-V distance were calculated. Though the exact formula for the model is not mentioned, the created model could be similar to a  $\mathbf{c1+c8+c15+sd}$  [ $\mathbf{s,d}$ ] model with linear scaling and an interaction radius of 4.48 Å considering only the cation sublattice. A model without V-V interactions and a model prohibiting vacancies from being on  $1_{\text{NN}}$  V-V position were used. As  $\mathbf{c1}$  is not calculated categorically and barely any V-V interactions are considered, large deviations between model and actual migration energies at high dopant fractions are expected.

Using a cluster expansion, Lee *et al.*<sup>[373]</sup> fitted 100 randomly chosen ionic configurations in yttria-stabilized zirconia using clusters with up to three ‘spins’ and an interaction radius that is 50 % larger than the lattice parameter. Though the model with 9 parameters has a good fit quality, insights into the significance of the parameters are limited.

In an earlier presented work,<sup>[55]</sup> the ionic conductivity in Y doped ceria was simulated using a  $\mathbf{c1+sd}$  [ $\mathbf{ds}$ ] model with linear scaling except for  $\mathbf{c1}$  and an interaction radius of 4.69 Å. The model has a high quality as shown in Fig. 7.39. As subsequent Metropolis Monte Carlo simulations revealed a significant influence of the  $4_{\text{NN}}$  V-V interactions on the ordering of the defects, in this work an interaction radius of 5.41 Å is used.

### Conclusion

Several models for the migration energy in doped ceria were developed. Interaction around the migrating oxygen ion in the initial, transition and final state were investigated. Lattices sites were grouped according to their distance to the initial and final position of the migrating oxygen ion. Defects appearing in these groups lead either to a linear change in migration energy with increasing number of dopants (linear scaling, e.g. around the start position) or categories for different numbers of dopants have to be defined (categorical scaling, e.g. c1 around the center position). Influences of groups are independent of each other. Therefore, the migration energy is given as sum of the migration energy in pure ceria and the influences of all groups. For a better understanding, contributions were separated in symmetric and asymmetric contributions. For example, Sm dopants in  $1_{NN} \leftrightarrow 2_{NN}$  RE-V influence the migration energy both through the configurational energy difference between final and initial state and an energy contribution per dopant near either start or destination position. The number of parameters for the migration energy model could be reduced by using an interaction radius of 1.91 Å around the jump center and 5.41 Å around the start and destination position. Even without symmetric contributions around the start and destination position, an acceptable quality and prediction capability of the model was reached. Over 1100 migration energies were calculated using DFT to successfully verify the quality of the proposed model for small and experimental defect concentrations.

## 7.3 Simulating the Ionic Conductivity for Different Models

Finally, the ionic conductivity is simulated using a `c1+sd [ds]` model with different interaction radii. In Fig. 7.43, the simulated ionic conductivity of Sm doped ceria at 500 °C using different interaction radii is shown. A randomly ordered cation-sublattice is assumed. Intuitive parameters for the infinitely large supercell are chosen with termination at the first neglected interaction as described above. As the V-V association energy does not monotonously decrease with increasing V-V distance (Chapter 5.1.1), an association of V-V takes place as shown in Fig. 7.44.

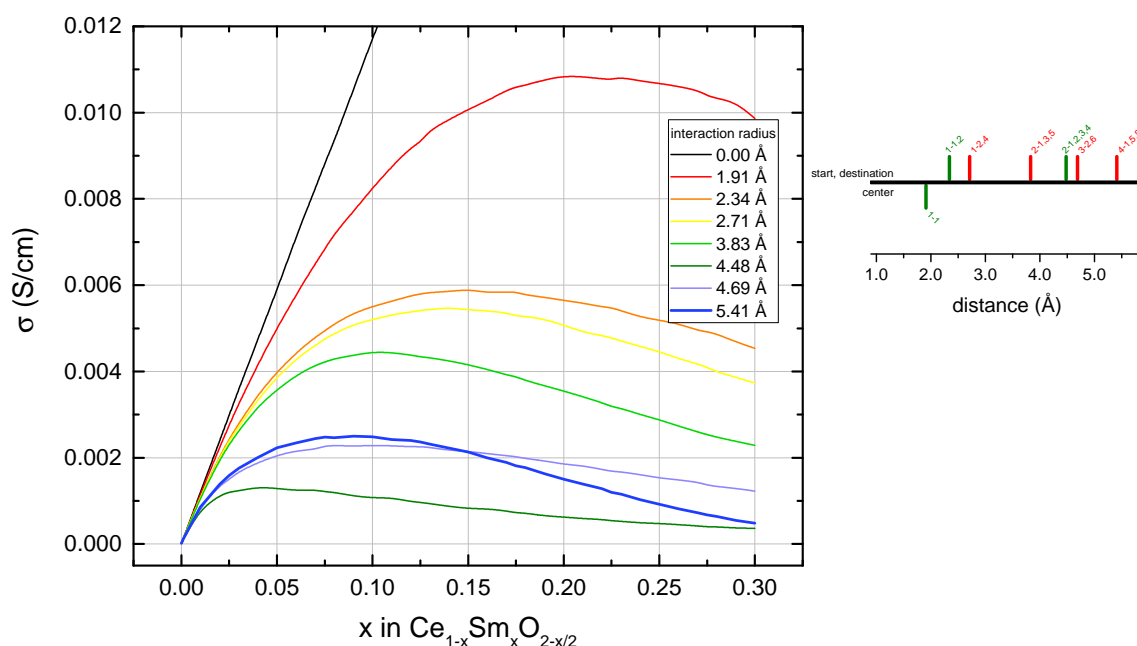


Figure 7.43: Simulated ionic conductivity of Sm doped ceria at 500 °C (left) using different interaction radii as shown on the right for the RE-V (green) and V-V interaction (red). Around the jump center at most the first interaction is used with categorical scaling. Intuitive parameters are used as described above.

Without considering any interactions (interaction radius of 0 Å), the conductivity is dominated by the number of charge carriers and the number of possible jump destinations. With increasing dopant fraction the number of charge carriers increases leading to an increase in conductivity.

If oxygen vacancies are considered as charge carriers, with the anion sublattice fraction  $c = \frac{x}{4}$ , the number of oxygen ion lattice sites decreases with increasing dopant fraction according to  $(1 - c)$  or  $2 \cdot (1 - \frac{x}{4})$ . As vacancies cannot be at the same lattice side, additional vacancies block the movement of an oxygen vacancy, which is referred to as site-blocking. The resulting conductivity is proportional to  $c(1 - c)$  or  $\frac{1}{2}x \cdot (1 - \frac{x}{4})$  with a maximum in conductivity at the dopant fraction  $x = 2$ , which does not only neglect solubility limits and phase transitions that occur in experiments (Chapter 2.1.2)

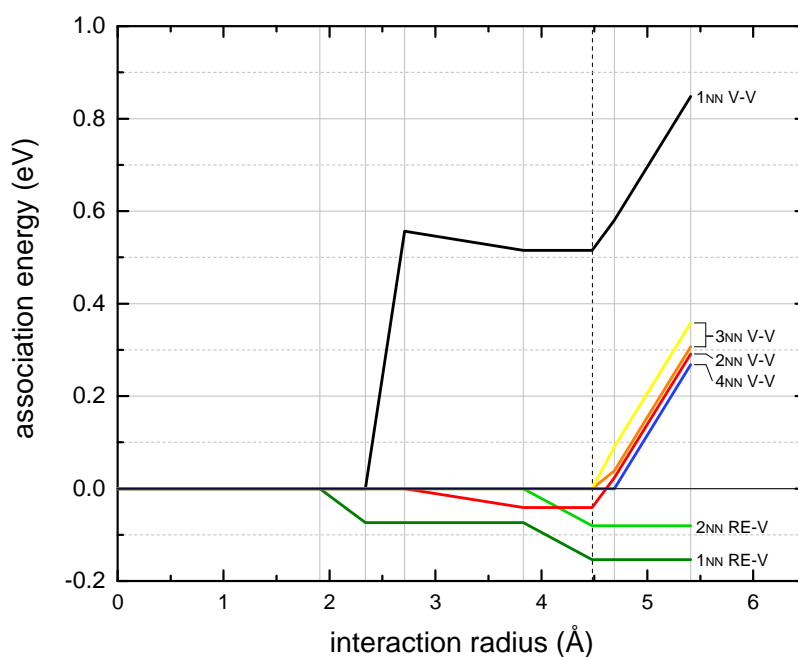


Figure 7.44: Association energies as intuitive model parameters as a function of interactions radius.

but also cannot even theoretical be reached by doping with a trivalent dopant.

For an increasing interaction radius around center, start and destination position, interactions of the migrating oxygen vacancy with dopants (RE-V) and vacancies (V-V) are subsequently considered. The conductivity as a function of dopant fraction changes in amplitude and curve shape. For an increasing interaction radius up to 4.48 Å, an overall decrease in the ionic conductivity can be found. From an interaction radius of 4.48 Å to 4.69 Å, the ionic conductivity increases again. From an interaction radius of 4.69 Å to 5.41 Å, an increase at low dopant fractions and decrease starting at intermediate dopants fractions can be found. The shape of the curves changes, the dopant fraction that leads to the largest conductivity decreases with decreasing overall conductivity. For an interaction radius of 5.41 Å, an exceptional ascending slope is found: The conductivity decreases strongly with increasing dopant fraction starting from intermediate dopant fractions.

For an interaction radius of 1.91 Å, the conductivity is not only influenced by site-blocking but also by increased symmetric migration barriers around dopants. This interaction around the jump center increases both forward and backward jumps and is in this work referred to as blocking. As a result, the equilibrium distribution of the defects is unaltered. However, vacancies stay longer near dopants due to the increased migration edges. Therefore, the ionic conductivity decreases.

Increasing the interaction radius to 2.34 Å introduces the 1<sub>NN</sub> RE-V interaction (Fig. 7.44). Jumps of the migrating oxygen vacancy to the dopant (2<sub>NN</sub>→1<sub>NN</sub> RE-V) possess a smaller migration energy than in pure ceria. Jumps away from the dopant (1<sub>NN</sub>→2<sub>NN</sub> RE-V) possess a larger migration energy than in pure ceria. The vacancy is trapped. The equilibrium distribution of the defects changes, RE-V associates appear. The conductivity decreases significantly.

Increasing the interaction radius to 2.71 Å introduces the 1<sub>NN</sub> V-V interaction. In contrast to the RE-V association, the V-V interaction is repulsive. Jumps of the migrating oxygen vacancy to an adjacent vacancy (2<sub>NN</sub>→1<sub>NN</sub> V-V) have a very large migration energy. Therefore, vacancies rarely appear in nearest neighborhood. The influence on the ionic conductivity is similar to an increased site-blocking: The conductivity decreases slightly. The result is in agreement with literature. Dholabhai *et al.* showed a decrease in conductivity and  $x_{\max}$  for a vacancy repelling model compared to a vacancy non-repelling model.<sup>[284]</sup>

Increasing the interaction radius to 3.83 Å introduces a 2<sub>NN</sub> V-V association. As the V-V association energy does not monotonously decrease with increasing V-V distance (Chapter 5.1.1), an association of V-V takes place. Vacancies appear more often in next nearest neighborhood. The conductivity decreases significantly.

Increasing the interaction radius to 4.48 Å introduces the 2<sub>NN</sub> RE-V interaction and increases the trapping effect. Similar to other association effects, the conductivity decreases significantly.

In summary, all interactions can decrease the conductivity: Increased symmetric migration barriers (blocking), RE-V association (trapping), V-V association and even V-V repulsion. The influence on the conductivity increases with increasing dopant fraction.

However, this is not always the case: Increasing the interaction radius to 4.69 Å increases the conductivity. Here, the V-V association changes to repulsion and the V-V repulsion is increased. Obviously, V-V repulsion can also increase the conductivity.

Increasing the interaction radius to 5.41 Å increases the V-V repulsion significantly. However, the influence on the conductivity up to  $x = 0.15$  is marginal. Here, the conductivity slightly increases. For larger dopant fractions the conductivity strongly decreases. While for small vacancy concentrations the V-V repulsion leads to an ordering of the vacancies that increases the conductivity, starting at intermediate vacancy concentrations the number of vacancies is too large leading to a decrease in conductivity.

In summary, repulsion between defects can both de- and increase the conductivity as it influences the defects distribution and can create an ordering of defects.

The simulated ionic conductivity of Sm doped ceria at 500 °C for an interaction radius of 5.41 Å was already compared to experiments in the last chapter in Fig. 6.15 (fixed attempt frequency).<sup>[74,179]</sup> Experimental and calculated conductivities are in agreement. However, a large scattering in experimental values was found. Therefore, a clear preference for an interaction radius cannot be determined. Therefore, the agreement between calculated DFT migration energies and the proposed model is used as a decisive criterion for an interaction radius of 5.41 Å. Thus, a migration energy model was successfully developed to calculate the ionic conductivity for various dopants and dopant fractions.

**Blocking, trapping and V-V interaction** During the discussion of different interaction radii, the effects of symmetric migration barriers (blocking), RE-V association (trapping), V-V repulsion and even V-V association have been discussed. To evaluate their influence on the con-

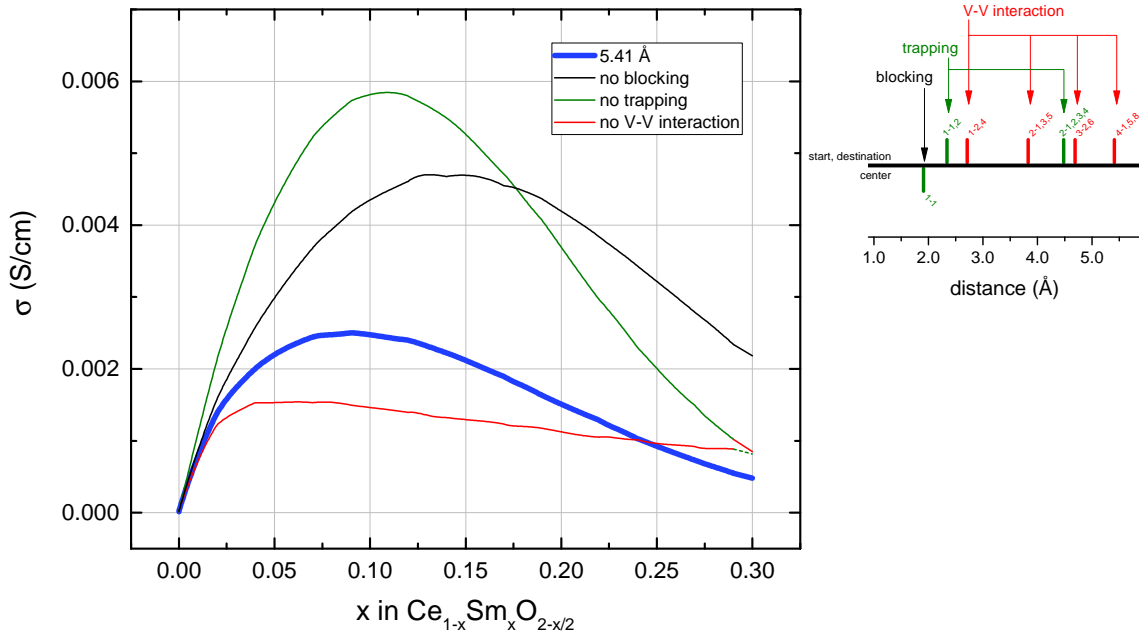


Figure 7.45: Simulated ionic conductivity of Sm doped ceria at 500 °C (left) using blocking, trapping and V-V interactions with an interaction radius of 5.41 Å as shown on the right for the RE-V (green) and V-V interaction (red). Additionally, interactions are switched off individually.

ductivity for the final migration energy model, they are switched off individually. This will improve the understanding of the underlying mechanism that determines the magnitude of the oxygen ion conductivity and the optimal dopant concentration.

In Fig. 7.45, blocking, trapping and V-V interaction are switched off individually. Therefore, increased symmetric migration barriers due to dopants around the jump center or association energy contributions due to RE-V association or V-V interaction are neglected. Additionally, the full model with an interaction radius of 5.41 Å is shown. In the following, the change in conductivity compared to the full model is discussed.

Neglecting RE-V interactions (blocking and trapping) leads to an increase in conductivity compared to the full model similar to the investigation above. For no trapping, the slope of the conductivity as a function of dopant fraction increases and the dopant fraction leading to the maximum in conductivity  $x_{\max}$  slightly increases. Trapping decreases the conductivity at all dopant fractions up to 60 %, especially at intermediate dopant fractions slightly above the optimal dopant concentrations. The strong deviation of the conductivity at low dopant fraction shows the importance of trapping for small defect concentrations. The small change in  $x_{\max}$  indicates that trapping reduces the optimal dopant concentration but is only a minor effect. For no blocking,  $x_{\max}$  increases significantly. Obviously, the dopant fraction leading to the maximum in conductivity is strongly limited by blocking.

Neglecting V-V interactions decreases the conductivity compared to the full model. Here, a strong

trapping of the oxygen vacancies takes place since no V-V repulsion is included. As a result, the conductivity decreases and  $x_{\max}$  is significantly smaller. This emphasizes the importance of V-V interactions, which are often neglected in literature (cp. Chapter 7.2.8).

#### Microscopic blocking and trapping are connected with the macroscopic conductivity.

The results are in agreement with literature. Using an analytical model, Martin showed the change in conductivity with the consideration of blocking, additional weak trapping and additional strong trapping.<sup>[37]</sup> Meyer and Nicoloso showed the typically maximum in conductivity as a function of dopant fraction using KMC simulations and only blocking.<sup>[220]</sup> Grope showed a similar influence on the conductivity for neglected blocking, trapping or V-V interaction for Sm and La doped ceria.<sup>[429]</sup>

KMC simulations of doped ceria have already been performed by several groups for YSZ<sup>[225,371–373]</sup> and doped ceria.<sup>[41,55,220,224,281–287]</sup> However, the strong influence of the chosen interaction radius shows the necessity for a more complex migration energy model than used in these studies. In this work, a model was developed with high complexity but few and intuitive *ab initio* parameters, which correlate with material properties. Grouping effects into blocking, trapping and V-V interaction allows a detailed understanding of the underlying mechanism that determines the magnitude of the oxygen ion conductivity and the optimal dopant concentration.



# 8 Oxygen Ion Conductivity

In this chapter, the oxygen ion conductivity in experiments and simulations is presented and several influences are analyzed: The influence of sample preparation on the conductivity is shown by varying the sintering temperature and sintering duration (Chapter 8.1). The influence of doping on the conductivity (Chapter 8.2) is simulated, compared with literature and separated into effects due to trapping, blocking and V-V interactions. For comparison, impedance measurements were performed for Sm, Gd and Lu doped ceria (Chapter 8.2.2, 8.2.3 and 8.2.5) and are compared with simulations (Chapter 8.2.6). Additionally, ceria co-doped with Sm-Zr and Gd-Zr are investigated including polycrystalline samples and agglomerates of single crystals (Chapter 8.2.4). Finally, the influence of time on the conductivity is shown: Long-term degradation caused by cation ordering is found in calculations and experiments (Chapter 8.3).

## 8.1 The Influence of Sample Preparation:

### Varying the Sintering Temperature and Duration

Due to scattering of the ionic conductivity in literature of materials with the same composition, influences of the sample preparation were investigated. It is assumed that the powder synthesis and the sintering process are the main influences on the ionic conductivity.<sup>[297,298,301,430]</sup> In Chapter 4.1.3, the influence of the sintering temperature and sintering duration on the macroscopic structure is investigated (see Fig. 4.2). Earlier investigations show that variations in the powder calcination duration, the milling and pressing of the powder, and the polishing procedure of the pellets have only minor influences on the conductivity.<sup>[1]</sup> In contrast, contacting the sample surface, which was painted with Pt paste, with either Pt wire or mesh leads to different conductivities. Therefore, all samples were contacted similarly. The impedance spectroscopy measurements and grain size analyses in this chapter were performed by Mark Bispinghoff.

For polycrystalline samples, the total conductivity is influenced by the bulk and grain boundary domain (see Chapter 2.4.2 and 4.1.5). Using impedance spectroscopy and the Bauerle model, Zajac and Molenda found for  $\text{Ce}_{0.85}\text{Sm}_{0.15}\text{O}_{1.925}$  that the grain boundary conductivity is only 4 % of the bulk conductivity at 320 °C.<sup>[170]</sup> In this work, the differences between both domains is smaller (Fig. 8.2). Nevertheless, the total conductivity is dominated by the smaller grain boundary conductivity.<sup>[301]</sup> Thus, an optimization of the grain boundary conductivity is desirable.

### Possible Influences on the Ionic Conductivity

For a sample with given composition, the conductivity can be influenced by intrinsic and extrinsic effects. Intrinsic influences are cation ordering, space charge zones and grain boundary segregation. Extrinsic influences are porosity and impurities.

Different sintering temperatures might lead to different cation distributions. Combined MMC and KMC simulations of  $\text{Ce}_{0.85}\text{Sm}_{0.15}\text{O}_{1.925}$  according to Chapter 4.2.2 showed no influence on the ionic conductivity at 173 °C (446 K) of the bulk for equilibration temperatures ( $T_2$ ) between 1111 °C (1384 K) and infinite temperature (see Fig. 8.1). MMC simulations were performed by Steffen Grieshammer.

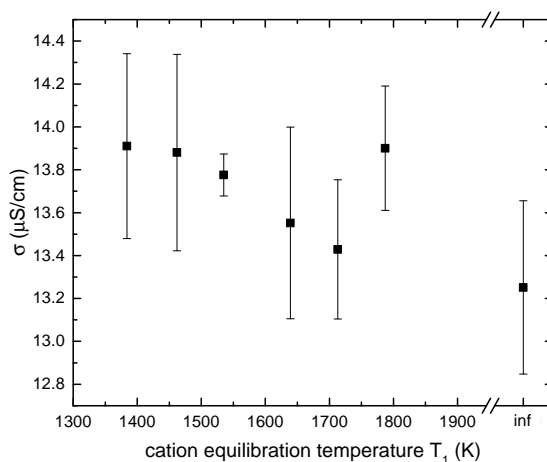


Figure 8.1: Ionic conductivity of  $\text{Ce}_{0.85}\text{Sm}_{0.15}\text{O}_{1.925}$  at 173 °C based on MMC and KMC simulations as a function of cation equilibration temperature. The infinite cation equilibration temperature is marked with ‘inf’.

Generally, in acceptor doped fluorite and perovskite structures, the grain boundary conductivity is smaller compared to the bulk conductivity since space charge zones are present.<sup>[431–435]</sup> TEM measurements show that at most dislocations rather oxygen vacancies than cation interstitials are present. Several studies confirm that the formation of oxygen vacancies in grain boundaries is favored<sup>[436]</sup> and the diffusion perpendicular to the grain boundary is hindered.<sup>[315,437–446]</sup> The positively charged dislocations lead to a depletion of oxygen vacancies near the grain boundary.<sup>[438,439,447]</sup> The same is true for other dislocations.<sup>[389]</sup> Therewith the charge carrier concentration is low and the grain boundary conductivity is low compared to the bulk.<sup>[337,434,444,448,449]</sup>

The positively charged dislocations may lead to an accumulation of cations, which have a lower valence than the host cation (e.g. rare-earth dopants). At high sintering temperatures, cations are mobile in ceria and dopants may move to the grain boundary due to the space charge zones.<sup>[450]</sup> This grain boundary segregation may increase the grain boundary conductivity. For very small dopant fractions, the dopant concentration in the bulk decreases significantly and may lead to a lower bulk conductivity. The grain boundary segregation increases for smaller grain sizes.<sup>[337]</sup>

Impurities beyond the powder composition are also deposited especially at the grain boundaries. In literature, especially silicon dioxide ( $\text{SiO}_2$ ) is detected, which originated probably from the furnace during the sintering process. X-ray Photoelectron Spectroscopy (XPS) shows that thin, uniform films of  $\text{SiO}_2$  are deposited at temperatures below  $1400\text{ }^\circ\text{C}$ . The deposited  $\text{SiO}_2$  decreases the ionic conductivity, especially for the grain boundary domain. At higher temperatures impurities appear at triple points between grains leading to a smaller influence on the grain boundary conductivity.<sup>[451]</sup> For smaller grain sizes, the impurity effect is assumed to be small since many grain boundaries are present and the impurity concentration per grain boundary is small. Thereby, also no continuous impurity films at the grain boundaries occur.<sup>[300]</sup>

Finally, high porosity blocks the conduction paths generally leading to lower conductivities.<sup>[298]</sup> In fact, also the pore shape, size and spatial distribution influence the conductivity.

### Sintering and the Ionic Conductivity according to Experiments in this Work

Influences of the porosity (Fig. 4.2) on the ionic conductivity are assumed to be small for samples sintered above  $1260\text{ }^\circ\text{C}$  or with sintering durations above 24 hours at  $1190\text{ }^\circ\text{C}$ .

For increasing sintering temperature (blue arrow in Fig. 4.3), Fig. 8.2 shows the macroscopic ionic conductivity of the bulk (left) and grain boundary domain (right) at constant sintering time. The order of precedence for the conductivity between samples is similar in bulk and grain boundary domain, with the exception of the sample sintered at  $1500\text{ }^\circ\text{C}$ . As the order of precedence is similar at all measured temperatures, Fig. 8.3 (left) gives a quick view of the conductivity trends. While grain size (and density) increases with increasing sintering temperatures, the conductivities change without a monotonous trend.

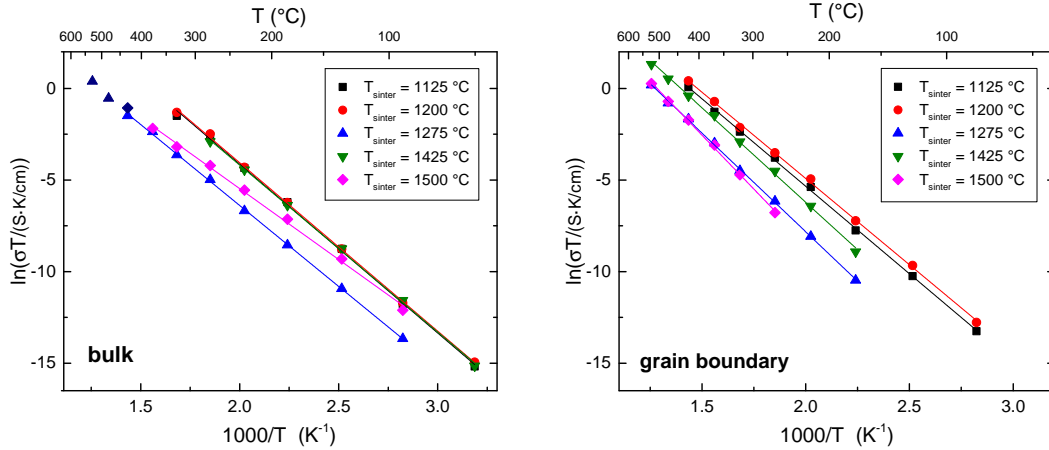


Figure 8.2: Ionic conductivity of bulk (left) and grain boundary domain (right) for different sintering temperatures after  $t_{\text{sinter}} = 10\text{ h}$  according to impedance experiments.

In Fig. 8.3 (right), all other measurements are included. For increasing sintering durations (red arrow in Fig. 4.3), no clear trend can be found for increasing grain size. While e.g. for the bulk

domain at 1200 °C the ionic conductivity first in- and then decreases with increasing sintering duration, at 1500 °C the ionic conductivity first de- and then increases. For similar grain sizes, few samples show similar properties in bulk and grain boundary domain (e.g. 1275-35 and 1350-20 for all temperatures) while others show different results (e.g. 1275-10 and 1275-35 for all temperatures). Generally, a decrease in conductivity with increasing grain size can be found with several exceptions.

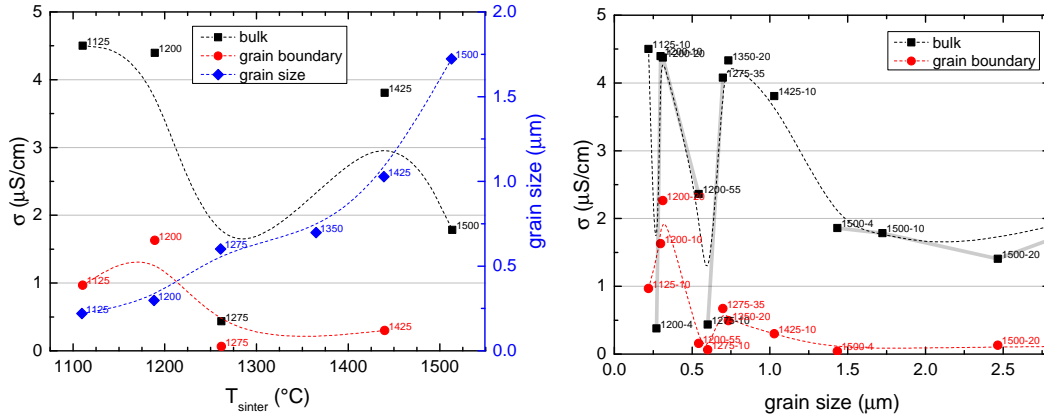


Figure 8.3: Ionic conductivity at 173 °C according to impedance experiments as a function of sintering temperature after  $t_{\text{sinter}} = 10$  h (left) and for all measurements as a function of grain size (right). Lines are a guide to the eye only.

This behavior is unexpected especially for the bulk domain, where the conductivity was reported to be either independent of the microstructure or increasing for higher densities. Though influences of the grain sizes and shape are reported in literature, these effects are assumed to be small in this work.<sup>[329]</sup> The scattering of the ionic conductivity can also be clearly seen in the Nyquist plot of the impedance measurements. Here, semicircles overlap resulting in semicircles, which are influenced by several domains. Therefore, the analysis method of the semicircles is probably not valid here. Having said that, the differences in the Nyquist plot show a significant influence on the conductivity behavior due to different sintering properties, confirming the initial thesis:

### The sintering process strongly influences the ionic conductivity.

Figure 8.4 (left) shows that the influence of the grain boundary domain on the total conductivity, according to the series brick layer model (S-BLM) (Eq. 4.12), decreases with increasing measuring temperature in this work and in literature.<sup>[297,300]</sup> Higher sintering temperatures lead to a larger influence on the total conductivity in literature and in this work, with the exception of the sample sintered at 1125 °C. Generally, for larger grain sizes, the influence of the grain boundary domain on the total conductivity increases in this work and in literature (Fig. 8.4 right).<sup>[74]</sup>

The activation enthalpy of the bulk domain decreases for larger sintering temperatures and grain sizes (Fig. 8.5). Again, no influence of the microstructure on the activation enthalpy of the bulk

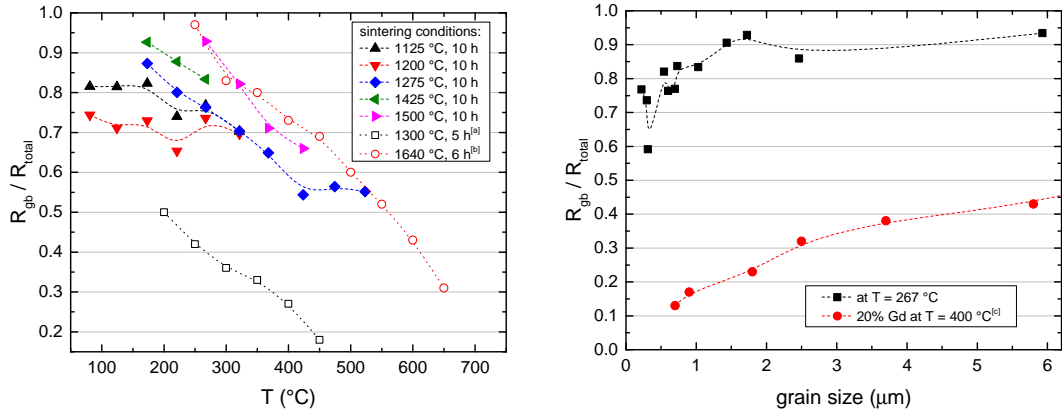


Figure 8.4: Grain boundary contribution to the resistivity according to impedance experiments as a function of measuring temperature (left) and grain size (right) for  $Ce_{0.85}Sm_{0.15}O_{1.925}$  with data from [a] Wang *et al.*,<sup>[297]</sup> [b] Zhan *et al.*<sup>[300]</sup> and [c] Zhan *et al.*<sup>[74]</sup> Lines are a guide to the eye only.

domain was reported in literature.<sup>[297,298]</sup> The activation enthalpy of the grain boundary domain increases for larger sintering temperatures and grain sizes (Fig. 8.5). Several outliers can be observed.

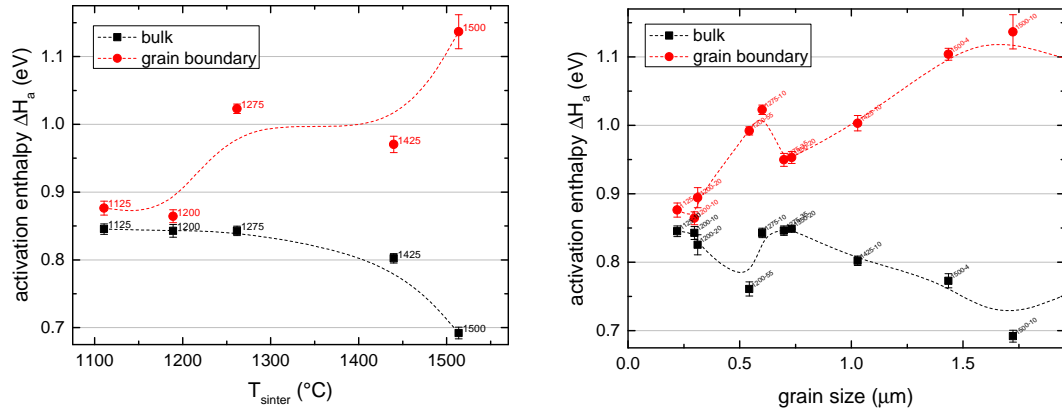


Figure 8.5: Activation enthalpy according to impedance experiments as a function of sintering temperature for  $t_{sinter} = 10$  h (left) and grain size (right). Lines are a guide to the eye only.

## Sintering and the Ionic Conductivity according to Literature

Generally, the ionic conductivity depends on the porosity and several methods have been developed to compare samples with different densities.<sup>[184,248,249]</sup> Pérez-Coll *et al.*,<sup>[298]</sup> Tian and Chan<sup>[194]</sup> and Reis *et al.*<sup>[430]</sup> reported an increase in bulk conductivity for samples with larger grain sizes and therefore higher densities. However, Singh *et al.*<sup>[404]</sup> reported a decrease in bulk conductivity with larger grain size due to an increase in grain boundary conductivity. Sánchez-Bautista *et al.*<sup>[69]</sup> showed for  $Ce_{0.9}Dy_{0.1}O_{1.95}$  slightly higher bulk conductivity at lower sintering temperature and

grain size. In this work, influences of the porosity (Fig. 4.2) on the ionic conductivity are assumed to be small especially for samples sintered above 1260 °C or with sintering durations above 24 hours at 1190 °C.

Beyond that, the ionic conductivity of the bulk domain is assumed to be independent of macroscopic structure. Zhang *et al.*<sup>[300]</sup> and Yan *et al.*<sup>[301]</sup> showed that the bulk conductivity is independent of grain size for samples with densities of at least 95 % (Fig. 8.6 left). Sánchez-Bautista *et al.*<sup>[69]</sup> showed for  $\text{Ce}_{0.85}\text{Dy}_{0.15}\text{O}_{1.925}$  and  $\text{Ce}_{0.8}\text{Dy}_{0.2}\text{O}_{1.9}$  a bulk conductivity independent of sintering temperature and grain size. Beyond that, it may be possible that samples are not fully oxidized due to short sintering at low temperatures. Especially the samples sintered at 1110 °C might be oxygen deficient (non-stoichiometric ceria, see Chapter 2.1.3).

The ionic conductivity of the grain boundary domain was reported to be both increasing<sup>[298,404]</sup> and decreasing<sup>[69,297,300,301]</sup> with larger grain sizes. Pérez-Coll *et al.*<sup>[298]</sup> attributed the increase in macroscopic grain boundary conductivity with increasing grain size to the brick layer model (see Chapter 4.1.5). With increasing grain size, the total number of grains decreases. For a constant microscopic grain boundary resistivity and thickness, the macroscopic grain boundary conductivity increases with increasing grain size. Ding *et al.*<sup>[297]</sup> and Sánchez-Bautista *et al.*<sup>[69]</sup> attributed the decrease in macroscopic grain boundary conductivity with increasing grain size to the space charge zones: For larger grain sizes, the space charge potential increases. Here, the depletion of oxygen vacancies near the grain boundary increases and the macroscopic grain boundary conductivity decreases. Zhang *et al.*<sup>[300]</sup> argued that, for larger grain sizes, the area of the grain boundary decreases. Therefore, the blocking impurity concentration increases and the macroscopic grain boundary conductivity decreases. Finally, Tian and Chan<sup>[194]</sup> found an increase followed by a decrease in grain boundary conductivity with increasing grain size. For the latter they assumed for large grain sizes, due to the high sintering temperatures, either that the dopant segregates to the grain boundaries and associates with oxygen vacancies or a continuous Si-rich glassy phase in the grain boundaries reduces the conductivity.

Ionic conductivities in this work and literature show strong scattering but are generally in agreement (Fig. 8.6 left).

The microstructure has only a minor influence on the activation enthalpy for the bulk and grain boundary domain according to literature (Fig. 8.6 right).<sup>[297,298,300,301]</sup> However, different sintering methods lead to significantly different activation enthalpies.<sup>[297]</sup> Van Dijk and Burggraaf<sup>[323]</sup> reported that in Gd doped zirconia the activation enthalpy for the grain boundary conductivity is independent of composition, grain size and preparation method.

The activation enthalpy in this work is in agreement with literature, where scattering occurs especially between different preparation methods.

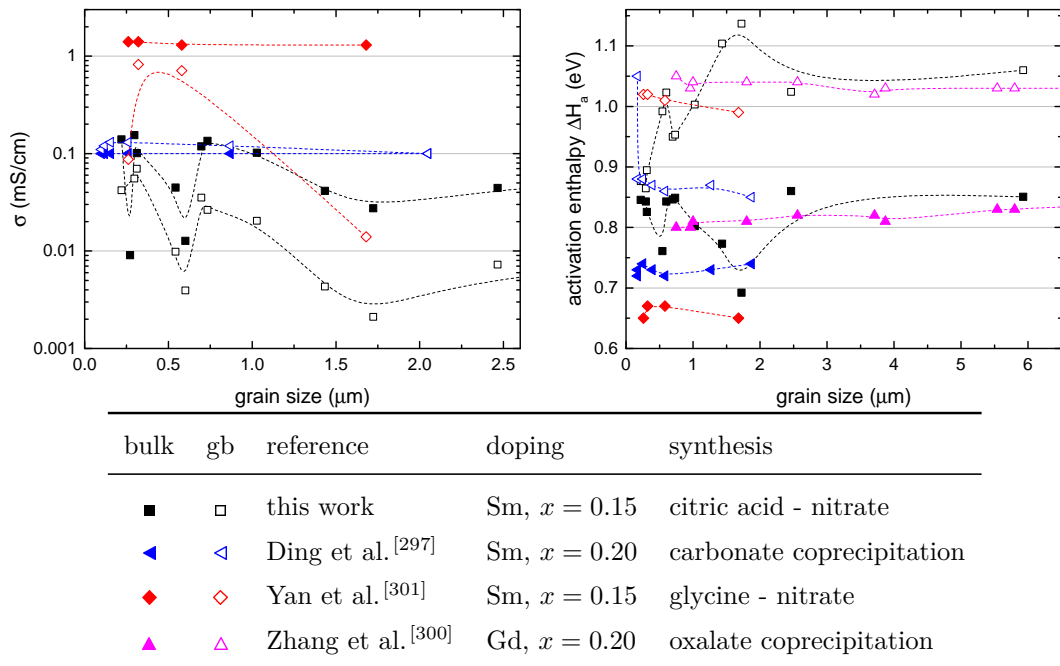


Figure 8.6: Conductivity at 267 °C and activation enthalpy according to impedance experiments as a function of grain size. Bulk and grain boundary (gb) domain is shown. Lines are a guide to the eye only.

## The Microscopic Grain Boundary Conductivity

The grain boundary thickness  $\delta_{gb}$  and the microscopic grain boundary conductivity were calculated according to Eqs. 4.9 and 4.10 (Fig. 8.7). While the pseudo-capacitance of the bulk domain is independent of the grain size, the pseudo-capacitance of the grain boundary domain increases with increasing grain size according to literature.<sup>[176]</sup> The behavior of the grain boundary capacitance is unexpected, since the number of grain boundaries decreases with increasing grain size leading to a decrease of the macroscopic grain boundary capacitance for similar grain boundary thicknesses.

A grain boundary thickness between 0.8 nm and 7.7 nm was calculated, the thickness mainly decreases with increasing grain size. Similar thicknesses were reported in literature with  $(3 \pm 0.5)$  nm for  $Ce_{0.8}Gd_{0.2}O_{1.9}$ ,<sup>[176]</sup> and  $1.2 \pm 0.5$  nm for  $Ce_{0.9}Gd_{0.1}O_{1.95}$ ,<sup>[298]</sup> or between 3 nm and 50 nm for differently doped ceria.<sup>[306]</sup> For nanocrystalline-structured doped ceria, also smaller grain boundary thicknesses can be found.<sup>[338]</sup>

The microscopic grain boundary conductivity is up to three orders of magnitude smaller than the macroscopic grain boundary conductivity. Both show a similar behavior with increasing grain sizes above 0.5  $\mu\text{m}$ , as the influence of the grain boundary thickness is small. The microscopic grain boundary conductivity decreases strongly from 35 nS/cm to about 1 nS/cm at 173 °C for increasing grain sizes up to 0.6  $\mu\text{m}$  and is independent of grain size for larger grain sizes. Christie and van Berkel<sup>[176]</sup> also report a strong decrease followed by similar microscopic grain boundary

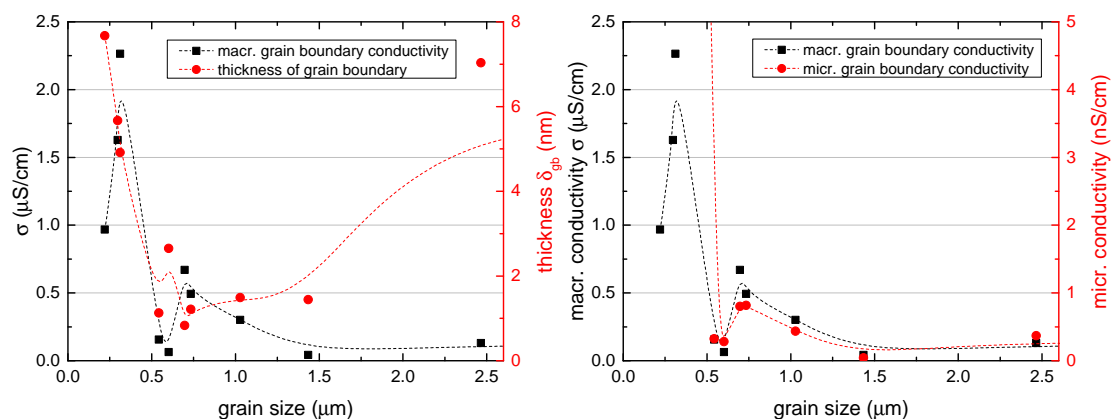


Figure 8.7: Macroscopic and microscopic conductivity at 173 °C according to impedance experiments as well as grain boundary thickness for different grain sizes. Lines are a guide to the eye only.

conductivities for increasing grain sizes. Large microscopic grain boundary conductivities were also reported in doped zirconia by van Dijk and Burggraaf.<sup>[323]</sup> The reason for this behavior may be the serial brick layer model, which cannot be used for small grain sizes. For larger grain sizes, Christie and van Berkel<sup>[176]</sup> explain a small increase in microscopic grain boundary conductivity based on the decreasing number of grain boundaries for a constant grain boundary thickness. In this work, the fluctuation of the macroscopic grain boundary conductivity propagates in the microscopic grain boundary conductivity, probably caused by several influences that superimpose.

In fact, different sintering durations and sintering temperatures lead to different bulk conductivities.

## 8.2 The Influence of Doping

### 8.2.1 Simulating the Ionic Conductivity

Ionic conductivities for different rare-earth doped ceria were calculated using KMC simulations based on the migration energy model  $c1+sd$  [ds] with an interaction radius of 5.41 Å, which was developed in Chapter 7.2. In Fig. 8.8, ionic conductivities at 500 °C for Lu, Yb, Y, Gd, Sm, Nd and La doped ceria are compared. A heat map of the data can be found in the appendix (Fig. 9.11). The conductivity depends strongly on temperature as shown in Fig. 8.9 for 267 °C and 600 °C. Error bars show the sample standard deviation  $\sigma_s$  of 10 simulations, which indicates the expected range for the next simulation. The error for the true conductivity value is significantly smaller.

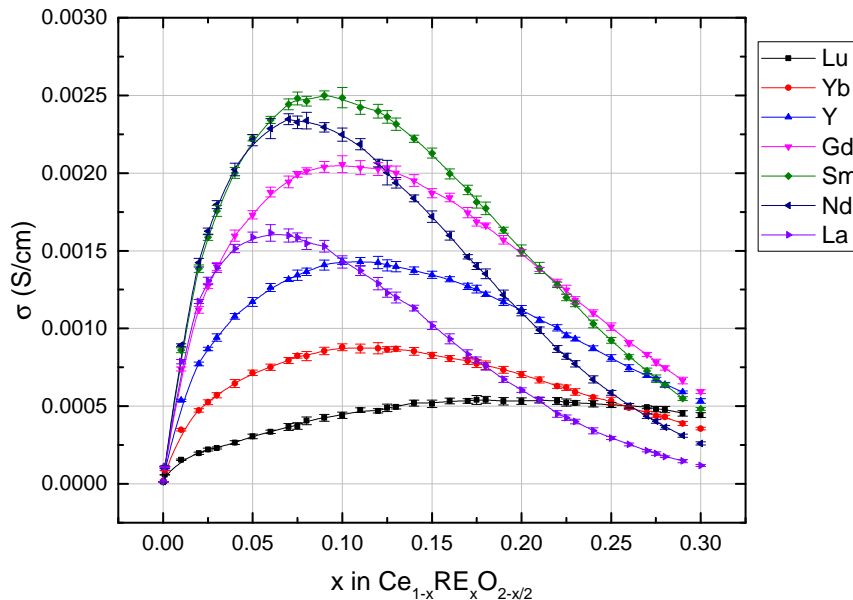


Figure 8.8: Ionic conductivity of rare-earth doped ceria at 500 °C with RE = Lu, Yb, Y, Gd, Sm, Nd and La calculated using KMC simulations. Lines are a guide to the eye only.

The KMC simulations predict smaller conductivities than found in most experiments. This may be caused by underestimated attempt frequencies or overestimated migration energies in the simulation. Alternatively, the separation of bulk and grain boundary conductivity in experiments may not be sufficient. Especially for impedance spectroscopy experiments, the bulk contributions cannot be seen at 500 °C due to the limited frequency range in experiments and is often extrapolated. Therefore, in this work, impedance measurements at low temperature were performed for Sm (Chapter 8.2.2), Gd (Chapter 8.2.3) and Lu doped ceria (Chapter 8.2.5) and compared with simulations (Chapter 8.2.6).

The ranking order for highest conductivity between different dopants is similar for different dopant fractions in simulations and experiments, despite the strong scattering. For low dopant fractions, measurements of Nd doped ceria often show higher conductivities than measurements of Gd doped ceria. For large dopant fractions, this ranking order is reversed similar to the KMC simulations.

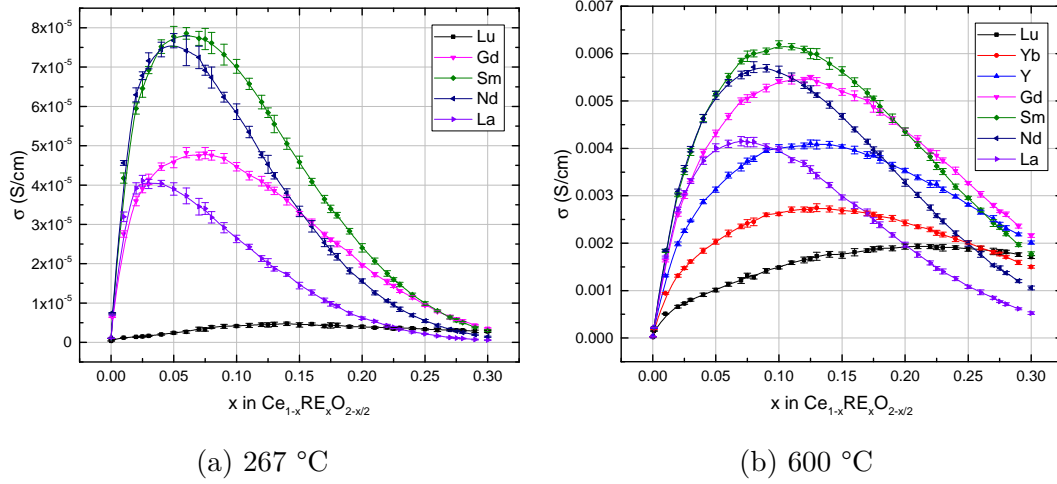


Figure 8.9: Ionic conductivity of rare-earth doped ceria at 267 °C and 600 °C with RE = Lu, Yb, Y, Gd, Sm, Nd and La calculated using KMC simulations. Lines are a guide to the eye only.

Similarly, measurements of Y doped ceria often show lower conductivities up to  $x = 0.2$ . The largest ionic conductivity is found for Sm doped ceria, dopants with smaller and larger ionic radii lead to lower maximal ionic conductivities. Conductivities of Gd and Sm doped ceria are high in simulations and experiments and are further investigated in Chapter 8.2.3. In the next chapter, a detailed comparison for  $x = 0.1$  and  $0.2$  is performed.

All calculated rare-earth doped ceria show the typical in- and decrease in ionic conductivity with increasing dopant fraction as found in experiments (Chapter 2.4.2). The dopant fraction leading to the maximum in conductivity  $x_{\max}$  (Chapter 2.4.3) and the slope of the curves vary for different dopants. For most dopants, the characteristic maximum  $x_{\max}$  is around 0.1. An exception is Lu doped ceria due to its migration edge energies, which are smaller than in pure ceria (cp. Fig. 7.6). Small errors in the KMC input parameters cause a significant difference in  $x_{\max}$ . Otherwise, the dopant fraction leading to the maximum in conductivity is in agreement with experiments (Table 2.3). Additionally, large dopants like Nd and La lead to small  $x_{\max}$  in simulations and experiments.<sup>[163]</sup> Compared to KMC simulations in literature, a better agreement for  $x_{\max}$  with experiments is found in this work. For example, Dholabhai *et al.* predict at 500 °C a maximum for  $\text{Ce}_{0.8}\text{Sm}_{0.2}\text{O}_{1.9}$  and at 400 °C a maximum for  $\text{Ce}_{0.8}\text{Gd}_{0.2}\text{O}_{1.9}$ .<sup>[224,286]</sup> Grope *et al.* predict at 620 °C a maximum for  $\text{Ce}_{0.85}\text{Y}_{0.15}\text{O}_{1.925}$ .<sup>[287]</sup> In the old model 2014, a maximum for  $\text{Ce}_{0.86}\text{Y}_{0.14}\text{O}_{1.93}$  at 527 °C was predicted.<sup>[55]</sup> In both this work and experiments (Table 2.3) the dopant fractions leading to the maximum in conductivity is smaller.

For 600 °C (Fig. 8.9b), all conductivities increase by a factor of about 2.5–4 (see also Inaba and Tagawa)<sup>[31]</sup> due to the Boltzmann probability. The increase in conductivity is higher for higher dopant fractions since the influence of blocking and trapping decreases with temperature. Though the (randomly ordered) cation configuration is independent of temperature, the number of jump attempts through Ce-Ce edges increases because the larger thermal energy increases the probability

for oxygen vacancies to leave the association radius of the dopant ions (trapping). Furthermore, the probability of jumps through doped migration edges, which have a larger migration energy (blocking), is increased.<sup>[55]</sup> As a result, the maximum of the simulated ionic conductivity is shifted to larger dopant fractions, which is in agreement with experimental data (see Chapter 2.4.3). Especially Y and Gd, which possess strong trapping, lead to high ionic conductivities at higher dopant fractions. At low temperature, the effects reverse and the dopant fractions leading to the maximum in conductivity decrease.

### **x = 0.1 and 0.2**

Similar to literature, the ionic conductivity for a single dopant fraction can be investigated. Though often the total conductivity is presented in literature (Fig. 2.8), only the bulk conductivity represents the inherent property of the doped material largely without influences of the microstructure of the sample. The bulk conductivity in experiments at 400 °C for  $x = 0.1$  and  $0.2$  was summarized in Fig. 2.12.

For comparison, simulated ionic conductivities are shown in Fig. 8.10. The ionic conductivity increases with increasing dopant radius up to Sm and decreases with increasing dopant radius for larger dopants. For  $x = 0.1$  and  $0.2$ , Sm is the optimal dopant with the highest conductivity as already seen in Fig. 8.8 and 8.9.

The bulk conductivity in experiments is about factor 2–4 ( $x = 0.1$ ) or 2–6 ( $x = 0.2$ ) larger than the simulated conductivity (Fig. 8.10c, 8.10d and 9.12 in the appendix). An exception is Nd doped ceria, whose experimental values scatter over more than an order of magnitude. The ranking order between different dopants is similar in experiments and simulation.

In Fig. 8.10 a linear relationship between the ionic radius and the conductivity (solid lines) or the logarithm of the conductivity (dashed lines) is shown. If the conductivity depends linearly on the ionic radius, a relation between lattice distortions and the ionic conductivity can be assumed. If the logarithm of the conductivity depends linearly on the ionic radius, a relation between the activation enthalpy and the ionic conductivity can be assumed. In fact, both relations were already reported in literature: First theories postulated that the highest oxygen ion conductivity occurs for dopants, which result into the least distortion of the crystal lattice as discussed in in Chapter 2.5.2.<sup>[25,30,33,34,167,226–229]</sup> A relation between the activation enthalpy and the ionic conductivity was investigated in Chapter 2.4.4.<sup>[163,164,167,169,196]</sup>

The results in this work and literature (cp. Chapter 2.4) suggest a linear relationship between ionic radius and conductivity. A fit for the linear relationship is shown with the red and blue line in Fig. 8.10. It should be noted that the dashed lines show a linear relationship between the ionic radius and the logarithm of the conductivity. For the simulated conductivity, clearly the former leads to a better regression result.

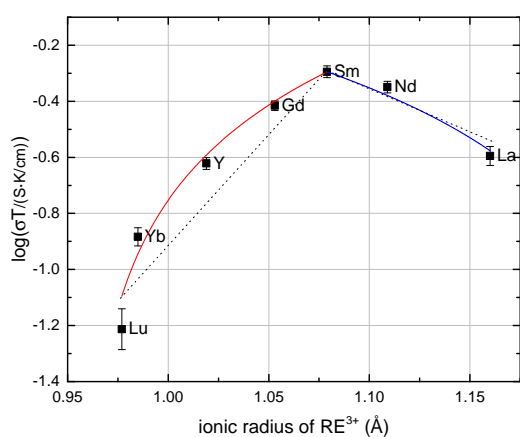
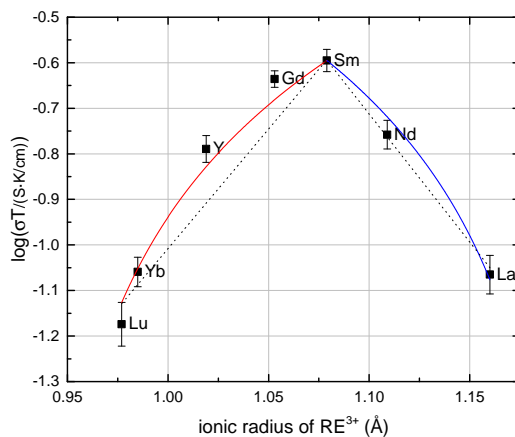
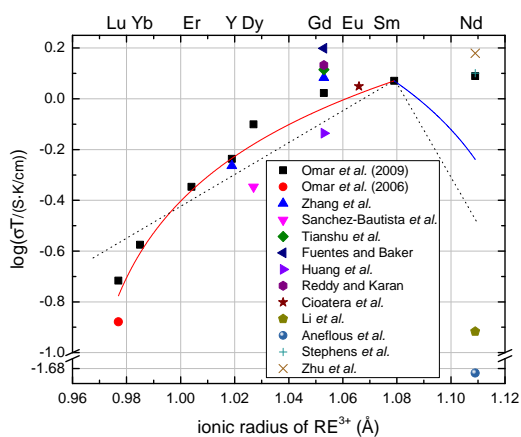
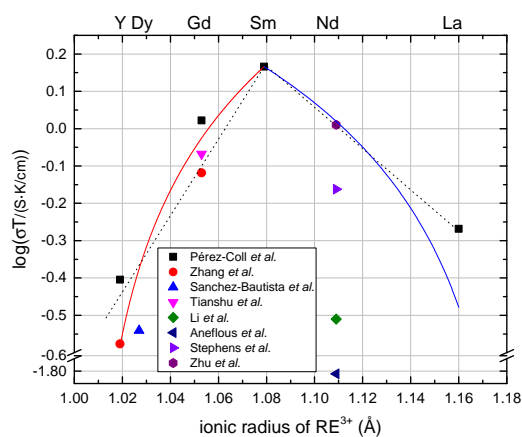
(a) simulation,  $x = 0.1$ (b) simulation,  $x = 0.2$ (c) experiment,  $x = 0.1$ (d) experiment,  $x = 0.2$ 

Figure 8.10: Simulated and experimental ionic conductivity (as already shown in Fig. 2.12) of  $\text{Ce}_{1-x}\text{RE}_x\text{O}_{2-x/2}$  at 400 °C for  $x = 0.1$ , [64,69,75,76,165,166,168,174,177,178,182,183,185] and 0.2, [64,69,75,76,168,169,182,183]. The lines show a possible linear relationship between the ionic radius and the conductivity (solid lines) or the logarithm of the conductivity (dashed lines).

## Trapping and Blocking

The ascending slope of  $\sigma(x)$  (Fig. 8.8) is small for small dopants (e.g. Lu, Yb and Y) and large for large dopants (e.g. La), obviously curve progression and ionic radius are related. This is not surprising, since the association energies (Chapter 5.1.1) and migration energies from DFT calculations (Chapter 7.1.2), which were used in the KMC simulations, are related to the dopant radius. For further investigations, the in- and output parameters of the KMC simulations are categorized and compared.

The migration energy model for the KMC simulations uses three migration edge energies and six association energies as input parameters. Changes in the migration energy compared to pure ceria can be classified as symmetric (blocking) and asymmetric contributions (trapping) as described in Chapter 7.2.3.

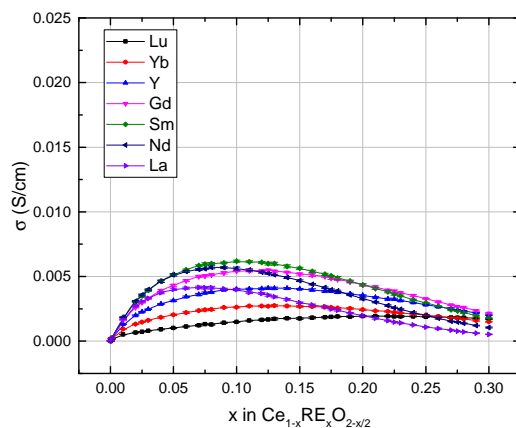
Trapping and blocking are used to describe the experimental ionic conductivity as discussed in Chapter 2.5.1 and theoretical studies.<sup>[54,55,287,429]</sup> Trapping describes the influence of the association between dopant ions and oxygen vacancies on the migration energy. Migration barriers for jumps of the migrating oxygen vacancy away from the associating dopant are higher than in pure ceria, while jumps to the dopant are even more favored. Vacancies appear more often in nearest neighborhood to the defect because they are trapped. Blocking describes energy contributions that increase the migration energy for both the forward jump and the backward jump. Oxygen vacancies are kinetically hindered and therefore blocked. The trapping decreases for larger ionic radii while the blocking effect increases.

In Chapter 7.3 the influence of blocking, trapping and V-V interaction on the ionic conductivity of Sm doped ceria was shown. For this purpose, increased symmetric migration barriers due to dopants around the jump center or association energy contributions due to RE-V association or V-V interaction were neglected. It was found that V-V interactions increase the conductivity as otherwise a strong association of dopants and vacancies takes place.

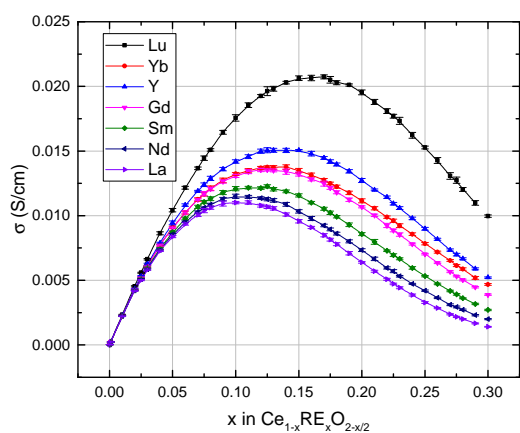
Dopants determine blocking and trapping. Both decrease the conductivity. The dopant fraction leading to the maximum in conductivity is especially limited by blocking.

While these observations were made for Sm doped ceria, similar effects might be found for other rare-earth dopants. The investigation of blocking and trapping is a main goal of this work as they are the only factors that distinguish the conductivity of different rare-earth dopants. Both effects are essential for the understanding of the underlying mechanism that determines the magnitude of the oxygen ion conductivity and the optimal dopant concentration.

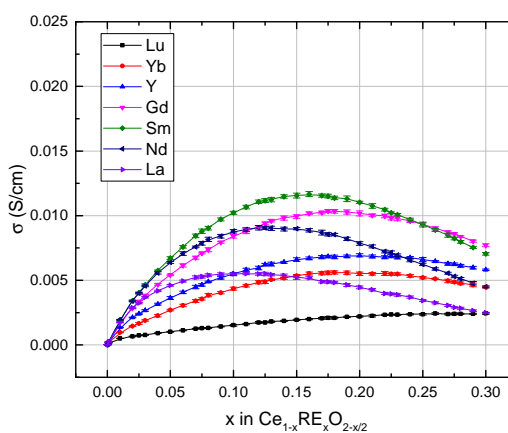
Therefore, KMC simulations at 600 °C were performed for different rare-earth dopants with all (Fig. 8.11a) or only selected interactions as discussed in Chapter 7.3. Either trapping (Fig. 8.11b) or blocking (Fig. 8.11c) was neglected. For the no-trapping case, the blocking effect can also be restricted to the Ce-RE edge by setting the RE-RE edge energy for all dopants to the largest observed value of 1.29 eV. Therefore, dopants differ only by the Ce-RE edge energy (Fig. 8.11d). For the no blocking case, the trapping effects can also be restricted to a 1<sub>NN</sub> RE-V interaction range by



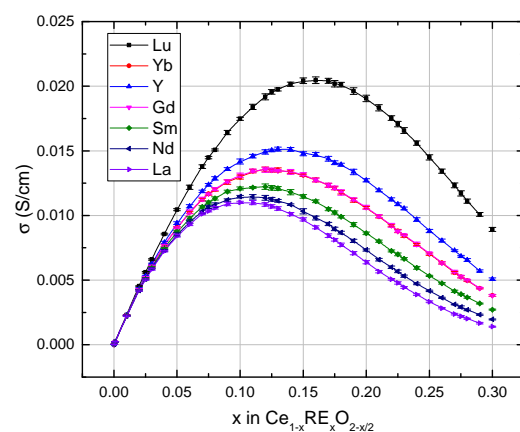
(a) all interactions



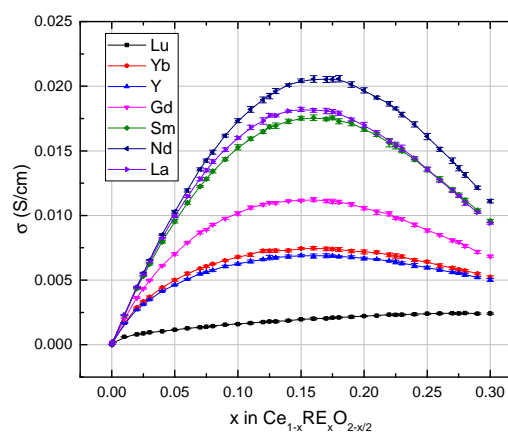
(b) no trapping



(c) no blocking



(d) only different Ce-RE edge



(e) only different  $1_{NN} \leftrightarrow 2_{NN}$  RE-V jump

Figure 8.11: Simulated ionic conductivity of rare-earth doped ceria at 600 °C without considering RE-V interactions around the start and destination position (left) or without considering different migration edges (right). Lines are a guide to the eye only.

terminating at the  $2_{\text{NN}}$  RE-V interaction. Therefore, dopants differ only by the asymmetric energy contribution to the  $1_{\text{NN}} \leftrightarrow 2_{\text{NN}}$  RE-V jump (Fig. 8.11e).

KMC simulations *with* (Fig. 8.11a) and *without trapping* (Fig. 8.11b) show the same ranking order of  $x_{\text{max}}$  between different rare-earth doped ceria. For Gd doped ceria, no change in  $x_{\text{max}}$  is found. Small dopants have lower  $x_{\text{max}}$ , large dopants have higher  $x_{\text{max}}$  with a change up to  $\Delta x = \pm 0.04$ . If the blocking effect is also restricted and dopants differ only by the Ce-RE edge energy (Fig. 8.11d), hardly any change in the conductivity is found. An exception is Yb doped ceria as it has the same Ce-RE edge energy as Gd doped ceria (Fig. 7.6), probably caused by the chosen DFT potential. A comparison between the Ce-RE edge energy and the dopant fraction of the maximum in conductivity is shown in Fig. 8.12 (left). The dopant fraction of the maximum decreases with larger blocking: For higher dopant fractions, the amount of jump configurations influenced by blocking increases. Larger blocking leads to lower conductivities and, therefore, with larger blocking the maximum appears at lower dopant fractions. Hence,  $x_{\text{max}}$  is determined by the Ce-RE edge energy.

However, the number of jumps through doped edges does not change much for larger dopant fractions. In KMC simulations of an earlier work at 700 K, between  $x = 0.02$  and  $0.14$  the number of jumps through Ce-Y edges increases totally only about 4% (35% to 39%).<sup>[55]</sup> Jumps through Y-Y edges are rare (0.04% to 0.14%). Significantly higher are the number of jump attempts, which are not weighted by the Boltzmann probability  $p = e^{-\frac{\Delta E_{\text{mig}}}{k_{\text{B}}T}}$  (cp. Chapter 3.2.2), with 45% to 54% (Ce-Y) and 2% to 11% (Y-Y). The large migration energy of doped edges decreases the number of performed jumps and therefore the ionic conductivity.

The ionic conductivity is high compared to KMC simulations with trapping. The ranking order of conductivities at all dopant fractions is equivalent to the ranking order of Ce-RE edge energies. The ionic conductivity decreases with increasing Ce-RE migration edge energy or rather increasing dopant radius. An exception is Yb doped ceria, due to its low Ce-RE migration edge energy probably caused by the chosen DFT potential.

**Blocking mainly limits the dopant fraction of the maximum.  
Here, the Ce-RE edge energy is decisive.**

KMC simulations at 600 °C *with* (Fig. 8.11a) and *without blocking* (Fig. 8.11c) show nearly the same ranking order of conductivities at all dopant fractions. If the trapping effect is also restricted and dopants differ only by the asymmetric contribution to the  $1_{\text{NN}} \leftrightarrow 2_{\text{NN}}$  RE-V jump (Fig. 8.11e), the ranking order of conductivities changes significantly and is equivalent to the ranking order of the absolute value of the  $|2_{\text{NN}} - 1_{\text{NN}}|$  RE-V association energy difference (Fig. 5.1). A comparison between association energy difference and ionic conductivity of the maximum is shown in Fig. 8.12 (right). The ionic conductivity decreases with increasing absolute value of the  $|2_{\text{NN}} - 1_{\text{NN}}|$  RE-V association energy difference or rather increasing dopant radius. Sm and La doped ceria have similar conductivities though in Sm doped ceria the  $1_{\text{NN}}$  RE-V association and in La doped ceria the  $2_{\text{NN}}$  RE-V association is favored. Large  $|2_{\text{NN}} - 1_{\text{NN}}|$  RE-V association energy differences lead to steep slopes. If

again the full trapping effect is considered and therefore  $2_{\text{NN}} \rightarrow 3_{\text{NN}}$ ,  $2_{\text{NN}} \rightarrow 4_{\text{NN}}$  and  $4_{\text{NN}} \rightarrow 4_{\text{NN}}$  RE-V jumps have different migration energies, the conductivities decrease with increasing  $2_{\text{NN}}$  RE-V association energy or rather  $|3_{\text{NN}} - 2_{\text{NN}}|$  RE-V association energy difference. The decrease occurs especially at large dopant fractions if the  $|2_{\text{NN}} - 1_{\text{NN}}|$  RE-V association energy difference is small. The decrease occurs especially at small dopant fractions if the  $|2_{\text{NN}} - 1_{\text{NN}}|$  RE-V association energy difference is large. In other words, if the conductivity in Fig. 8.11e is high, the conductivity in Fig. 8.11c is smaller, especially at large dopant fractions. For intermediate  $2_{\text{NN}}$  RE-V association energies, even an increase in conductivity at large dopant fractions can be found. This results into crossings in the ranking order of conductivities. Hence, the ranking order of conductivities is determined by the  $|2_{\text{NN}} - 1_{\text{NN}}|$  and  $|3_{\text{NN}} - 2_{\text{NN}}|$  RE-V association energy differences.

The dopant fraction leading to the maximum in conductivity is similar for different dopants if only the  $|2_{\text{NN}} - 1_{\text{NN}}|$  RE-V association energy differences are considered. An exception is Lu doped ceria due to strong trapping. Including the  $|3_{\text{NN}} - 2_{\text{NN}}|$  RE-V association energy differences increases  $x_{\text{max}}$  for large  $2_{\text{NN}} - 1_{\text{NN}}$  RE-V association energy differences and decreases  $x_{\text{max}}$  for negligible or negative  $2_{\text{NN}} - 1_{\text{NN}}$  RE-V association energy differences. Here, Sm and La doped ceria show different behavior. This is shown in Fig. 8.12 (left). Surprisingly, the change in  $x_{\text{max}}$  seems to be independent of the  $3_{\text{NN}} - 2_{\text{NN}}$  RE-V association energy difference. The dopant fraction leading to the maximum in conductivity is only directly controlled by the formation of RE-V associates if vacancies are already decelerated in the vicinity of the dopant due to the  $2_{\text{NN}}$  association energy.

Though the resulting ranking order of  $x_{\text{max}}$  between different rare-earth doped ceria is similar to the final KMC simulations, the values of  $x_{\text{max}}$  are too large. Figure 8.12 (left) shows the dopant fraction of the maximum if only blocking is considered. Large  $2_{\text{NN}} - 1_{\text{NN}}$  RE-V association energy differences increase and small  $2_{\text{NN}} - 1_{\text{NN}}$  RE-V association energy differences decrease  $x_{\text{max}}$ . Therefore, the dopant fraction leading to the maximum in conductivity is influenced by both trapping and blocking, but dominated by blocking.

Trapping mainly limits the maximum ionic conductivity.  
Here, the association energy differences are decisive.

In summary, both trapping and blocking decrease the conductivity. However, the ranking order of conductivities is only reproduced by trapping. The dopant fraction of the maximum  $x_{\text{max}}$  is limited by blocking as neglecting the RE-V association barely influences the dopant fraction of the maximum. For 500 °C, similar observations can be made (Fig. 9.13 in the appendix). In literature, the common assumption is made that association between oxygen vacancies and dopants cause the maximum in oxygen ion conductivity (Chapter 2.5.1). On the one hand, the result of this work indeed shows that trapping creates the ranking order of conductivities between different dopants and even has an influence on  $x_{\text{max}}$ . On the other hand, this work shows that the dopant fraction leading to the maximum in conductivity is limited by blocking. The optimal dopant concentration cannot be predicted based on trapping. This defies the assumption in literature.

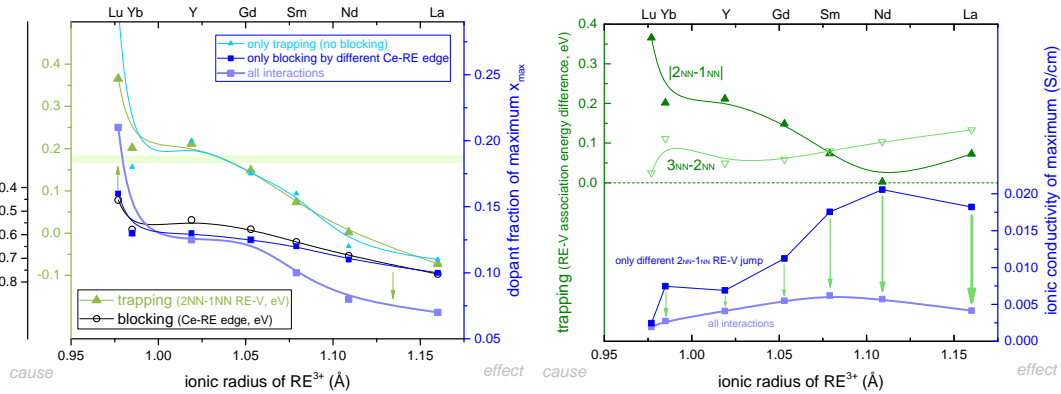


Figure 8.12: Relationship between blocking and trapping and the simulated ionic conductivity for different dopants at 600 °C. A comparison between the Ce-RE migration edge energy (blocking) and the dopant fraction of the maximum (left) or the the RE-V association energy difference (trapping) and the ionic conductivity of the maximum (right) is shown. For comparison, interactions are switched off individually. Lines are a guide to the eye only.

### Blocking is strongly underrated in literature.

The largest conductivity can be found if the absolute values of the association energy differences are small. The  $2_{NN} \leftrightarrow 1_{NN}$  RE-V association leads to the formation of associates (either  $1_{NN}$  or  $2_{NN}$ ). As a result, vacancies are held by the dopants as their movement is hindered. The long-range  $3_{NN} \leftrightarrow 2_{NN}$  RE-V association pulls vacancies into the vicinity of dopants. Both need to be small for a large ionic conductivity.

Not only a low associate formation but also a low vacancy pull  
is important for a large ionic conductivity.

For this purpose, the associate formation can be described as a hold of the vacancy and the vacancy pull as a catch of the vacancy, resulting in the term catch-and-hold principle. Sm with medium blocking and medium trapping has the largest maximum ionic conductivity. If the right value of the maximum ionic conductivity should be predicted, both trapping and blocking should be included.

### Activation Enthalpy

Macroscopic activation enthalpies and experimental attempt frequencies deduced from the KMC simulations were calculated at 500 °C and 600 °C (Fig. 8.13) according to Eqs. 2.3 and 2.4. It should be noted that the input parameter for the KMC simulations like the microscopic attempt frequency (here similar for all ionic configurations) and migration energy model are independent of dopant fraction and temperature. No reduction of ceria was taken into account.

The activation enthalpy at low dopant fractions is equal to the migration energy in pure ceria

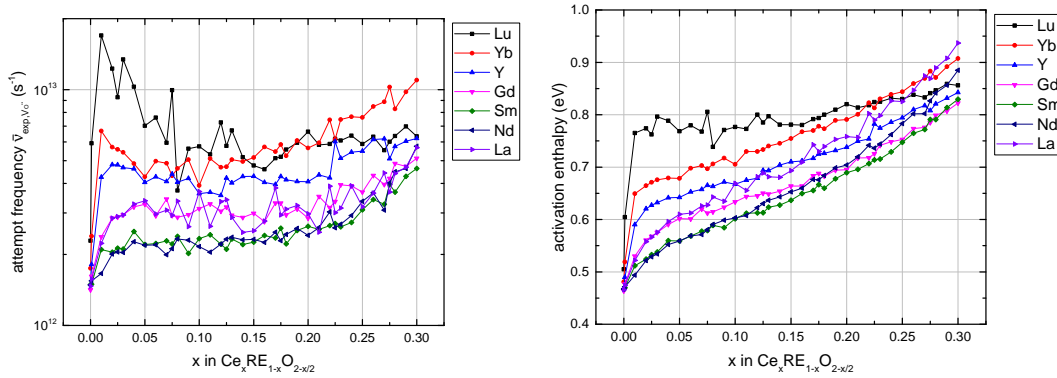


Figure 8.13: Apparent attempt frequency (left) and activation enthalpy (right) for the simulated conductivity of rare-earth doped ceria at 500 °C and 600 °C. Lines are a guide to the eye only.

of about 0.47 eV. The activation enthalpy increases with increasing dopant fraction. Here, RE-V and V-V interactions increase the appearing migration energies. Contrary to literature results (cp. Fig. 2.16), no minimum in the activation enthalpy can be found. Impurities, reduction dominated conductivities or association could explain the higher activation enthalpies in experiments at low dopant fractions (cp. Chapter 6.3.2). Activation enthalpies in simulations are smaller than in experiments (Fig. 9.14 in the appendix). A non-sufficient separation of bulk and grain boundary conductivity in experiments may lead to overall higher activation enthalpies. In simulations, large and small dopants have high activation enthalpies. Dopants that lead to high conductivities have low activation enthalpies (Sm and Nd). Similarly, the change in rank of dopants at a specific concentration correlates in conductivity and activation enthalpy. Both effects are expected since the activation enthalpy dominates the conductivity according to Eqs. 2.3 and 2.4. The ranking order between different dopants is similar in simulations and experiments; even the crossing between La and Gd doped ceria at low dopant fractions is found in simulations similar to the work of Faber *et al.*<sup>[163]</sup> Exceptions are low activation enthalpies in simulations for Nd doped ceria at all dopant fractions and high activation enthalpies in simulations for La doped ceria at high dopant fractions. However, for the former, the ionic conductivity strongly scatters between different groups and, for the latter, only few activation enthalpies are reported.

Similar to the conductivity, the activation enthalpy can be calculated for KMC simulations with all (Fig. 9.15a in the appendix) or only selected interactions. Either trapping (Fig. 9.15b) or blocking (Fig. 9.15c) was neglected. Both influence the final activation enthalpy. Again, the no-trapping case (Fig. 9.15b) and the only different Ce-RE edges case (Fig. 9.15d) are similar. Here, the activation enthalpy increases with increasing Ce-RE edge energy and increasing dopant fraction. Again, the no blocking (Fig. 9.15c) and the only different  $1_{NN} \leftrightarrow 2_{NN}$  RE-V jump case (Fig. 9.15e) differ. Here, the activation enthalpy increases with increasing  $|2_{NN}-1_{NN}|$  and  $3_{NN}-2_{NN}$  RE-V association energy differences and increasing dopant fraction. Again, the increase occurs especially at large dopant fractions if the  $|2_{NN}-1_{NN}|$  RE-V association energy difference is small (e.g. for Nd doped ceria).

Similar to the maximum ionic conductivity,  
the activation enthalpy is dominated by trapping.

The apparent, average or experimental attempt frequency at low dopant fractions is equal to the microscopic attempt frequency of about  $1.47 \cdot 10^{12} \text{ s}^{-1}$ , which was used for the KMC simulations. Again, contrary to experiments (cp. Fig. 9.16 in the appendix), the apparent attempt frequency is low and no minimum at low dopant fractions was found. Impurities, reduction dominated conductivities or association could explain the higher activation enthalpies in experiments at low dopant fractions (cp. Chapter 6.3.2). Similar to the activation enthalpy, the experimental attempt frequency increases with increasing dopant fraction. In fact, the experimental attempt frequency can be shown as a function of the activation enthalpy (Fig. 8.14 left).

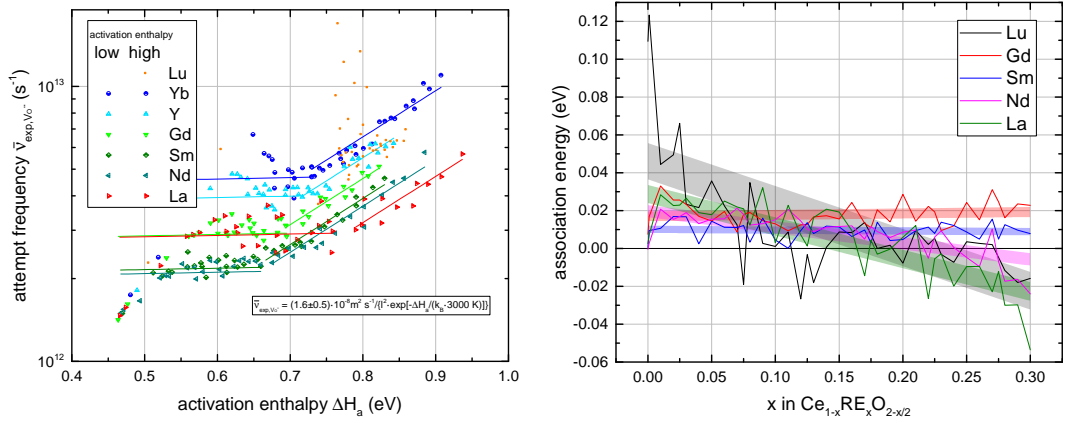


Figure 8.14: Apparent attempt frequency as a function of activation enthalpy for simulations at 500 °C and 600 °C (left). A fit according to Eq. 6.5 for infinite large temperature (constant attempt frequency) and 3000 K is shown. Experimental association energy calculated from the activation enthalpy difference between 500 °C and 600 °C as well as 267 °C and 500 °C (right). For comparison, a 80 % confidence interval of a linear fit is shown.

For low dopant fractions and activation enthalpies, the apparent attempt frequency is independent of activation enthalpy. For large dopant fractions and activation enthalpies, an increase of the apparent attempt frequency with increasing activation enthalpy is found as discussed in Chapter 6.3.2 according to Eq. 6.5 with a high temperature of 3000 K. The correlation verifies that the apparent attempt frequency is changed by the distribution of appearing migration energies even for doped ceria. The dependence of the apparent attempt frequency on the activation enthalpy still depends on the type of dopant. Therefore, activation enthalpy and apparent attempt frequency depend differently on the distribution of appearing migration energies.

For large and small dopants, the change between both regimes takes place at high activation energies ( $H_a = 0.73 \text{ eV}$  for Yb and  $0.76 \text{ eV}$  for La). For dopants that lead to high conductivities, the change takes place at low activation energies ( $H_a = 0.66 \text{ eV}$  for Sm and Nd). Large and small

dopants have high attempt frequencies, dopants that lead to high conductivities have low attempt frequencies. Though high conductivities can be caused by high attempt frequencies as well as low activation enthalpies, the KMC simulations show that for differently doped ceria especially low activation enthalpies are important. The low apparent attempt frequencies for Sm doped ceria are a result of these low activation enthalpies.

The change in the attempt frequency behavior appears around  $x = 0.12$  (Yb) and  $0.22$  (La). The increase in attempt frequency at higher dopant fractions can also be seen in Fig. 8.14. This increase appears even without considering trapping effects or the RE-RE edge energy as shown in Fig. 9.16d in the appendix, where a minimum in attempt frequency appears. The transition between the two regimes where the attempt frequency is either independent or dependent on the activation enthalpy is therefore controlled by the Ce-RE edge energy. If vacancies are blocked, the apparent attempt frequency increases as already demonstrated using a simple model in Chapter 6.3.3.

If only the Ce-RE edge is considered, the attempt frequency de- and increases with increasing dopant fraction. Starting from the KMC input value  $1.47 \cdot 10^{12} \text{ s}^{-1}$ , the decrease appears especially for large Ce-RE edge energies. It has already been shown that for single vacancy and increasing blocking the apparent attempt frequency increases (Chapter 6.3.3). The observed decrease is, therefore, a concentration effect. The number of vacancies increases with increasing dopant fraction, but many of them are blocked. The diffusion of the remaining free vacancies is summed up relative to the number of all vacancies. If, theoretically, all vacancies would be blocked on a microscopic level, the macroscopic attempt frequency and especially the macroscopic activation enthalpy would increase. This happens at intermediate and large dopant fractions. The no-trapping case is similar (Fig. 9.16b).

Again, the no blocking (Fig. 9.16c) and only different  $1_{\text{NN}} \leftrightarrow 2_{\text{NN}}$  RE-V jump case (Fig. 9.16e) differ. For the latter and a negligible  $|2_{\text{NN}} - 1_{\text{NN}}|$  RE-V association energy difference (e.g. for Nd doped ceria), the attempt frequency is similar to Lu and Yb doped ceria of the only different Ce-RE edge case. The decrease in attempt frequency for intermediate dopant fractions is obviously also caused by considering only V-V interactions, their behavior similar to site-blocking and the resulting blocking of selected diffusion paths. If  $|2_{\text{NN}} - 1_{\text{NN}}|$  and  $3_{\text{NN}} - 2_{\text{NN}}$  RE-V association energy differences increase, the attempt frequency increases similar to the activation enthalpy.

Macroscopic activation enthalpies and experimental attempt frequencies for the KMC simulations can also be calculated for lower temperatures, e.g. between  $267 \text{ }^\circ\text{C}$  and  $600 \text{ }^\circ\text{C}$  as shown in Fig. 9.17 in the appendix. A shift to mostly higher experimental attempt frequencies and higher activation enthalpies can be found. This is expected since less thermal energy is available for successful jumps with high migration barriers, which could already be shown in Chapter 6.3.3 using a simple migration energy model. For Lu doped ceria, a maximum in activation enthalpy appears at low dopant fractions. This results in a minimum at low dopant fractions, which is promising as Faber *et al.* found a minimum in activation enthalpy for several dopants at low dopant fractions. The high activation enthalpy at very low dopant fractions could be reproduced in simulations by including impurities and reduction dominated conductivities for even smaller dopant fractions.<sup>[163]</sup>

For the temperature dependence of the conductivities at low temperature, the same behavior of the apparent attempt frequency as a function of activation enthalpy can be found with a shift to higher experimental attempt frequencies.

### Experimental Association Enthalpy

The difference in activation enthalpy for the low and high temperature region can be used to calculate an experimental association energy as proposed in experiments (see Chapter 2.4.4). The resulting experimental association energies are small. On the one hand, some experiments show no kink in the Arrhenius behavior of the conductivity at all. On the other hand, association energies up to e.g. 0.47 eV for  $\text{Ce}_{0.7}\text{Gd}_{0.3}\text{O}_{1.85}$  were reported.<sup>[168]</sup> Omar *et al.* performed impedance spectroscopy experiments on  $\text{Ce}_{0.9}\text{RE}_{0.1}\text{O}_{1.95}$  and calculated the association energy as activation enthalpy difference below and above 475 °C, which is close to the chosen temperature of 500 °C in this work. Association energies in the same order of magnitude were found.<sup>[166]</sup> In KMC simulations, the association energy does not increase if lower temperatures are considered. For example, the experimental attempt frequencies and activation enthalpies between 267 °C and 368 °C as well as 267 °C and 500 °C for Lu doped ceria are similar.

The resulting experimental association energies depend strongly on the dopant fraction. For Lu, Nd and La doped ceria, a decrease in association energy with increasing dopant fraction was found. For Gd and Sm doped ceria, the association energy is nearly independent of dopant fraction. In experiments, a decrease ( $x \leq 0.03$ ) and increase ( $0.03 \leq x \leq 0.4$ ) in association energy with increasing dopant fraction was found (see Chapter 2.4.4). This experimental result is contradictory to the KMC simulations. However, other experiments show no kink in the Arrhenius behavior of the conductivity at all.

The resulting experimental association energies are even negative for large dopant fractions of Lu, Nd and La doped ceria. This means that the activation enthalpies increase with increasing temperature, which is in conflict with the assumption in experiments that trapped vacancies are freed at high temperature.

## 8.2.2 Sm Doped Ceria

For experimental studies of Sm doped ceria, the total conductivity for polycrystalline materials for several dopant fractions was shown in Chapter 2.4.1. Bulk conductivities for multiple dopant fractions were presented only by few groups. Zhan *et al.*<sup>[74]</sup> investigated polycrystalline ceria using impedance spectroscopy and found a maximum conductivity for  $x = 0.1$  for 250–550 °C. Sanghavi *et al.*<sup>[179]</sup> investigated single crystal thin films, which might share characteristics with the total domain due to its thin film properties, and found a maximum conductivity for  $x = 0.15$  for 500–700 °C. Both groups only chose very few dopant fractions with a spacing of  $\Delta x \geq 0.08$ .

In this work, a large number of compositions for Sm doped ceria are investigated in experiments with a spacing of  $\Delta x = 0.025$ . Additionally, 7% Sm doped ceria was prepared and measured by Gerald Dück. Using impedance spectroscopy, bulk and (macroscopic) grain boundary contributions have been separated according to Chapter 4.1.5. In Fig. 8.15, the temperature dependence or Arrhenius behavior of the ionic conductivity is shown.

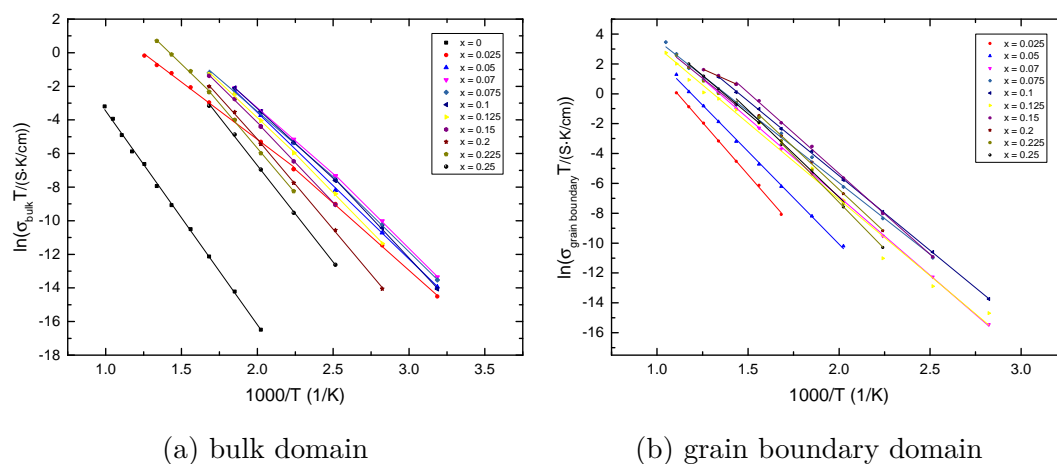


Figure 8.15: Arrhenius behavior of the ionic conductivity in  $\text{Ce}_{1-x}\text{Sm}_x\text{O}_{2-x/2}$  according to impedance experiments.

The bulk conductivity shows the typical in- and decrease in conductivity with increasing dopant fraction (Fig. 8.16). A global maximum in the ionic conductivity can be found for  $x = 0.07$ . Measurements show at  $x = 0.1$  a local maximum, which may be in the error range of the measurement and is therefore not significant. Above 200 °C, the bulk conductivity of both investigated Sm doped ceria compositions is similar. This is in agreement with the measurements of Zhan *et al.*, who found a maximum for  $x = 0.1$ .<sup>[74]</sup>

The separation of the grain boundary and electrode semicircle in the impedance spectrum of Sm doped ceria with  $x \geq 0.1$  is very difficult. Therefore, all macroscopic grain boundary conductivities with  $x \geq 0.1$  may have a systematic error of one order of magnitude. Observed trends show a high degree of uncertainty. However, maxima at  $x = 0.1$  and  $0.15$  and a decrease (for low temperatures) or increase (for high temperatures) of the conductivity between  $x = 0.225$  and  $0.25$  can be observed.

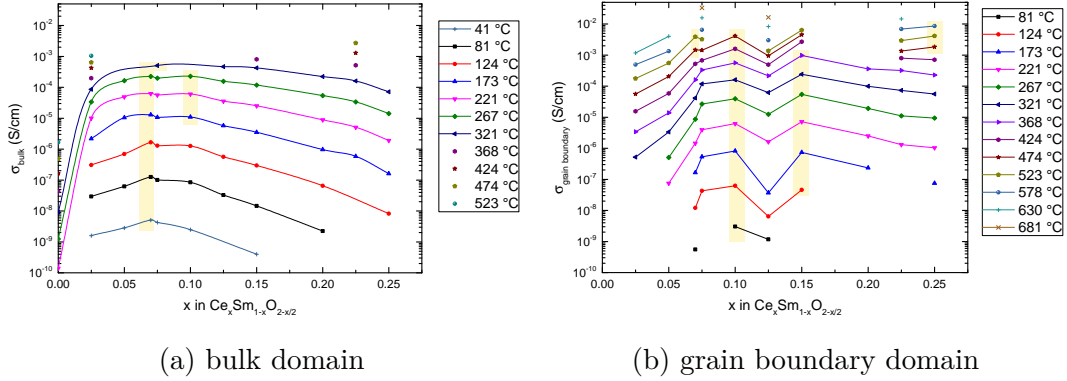


Figure 8.16: Ionic conductivity of Sm doped ceria according to impedance experiments. Lines are a guide to the eye only.

The latter is even true for different fitting methods. The result is in agreement with literature, Zhan *et al.* found a maximum in the grain boundary conductivity for  $x = 0.1$  for low temperature.<sup>[74]</sup>

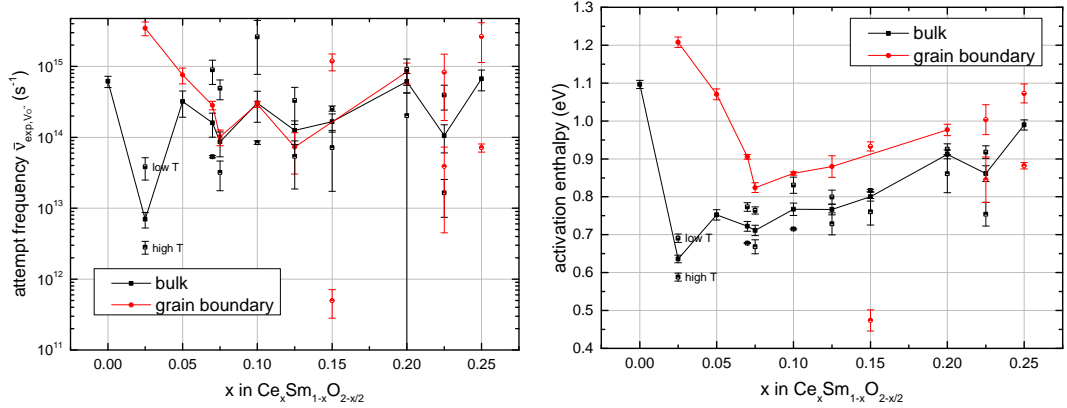


Figure 8.17: Experimental attempt frequency (left) and activation enthalpy (right) of Sm doped ceria for all temperatures (solid symbols) or low and high temperatures according to impedance experiments. Lines are a guide to the eye only.

The experimental attempt frequency and activation enthalpy extracted from the Arrhenius behavior of the ionic conductivity according to Eqs. 2.3 and 2.4 is shown in Fig. 8.17. Several patterns similar to other experiments (Chapter 2.4.4 and Fig. 9.18) can be observed: Experimental attempt frequencies and activation enthalpies are higher than in the KMC simulations. A de- and increase with increasing dopant fraction with a minimum at low dopant fractions can be found. Values for the high temperature region are always smaller than for the low temperature region. A large association energy compared to KMC simulations of about 0.1 eV is found.

In conclusion,  $\text{Ce}_{0.93}\text{Sm}_{0.07}\text{O}_{1.965}$  leads to the largest bulk conductivity. An increase in the dopant fraction leading to the maximum in conductivity with increasing temperature can be found. A comparison of experimental and simulated conductivities is shown in Chapter 8.2.6.

### 8.2.3 The Best Dopant: Sm or Gd?

For a long time it has been discussed in literature, which rare-earth doped ceria, using only a single dopant, leads to the best ionic conductivity in experiments.<sup>[25]</sup> In fact, there is no short answer to this question since the ionic conductivity not only depends on the kind of dopant but also on the dopant fraction, the measured temperature and the choice between total or bulk conductivity.

In literature, the conductivity of  $\text{Ce}_{0.8}\text{RE}_{0.2}\text{O}_{1.9}$  is used as a first indication for the optimal dopant. Conductivities for the total (Fig. 2.8) and bulk domain (Fig. 2.12) suggest a high conductivity for Sm and Gd doped ceria.

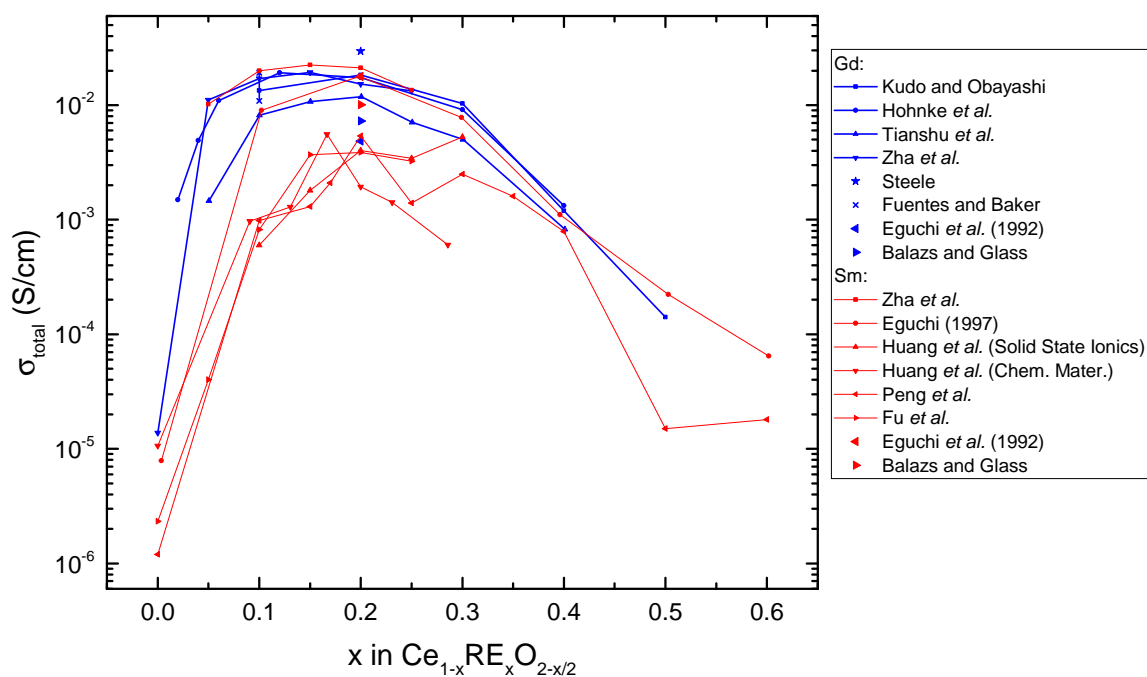


Figure 8.18: Total ionic conductivity of polycrystalline Sm and Gd doped ceria according to experiments at 600 °C. [27,28,36,62,64,73,156–158,160,185,190,452] Lines are a guide to the eye only.

The total conductivity in polycrystalline Sm and Gd doped ceria is shown in Fig. 8.18 for 600 °C. Huang *et al.*,<sup>[156,160]</sup> Peng *et al.*<sup>[158]</sup> and Fu *et al.*<sup>[157]</sup> investigated Sm doped ceria for several dopant fractions leading to the lowest total conductivity, here. Significantly higher total conductivities were found by Kudo and Obayashi,<sup>[162,190]</sup> Hohnke *et al.*,<sup>[36]</sup> Tianshu *et al.*<sup>[64]</sup> and Zha *et al.*<sup>[73]</sup> for several dopant fractions of Gd doped ceria. However, for  $\text{Ce}_{0.8}\text{RE}_{0.2}\text{O}_{1.9}$  and sample preparation by the same group, the results of Eguchi *et al.* (1992)<sup>[27]</sup> and Balazs and Glass<sup>[62]</sup> suggest higher conductivities for Sm doped ceria. Obviously, this discrepancy shows the strong influence of the sample synthesis and preparation. For instance, Fuentes and Baker<sup>[185]</sup> showed even higher total conductivities for  $\text{Ce}_{0.9}\text{Gd}_{0.1}\text{O}_{1.95}$  between 0.011 and 0.019 S/cm. The results are again surpassed by the result of Zha *et al.*<sup>[73]</sup> and especially Eguchi *et al.* (1997)<sup>[28]</sup> for Sm doped ceria. Still, the highest total conductivity is reported for  $\text{Ce}_{0.9}\text{Gd}_{0.1}\text{O}_{1.95}$  by Steele<sup>[452]</sup>.

This behavior may be related to the influence of the grain boundary domain on the total conductivity as already shown before in Fig. 2.9, Chapter 4.1.5 and Fig. 8.4 (right). Therefore, bulk and grain boundary conductivity should be separated e.g. by using impedance spectroscopy.

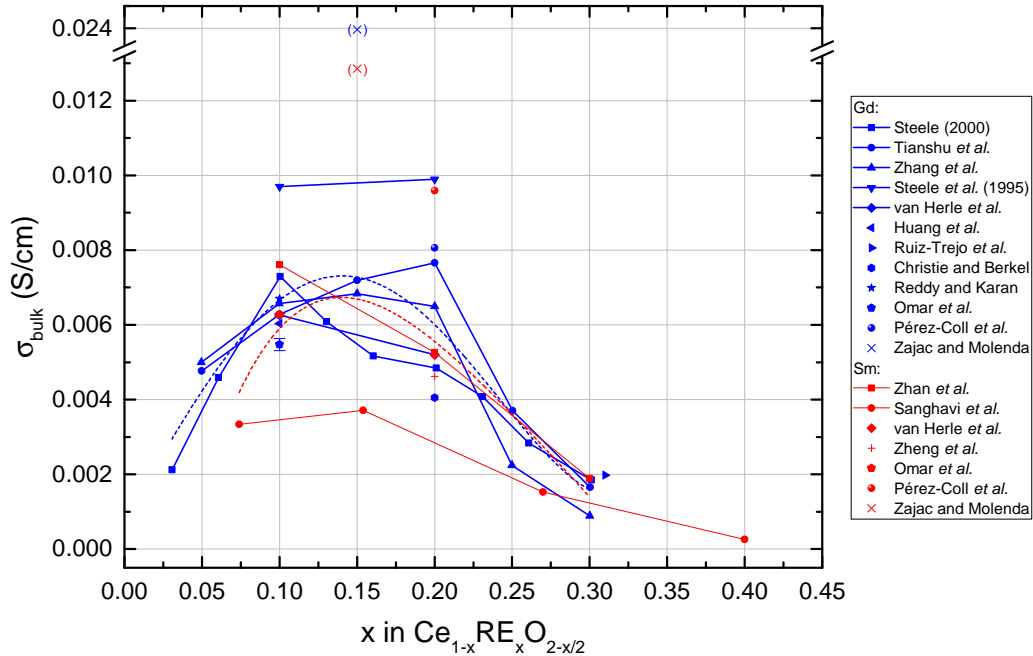


Figure 8.19: Bulk ionic conductivity of Sm<sup>[74,166,169–172,179–181]</sup> and Gd doped ceria<sup>[64,86,166,169–177]</sup> according to experiments at 500 °C. Fourth order polynomials were fitted to the data with exception of the data of Zajac and Molenda to show the general trend of the data (dashed lines) other Lines are a guide to the eye only.

The bulk conductivity for Sm and Gd doped ceria is shown in Fig. 8.19 for 500 °C. Similar to the total conductivity, different research groups present different optimal dopants and dopant fractions. As discussed in Chapter 8.1, these differences may be a result of different sample preparation techniques. Therefore, only similar prepared Sm and Gd doped ceria should be compared.

Similar compositions for both dopants were presented by several groups: Van Herle *et al.* found similar conductivities for both dopants, Omar *et al.* and Pérez-Coll *et al.* found higher conductivities for Sm doped ceria, Zajac and Molenda found higher conductivities for Gd doped ceria.<sup>[166,169–172]</sup> However, Zajac and Molenda presented rather high conductivities compared to all other studies, which are therefore neglected in this study. As a result, the highest bulk conductivity in experiments at 500 °C is expected for Sm doped ceria. This is in agreement with the KMC simulations, which were presented above (Fig. 8.8).

In this study, these results were analyzed in more detail. Therefore, dopant fractions at the maxima of the bulk conductivity (and grain boundary conductivity) for Sm doped ceria were also investigated with Gd doped ceria in impedance experiments. Of course, the maxima for Gd doped ceria may be at different dopant fractions though Fig. 8.18 and 8.19 suggest a similar curve progression.

Therefore, the samples  $\text{Ce}_{0.93}\text{Sm}_{0.07}\text{O}_{1.965}$  and  $\text{Ce}_{0.9}\text{Sm}_{0.1}\text{O}_{1.95}$  as well as  $\text{Ce}_{0.93}\text{Gd}_{0.07}\text{O}_{1.965}$  and  $\text{Ce}_{0.9}\text{Gd}_{0.1}\text{O}_{1.95}$  were investigated. Gd doped ceria and 7% Sm doped ceria samples were prepared and measured by Gerald Dück.

Figure 8.20 shows the bulk ionic conductivity of Sm and Gd doped ceria. Sm doped ceria exhibits a larger bulk conductivity than Gd doped ceria. The largest bulk conductivity is found for  $\text{Ce}_{0.93}\text{Sm}_{0.07}\text{O}_{1.965}$ . For Gd doped ceria, doping with  $x = 0.1$  leads to the higher bulk conductivity, which indicates a maximum at larger dopant fractions for Gd compared to Sm doped ceria as predicted by KMC simulations. Above 200 °C, the bulk conductivity of both investigated Sm doped ceria compositions is similar.

The largest bulk conductivity is found for  $\text{Ce}_{0.93}\text{Sm}_{0.07}\text{O}_{1.965}$ .

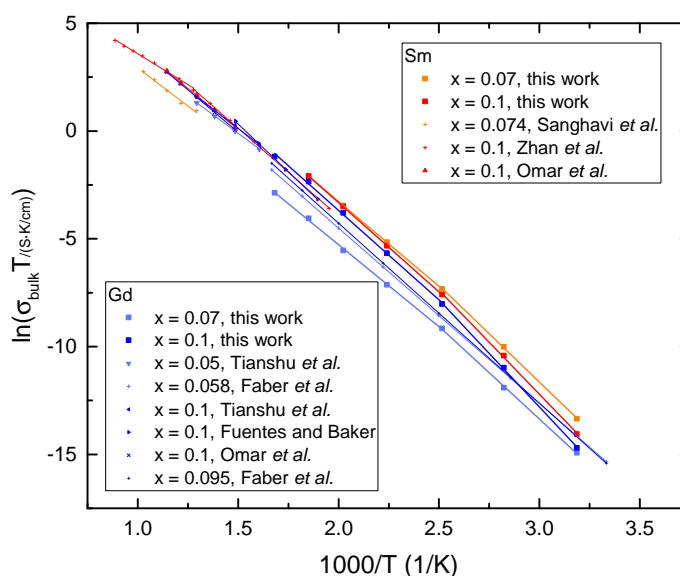


Figure 8.20: Bulk ionic conductivity of Sm and Gd doped ceria according to impedance experiments. [64,74,163,166,179,185]

The measured bulk conductivities are in good agreement with literature. [74] The ranking order in literature is similar to the ranking order in this work. Exceptions are the conductivities by Sanghavi *et al.*, [179] which might share characteristics with the total domain due to its thin film properties. Zhan *et al.* [74] found a kink in the bulk conductivity allegedly due to association around 500 °C. In this work, already around 125 °C a change in the Arrhenius behavior is found. A comparison is difficult since Zhan *et al.* measured only at higher temperatures and at 500 °C the bulk conductivity can only be deduced from the grain boundary conductivity. As a result, the kink at 500 °C may be influenced by the grain boundary conductivity.

The macroscopic grain boundary conductivity, which is shown in Fig. 8.21 (left), is generally several orders of magnitude smaller than the bulk conductivity. Only the bulk conductivity of  $\text{Ce}_{0.93}\text{Gd}_{0.07}\text{O}_{1.965}$  above 250 °C is similar to the grain boundary conductivity of 10% Sm or Gd

doped ceria. As the activation energies for the grain boundary domain are larger than for the bulk, conductivities may be similar around 800 °C and 1000 °C. Especially for high dopant fractions, similar conductivities occur already at low temperature according to literature.<sup>[187]</sup> The ranking order for the grain boundary conductivity is different from the bulk domain. Here, all 10 % doped samples have larger conductivities than the 7 % doped ceria indicating a maximum at larger dopant fractions as seen in Chapter 2.4.3. For both dopant fractions, Sm doped ceria has the larger conductivity.

In literature, the macroscopic grain boundary conductivity scatters even more than the bulk conductivity, though measurements of Tianshu *et al.*<sup>[64]</sup> are in good agreement with this work. The reasons for this scattering are the different syntheses and preparation methods, which especially influence the grain boundary domain, as discussed before. As a result, the conductivities for  $\text{Ce}_{0.9}\text{Sm}_{0.1}\text{O}_{1.95}$  according to Zhan *et al.*<sup>[74]</sup> are significantly lower, thus  $\text{Ce}_{0.9}\text{Gd}_{0.1}\text{O}_{1.95}$  according to Tianshu *et al.*<sup>[64]</sup> and Fuentes *et al.*<sup>[185]</sup> has larger conductivities.

The total conductivity (Fig. 8.21 right) was calculated according to Chapter 4.1.5. As the grain boundary conductivity is orders of magnitude smaller than the bulk conductivity in the investigated temperature range, the total conductivity is very similar to the grain boundary conductivity. Deviations between both increase with temperature, are at least four times larger for the  $x = 0.1$  dopant fractions and are larger for Sm doped ceria.

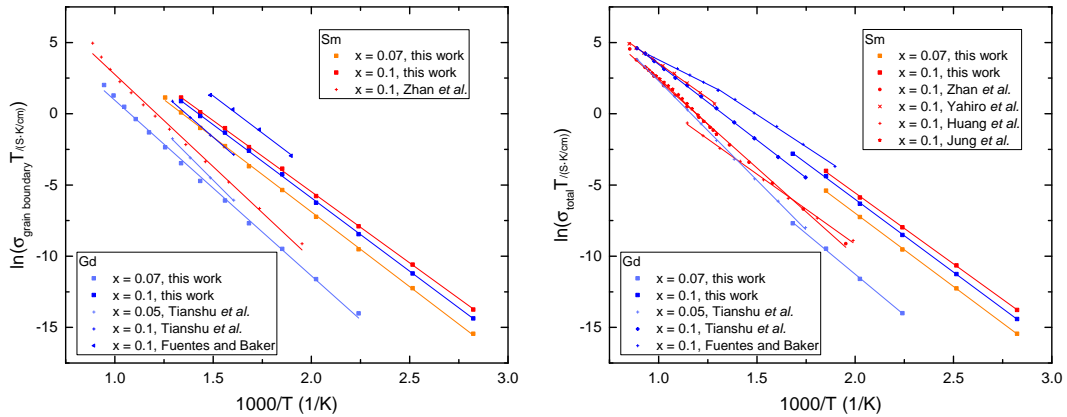


Figure 8.21: Grain boundary (left) and total ionic conductivity (right) of Sm and Gd doped ceria according to experiments.<sup>[64,74,156,161,185,317]</sup>

As a result, the activation energy for the total domain may change between the grain boundary dominated low temperature region and the bulk dominated high temperature region. Of course, a kink in the bulk conductivity due to association can also influence the total conductivity. In fact, Fuentes *et al.*<sup>[185]</sup> fits two activation enthalpies below and above 500 °C. Jung *et al.*<sup>[317]</sup> found significantly better regression coefficients using two straight lines for the Arrhenius plot though they do not use this result for their final evaluation. Several other measurements could also be fitted with two temperature regions as can be seen in Fig. 8.21.

The strong scattering in the grain boundary domain propagates in the total domain. The total

conductivities for the 10% dopant fraction scatters several orders of magnitude explaining the different results in literature for the best rare-earth dopant in ceria. In this work,  $\text{Ce}_{0.9}\text{Sm}_{0.1}\text{O}_{1.95}$  shows the highest total conductivity, which is in good agreement with Tianshu *et al.*<sup>[64]</sup> and Yahiro *et al.*<sup>[161]</sup> However, Fuentes and Baker<sup>[185]</sup> show higher conductivities for  $\text{Ce}_{0.9}\text{Gd}_{0.1}\text{O}_{1.95}$ . Figure 8.18 shows an increase in total conductivity for higher dopant fractions.

The largest total conductivity is found for Sm doped ceria. In literature, different syntheses and sample preparation methods lead to larger total conductivities for Gd doped ceria.

$\text{Ce}_{0.93}\text{Gd}_{0.07}\text{O}_{1.965}$  exhibits exceptionally low conductivities in all domains and a larger activation enthalpy in the grain boundary and total domain compared to this work and literature. In fact, this was the only powder in this investigation that was milled in ethanol for a long time. Therefore, abrasion from the zirconia balls could have led to a mild doping with Zr. However, Zr doping levels were below the resolution limits of XRD and EDX measurements.

The experimental attempt frequency and activation enthalpy for different domains of Sm and Gd doped ceria are summarized in Fig. 8.22.

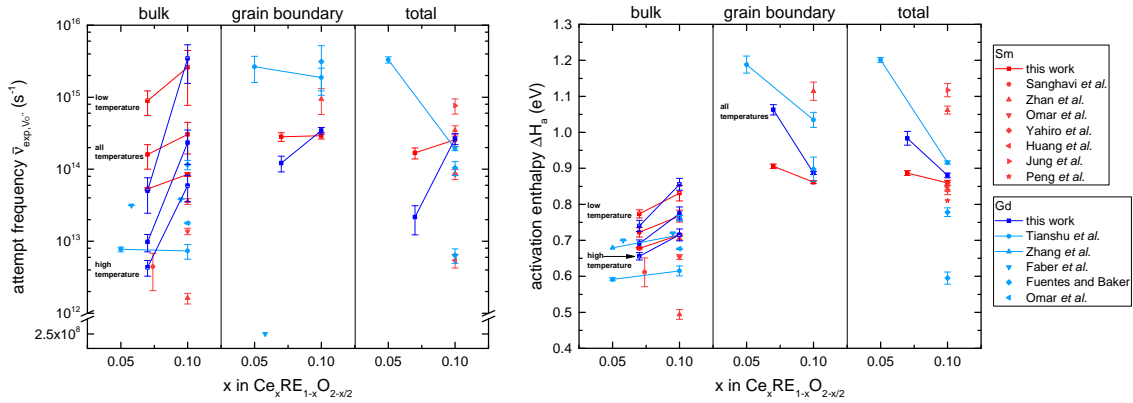


Figure 8.22: Experimental attempt frequency (left) and activation enthalpy (right) for different domains of Sm and Gd doped ceria according to experiments.<sup>[64,74,156,158,161,163,166,168,179,185,317]</sup> Lines are a guide to the eye only.

Activation enthalpies in the grain boundary domain are significantly higher than in the bulk domain. While the activation enthalpy mostly increases for larger dopant fractions in the bulk domain, it mostly decreases in the grain boundary and total domain. This was expected, as in experiments the minimum in activation enthalpy correlates with the maximum in conductivity as a function of dopant fraction (Chapter 2.4.4). Activation enthalpies in Sm and Gd doped ceria are similar with the exception of the grain boundary and total domain for  $\text{Ce}_{0.93}\text{Gd}_{0.07}\text{O}_{1.965}$  as discussed above. Activation enthalpies in grain boundary and total domain are similar as the total conductivity is dominated by the grain boundary domain.

Experimental attempt frequencies in the grain boundary domain are similar to the bulk domain

except for  $\text{Ce}_{0.93}\text{Gd}_{0.07}\text{O}_{1.965}$ . In this work, the experimental attempt frequency increases for larger dopant fractions in the bulk, which propagates in the total domain, as the experimental attempt frequency is independent of dopant fraction in the grain boundary domain. According to Tianshu *et al.*,<sup>[64]</sup> the experimental attempt frequency decreases for all domains. Surprisingly, all experimental attempt frequencies for the grain boundary domain in this work are similar and low compared to literature. Experimental attempt frequencies in the total domain tend to be lower than in the grain boundary domain. This may be caused by an Arrhenius fit with a single activation enthalpy though one or more kinks in the conductivity are observed. Here, kinks result from a decrease in activation enthalpy for higher temperature due to either no longer existing association or change between grain boundary to bulk dominated total domain.

Overall, both the experimental attempt frequency and activation enthalpy in this work are in agreement with literature.

In conclusion, Sm doped ceria leads to the largest bulk and total conductivity, in this work. While the largest bulk conductivity is found for  $\text{Ce}_{0.93}\text{Sm}_{0.07}\text{O}_{1.965}$ , the dopant fraction leading to the maximum in total conductivity is larger. For Gd doped ceria,  $x_{\text{max}}$  is larger as predicted by KMC simulations. A comparison of experimental and simulated conductivities is shown in Chapter 8.2.6.

### 8.2.4 Co-Doped Ceria: Sm-Zr and Gd-Zr

After successfully investigating Sm and Gd doped ceria, the next challenge is co-doped ceria, for example Sm-Zr doped ceria ( $\text{Ce}_{1-x-y}\text{Zr}_y\text{Sm}_x\text{O}_{2-x/2}$ ). Here, migration energies depend not only on the individual migration edges (Ce-Ce, Ce-Sm, Sm-Sm, Ce-Zr and Zr-Zr) and association energies but also on mixed migration edge energies (Sm-Zr). Beyond that, the question remains whether the simplified migration energy model still works for co-doped ceria. Doping ceria with zirconia is also of particular interest since zirconium has the same valence as the host cation ceria. Therefore, doping with zirconia does not create additional oxygen vacancies and the conductivity is only influenced by the additional association or blocking of the oxygen vacancies. Previous studies in Y doped ceria show that doping with Zr decreases the conductivity.<sup>[453]</sup>

In this work, both polycrystalline samples and agglomerates of single crystals are investigated to compare their conductivities in bulk and total domain according to impedance experiments.

Single crystals with the compositions  $\text{Ce}_{0.889}\text{Zr}_{0.006}\text{Gd}_{0.105}\text{O}_{1.9475-\delta}$  and  $\text{Ce}_{0.887}\text{Zr}_{0.043}\text{Sm}_{0.070}\text{O}_{1.965-\delta}$  were synthesized by skull-melting by Gregor Ulbrich.<sup>[454]</sup> Ceria single crystals synthesized by skull-melting need Zr as an ignition material. During skull-melting, an agglomerate of single crystals is grown. In this work, the single crystals could not be isolated. Therefore, still, an agglomerate of single crystals with very large grain sizes (about 500  $\mu\text{m}$ ) is investigated. The single crystals were compared with polycrystalline samples, which were prepared and measured by Gerald Dück.

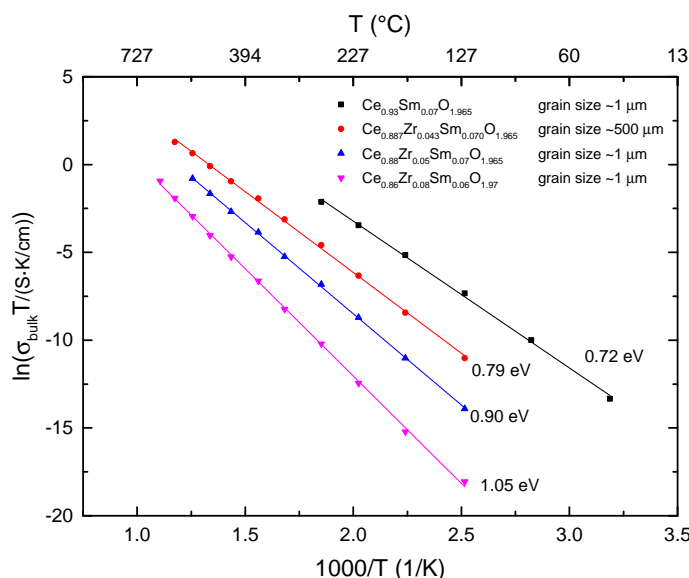


Figure 8.23: Ionic conductivity for the bulk domain of Sm-Zr doped ceria according to impedance experiments. Both, polycrystalline samples and agglomerates of single crystals are investigated. Doping with Zr decreases the conductivity.

Impedance spectroscopy measurements reveal three semicircles, which can be attributed to the

bulk domain, with a capacitance of about  $5 \cdot 10^{-11}$  F, the grain boundary domain, with a capacitance of about  $5 \cdot 10^{-9}$  F, and the electrode with an even larger capacitance according to literature.<sup>[167,170,315]</sup>

Figure 8.23 shows the ionic conductivity for the bulk domain of Sm-Zr doped ceria. Doping with Zr decreases the conductivity significantly. At the same time, the activation enthalpy increases with Zr content. In fact, the Sm dopant fraction changes about 1%, simultaneously. However, the influence of the conductivity of the variation in the Sm dopant fraction is estimated to be below 30%, while the measured conductivities decrease for more than 95%. Therefore, the influence of Zr dominates the conductivity. Polycrystalline samples and single crystals show supposedly similar bulk conductivities.

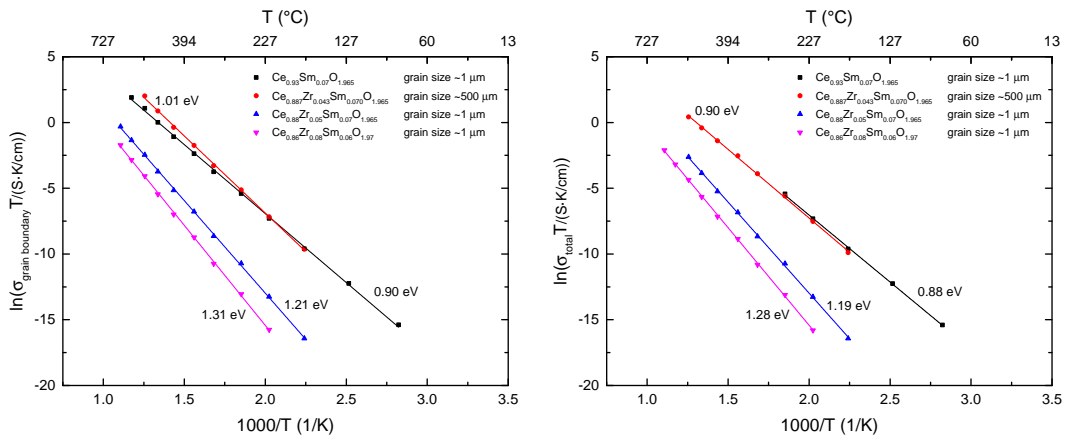


Figure 8.24: Macroscopic grain boundary (left) and total (right) conductivity of Sm-Zr doped ceria according to impedance experiments. Both, polycrystalline samples and agglomerates of single crystals are investigated.

For the polycrystalline samples, the macroscopic grain boundary conductivity is significantly lower in accordance with literature. The grain boundary conductivity (Fig. 8.24) also decreases with Zr dopant fraction while the activation enthalpy increases. An exception is the single crystal agglomerate, which has an exceptionally high macroscopic grain boundary conductivity, which is more than factor 15 larger than approximated due to comparison with the other samples. According to the serial brick layer model (see Chapter 4.1.5), the macroscopic grain boundary conductivity is proportional to the grain size. Therefore, for similar microscopic grain boundary conductivities, similar grain thicknesses and larger grain sizes an increase in macroscopic grain boundary conductivity is expected. As the increase in macroscopic grain boundary conductivity is not proportional to the increase in grain size, either the microscopic grain boundary conductivity or grain thickness is not constant or the serial brick layer model is not valid for the single crystal agglomerate.

The macroscopic grain boundary conductivity increases with  
increasing grain size.

The total conductivity is again very similar to the grain boundary conductivity and deviates only at high temperatures. Due to the influence of the bulk domain, the activation enthalpies are slightly lower as well.

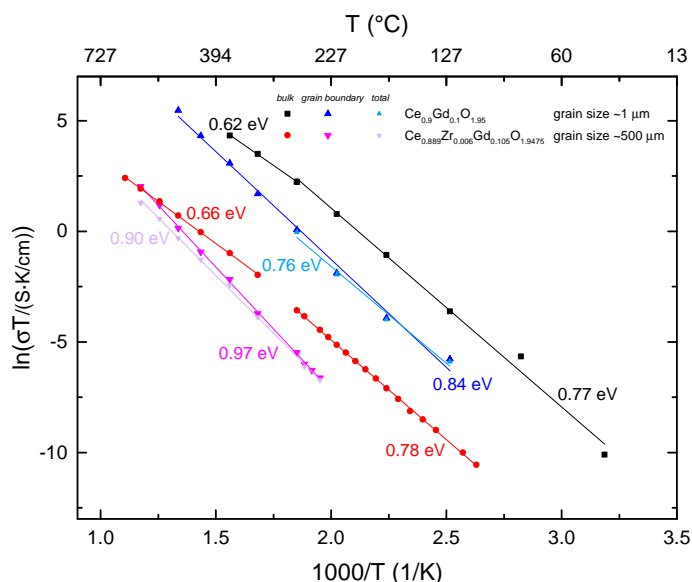


Figure 8.25: Ionic conductivity for the bulk, grain boundary and total domain of Gd-Zr doped ceria according to impedance experiments. Both, polycrystalline samples and agglomerates of single crystals are investigated.

Ionic conductivities for the bulk, grain boundary and total domain of Gd-Zr doped ceria are shown in Fig. 8.25. Compared to Sm-Zr co-doped ceria, co-doping with Zr decreases the conductivity of Gd doped ceria more pronounced.

In conclusion, the ionic conductivity decreases with increasing Zr fraction according to impedance experiments in this work and literature.<sup>[453]</sup> Therefore, Zr impurities, which are for example caused by grinding the powder, have to be minimized for applications demanding a high ionic conductivity.

Doping ceria with Zr decreases the conductivity significantly. The decrease is more pronounced in Gd than in Sm co-doped ceria.

### 8.2.5 Lu Doped Ceria

In literature, Lu doped ceria is rarely investigated due to its low ionic conductivity. Only a few dopant fractions have been measured investigating the bulk<sup>[165,166]</sup> and total conductivity.<sup>[62]</sup>

However, Lu doped ceria is of particular interest as the dopant  $\text{Lu}^{3+}$  has a similar ionic radius as the host cation  $\text{Ce}^{4+}$ .<sup>[32]</sup> This results in a similar migration barrier (Ce-Lu edge) as already shown in Fig. 7.6. The Lu-Lu edge has a larger migration barrier but only appears rarely. Therefore, the migration energy is mainly determined by the association between dopants and oxygen vacancies (Fig. 5.1) and the repulsion between oxygen vacancies (Fig. 5.5).

Lu doped ceria is investigated using impedance spectroscopy experiments. Lu doped ceria was synthesized, prepared and measured by Gerald Dück.<sup>[295]</sup>

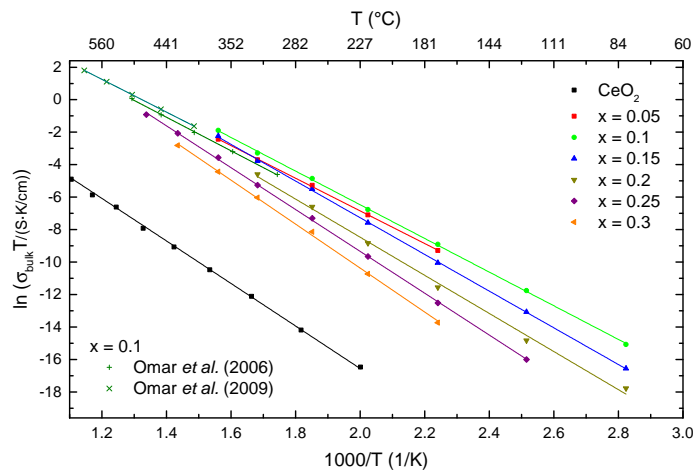


Figure 8.26: Arrhenius behavior of the bulk conductivity in  $\text{Ce}_{1-x}\text{Lu}_x\text{O}_{2-x/2}$  according to experiments by Dück<sup>[295]</sup> in comparison with literature.<sup>[165,166]</sup>

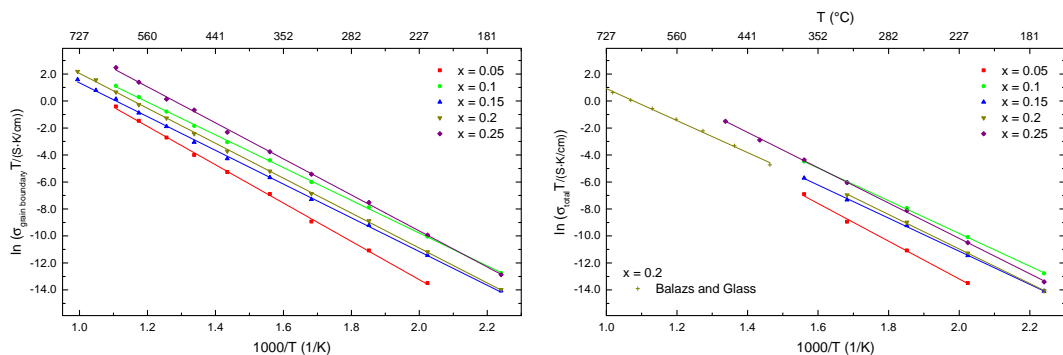


Figure 8.27: Arrhenius behavior of the macroscopic grain boundary (left) and total conductivity (right) in  $\text{Ce}_{1-x}\text{Lu}_x\text{O}_{2-x/2}$  according to experiments by Dück<sup>[295]</sup> in comparison with literature.<sup>[62]</sup>

In experiments, bulk and grain boundary conductivity follow the Arrhenius behavior (Fig. 8.26

and 8.27). Figure 8.28 and 8.29 show the conductivity as a function of the dopant fraction. The pre-exponential factor and activation enthalpy are shown in Fig. 8.30.

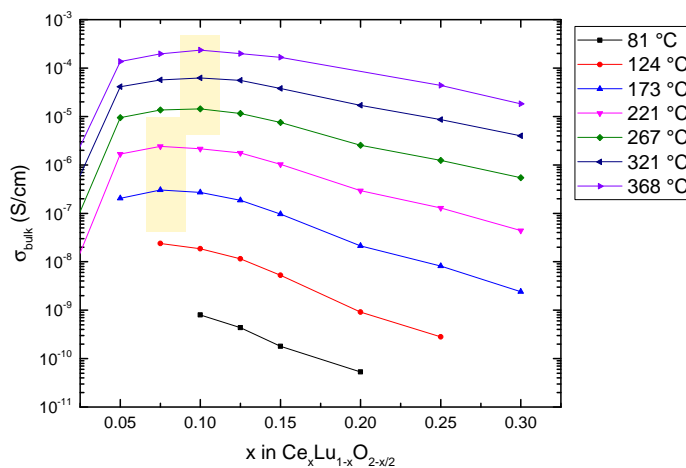


Figure 8.28: Ionic conductivity of bulk domain in Lu doped ceria according to experiments by Dück.<sup>[295]</sup> Lines are a guide to the eye only.

The bulk conductivity increases with increasing dopant fraction to a maximum at about  $x = 0.075$  below 250 °C or  $x = 0.1$  above 250 °C. For higher dopant fractions, the bulk conductivity decreases. The behavior of the conductivity is similar to Sm doped ceria though the conductivity is 1–2 orders of magnitude smaller. The activation enthalpy for the bulk domain increases with increasing dopant fraction and is significantly higher than in Sm doped ceria, which was expected due to the low conductivity. The experimental attempt frequency shows a similar behavior and has the same order of magnitude compared to Sm doped ceria. As seen in KMC simulations, the activation enthalpy is more important for a high conductivity than the experimental attempt frequency. The bulk conductivity and activation enthalpy for 10% Lu doped ceria is in agreement with measurements by Omar *et al.*<sup>[165,166]</sup>

The grain boundary conductivity (Fig. 8.27 and 8.29) exhibits a maximum in conductivity as a function of dopant fraction for  $x = 0.1$  for all measured temperatures similar to Sm doped ceria. At higher dopant fractions, the conductivity increases again above  $x = 0.15$  leading to the highest conductivities at  $x = 0.25$  above 330 °C for all dopant fractions. In Sm doped ceria, the minimum in conductivity was already found at  $x = 0.125$  while above  $x = 0.15$  the conductivity decreases again. However, for the interpretation of the impedance measurements for Sm doped ceria may be imprecise as the separation of the grain boundary and the electrode semicircle is challenging for dopant fractions above 10%. The grain boundary conductivity is 1–2 orders of magnitude smaller than in Sm doped ceria. The grain boundary conductivity is more than one order of magnitude smaller with exception of  $\text{Ce}_{0.75}\text{Lu}_{0.25}\text{O}_{1.875}$ , where bulk and grain boundary conductivity are similar. The activation enthalpy for the grain boundary domain decreases up to a dopant fraction of  $x = 0.1$  significantly and increases slightly for higher dopant fractions. This correlates with the

maximum in conductivity. The activation enthalpy is higher than in Sm doped ceria. Surprisingly, the experimental attempt frequency de-, in- and again decreases with increasing dopant fraction and therefore deviates from the behavior of the activation enthalpy.

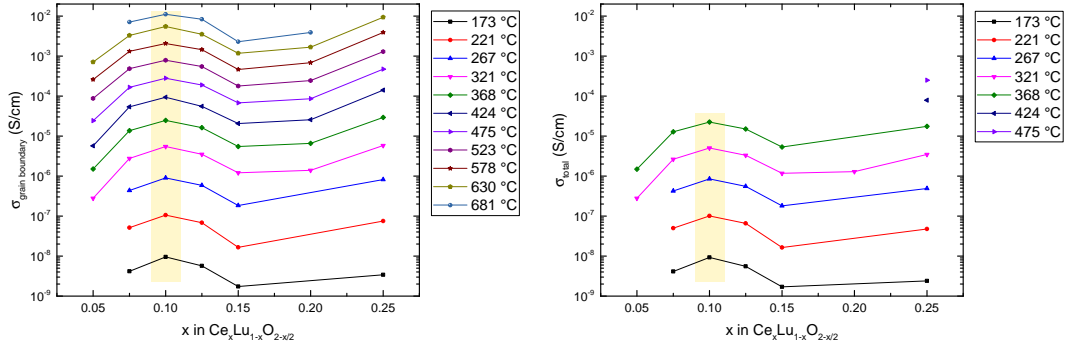


Figure 8.29: Macroscopic ionic conductivity of grain boundary domain according to experiments by Dück (left)<sup>[295]</sup> and total conductivity (right) in Lu doped ceria. Lines are a guide to the eye only.

The total conductivity is nearly identical to the grain boundary conductivity except for lower conductivities for  $\text{Ce}_{0.75}\text{Lu}_{0.25}\text{O}_{1.875}$ . The total conductivity and activation enthalpy for 20% Lu doped ceria is in agreement with measurements by Balazs and Glass.<sup>[62]</sup>

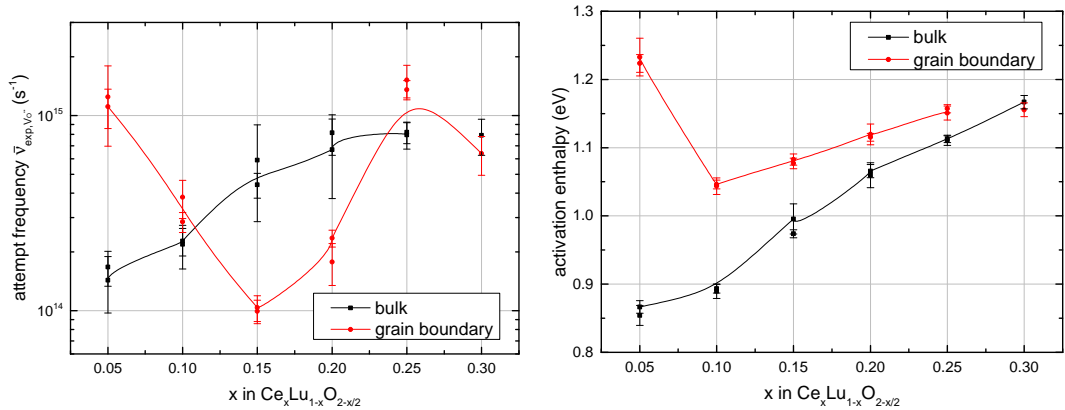


Figure 8.30: Experimental attempt frequency (left) and activation enthalpy (right) of Lu doped ceria according to impedance experiments. Lines are a guide to the eye only.

In conclusion, the dependence of the conductivity on the dopant fraction is similar in Lu and Sm doped ceria. The low conductivity for Lu doped ceria results from a high activation enthalpy. A comparison of experimental and simulated conductivities is shown in the next section.

## 8.2.6 Comparing Simulations and Experiments

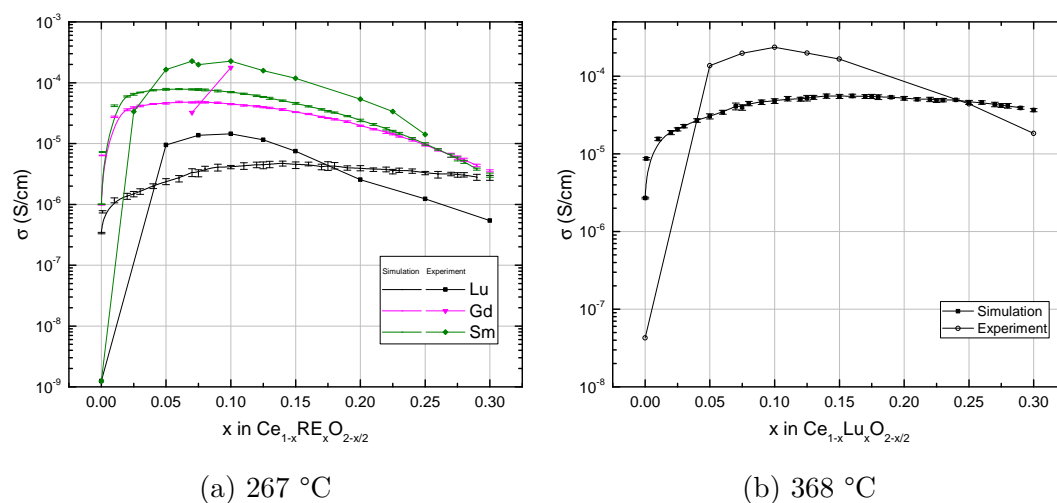


Figure 8.31: Simulated ionic conductivity of rare-earth doped ceria at 267 °C and 368 °C with RE = Lu, Gd and Sm. In comparison, ionic conductivities according to impedance experiments are shown. Lines are a guide to the eye only.

Figure 8.31 shows the simulated and experimental ionic conductivity of Lu, Gd and Sm doped ceria according to this work. For Sm doped ceria, a similar curve progression in simulations and experiments is found. An exception are small dopant fractions in experiments, where impurities influence the conductivity and additional oxygen vacancies are formed due to non-stoichiometry. For Gd doped ceria, similar observations can be made.

For Lu doped ceria, the dependence of the conductivity on the dopant fraction is similar to Sm doped ceria. The KMC simulations for Lu doped ceria show a maximum in conductivity as a function of dopant fraction at far higher dopant fractions. It has already been shown that the dopant fraction leading to the maximum in conductivity is limited by blocking. KMC simulations for Yb doped ceria show a significantly higher  $x_{\max}$  though the Lu-Lu and Yb-Yb edge energies are similar. The Ce-Yb edge energy is significantly higher than the Ce-Lu edge energy. The reason for the discrepancy between experiments and simulations for Lu doped ceria is therefore the Ce-Lu migration edge energy, which is smaller than the Ce-Ce edge energy. Minor errors in the energy difference result in significant changes in the simulated conductivities.

Experiments suggest that the Ce-Lu edge energy  
is higher than the Ce-Ce edge energy.

## 8.3 The Influence of Time: Long-term Degradation Due to Cation Ordering

**In literature** In experiments, Zhan *et al.* investigated the conductivity of Gd and Y doped ceria.<sup>[168]</sup> Subsequently, they tempered the samples at 1000 °C for 8 days, investigated the conductivity again and found decreased bulk conductivities for high dopant fractions: At 400 °C, the bulk conductivity decreases by 30 % ( $\text{Ce}_{0.75}\text{Gd}_{0.25}\text{O}_{1.875}$ ) and by 50 % ( $\text{Ce}_{0.7}\text{Gd}_{0.3}\text{O}_{1.85}$ ) for Gd doped ceria and by about 4 % ( $\text{Ce}_{0.75}\text{Y}_{0.25}\text{O}_{1.875}$ ) and by 11 % ( $\text{Ce}_{0.7}\text{Y}_{0.3}\text{O}_{1.85}$ ) for Y doped ceria. The aged samples showed a significant degradation in conductivity.

**Simulations** In an earlier publication,<sup>[55]</sup> the conductivity for Y doped ceria was simulated theoretically using combination of DFT, MMC and KMC simulations with the model 2014 (see Chapter 5.1.1) with three different types of lattices (Chapter 4.2.2):

In a RND lattice, the cation sublattice is randomly ordered (or equilibrated at infinite temperature  $T_1 = \text{inf}$ ), while the anion sublattice is in thermodynamic equilibrium at the investigated temperature  $T_2$ . In an EQ lattice, both sublattices are equilibrated at 2/3 of the melting point of ceria ( $T_1 = 1500 \text{ K}$ ), similar to the sintering process in experiments and the Tammann rule.<sup>[455]</sup> At lower temperatures, the cations are frozen due to their low mobility and the anions are equilibrated at  $T_2$ . In a DEG lattice, both sublattices are equilibrated at the final investigated temperature  $T_1 = T_2$ , simulating a degraded lattice, which had a very long time to reach thermodynamic equilibrium.

The ionic conductivity of a randomly ordered cation sublattice (RND) is comparable to the ionic conductivity of an equilibrated cation sublattice (EQ). This supports the general use of randomly ordered cation sublattices in this work for KMC simulations.

For an aged sample, the degraded lattice (EQ) shows a significant decrease in ionic conductivity, which is considerably larger than in the experiments of Zhan *et al.*<sup>[168]</sup> The deviation was expected as a degraded lattice is in thermodynamic equilibrium at the impedance temperature, which is only reached after a very long time.

However, the degree of degradation was surprising. In literature, degradations caused only by a change in the ordering of the cations are rarely reported. While degradations of SOFC are intensively studied, aging phenomena are assigned to mechanical problems like ablation or chemical problems like poisoning of electrodes or demixing of materials. A degradation of the electrolyte and decrease in ionic conductivity by 80 % caused by cation ordering would be a major issue for long-term performance and should be investigated thoroughly.

The degradation is caused by a clustering of dopants and oxygen vacancies. At high temperatures, the cation ordering is dominated by the number of possible configurations (configurational entropy). This is the case for the RND and EQ lattice. For low temperature (e.g. the EQ lattice), the defect distribution is controlled by the formation of energetically most favored configurations. A typical energetically favored configuration consists of an oxygen vacancy with two yttrium ions in the  $1_{\text{NN}}$

position. Investigations show that this cluster appears more often in an EQ lattice up to intermediate dopant fractions for 1000 K and for all dopant fractions for 700 K.<sup>[55]</sup> Furthermore, the number of Y-Y pairs in  $2_{NN}$ ,  $3_{NN}$  and  $4_{NN}$  increases for all dopant fractions, which is evidence for the formation of larger clusters that can effectively trap and block the oxygen vacancies and lead to a lowered conductivity.

**Experiments** To verify this behavior, impedance spectroscopy experiments were performed. In this work, Sm doped ceria was chosen due to its high bulk conductivity. In Fig. 8.32, the bulk ionic conductivity of  $\text{Ce}_{0.8}\text{Sm}_{0.2}\text{O}_{1.9}$  at 500 K as a function of equilibration time at 800 K is shown. In fact, the ionic conductivity for the bulk decreases with increasing equilibration time at 800 K until after 55 days a constant value is reached.

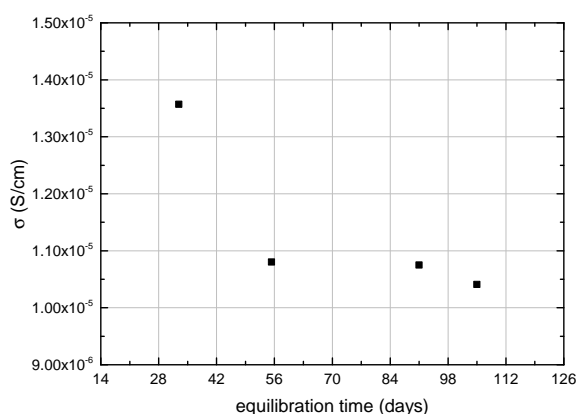


Figure 8.32: Degradation of the ionic conductivity of the bulk domain of  $\text{Ce}_{0.8}\text{Sm}_{0.2}\text{O}_{1.9}$  at 500 K as a function of equilibration time at 800 K according to impedance experiments.

Further measurements for the early decay in ionic conductivity with equilibration times up to 20 days are shown in Fig. 8.33. In the left figure, the influence of different methods of data analysis is shown. According to Chapter 4.1.5, the bulk semicircle found in the Nyquist plot for impedance measurements overlaps with the grain boundary semicircle. Therefore, the full semicircle or only the high frequency part of the bulk semicircle can be used. While the full semicircle may be influenced by the grain boundary conductivity, the high frequency part may be dominated by a change in conductivity behavior according to literature.<sup>[456]</sup> Additionally, either resistivity  $R$ ,  $Q$ -, and  $n$ -value can be fitted for each measurement or  $Q$ -, and  $n$ -value are kept constant while only the resistivity is fitted for each measurement. In Fig. 8.33 (right), the fit of the full semicircle with variable  $R$ ,  $Q$ -, and  $n$ -value for each measurement is shown, which was used for all impedance data in this work.

After 5.5 equilibration days, the sample was reinstalled, which led to a large jump in conductivity. The jump suggests a strong dependence of the bulk ionic conductivity on the contact between sample and Pt-wires. If this contact also degenerates with equilibration time, the result may be solely dependent on the contacting.

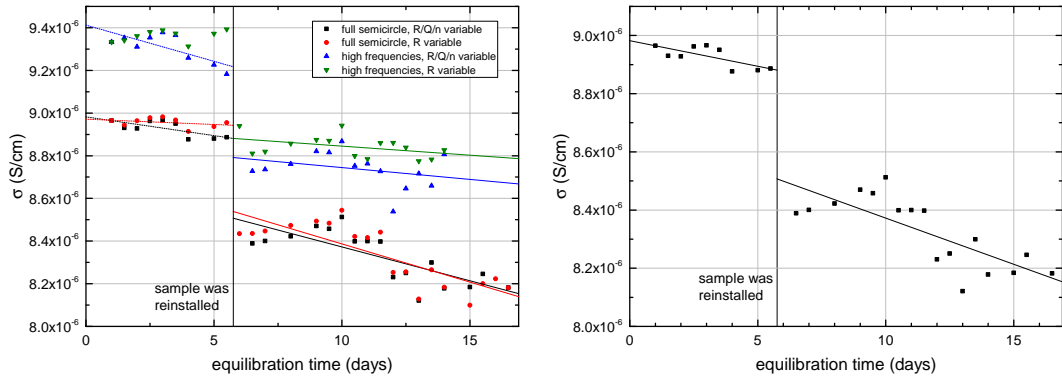


Figure 8.33: Ionic conductivity of bulk domain in  $\text{Ce}_{0.8}\text{Sm}_{0.2}\text{O}_{1.9}$  at 500 K as a function of equilibration time at 800 K according to impedance experiments.

The ionic conductivity decreases with increasing equilibration time at 800 K with about  $0.1 \cdot 10^{-6}$  S/cm to  $0.4 \cdot 10^{-6}$  S/cm per 10 days, which is about 1% to 4%. This is significantly less than found by Zhan *et al.* for Gd doped ceria,<sup>[168]</sup> which might be a result of the equilibration, which was not performed on a fresh sample in this work. The decrease is much larger than acceptable degradation rates for applications (about 1% per 1000 h). The measured decrease in conductivity could be caused by cation ordering, however, as discussed other reasons for the degradation are possible.



## 9 Summary and Outlook

In this work, the ionic conductivity in the bulk of doped ceria was investigated with experiments and theoretical calculations. For a detailed understanding of the underlying mechanism that determines the magnitude of the oxygen ion conductivity and the optimal dopant concentration, influences of microscopic defect interactions and the local structure on the macroscopic conductivity were shown.

The determination of the coordination number in ceria using Extended X-Ray Absorption Fine Structure (EXAFS) spectroscopy experiments was improved. The local structure was calculated for diluted defects or high defect concentrations using a pair interaction model and the association energies. Here, the Density Functional Theory (DFT) calculations and Metropolis Monte Carlo (MMC) simulations confirm the experimental results.

The ionic conductivity was predicted using Kinetic Monte Carlo (KMC) simulations, for which microscopic attempt frequencies and migration energies for different ionic configurations were calculated by means of DFT.

The attempt frequency in pure ceria was calculated as  $1.47 \cdot 10^{12} \text{ s}^{-1}$  at constant volume and  $7.67 \cdot 10^{12} \text{ s}^{-1}$  at constant pressure. For doping at the migration edge, large dopants lead to an increase and small dopants to a decrease in attempt frequency. One samarium dopant does not influence the attempt frequency due to a curved migration path. Doping with Sm in nearest neighborhood to the initial position of the migrating oxygen vacancy increases the attempt frequency.

The experimental attempt frequency for pure ceria varies vastly between  $10^{13} \text{ s}^{-1}$  and  $10^{22} \text{ s}^{-1}$ . The vast scattering of the experimental attempt frequency is caused by a change in activation enthalpy. The direct correlation of both properties was shown. Especially different contributions of the bulk and grain boundary domain to the total conductivity, different impurities, a change from an impurity- to a reduction-dominated regime and a change in the diffusion behavior can lead to significant changes in the activation enthalpy. Consequently, the experimental attempt frequency can be described as a function of the activation enthalpy for all measurements. In a simple model, the strong influence of the distribution of the different migration energies on the experimental attempt frequency was shown. Beyond that, the microscopic increase in local attempt frequency leads to a macroscopic increase in experimental attempt frequency in an Arrhenius plot.

The migration energy was calculated for ionic configurations in pure and doped ceria. A correlation between the migration energy and the widening of the edge cations distance was shown. Due to a strong dependence on the supercell size, the migration energy was extrapolated for an infinitely large supercell.

Numerous ionic configurations exist in doped ceria. While it is possible to reduce the number of arrangements if configurations are symmetrically equivalent and can be converted into each other, nevertheless every configuration cannot be calculated. In this work, the migration energy was predicted by creating a model including all possible configurations for the migration energy. Lattice positions were grouped if they had the same distance to the start, center or destination position. The migration energy increases categorically with increasing number of dopants at the migration edge (zero, one and two). The migration energy either increases or decreases linearly with increasing number dopants at start or destination position. If the number of dopants at both the start and destination position increases, the migration energy generally decreases. Using over 1100 migration energies proved that a pair interaction model is appropriate to describe the migration energy in doped ceria. The interaction between both sublattices (cation and anion) is small, and migration energies for diluted defects as well as high defect concentrations can be predicted using the proposed model.

The ionic conductivity is influenced by trapping, blocking and vacancy-vacancy interactions. Blocking mainly limits the dopant fraction of the maximum of the ionic conductivity. Here, the edge with one dopant is decisive. This shows that blocking is strongly underrated in literature. Trapping mainly limits the maximum ionic conductivity. Here, the association energy differences are decisive. Not only a low associate formation (hold) but also a low vacancy pull (catch) is important for a large ionic conductivity. Similar to the maximum ionic conductivity, the activation enthalpy is predominately influenced by trapping.

For comparison, impedance measurements were performed for Sm, Gd and Lu doped ceria. The measurements agree well with the data predicted by theoretical methods, namely the DFT calculations and KMC simulations. The largest bulk conductivity is found for  $\text{Ce}_{0.93}\text{Sm}_{0.07}\text{O}_{1.965}$ . In literature, different syntheses and sample preparation methods lead to larger total conductivities for Gd doped ceria. Experiments suggest that the Ce-Lu edge energy is higher than the Ce-Ce edge energy. Additionally, co-doped Sm-Zr and Gd-Zr ceria were investigated because the analyzed ceria single crystals synthesized by skull-melting need Zr as an ignition material. Doping ceria with Zr decreases the conductivity significantly. The decrease is more pronounced in Gd than in Sm doped ceria.

Due to scattering of the ionic conductivity in literature for materials with the same composition, influences of the sample preparation were investigated. Different sintering times and temperatures not only lead to different grain sizes but also to different bulk conductivities.

Finally, MMC and KMC simulations were combined to simulate the degradation of the oxygen ion conductivity due to a change in cation distribution. Impedance spectroscopy experiments verified a decrease in bulk conductivity with operation time.

For the development of future materials, the presented computational methods can be used to model the migration energy and simulate the ionic conductivity of any crystalline material. Blocking effects and V-V interactions must be included as their importance has been discussed in this work

---

and has often been underestimated in literature. In this way, properties can be identified, which lead to high conductivities according to the proposed catch-and-hold principle or low conductivities as in the case of Zr co-doped ceria. In addition, degradation effects should be included in the search for new materials, as long-term performance is crucial for the new generation of ionic conductors.



# References

- [1] J. Köttgen, *Sauerstoffionenleitfähigkeit in dotierten Ceroxiden aus experimenteller und quantenmechanischer Sicht: Masterarbeit*, 2011.
- [2] Renewable Energy Policy Network for the 21st Century, *Renewables 2016 Global Status Report*, 2016, <http://www.ren21.net/status-of-renewables/global-status-report/>.
- [3] *Positionspapier Energiespeicher: Der Beitrag der Chemie ; [Energiespeicher als Element einer sicheren Energieversorgung]*, ed. F. Ausfelder and K. Wagemann, 2015.
- [4] *IPCC special report on carbon dioxide capture and storage*, ed. B. Metz, Cambridge University Press, Cambridge, 2005.
- [5] Bundesministerium für Wirtschaft und Technologie, *Leuchtturm COORETEC*, 2007.
- [6] Bundesministerium für Wirtschaft und Technologie, *Empfehlungen des COORETEC-Beirats zur Förderung von Forschung und Entwicklung CO2-emissionsarmer Kraftwerkstechnologien und CO2-Abscheide- und Speichertechnologien*, 2009.
- [7] B. C. H. Steele and A. Heinzl, *Nature*, 2001, **414**, 345–352.
- [8] X.-D. Zhou and S. C. Singhal, *Fuel Cells and Hydrogen Storage*, Springer Berlin Heidelberg, Berlin, Heidelberg, 2011, vol. 141, pp. 1–32.
- [9] K. Eguchi, *Solid State Ionics*, 1996, **86-88**, 1245–1249.
- [10] A. Heinzl, J. Wartmann, G. Dura and P. Helm, *Hydrogen and Fuel Cell*, Springer Berlin Heidelberg, Berlin, Heidelberg, 2016, pp. 163–171.
- [11] J. M. Gaugain, *CR Séances Acad Sci*, 1853, **37**, 82–84.
- [12] H. Buff, *Ann. Chem. Pharm.*, 1854, **90**, 257–283.
- [13] H.-H. Möbius, *Journal of Solid State Electrochemistry*, 1997, **1**, 2–16.
- [14] W. Nernst, patent, DRP 104 872, 1899.

- [15] W. Nernst, *Zeitschrift für Elektrochemie und angewandte physikalische Chemie*, 1899, **6**, 41–43.
- [16] W. Schottky, *Wiss. Veröffentl. Siemens-Werken*, 1935, **14**, 1–19.
- [17] E. Baur and H. Preis, *Zeitschrift für Elektrochemie und angewandte physikalische Chemie*, 1937, **43**, 727–732.
- [18] C. Wagner, *Naturwissenschaften*, 1943, **31**, 265–268.
- [19] F. Hund, *Z. physik. Chem.*, 1952, **199**, 142.
- [20] A. Okada, *Materials Science and Engineering: B*, 2009, **161**, 182–187.
- [21] P. N. Dyer, R. E. Richards, S. L. Russek and D. M. Taylor, *Solid State Ionics*, 2000, **134**, 21–33.
- [22] A. Julbe, D. Farrusseng and C. Guizard, *Journal of Membrane Science*, 2001, **181**, 3–20.
- [23] S. P. S. Badwal and F. T. Ciacchi, *Advanced materials*, 2001, **13**, 993–996.
- [24] J. Gibbins and H. Chalmers, *Energy Policy*, 2008, **36**, 4317–4322.
- [25] M. Mogensen, *Solid State Ionics*, 2000, **129**, 63–94.
- [26] M. Panhans and R. Blumenthal, *Solid State Ionics*, 1993, **60**, 279–298.
- [27] K. Eguchi, T. Setoguchi, T. Inoue and H. Arai, *Solid State Ionics*, 1992, **52**, 165–172.
- [28] K. Eguchi, *Journal of Alloys and Compounds*, 1997, **250**, 486–491.
- [29] H. Yahiro, *Solid State Ionics*, 1989, **36**, 71–75.
- [30] M. Mogensen, T. Lindegaard, U. R. Hansen and G. Mogensen, Proceedings of the Second International Symposium on Ionic and Mixed Conducting Ceramics, Pennington, NJ, 1994, pp. 448–465.
- [31] H. Inaba and H. Tagawa, *Solid State Ionics*, 1996, **83**, 1–16.
- [32] R. D. Shannon, *Acta Crystallographica Section A*, 1976, **32**, 751–767.
- [33] R. Gerhardt-Anderson and A. A. Nowick, *Solid State Ionics*, 1981, **5**, 547–550.
- [34] D. W. Strickler and W. G. Carlson, *Journal of the American Ceramic Society*, 1965, **48**, 286–289.
- [35] H. Schmalzried, *Zeitschrift für Physikalische Chemie*, 1977, **105**, 47–62.

- 
- [36] D. K. Hohnke, *Solid State Ionics*, 1981, **5**, 531–534.
- [37] M. Martin, *Journal of Electroceramics*, 2006, **17**, 765–773.
- [38] C. R. Catlow and S. C. Parker, *Computer Simulation of Solids*, Springer Berlin Heidelberg, 1982, vol. 166, pp. 222–242.
- [39] V. Butler, C. Catlow, B. Fender and J. Harding, *Solid State Ionics*, 1983, **8**, 109–113.
- [40] C. Catlow, *Solid State Ionics*, 1984, **12**, 67–73.
- [41] A. Murray, G. Murch and C. Catlow, *Solid State Ionics*, 1986, **18-19**, 196–202.
- [42] N. V. Skorodumova, M. Baudin and K. Hermansson, *Physical Review B*, 2004, **69**, 075401.
- [43] Z. Yang, T. K. Woo, M. Baudin and K. Hermansson, *The Journal of Chemical Physics*, 2004, **120**, 7741.
- [44] D. A. Andersson, S. I. Simak, N. V. Skorodumova, I. A. Abrikosov and B. Johansson, *Proceedings of the National Academy of Sciences of the United States of America*, 2006, **103**, 3518–3521.
- [45] A. Ismail, J. Hooper, J. B. Giorgi and T. K. Woo, *Physical Chemistry Chemical Physics*, 2011, **13**, 6116.
- [46] *International tables for crystallography*, ed. T. Hahn, Springer Netherland, Berlin, 5th edn, 2007.
- [47] E. Riedel and R. Alsfasser, *Moderne anorganische Chemie*, Gruyter, Berlin [u.a.], 3rd edn, 2007.
- [48] B. Roling, *Bunsen-Magazin*, 2005, **7**, 63.
- [49] J. Schoonman, *Nanostructured and Advanced Materials for Applications in Sensor, Optoelectronic and Photovoltaic Technology*, Springer Science+Business Media B.V, Dordrecht, 2005, vol. 204, p. 259.
- [50] S. Grieshammer, T. Zacherle and M. Martin, *Physical Chemistry Chemical Physics*, 2013, **15**, 15935–15942.
- [51] T. Zacherle, A. Schrieffer, R. A. De Souza and M. Martin, *Physical Review B*, 2013, **87**, 134104.
- [52] H. L. Tuller, *Journal of The Electrochemical Society*, 1979, **126**, 209.
- [53] M. Martin, T. Zacherle, A. Schrieffer, R. A. d. Souza and S. Grieshammer, *ECS Transactions*, 2013, **57**, 2405–2410.

- [54] M. Nakayama and M. Martin, *Physical Chemistry Chemical Physics*, 2009, **11**, 3241–3249.
- [55] S. Grieshammer, B. O. H. Grope, J. Koettgen and M. Martin, *Physical Chemistry Chemical Physics*, 2014, **16**, 9974.
- [56] C. Loschen, J. Carrasco, K. Neyman and F. Illas, *Physical Review B*, 2007, **75**, 035115.
- [57] L. Gerward and J. S. Olsen, *Powder Diffraction*, 1993, **8**, 127–129.
- [58] G. J. VanHandel and R. N. Blumenthal, *Journal of The Electrochemical Society*, 1974, **121**, 1198.
- [59] M. Martin, *Diffusion in Condensed Matter*, Springer-Verlag Berlin Heidelberg, Berlin, Heidelberg, 2005, pp. 209–247.
- [60] T. H. Etsell and S. N. Flengas, *Chemical Reviews*, 1970, **70**, 339–376.
- [61] D. J. Bevan and E. Summerville, *Handbook on the Physics and Chemistry of Rare Earths: Non-metallic compounds*, North-Holland Pub. Co, 1979, pp. 401–524.
- [62] G. Balazs, *Solid State Ionics*, 1995, **76**, 155–162.
- [63] S. Dikmen, P. Shuk and M. Greenblatt, *Solid State Ionics*, 1999, **126**, 89–95.
- [64] Z. Tianshu, P. Hing, H. Huang and J. Kilner, *Solid State Ionics*, 2002, **148**, 567–573.
- [65] W. Mišta, M. A. Małecka and L. Kępiński, *Applied Catalysis A: General*, 2009, **368**, 71–78.
- [66] V. Grover, A. Banerji, P. Sengupta and A. Tyagi, *Journal of Solid State Chemistry*, 2008, **181**, 1930–1935.
- [67] M. A. Małecka, L. Kępiński and M. Mączka, *Journal of Solid State Chemistry*, 2008, **181**, 2306–2312.
- [68] B. Matović, M. Stojmenović, J. Pantić, A. Varela, M. Žunić, N. Jiraborvornpongsa and T. Yano, *Journal of Asian Ceramic Societies*, 2014, **2**, 117–122.
- [69] C. Sánchez-Bautista, Dos santos-Garcia, Antonio J., J. Peña-Martínez and J. Canales-Vázquez, *Solid State Ionics*, 2010, **181**, 1665–1673.
- [70] S. A. Acharya, *Journal of Power Sources*, 2012, **198**, 105–111.
- [71] L. Li, G. Li, Y. Che and W. Su, *Chemistry of Materials*, 2000, **12**, 2567–2574.
- [72] P. Shuk, M. Greenblatt and M. Croft, *Chemistry of Materials*, 1999, **11**, 473–479.
- [73] S. Zha, C. Xia and G. Meng, *Journal of Power Sources*, 2003, **115**, 44–48.

- 
- [74] Z. Zhan, T.-L. Wen, H. Tu and Z.-Y. Lu, *Journal of The Electrochemical Society*, 2001, **148**, A427.
- [75] L. Aneflous, J. A. Musso, S. Villain, J.-R. Gavarri and H. Benyaich, *Journal of Solid State Chemistry*, 2004, **177**, 856–865.
- [76] L. P. Li, X. M. Lin, G. S. Li and H. Inomata, *J. Mater. Res*, 2001, **16**, 3207.
- [77] Y. Zheng, Y. Shi, H. Gu, L. Gao, H. Chen and L. Guo, *Materials Research Bulletin*, 2009, **44**, 1717–1721.
- [78] R. T. Dirstine, *Journal of The Electrochemical Society*, 1979, **126**, 264.
- [79] G. Brauer and H. Gradinger, *Zeitschrift für anorganische und allgemeine Chemie*, 1954, **276**, 209–226.
- [80] J. Sunarso, S. Baumann, J. M. Serra, W. A. Meulenber, S. Liu, Y. S. Lin and J. C. D. da Costa, *Journal of Membrane Science*, 2008, **320**, 13–41.
- [81] R. Blumenthal and R. Panlener, *Journal of Physics and Chemistry of Solids*, 1970, **31**, 1190–1192.
- [82] R. N. Blumenthal and R. L. Hofmaier, *Journal of The Electrochemical Society*, 1974, **121**, 126.
- [83] H. Tuller and A. Nowick, *Journal of Physics and Chemistry of Solids*, 1977, **38**, 859–867.
- [84] I. K. Naik and T. Y. Tien, *Journal of Physics and Chemistry of Solids*, 1978, **39**, 311–315.
- [85] M. Nakayama, H. Ohshima, M. Nogami and M. Martin, *Physical Chemistry Chemical Physics*, 2012, **14**, 6079.
- [86] B. Steele, *Solid State Ionics*, 2000, **129**, 95–110.
- [87] B. Steele and J. M. Floyd, *Proc. Brit. Ceramic Soc.*, 1971, **19**, 55–76.
- [88] H. L. Tuller, *Journal of The Electrochemical Society*, 1975, **122**, 255.
- [89] H. L. Tuller, *Nonstoichiometric oxides*, Acad. Pr, New York, 1981, p. 271.
- [90] S. Wang, H. Inaba, H. Tagawa and T. Hashimoto, *Journal of The Electrochemical Society*, 1997, **144**, 4076–4080.
- [91] D. Schneider, M. Gödickemeier and L. J. Gauckler, *Journal of Electroceramics*, 1997, **1**, 165–172.

- [92] S. Wang, *Solid State Ionics*, 1998, **107**, 73–79.
- [93] E. K. Chang and R. Blumenthal, *Journal of Solid State Chemistry*, 1988, **72**, 330–337.
- [94] W. Noddack and H. Walch, *Zeitschrift für Physikalische Chemie*, 1959, **211**, 194.
- [95] E. Greener, J. Wimmer and W. Hirthe, *Rare Earth Research, Vol III*, Gordon and Breach, New York, 1964, p. 539.
- [96] R. Blumenthal and R. Sharma, *Journal of Solid State Chemistry*, 1975, **13**, 360–364.
- [97] J. Campserveux and P. Gerdanian, *Journal of Solid State Chemistry*, 1978, **23**, 73–92.
- [98] R. Panlener, R. Blumenthal and J. Garnier, *Journal of Physics and Chemistry of Solids*, 1975, **36**, 1213–1222.
- [99] O. Sørensen, *Journal of Solid State Chemistry*, 1976, **18**, 217–233.
- [100] S.-N. Wang, R. P. Wyeth and R. H. Kennedy, *European Journal of Pharmacology*, 1998, **361**, 73–77.
- [101] H. Yokokawa, N. Sakai, T. Horita and K. Yamaji, *Fuel Cells*, 2001, **1**, 117–131.
- [102] G. Murch, *Solid State Ionics*, 1982, **7**, 177–198.
- [103] L. T. Kong and L. J. Lewis, *Physical Review B*, 2006, **74**, 073412.
- [104] W. D. Kingery, H. K. Bowen and D. R. Uhlmann, *Introduction to ceramics*, Wiley, New York, 2nd edn, 1976.
- [105] M. v. Ardenne, *Effekte der Physik und ihre Anwendungen*, Deutsch, Frankfurt am Main, 3rd edn, 2005.
- [106] S. Arrhenius, *Zeitschrift für Physikalische Chemie*, 1889, **4**, 226–248.
- [107] M. Trautz, *Chemistry*, 1916, **96**, 1–28.
- [108] W. C. Lewis, *Journal of the Chemical Society*, 1918, **113**, 471.
- [109] H. Eyring, *The Journal of Chemical Physics*, 1935, **3**, 107.
- [110] G. H. Vineyard, *Journal of Physics and Chemistry of Solids*, 1957, **3**, 121–127.
- [111] R. D. Present, *Proceedings of the National Academy of Sciences*, 1955, **41**, 415–417.
- [112] V. Pontikis, *Diffusion in materials*, Kluwer Acad. Publ, Dordrecht, 1990, vol. 179, p. 37.
- [113] H. A. Kramers, *Physica*, 1940, **7**, 284–304.

- 
- [114] M. Toller, G. Jacucci, G. DeLorenzi and C. P. Flynn, *Physical Review B*, 1985, **32**, 2082–2095.
- [115] G. De Lorenzi, G. Jacucci and C. P. Flynn, *Physical Review B*, 1987, **36**, 9461–9468.
- [116] M. Marchese, G. Jacucci and C. P. Flynn, *Physical Review B*, 1987, **36**, 9469–9481.
- [117] M. Marchese and C. P. Flynn, *Physical Review B*, 1988, **38**, 12200–12207.
- [118] J. H. Harding, *Reports on Progress in Physics*, 1990, **53**, 1403–1466.
- [119] P. Hänggi and M. Borkovec, *Reviews of Modern Physics*, 1990, **62**, 251–341.
- [120] S. Glasstone, K. J. Laidler and H. Eyring, *The theory of rate processes: the kinetics of chemical reactions, viscosity, diffusion and electrochemical phenomena*, McGraw-Hill Book Company, inc, 1941.
- [121] H. Eyring, *Chemical Reviews*, 1935, **17**, 65–77.
- [122] H. Eyring, S. H. Lin and S. M. Lin, *Basic Chemical Kinetics*, Wiley, New York, 1980.
- [123] H. Mehrer, *Diffusion in solids: fundamentals, methods, materials, diffusion-controlled processes*, Springer, 2007.
- [124] C. P. Flynn, *Point defects and diffusion*, Clarendon Press, 1972.
- [125] E. Whalley, *Advances in Physical Organic Chemistry*, 2, Elsevier, Burlington, 1964, pp. 93–162.
- [126] J. Philibert, *Atom movements*, Éd. de Physique, Les Ulis, 1991.
- [127] H. Yildirim, A. Kara, S. Durukanoglu and T. S. Rahman, *Surface Science*, 2006, **600**, 484–492.
- [128] T. D. B. Jacobs, B. Gotsmann, M. A. Lantz and R. W. Carpick, *Tribology Letters*, 2010, **39**, 257–271.
- [129] C. H. Bennett and B. J. Alder, *Journal of Physics and Chemistry of Solids*, 1971, **32**, 2111–2122.
- [130] C. H. Bennett, *Diffusion in solids*, Acad. Press, New York, 1975, p. 73.
- [131] A. Da Fano and G. Jacucci, *Physical Review Letters*, 1977, **39**, 950–953.
- [132] S. Rice, *Physical Review*, 1958, **112**, 804–811.
- [133] H. Glyde, *Reviews of Modern Physics*, 1967, **39**, 373–382.
- [134] M. Feit, *Physical Review B*, 1972, **5**, 2145–2153.

- [135] A. D. Le Claire, *Philosophical Magazine*, 1966, **14**, 1271–1284.
- [136] Y. Ebisuzaki, W. J. Kass and M. O’Keeffe, *The Journal of Chemical Physics*, 1967, **46**, 1373.
- [137] W. Franklin, *Physical Review*, 1969, **180**, 682–694.
- [138] D. G. Truhlar, B. C. Garrett and S. J. Klippenstein, *The Journal of Physical Chemistry*, 1996, **100**, 12771–12800.
- [139] Y. Lu, F. Zheng and P. Zhang, *Journal of Applied Physics*, 2013, **114**, 153507.
- [140] E. Wimmer, W. Wolf, J. Sticht, P. Saxe, C. B. Geller, R. Najafabadi and G. A. Young, *Physical Review B*, 2008, **77**, 134305.
- [141] K.-P. Bohnen, R. Heid and B. Renker, *Physical Review Letters*, 2001, **86**, 5771–5774.
- [142] K.-P. Bohnen, R. Heid and M. Krauss, *Europhysics Letters (EPL)*, 2003, **64**, 104–110.
- [143] G. Deinzer, G. Birner and D. Strauch, *Physical Review B*, 2003, **67**, 144304.
- [144] I. I. Mazin, D. J. Singh, M. D. Johannes and M. H. Du, *Physical Review Letters*, 2008, **101**, 057003.
- [145] A. Shukla, M. Calandra, M. d’Astuto, M. Lazzeri, F. Mauri, C. Bellin, M. Krisch, J. Karpinski, S. M. Kazakov, J. Jun, D. Daghero and K. Parlinski, *Physical Review Letters*, 2003, **90**, 095506.
- [146] Y. Ma, J. S. Tse, T. Cui, D. D. Klug, L. Zhang, Y. Xie, Y. Niu and G. Zou, *Physical Review B*, 2005, **72**, 014306.
- [147] B. Grabowski, T. Hickel and J. Neugebauer, *Physical Review B*, 2007, **76**, 024309.
- [148] L. T. Kong and L. J. Lewis, *Physical Review B*, 2008, **77**, 165422.
- [149] M. Mantina, L. Q. Chen and Z. K. Liu, *Defect Diffus. Forum (Defect and Diffusion Forum)*, 2009, **294**, 1–13.
- [150] O. N. Bedoya-Martínez and G. Roma, *Physical Review B*, 2010, **82**, 134115.
- [151] M. Mantina, Y. Wang, R. Arroyave, S. L. Shang, L. Q. Chen and Z. K. Liu, *Journal of Physics: Condensed Matter*, 2012, **24**, 305402.
- [152] A. S. Fedorov and A. F. Sadreev, *Physical Status Solidi B*, 2009, **246**, 2598–2601.
- [153] A. A. Maradudin, *Theory of lattice dynamics in the harmonic approximation. 2. ed*, Academic Press, New York, N.Y., 1971, vol. 3.
- [154] P. G. Sundell, M. E. Björketun and G. Wahnström, *Physical Review B*, 2007, **76**, 094301.

- 
- [155] K. Toyoura, Y. Koyama, A. Kuwabara, F. Oba and I. Tanaka, *Physical Review B*, 2008, **78**, 214303.
- [156] W. Huang, *Solid State Ionics*, 1997, **100**, 23–27.
- [157] Y.-P. Fu, S.-B. Wen and C.-H. Lu, *Journal of the American Ceramic Society*, 2008, **91**, 127–131.
- [158] C. Peng, Y. Zhang, Z. W. Cheng, X. Cheng and J. Meng, *Journal of Materials Science: Materials in Electronics*, 2002, **13**, 757–762.
- [159] Z. Q. Yu, Kuchibhatla, Satyanarayana V. N. T., L. V. Saraf, O. A. Marina, C. M. Wang, M. H. Engelhard, V. Shutthanandan, P. Nachimuthu and S. Thevuthasan, *Electrochemical and Solid-State Letters*, 2008, **11**, B76.
- [160] W. Huang, P. Shuk and M. Greenblatt, *Chemistry of Materials*, 1997, **9**, 2240–2245.
- [161] H. Yahiro, Y. Eguchi, K. Eguchi and H. Arai, *Journal of Applied Electrochemistry*, 1988, **18**, 527–531.
- [162] T. Kudo, *Journal of The Electrochemical Society*, 1975, **122**, 142.
- [163] J. Faber, C. Geoffroy, A. Roux, A. Sylvestre and P. Abélard, *Applied Physics A Solids and Surfaces*, 1989, **49**, 225–232.
- [164] A. Nowick, D. Wang, D. Park and J. Griffith, *Fast ion transport in solids*, North Holland, New York, 1979, p. 673.
- [165] S. Omar, E. Wachsman and J. Nino, *Solid State Ionics*, 2006, **177**, 3199–3203.
- [166] S. Omar, E. D. Wachsman, J. L. Jones and J. C. Nino, *Journal of the American Ceramic Society*, 2009, **92**, 2674–2681.
- [167] D. Wang, D. Park, J. Griffith and A. Nowick, *Solid State Ionics*, 1981, **2**, 95–105.
- [168] T. Zhang, J. Ma, L. Kong, S. Chan and J. Kilner, *Solid State Ionics*, 2004, **170**, 209–217.
- [169] D. Pérez-Coll, D. Marrero-López, P. Núñez, S. Piñol and J. R. Frade, *Electrochimica Acta*, 2006, **51**, 6463–6469.
- [170] W. Zajac, *Solid State Ionics*, 2008, **179**, 154–158.
- [171] J. van Herle, D. Seneviratne and A. McEvoy, *Journal of the European Ceramic Society*, 1999, **19**, 837–841.

## References

---

- [172] J. Van herle, T. Horita, T. Kawada, N. Sakai, H. Yokokawa and M. Dokiya, *Solid State Ionics*, 1996, **86-88**, 1255–1258.
- [173] B. Steele, K. Zheng, R. Rudkin, N. Kiratzis and M. Cristie, *Proceedings of the Fourth International Symposium on Solid Oxide Fuel Cells (SOFC-IV)*, Electrochemical Society, Pennington, NJ, 1995, vol. 95-1, pp. 1028–1038.
- [174] K. Huang, M. Feng and J. B. Goodenough, *Journal of the American Ceramic Society*, 1998, **81**, 357–362.
- [175] E. Ruiz-Trejo, J. D. Sirman, Y. M. Baikov and J. A. Kilner, *Solid State Ionics*, 1998, **113-115**, 565–569.
- [176] G. Christie, *Solid State Ionics*, 1996, **83**, 17–27.
- [177] K. R. Reddy and K. Karan, *Journal of Electroceramics*, 2005, **15**, 45–56.
- [178] N. Cioatera, V. Pârvulescu, A. Rolle and R. N. Vannier, *Solid State Ionics*, 2009, **180**, 681–687.
- [179] R. Sanghavi, R. Devanathan, M. I. Nandasiri, S. Kuchibhatla, L. Kovarik, S. Thevuthasan and S. Prasad, *Solid State Ionics*, 2011, **204-205**, 13–19.
- [180] M. G. Bellino, D. G. Lamas and N. E. Walsøe de Reca, *Advanced Functional Materials*, 2006, **16**, 107–113.
- [181] Y. Zheng, M. Zhou, L. Ge, S. Li, H. Chen and L. Guo, *Journal of Alloys and Compounds*, 2011, **509**, 1244–1248.
- [182] I. Stephens and J. Kilner, *Solid State Ionics*, 2006, **177**, 669–676.
- [183] J. X. Zhu, D. F. Zhou, S. R. Guo, J. F. Ye, X. F. Hao, X. Q. Cao and J. Meng, *Journal of Power Sources*, 2007, **174**, 114–123.
- [184] M. Mogensen, T. Lindegaard, U. R. Hansen and G. Mogensen, *Journal of The Electrochemical Society*, 1994, **141**, 2122.
- [185] R. O. Fuentes and R. T. Baker, *Journal of Power Sources*, 2009, **186**, 268–277.
- [186] D. R. Ou, T. Mori, F. Ye, T. Kobayashi, J. Zou, G. Auchterlonie and J. Drennan, *Applied Physics Letters*, 2006, **89**, 171911.
- [187] J. Van herle, T. Horita, T. Kawada, N. Sakai, H. Yokokawa and M. Dokiya, *Journal of the European Ceramic Society*, 1996, **16**, 961–973.
- [188] G. B. Balazs and R. S. Glass, *Proceedings of the Second International Symposium on Ionic and Mixed Conducting Ceramics*, Pennington, NJ, 1994, pp. 478–488.

- 
- [189] S. A. Acharya, K. Singh and S. S. Bhoga, *Integrated Ferroelectrics*, 2010, **121**, 13–23.
- [190] T. Kudo, *Journal of The Electrochemical Society*, 1976, **123**, 415.
- [191] Y. Takasu, T. Sugino and Y. Matsuda, *Journal of Applied Electrochemistry*, 1984, **14**, 79–81.
- [192] P. Shuk, *Solid State Ionics*, 1999, **116**, 217–223.
- [193] C. Tian and S.-W. Chan, *MRS Proceedings*, 1998, **548**, 623–629.
- [194] C. Tian, *Solid State Ionics*, 2000, **134**, 89–102.
- [195] D. Pérez-Coll, P. Núñez and J. R. Frade, *Journal of The Electrochemical Society*, 2006, **153**, A478.
- [196] T. Mori, R. Buchanan, D. Ou, F. Ye, T. Kobayashi, J.-D. Kim, J. Zou and J. Drennan, *Journal of Solid State Electrochemistry*, 2008, **12**, 841–849.
- [197] N. Q. Minh, *Journal of the American Ceramic Society*, 1993, **76**, 563–588.
- [198] A. Hammou and J. Guindet, *The CRC handbook of solid state electrochemistry*, CRC Press, Boca Raton and Fla, 1997, pp. 407–444.
- [199] R. N. Blumenthal, P. W. Lee and R. J. Panlener, *Journal of The Electrochemical Society*, 1971, **118**, 123.
- [200] H. Arai, *Solid State Ionics*, 1986, **20**, 241–248.
- [201] K. Eguchi, T. Kunishaki and H. Arai, *Journal of the American Ceramic Society*, 1986, **69**, C-282–C-285.
- [202] H. Yahiro, *Solid State Ionics*, 1986, **21**, 37–47.
- [203] J. M. Ralph, *PhD thesis*, Imperial College London, 1998.
- [204] D. Steele and B. E. F. Fender, *Journal of Physics C: Solid State Physics*, 1974, **7**, 1–11.
- [205] M. Abraham, R. Weeks, G. Clark and C. Finch, *Physical Review*, 1966, **148**, 350–352.
- [206] T. Ohashi, *Solid State Ionics*, 1998, **113-115**, 559–564.
- [207] S. Yamazaki, *Solid State Ionics*, 2000, **136-137**, 913–920.
- [208] S. Yamazaki, *Solid State Ionics*, 2002, **154-155**, 113–118.
- [209] H. Deguchi, H. Yoshida, T. Inagaki and M. Horiuchi, *Solid State Ionics*, 2005, **176**, 1817–1825.

## References

---

- [210] P. Jain, H. J. Avila-Paredes, C. Gapuz, S. Sen and S. Kim, *The Journal of Physical Chemistry C*, 2009, **113**, 6553–6560.
- [211] N. Kim and J. F. Stebbins, *Chemistry of Materials*, 2007, **19**, 5742–5747.
- [212] H. Maekawa, K. Kawata, Y. P. Xiong, N. Sakai and H. Yokokawa, *Solid State Ionics*, 2009, **180**, 314–319.
- [213] W. O'Neill and M. Morris, *Chemical Physics Letters*, 1999, **305**, 389–394.
- [214] T. Y. Tien and E. C. Subbarao, *The Journal of Chemical Physics*, 1963, **39**, 1041.
- [215] A. Nakamura, *Journal of The Electrochemical Society*, 1980, **127**, 2325.
- [216] A. Nakamura, *Journal of The Electrochemical Society*, 1986, **133**, 1542.
- [217] D. Ou, T. Mori, F. Ye, J. Zou, G. Auchterlonie and J. Drennan, *Physical Review B*, 2008, **77**, 024108.
- [218] J. Hooper, A. Ismail, J. B. Giorgi and T. K. Woo, *Physical Chemistry Chemical Physics*, 2010, **12**, 12969.
- [219] F. Shimojo, T. Okabe, F. Tachibana, M. Kobayashi and H. Okazaki, *Journal of the Physics Society Japan*, 1992, **61**, 2848–2857.
- [220] M. Meyer and N. Nicoloso, *Berichte der Bunsen-Gesellschaft*, 1997, **101**, 1393–1398.
- [221] H. Yoshida, *Solid State Ionics*, 2003, **160**, 109–116.
- [222] K. Muthukkumaran, R. Bokalawela, T. Mathews and S. Selladurai, *Journal of Materials Science*, 2007, **42**, 7461–7466.
- [223] C. Frayret, A. Villesuzanne, M. Pouchard, F. Mauvy, J.-M. Bassat and J.-C. Grenier, *The Journal of Physical Chemistry C*, 2010, **114**, 19062–19076.
- [224] P. P. Dholabhai and J. B. Adams, *Journal of Materials Science*, 2012, **47**, 7530–7541.
- [225] R. Krishnamurthy, Y.-G. Yoon, D. J. Srolovitz and R. Car, *Journal of the American Ceramic Society*, 2004, **87**, 1821–1830.
- [226] J. Kilner, *Solid State Ionics*, 1983, **8**, 201–207.
- [227] S. J. Hong and A. V. Virkar, *Journal of the American Ceramic Society*, 1995, **78**, 433–439.
- [228] D.-J. Kim, *Journal of the American Ceramic Society*, 1989, **72**, 1415–1421.
- [229] J. Kilner and R. Brook, *Solid State Ionics*, 1982, **6**, 237–252.

- 
- [230] H. Yoshida, *Solid State Ionics*, 2001, **140**, 191–199.
- [231] X. Wei, W. Pan, L. Cheng and B. Li, *Solid State Ionics*, 2009, **180**, 13–17.
- [232] L. Minervini, *Solid State Ionics*, 1999, **116**, 339–349.
- [233] M. Zacate, L. Minervini, D. Bradfield, R. Grimes and K. Sickafus, *Solid State Ionics*, 2000, **128**, 243–254.
- [234] A. Navrotsky, P. Simoncic, H. Yokokawa, W. Chen and T. Lee, *Faraday Discussions*, 2006, **134**, 171.
- [235] J. M. Ralph, J. Przydatek, J. A. Kilner and T. Seguelong, *Berichte der Bunsen-Gesellschaft*, 1997, **101**, 1403–1407.
- [236] P. Li, I.-W. Chen, J. E. Penner-Hahn and T.-Y. Tien, *Journal of the American Ceramic Society*, 1991, **74**, 958–967.
- [237] S. Omar, E. D. Wachsman and J. C. Nino, *Applied Physics Letters*, 2007, **91**, 144106.
- [238] D. Maricle, T. Swarr and S. Karavolis, *Solid State Ionics*, 1992, **52**, 173–182.
- [239] J. Ralph and J. Kilner, *Proceedings of the Fifth International Symposium on Solid Oxide Fuel Cells (SOFC-V)*, Electrochemical Society, Pennington, NJ, 1997, pp. 1021–1030.
- [240] J. M. Ralph, J. A. Kilner and B. C. H. Steele, *MRS Proceedings*, 1999, **575**, 309–314.
- [241] O. Parkash, N. Singh, N. K. Singh and D. Kumar, *Solid State Ionics*, 2012, **212**, 100–105.
- [242] *Moderne Röntgenbeugung*, ed. L. Spieß, Vieweg + Teubner, Wiesbaden, 2009.
- [243] W. Massa, *Kristallstrukturbestimmung*, Vieweg & Teubner, Wiesbaden, 2011.
- [244] H. Krischner and B. Koppelhuber-Bitschnau, *Röntgenstrukturanalyse und Rietveldmethode: Eine Einführung*, Vieweg+Teubner Verlag, Wiesbaden, s.l., 5th edn, 1994.
- [245] W. H. Bragg and W. L. Bragg, *Proceedings of the Royal Society A: Mathematical, Physical and Engineering Sciences*, 1913, **88**, 428–438.
- [246] H. M. Rietveld, *Zeitschrift für Kristallographie*, 2010, **225**, 545–547.
- [247] E. Barsoukov and J. R. Macdonald, *Impedance spectroscopy: Theory, experiment, and applications*, Wiley-Interscience, Hoboken and N.J, 2nd edn, 2005.
- [248] F. S. Brugner and R. N. Blumenthal, *Journal of the American Ceramic Society*, 1971, **54**, 57.
- [249] J. M. Montes, F. G. Cuevas and J. Cintas, *Applied Physics A*, 2008, **92**, 375–380.

- [250] Georg Thieme Verlag, *RÖMPP Online*, 2011, <http://www.roempp.com/prod/>.
- [251] B. Heine, *Werkstoffprüfung Ermittlung von Werkstoffeigenschaften; mit zahlreichen Tabellen*, Burkhard Heine, Fachbuchverl. Leipzig im Carl-Hanser-Verl., München Wien, 2003.
- [252] A. Einstein, *Annalen der Physik*, 1905, **322**, 132–148.
- [253] D. C. Koningsberger and R. Prins, *X-Ray Absorption: Principles, Applications, Techniques of EXAFS, SEXAFS and XANES*, Wiley, 1988.
- [254] B. K. Teo and D. C. Joy, *EXAFS Spectroscopy: Techniques and Applications*, Springer, Boston, MA, 1981.
- [255] P. Heitjans and S. Indris, *Journal of Physics: Condensed Matter*, 2003, **15**, R1257–R1289.
- [256] H. J. Avila-Paredes, P. Jain, S. Sen and S. Kim, *Chemistry of Materials*, 2010, **22**, 893–897.
- [257] J. Subbi, I. Heinmaa, R. Pöder and H. Kooskora, *Solid State Ionics*, 2012, **225**, 488–492.
- [258] J. M. Floyd, *Indian J. Tech.*, 1973, **11**, 589–594.
- [259] M. Kamiya, E. Shimada and Y. Ikuma, *Journal of the Ceramic Society of Japan*, 1998, **106**, 1023–1026.
- [260] M. Kamiya, E. Shimada, Y. Ikuma, M. Komatsu and H. Haneda, *Journal of The Electrochemical Society*, 2000, **147**, 1222.
- [261] D. Ende and K.-M. Mangold, *Chemie in unserer Zeit*, 1993, **27**, 134–140.
- [262] R. Dronskowski, *Computational Chemistry of Solid State Materials: A guide for materials scientists, chemists, physicists and others*, Wiley-VCH, Weinheim, 2005.
- [263] C. A. Ullrich, *Time-dependent density-functional theory: Concepts and applications*, Oxford Univ. Press, Oxford, Reprint., with corr edn, 2014.
- [264] W. Kohn, A. D. Becke and R. G. Parr, *The Journal of Physical Chemistry*, 1996, **100**, 12974–12980.
- [265] M. Born and R. Oppenheimer, *Annalen der Physik*, 1927, **389**, 457–484.
- [266] L. H. Thomas, *Mathematical Proceedings of the Cambridge Philosophical Society*, 1927, **23**, 542.
- [267] E. Fermi, *Z. Physik (Zeitschrift für Physik)*, 1928, **48**, 73–79.
- [268] P. Hohenberg and W. Kohn, *Physical Review*, 1964, **136**, B864–B871.

- 
- [269] T. Zacherle, P. C. Schmidt and M. Martin, *Resistive switching*, 2016.
- [270] W. Kohn and L. J. Sham, *Physical Review*, 1965, **140**, A1133–A1138.
- [271] S. H. Vosko, L. Wilk and M. Nusair, *Canadian Journal of Physics*, 1980, **58**, 1200–1211.
- [272] S. L. Dudarev, G. A. Botton, S. Y. Savrasov, C. J. Humphreys and A. P. Sutton, *Physical Review B*, 1998, **57**, 1505–1509.
- [273] M. Cococcioni and S. d. Gironcoli, *Physical Review B*, 2005, **71**, 035105.
- [274] C. W. M. Castleton, J. Kullgren and K. Hermansson, *The Journal of Chemical Physics*, 2007, **127**, 244704.
- [275] P. P. Dholabhai, J. B. Adams, P. Crozier and R. Sharma, *Physical Chemistry Chemical Physics*, 2010, **12**, 7904.
- [276] F. Bloch, *Z. Phys.*, 1929, **52**, 555–600.
- [277] G. Kresse, M. Marsman and J. Furthmüller, *VASP Manual*, 2011, <http://cms.mpi.univie.ac.at/vasp/vasp/vasp.html>.
- [278] P. E. Blöchl, *Physical Review B*, 1994, **50**, 17953–17979.
- [279] N. Metropolis, A. W. Rosenbluth, M. N. Rosenbluth, A. H. Teller and E. Teller, *The Journal of Chemical Physics*, 1953, **21**, 1087.
- [280] K. Binder and D. Heermann, *Monte Carlo simulation in statistical physics: An Introduction*, Springer, Heidelberg, 2010.
- [281] S. B. Adler and J. W. Smith, *Journal of the Chemical Society, Faraday Transactions*, 1993, **89**, 3123.
- [282] A. Oaks, *Development of Generalized KMC Code to Study Defect Mobility in Ceramic Materials towards Nuclear Fuel Applications*, May 11, 2010, <https://courses.physics.illinois.edu/phys466/sp2013/projects/2010/Oaks/html/index.html>.
- [283] A. Oaks, Di Yun, B. Ye, W.-Y. Chen and J. F. Stubbins, *Journal of Nuclear Materials*, 2011, **414**, 145–149.
- [284] P. P. Dholabhai, S. Anwar, J. B. Adams, P. Crozier and R. Sharma, *Journal of Solid State Chemistry*, 2011, **184**, 811–817.
- [285] P. P. Dholabhai, J. B. Adams, P. A. Crozier and R. Sharma, *Journal of Materials Chemistry*, 2011, **21**, 18991.

- [286] P. P. Dholabhai, S. Anwar, J. B. Adams, P. A. Crozier and R. Sharma, *Modelling and Simulation in Materials Science and Engineering*, 2012, **20**, 015004.
- [287] B. O. H. Grope, T. Zacherle, M. Nakayama and M. Martin, *Solid State Ionics*, 2012, **225**, 476–483.
- [288] G. E. Murch, *American Journal of Physics*, 1979, **47**, 78.
- [289] A. F. Voter, *Radiation effects in solids*, Springer, Dordrecht, 2007, vol. 235, pp. 1–23.
- [290] S. L. Lin and J. N. Bardsley, *Computer Physics Communications*, 1978, **15**, 161–163.
- [291] J. Köttgen, *Herstellung und Charakterisierung von asymmetrischen Sauerstoffpermeationsmembranen auf Ceroxid-Basis: Bachelorarbeit*, 2009.
- [292] M. P. Pechini, patent, *United States*, 3 330 697, 1967.
- [293] P. Courty, B. Delmon, C. Marcilly and A. Sugier, patent, *France*, 1 604 707, 1968.
- [294] R. A. Rocha and E. N. S. Muccillo, *Materials Research Bulletin*, 2003, **38**, 1979–1986.
- [295] G. Dück, *Synthesis, Characterization and Impedance Spectroscopy of Lu doped ceria: master thesis*, RWTH Aachen University, 2015.
- [296] N. Stelzer, J. Nölting and I. Riess, *Journal of Solid State Chemistry*, 1995, **117**, 392–397.
- [297] D. Ding, B. Liu, M. Gong, X. Liu and C. Xia, *Electrochimica Acta*, 2010, **55**, 4529–4535.
- [298] D. Pérez-Coll, E. Sánchez-López and G. C. Mather, *Solid State Ionics*, 2010, **181**, 1033–1042.
- [299] J.-G. Li, T. Ikegami and T. Mori, *Acta Materialia*, 2004, **52**, 2221–2228.
- [300] T. Zhang, J. Ma, Y. Chen, L. Luo, L. Kong and S. Chan, *Solid State Ionics*, 2006, **177**, 1227–1235.
- [301] D. Yan, X. Liu, X. Bai, L. Pei, M. Zheng, C. Zhu, D. Wang and W. Su, *Journal of Power Sources*, 2010, **195**, 6486–6490.
- [302] X.-D. Zhou, W. Huebner, I. Kosacki and H. U. Anderson, *Journal of the American Ceramic Society*, 2002, **85**, 1757–1762.
- [303] R. Tian, F. Zhao, F. Chen and C. Xia, *Solid State Ionics*, 2011, **192**, 580–583.
- [304] M. Kamiya, E. Shimada and Y. Ikuma, *Journal of materials synthesis and processing*, 1998, **6**, 283–286.
- [305] M. I. Mendelson, *Journal of the American Ceramic Society*, 1969, **52**, 443–446.

- 
- [306] R. Gerhardt, A. S. Nowick, M. E. Mochel and I. Dumler, *Journal of the American Ceramic Society*, 1986, **69**, 647–651.
- [307] B. Ravel and M. Newville, *Journal of synchrotron radiation*, 2005, **12**, 537–541.
- [308] M. Newville, P. Livinš, Y. Yacoby, J. J. Rehr and E. A. Stern, *Physical Review B*, 1993, **47**, 14126–14131.
- [309] D. C. Koningsberger, B. L. Mojet, G. E. van Dorssen and D. E. Ramaker, *Topics in Catalysis*, 2000, **10**, 143–155.
- [310] D. E. Sayers, E. A. Stern and F. W. Lytle, *Physical Review Letters*, 1971, **27**, 1204–1207.
- [311] Rehr, Albers and Zabinsky, *Physical review letters*, 1992, **69**, 3397–3400.
- [312] J. J. Rehr and R. C. Albers, *Reviews of Modern Physics*, 2000, **72**, 621–654.
- [313] J. Bauerle, *Journal of Physics and Chemistry of Solids*, 1969, **30**, 2657–2670.
- [314] C. H. Hsu and F. Mansfeld, *Corrosion*, 2001, **57**, 747.
- [315] D. Y. Wang and A. S. Nowick, *Journal of Solid State Chemistry*, 1980, **35**, 325–333.
- [316] K. Eladham and A. Hammou, *Solid State Ionics*, 1983, **9-10**, 905–912.
- [317] G.-B. Jung, T.-J. Huang and C.-L. Chang, *Journal of Solid State Electrochemistry*, 2002, **6**, 225–230.
- [318] N. J. Kidner, N. H. Perry, T. O. Mason and E. J. Garboczi, *Journal of the American Ceramic Society*, 2008, **91**, 1733–1746.
- [319] C. Monty, *Ionics*, 2002, **8**, 461–469.
- [320] S. Rodewald, J. Fleig and J. Maier, *Journal of the American Ceramic Society*, 2001, **84**, 521–530.
- [321] C. W. Nan, X. Zhou, J. Nan and J. Wu, *Journal of Applied Physics*, 2001, **89**, 3955.
- [322] J. Fleig, P. Pham, P. Sztulzaft and J. Maier, *Solid State Ionics*, 1998, **113-115**, 739–747.
- [323] T. van Dijk and A. J. Burggraaf, *Physical Status Solidi A*, 1981, **63**, 229–240.
- [324] J. C. Maxwell, *A Treatise on Electricity and Magnetism*, Clarendon Press, Oxford, 1881.
- [325] D. S. McLachlan, M. Blaszkiewicz and R. E. Newnham, *Journal of the American Ceramic Society*, 1990, **73**, 2187–2203.

- [326] R. Landauer, AIP conference proceedings Vol. 40, Melville, NY, 1978, pp. 2–45.
- [327] R. E. Meredith and C. W. Tobias, *Advances in electrochemistry and electrochemical engineering*, 1962, **2**, 15–47.
- [328] N. J. Kidner, Z. J. Homrighaus, B. J. Ingram, T. O. Mason and E. J. Garboczi, *Journal of Electroceramics*, 2005, **14**, 283–291.
- [329] N. J. Kidner, Z. J. Homrighaus, B. J. Ingram, T. O. Mason and E. J. Garboczi, *Journal of Electroceramics*, 2005, **14**, 293–301.
- [330] Z. Hashin and S. Shtrikman, *Journal of Applied Physics*, 1962, **33**, 3125.
- [331] N. M. Beekmans and L. Heyne, *Electrochimica Acta*, 1976, **21**, 303–310.
- [332] M. Verkerk, B. Middelhuis and A. Burggraaf, *Solid State Ionics*, 1982, **6**, 159–170.
- [333] E. J. Schouler, G. Giroud and M. Kleitz, *J. chim. Phys*, 1973, **70**, 1309–1316.
- [334] H. Näfe, *Solid State Ionics*, 1984, **13**, 255–263.
- [335] N. Bonanos and E. Lilley, *Journal of Physics and Chemistry of Solids*, 1981, **42**, 943–952.
- [336] X. Guo and R. Waser, *Progress in Materials Science*, 2006, **51**, 151–210.
- [337] X. Guo and Z. Zhang, *Acta Materialia*, 2003, **51**, 2539–2547.
- [338] C. Kleinlogel, *Journal of Electroceramics*, 2000, **5**, 231–243.
- [339] X. Guo and J. Maier, *Journal of The Electrochemical Society*, 2001, **148**, E121.
- [340] X. Guo, W. Sigle, J. Fleig and J. Maier, *Solid State Ionics*, 2002, **154-155**, 555–561.
- [341] J.-S. Lee and D.-Y. Kim, *Journal of Materials Research*, 2001, **16**, 2739–2751.
- [342] G. Kresse and J. Furthmüller, *Physical Review B*, 1996, **54**, 11169–11186.
- [343] G. Kresse and D. Joubert, *Physical Review B*, 1999, **59**, 1758–1775.
- [344] J. P. Perdew, K. Burke and M. Ernzerhof, *Physical Review Letters*, 1997, **78**, 1396.
- [345] J. Hafner, *Journal of Computational Chemistry*, 2008, **29**, 2044–2078.
- [346] M. Nolan and J. E. W. G. W. Fearon, *Solid State Ionics*, 2006, **177**, 3069–3074.
- [347] Z. Yang, G. Luo, Z. Lu and K. Hermansson, *The Journal of chemical physics*, 2007, **127**, 074704.

- 
- [348] Z. Yang, G. Luo, Z. Lu, T. K. Woo and K. Hermansson, *Journal of Physics: Condensed Matter*, 2008, **20**, 035210.
- [349] M. Nolan, V. S. Verdugo and H. Metiu, *Surface Science*, 2008, **602**, 2734–2742.
- [350] P. P. Dholabhai, J. B. Adams, P. Crozier and R. Sharma, *The Journal of Chemical Physics*, 2010, **132**, 094104.
- [351] S. Fabris, G. Vicario, G. Balducci, S. d. Gironcoli and S. Baroni, *The Journal of Physical Chemistry B*, 2005, **109**, 22860–22867.
- [352] H. Jiang, R. Gomez-Abal, P. Rinke and M. Scheffler, *Physical Review Letters*, 2009, **102**, 126403.
- [353] H.-T. Chen, J.-G. Chang, H.-L. Chen and S.-P. Ju, *Journal of Computational Chemistry*, 2009, **30**, 2433–2442.
- [354] H.-T. Chen and J.-G. Chang, *The Journal of Chemical Physics*, 2010, **132**, 214702.
- [355] T. Zacherle, P. C. Schmidt and M. Martin, *Physical Review B*, 2013, **87**, 235206.
- [356] F. D. Murnaghan, *American Journal of Mathematics*, 1937, **59**, 235.
- [357] F. D. Murnaghan, *Proceedings of the National Academy of Sciences*, 1944, **30**, 244–247.
- [358] F. Birch, *Physical Review*, 1947, **71**, 809–824.
- [359] J. L. F. Da Silva, M. V. Ganduglia-Pirovano, J. Sauer, V. Bayer and G. Kresse, *Physical Review B*, 2007, **75**, 045121.
- [360] P. R. L. Keating, D. O. Scanlon, B. J. Morgan, N. M. Galea and G. W. Watson, *The Journal of Physical Chemistry C*, 2012, **116**, 2443–2452.
- [361] A. Eichler, *Physical Review B*, 2001, **64**, 174103.
- [362] G. Mills, H. Jónsson and G. K. Schenter, *Surface Science*, 1995, **324**, 305–337.
- [363] H. Jónsson, G. Mills and K. M. Jacobsen, *Classical and quantum dynamics in condensed phase simulations*, World Scientific, Singapore, 1998, pp. 385–404.
- [364] M. Lumeij, J. Koettgen, M. Gilleßen, T. Itoh and R. Dronskowski, *Solid State Ionics*, 2012, **222-223**, 53–58.
- [365] G. Henkelman, B. P. Uberuaga and H. Jónsson, *The Journal of Chemical Physics*, 2000, **113**, 9901.

- [366] G. Henkelman and H. Jónsson, *The Journal of Chemical Physics*, 1999, **111**, 7010.
- [367] A. Heyden, A. T. Bell and F. J. Keil, *The Journal of chemical physics*, 2005, **123**, 224101.
- [368] C. Freysoldt, J. Neugebauer and C. van de Walle, *Physical Review Letters*, 2009, **102**, 016402.
- [369] G. Makov and M. C. Payne, *Physical Review B*, 1995, **51**, 4014–4022.
- [370] K. Parlinski, Z. Q. Li and Y. Kawazoe, *Physical Review Letters*, 1997, **78**, 4063–4066.
- [371] R. Pornprasertsuk, P. Ramanarayanan, C. B. Musgrave and F. B. Prinz, *Journal of Applied Physics*, 2005, **98**, 103513.
- [372] R. Pornprasertsuk, J. Cheng, H. Huang and F. B. Prinz, *Solid State Ionics*, 2007, **178**, 195–205.
- [373] E. Lee, F. Prinz and W. Cai, *Physical Review B*, 2011, **83**, 052301.
- [374] S. P. Grieshammer, *PhD thesis*, Aachen, Techn. Hochsch, Aachen, 2015.
- [375] A. Ismail, J. B. Giorgi and T. K. Woo, *The Journal of Physical Chemistry C*, 2012, **116**, 704–713.
- [376] A. Nakamura, *Solid State Ionics*, 2010, **181**, 1631–1653.
- [377] D. J. Bevan, W. W. Baker, R. L. Martin and T. C. Park, *Proc. 4th Conf. on Rare Earth Research*, 1964, p. 411.
- [378] A. Nakamura, K. Imai, N. Igawa, Y. Okamoto, E. Yamamoto, S. Matsukawa and M. Takahashi, *ICAME 2011*, Springer Netherlands, Dordrecht, 2013, pp. 503–507.
- [379] J. Hormes, *Solid State Ionics*, 2000, **136-137**, 945–954.
- [380] F. Deganello, *Journal of Solid State Chemistry*, 2003, **175**, 289–298.
- [381] H. Nitani, T. Nakagawa, M. Yamanouchi, T. Osuki, M. Yuya and T. A. Yamamoto, *Materials Letters*, 2004, **58**, 2076–2081.
- [382] Y. Wang, H. Kageyama, T. Mori, H. Yoshikawa and J. Drennan, *Solid State Ionics*, 2006, **177**, 1681–1685.
- [383] A. V. Chadwick and S. L. Savin, *Journal of Alloys and Compounds*, 2009, **488**, 1–4.
- [384] H. Hayashi, *Solid State Ionics*, 2000, **131**, 281–290.
- [385] H. Inaba, *Solid State Ionics*, 1999, **122**, 95–103.

- 
- [386] A. Gotte, D. Spangberg, K. Hermansson and M. Baudin, *Solid State Ionics*, 2007, **178**, 1421–1427.
- [387] A. Tarancón, A. Morata, F. Peiró and G. Dezanneau, *Fuel Cells*, 2011, **11**, 26–37.
- [388] M. Burbano, S. Nadin, D. Marrocchelli, M. Salanne and G. W. Watson, *Physical Chemistry Chemical Physics*, 2014, **16**, 8320–8331.
- [389] L. Sun, D. Marrocchelli and B. Yildiz, *Nature communications*, 2015, **6**, 6294.
- [390] A. Franke and E. Pehlke, *Physical Review B*, 2009, **79**, 235441.
- [391] D. E. Jiang and E. A. Carter, *Physical Review B*, 2003, **67**, 214103.
- [392] D. F. Johnson and E. A. Carter, *The Journal of Physical Chemistry C*, 2010, **114**, 4436–4444.
- [393] P. Ágoston and K. Albe, *Physical Chemistry Chemical Physics*, 2009, **11**, 3226.
- [394] Y. Mishin, M. R. Sørensen and A. F. Voter, *Philosophical Magazine A*, 2001, **81**, 2591–2612.
- [395] A. Suzuki and Y. Mishin, *Interface Science*, 2003, **11**, 131–148.
- [396] I. Riess, M. Ricken and J. Nölting, *Journal of Solid State Chemistry*, 1985, **57**, 314–322.
- [397] T. Hisashige, Y. Yamamura and T. Tsuji, *Journal of Alloys and Compounds*, 2006, **408–412**, 1153–1156.
- [398] H. Hayashi, M. Kanoh, C. J. Quan, H. Inaba, S. Wang, M. Dokiya and H. Tagawa, *Solid State Ionics*, 2000, **132**, 227–233.
- [399] H. Inaba and H. Tagawa, *Journal of the Ceramic Society of Japan*, 1998, **106**, 272–278.
- [400] G. E. Murch, *Philosophical Magazine A*, 1982, **45**, 685–692.
- [401] P. S. Manning, J. D. Sirman, R. A. De Souza and J. A. Kilner, *Solid State Ionics*, 1997, **100**, 1–10.
- [402] K. Fuda, *Journal of Physics and Chemistry of Solids*, 1984, **45**, 1253–1257.
- [403] U. Anselmi-Tamburini, F. Maglia, G. Chiodelli, A. Tacca, G. Spinolo, P. Riello, S. Bucella and Z. A. Munir, *Advanced Functional Materials*, 2006, **16**, 2363–2368.
- [404] K. Singh, S. A. Acharya and S. S. Bhoga, *Ionics*, 2007, **13**, 429–434.
- [405] S. P. Harvey, R. A. De Souza and M. Martin, *Energy Environ. Sci.*, 2012, **5**, 5803–5813.
- [406] P. Manning, *Solid State Ionics*, 1996, **93**, 125–132.

- [407] C. Tian and S.-W. Chan, *MRS Proceedings*, 1998, **548**, 629–634.
- [408] J. Conesa, *Surface Science*, 1995, **339**, 337–352.
- [409] Pryde, Alexandra K. A., S. Vyas, R. W. Grimes, J. A. Gardner and R. Wang, *Physical Review B*, 1995, **52**, 13214–13222.
- [410] G. Balducci, J. Kašpar, P. Fornasiero, M. Graziani, M. S. Islam and J. D. Gale, *The Journal of Physical Chemistry B*, 1997, **101**, 1750–1753.
- [411] G. Balducci, M. S. Islam, J. Kašpar, P. Fornasiero and M. Graziani, *Chemistry of Materials*, 2000, **12**, 677–681.
- [412] N. N. Bulgakov, V. A. Sadykov, V. V. Lunin and E. Kemnitz, *Reaction Kinetics and Catalysis Letters*, 2002, **76**, 103–110.
- [413] P. Geerlings, F. d. Proft, C. van Alsenoy, C. Frayret, A. Villesuzanne, M. Pouchard and S. Matar, *International Journal of Quantum Chemistry*, 2005, **101**, 826–839.
- [414] L. Gerward, J. Staun Olsen, L. Petit, G. Vaitheeswaran, V. Kanchana and A. Svane, *Journal of Alloys and Compounds*, 2005, **400**, 56–61.
- [415] S. Rossignol, F. Gérard, D. Mesnard, C. Kappenstein and D. Duprez, *Journal of Materials Chemistry*, 2003, **13**, 3017.
- [416] J. Koettgen, P. C. Schmidt, T. Bucko and M. Martin, *Ab initio calculation of the migration free energy of oxygen diffusion in pure and samarium doped ceria (submitted)*.
- [417] D. Wang and A. Nowick, *Journal of Physics and Chemistry of Solids*, 1983, **44**, 639–646.
- [418] S. B. Adler, J. W. Smith and J. A. Reimer, *The Journal of Chemical Physics*, 1993, **98**, 7613.
- [419] L. Fahrmeir, T. Kneib and S. Lang, *Regression: Modelle Methoden und Anwendungen*, Springer, Berlin, 2nd edn, 2009.
- [420] J. Gross, *Linear regression*, Springer, Berlin, 2003, vol. 175.
- [421] H. Theil, *Economic forecasts and policy*, North-Holland Pub. Co, 1961.
- [422] G. Arminger, C. C. Clogg and M. E. Sobel, *Handbook of statistical modeling for the social and behavioral sciences*, 1995.
- [423] A. Van der Ven, G. Ceder, M. Asta and P. D. Tepesch, *Physical Review B*, 2001, **64**, 184307.
- [424] A. Van der Ven and G. Ceder, *Physical review letters*, 2005, **94**, 045901.

- 
- [425] R. Kikuchi, *Physical Review*, 1951, **81**, 988–1003.
- [426] J. M. Sanchez, F. Ducastelle and D. Gratias, *Physica A: Statistical Mechanics and its Applications*, 1984, **128**, 334–350.
- [427] T. X. T. Sayle, S. C. Parker and C. R. A. Catlow, *Journal of the Chemical Society, Chemical Communications*, 1992, 977.
- [428] F. Shimojo and H. Okazaki, *Journal of the Physics Society Japan*, 1992, **61**, 4106–4118.
- [429] B. O. H. Grope, *PhD thesis*, Aachen, Techn. Hochsch, Aachen, 2015.
- [430] S. L. Reis, E. Souza and E. Muccillo, *Solid State Ionics*, 2011, **192**, 172–175.
- [431] J. Frenkel, *Kinetic Theory of Liquids*, Oxford University Press, New York, 1946.
- [432] K. L. Kliewer and J. S. Koehler, *Physical Review*, 1965, **140**, A1226–A1240.
- [433] J. Jamnik, J. Maier and S. Pejovnik, *Solid State Ionics*, 1995, **75**, 51–58.
- [434] R. A. De Souza, *Physical Chemistry Chemical Physics*, 2009, **11**, 9939–9969.
- [435] D. Bingham, P. W. Tasker and A. N. Cormack, *Philosophical Magazine A*, 1989, **60**, 1–14.
- [436] D. S. Aidhy, Y. Zhang and W. J. Weber, *J. Mater. Chem. A*, 2014, **2**, 1704–1709.
- [437] A. Tschöpe, *Solid State Ionics*, 2001, **139**, 255–265.
- [438] A. Tschöpe, *Solid State Ionics*, 2001, **139**, 267–280.
- [439] A. Tschöpe, S. Kilassonia and R. Birringer, *Solid State Ionics*, 2004, **173**, 57–61.
- [440] I. Kosacki, T. Suzuki and H. U. Anderson, *Solid-state ionic devices*, Electrochemical Society, Pennington, NJ, 1999, vol. 99-13, pp. 190–198.
- [441] J.-H. Hwang and T. O. Mason, *Zeitschrift für Physikalische Chemie*, 1998, **207**, 21–38.
- [442] Y.-M. Chiang, E. B. Lavik, I. Kosacki, H. L. Tuller and J. Y. Ying, *Applied Physics Letters*, 1996, **69**, 185.
- [443] S. Kim and J. Maier, *Journal of The Electrochemical Society*, 2002, **149**, J73.
- [444] X. Guo, W. Sigle and J. Maier, *Journal of the American Ceramic Society*, 2003, **86**, 77–87.
- [445] M. C. Göbel, G. Gregori, X. Guo and J. Maier, *Physical Chemistry Chemical Physics*, 2010, **12**, 14351–14361.
- [446] A. Tschöpe, C. Bäuerle and R. Birringer, *Journal of Applied Physics*, 2004, **95**, 1203.

- [447] Y. Lei, Y. Ito, N. D. Browning and T. J. Mazanec, *Journal of the American Ceramic Society*, 2002, **85**, 2359–2363.
- [448] X. Guo, *Solid State Ionics*, 1997, **96**, 247–254.
- [449] J. Maier and B. Reichert, *Berichte der Bunsengesellschaft für physikalische Chemie*, 1986, **90**, 666–670.
- [450] F. Li, T. Ohkubo, Y. M. Chen, M. Kodzuka and K. Hono, *Ultramicroscopy*, 2011, **111**, 589–594.
- [451] A. E. Hughes and B. A. Sexton, *Journal of Materials Science*, 1989, **24**, 1057–1061.
- [452] B. Steele, *High conductivity solid ionic conductors*, World Scientific, Singapore and Teaneck and N.J, 1989, pp. 402–446.
- [453] J.-P. Eufinger, M. Daniels, K. Schmale, S. Berendts, G. Ulbrich, M. Lerch, H.-D. Wiemhöfer and J. Janek, *Physical Chemistry Chemical Physics*, 2014, **16**, 25583–25600.
- [454] G. Ulbrich, *PhD thesis*, Technische Universität Berlin, Berlin, 2015.
- [455] G. Tammann, *Lehrbuch der Metallkunde*, Voss, Leipzig, 1932.
- [456] J. Fleig, *Journal of Electroceramics*, 2004, **13**, 637–644.

# Appendix

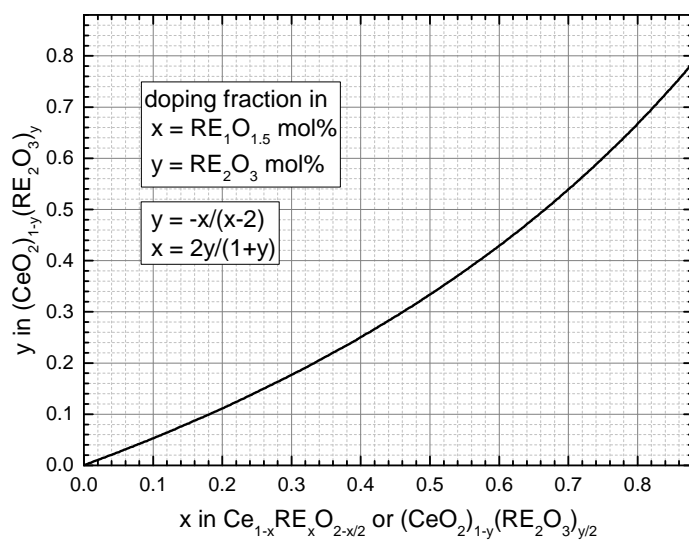


Figure 9.1: Calculating the dopant fraction in  $\text{RE}_1\text{O}_{1.5}\text{mol}\%$  and  $\text{RE}_2\text{O}_3\text{mol}\%$ .

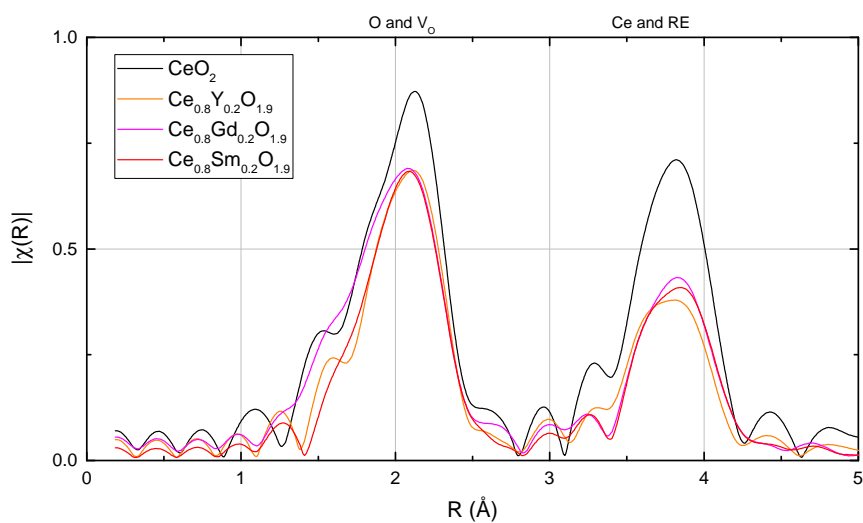


Figure 9.2: Radial Distribution Function at Ce(K)-edge of  $\text{Ce}_{0.8}\text{RE}_{0.2}\text{O}_{1.9}$ .

$x$	$amp_i$		$R_i$ (Å)	
	1 <sup>st</sup> shell	2 <sup>nd</sup> shell	1 <sup>st</sup> shell	2 <sup>nd</sup> shell
0	0.89(4)	0.93(5)	2.338(4)	3.859(3)
0.025	0.64(5)	0.85(6)	2.356(6)	3.870(4)
0.05	0.62(4)	0.66(5)	2.336(5)	3.862(4)
0.075	0.70(5)	0.84(6)	2.348(5)	3.865(3)
0.1	0.72(4)	0.68(5)	2.335(4)	3.859(3)
0.125	0.65(4)	0.68(5)	2.341(5)	3.863(4)
0.15	0.61(4)	0.60(5)	2.329(5)	3.860(4)
0.2	0.63(4)	0.50(5)	2.323(5)	3.853(5)
0.225	0.60(4)	0.45(5)	2.319(5)	3.853(6)
0.25	0.61(4)	0.40(5)	2.312(5)	3.848(6)

Table 9.1: Fit results of the EXAFS data of  $Ce_{1-x}Sm_xO_{2-x/2}$  at the Ce-edge. The amplitude  $amp_i$  and the distance to the scattering ion  $R_i$  is shown.

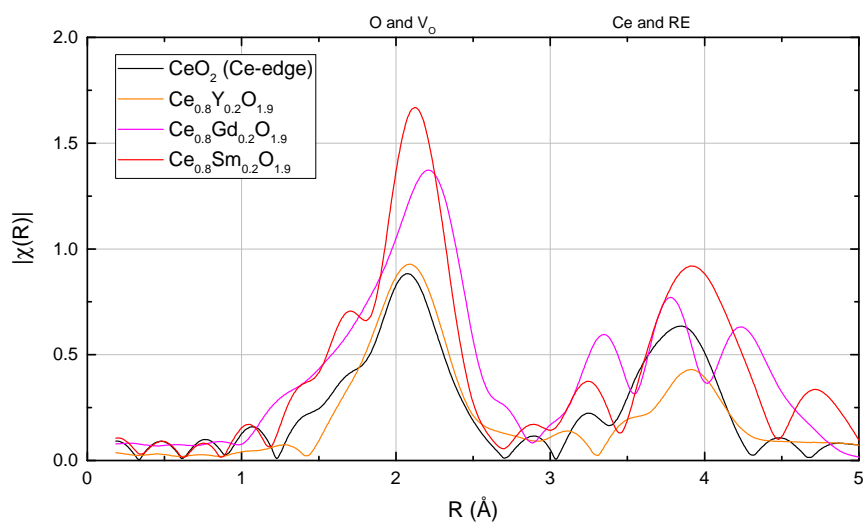


Figure 9.3: Radial Distribution Function at RE(K)-edge of  $Ce_{0.8}RE_{0.2}O_{1.9}$ .

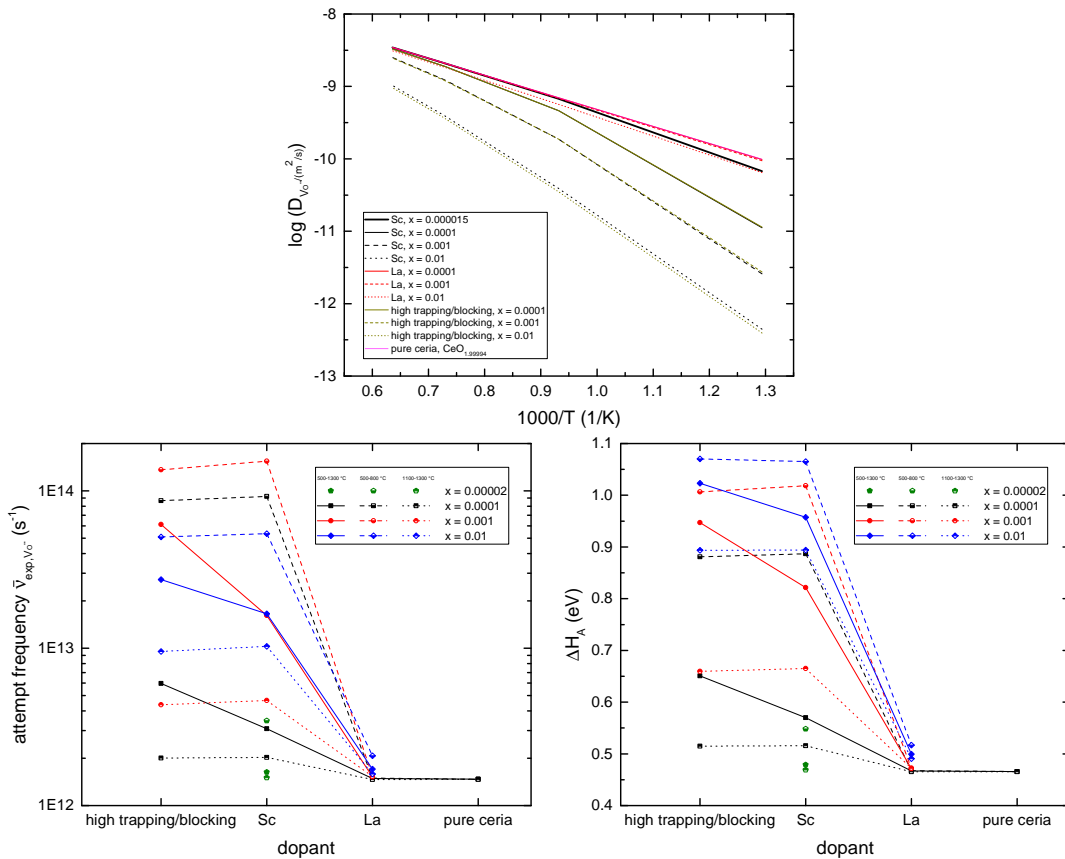


Figure 9.4: Oxygen vacancy diffusion coefficient (above), apparent attempt frequency (left) and activation enthalpy (right) for the conductivity of simulated rare-earth doped ceria. ‘high trapping/blocking’ refers to a virtual material with possess association energies according to Sc and migration edges according to La. Lines are a guide to the eye only.

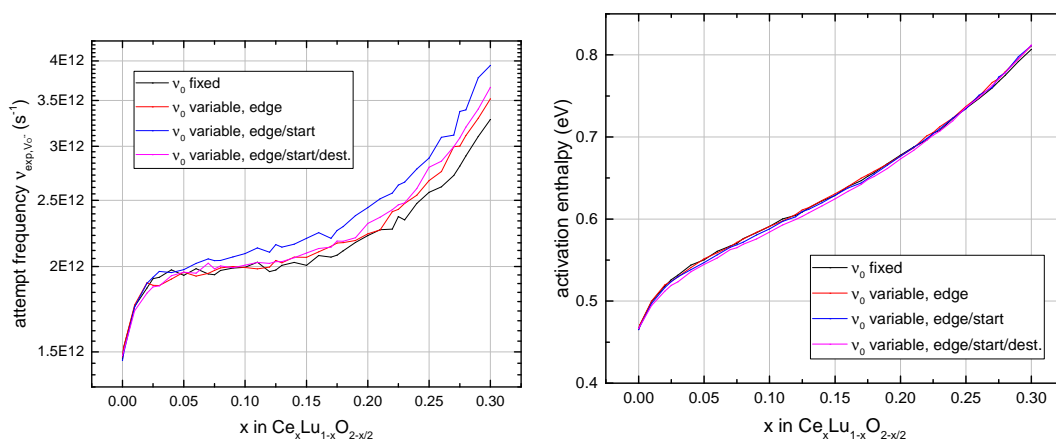


Figure 9.5: Apparent attempt frequency (left) and activation enthalpy (right) for the conductivity of simulated Sm doped ceria using different microscopic attempt frequencies between 500 °C and 1100 °C. Lines are a guide to the eye only.

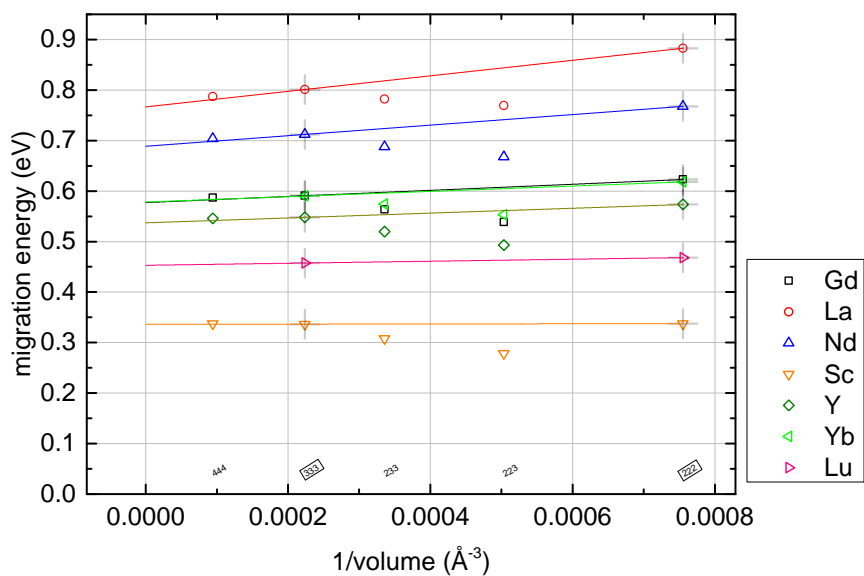


Figure 9.6: Migration energy of Ce-RE edge at different supercell sizes.

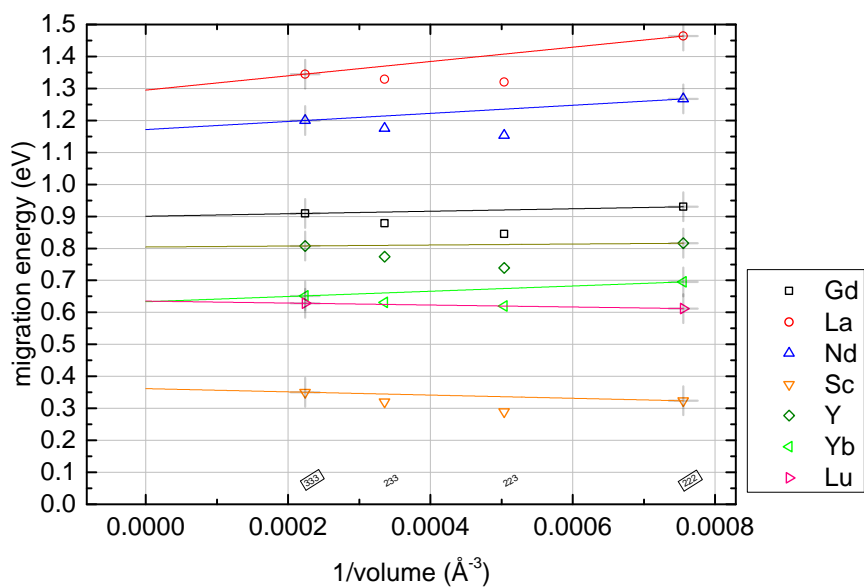


Figure 9.7: Migration energy of RE-RE edge at different supercell sizes.

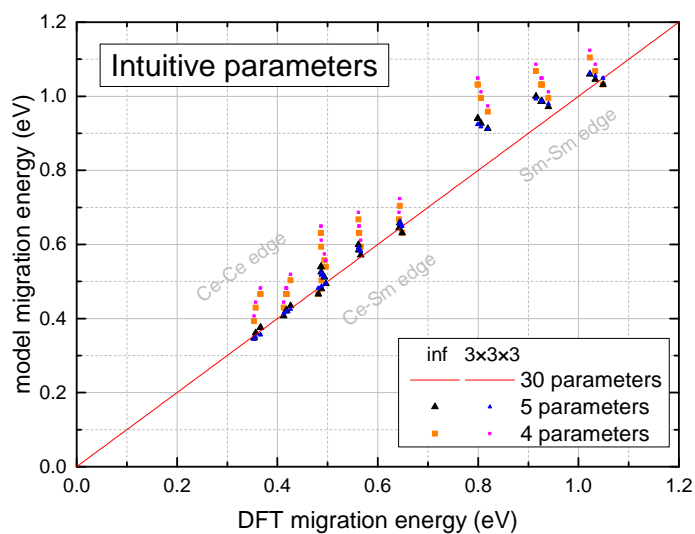


Figure 9.8: Model (4, 5 and 30 parameters model) and DFT migration energies for 6-cation environment with intuitive parameters for the infinite large or  $3 \times 3 \times 3$  supercell. DFT energies for Sm doped ceria in  $3 \times 3 \times 3$  supercell.

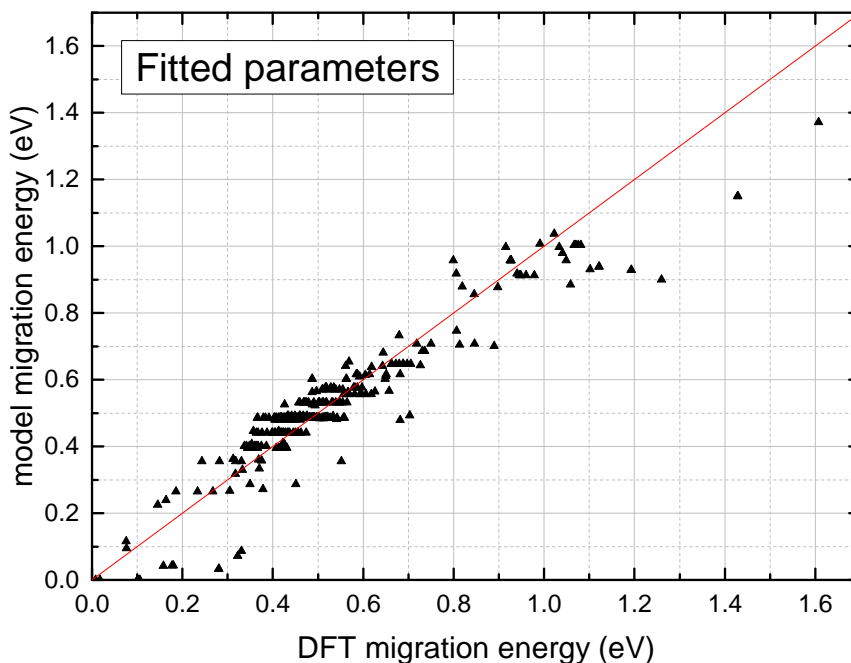


Figure 9.9: Model and DFT migration energies with fitted parameters. The jumping oxygen vacancy interacts with either dopants and vacancies. Both sublattices do not interact. The model  $c1+vn$  [vn] up to the 13<sup>th</sup> shell (5.41 Å) is used. Sm doped ceria in  $3 \times 3 \times 3$  supercell.

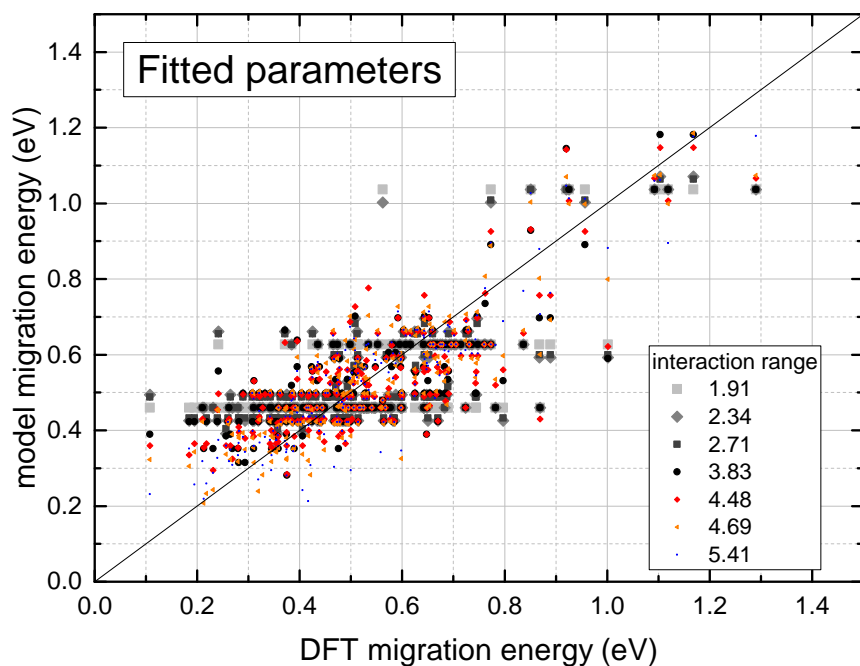


Figure 9.10: Model and DFT migration energies with fitted parameters. The jumping oxygen vacancy interacts with both dopants and vacancies. Both sublattices interact. The model  $c1+vn$  [ $vn$ ] up to the 13<sup>th</sup> shell (5.41 Å) is used. Sm doped ceria in  $3 \times 3 \times 3$  supercell.

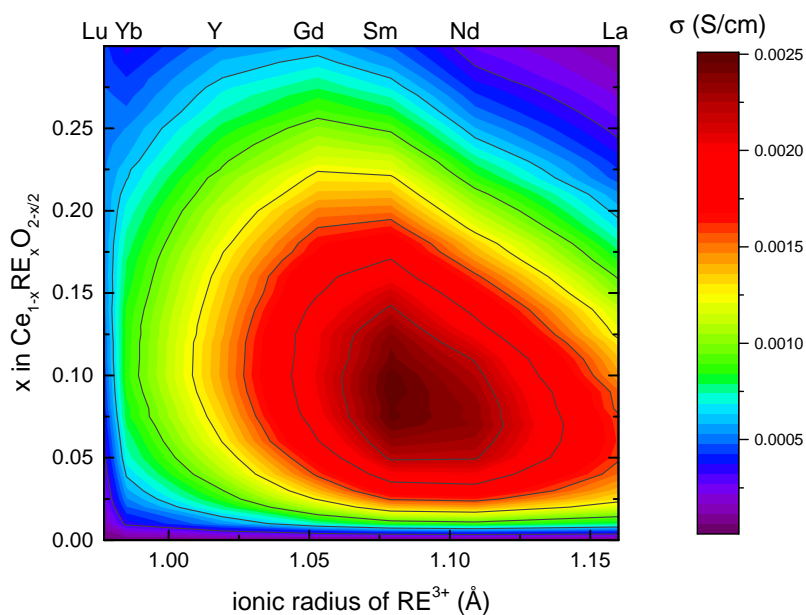


Figure 9.11: Ionic conductivity of rare-earth doped ceria at 500 °C with RE = Lu, Yb, Y, Gd, Sm, Nd and La.

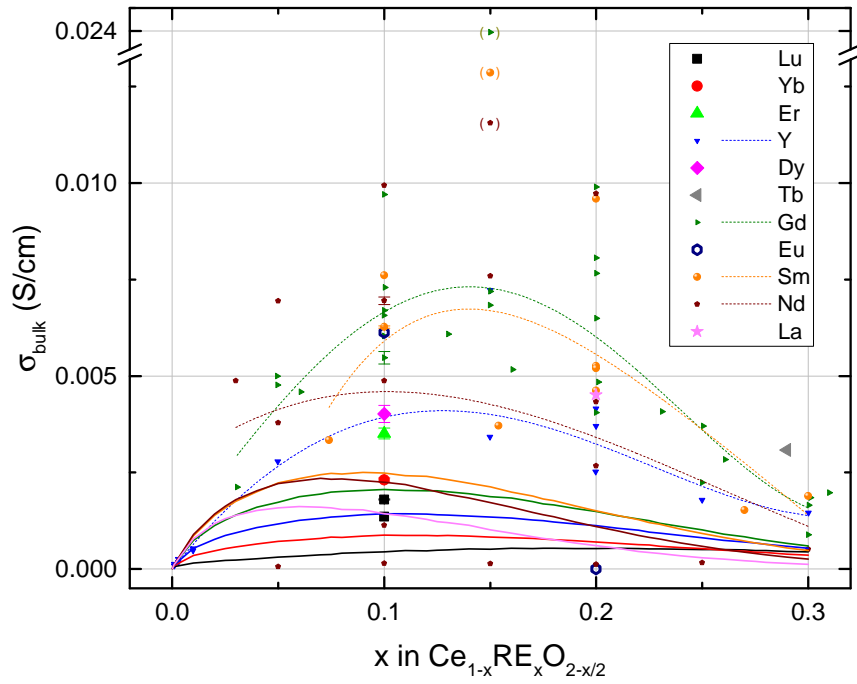
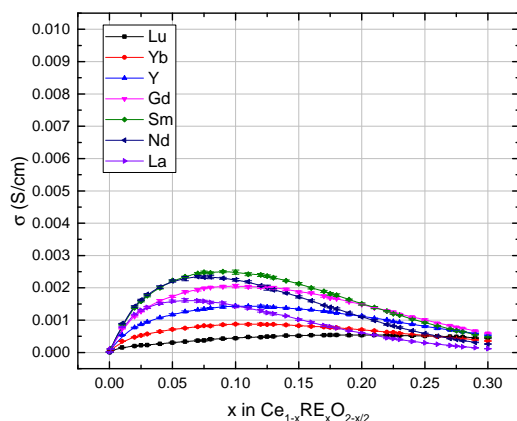
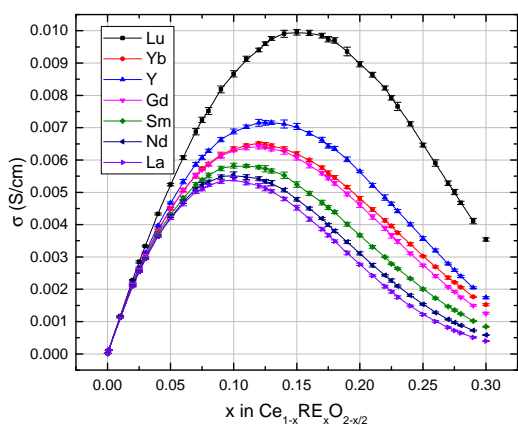


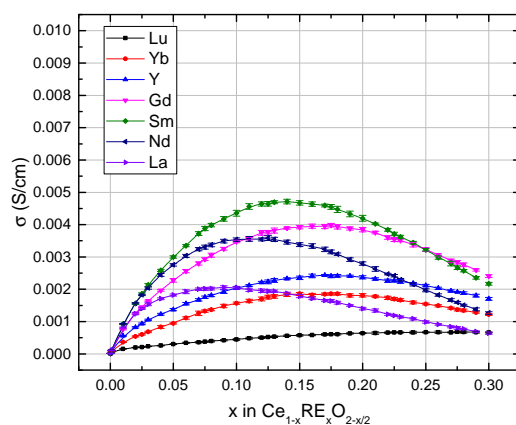
Figure 9.12: Bulk ionic conductivity at 500 °C in KMC simulation in this work (lines) and experiments (dots) for Lu,<sup>[165,166]</sup> Yb,<sup>[166]</sup> Er,<sup>[166]</sup> Y,<sup>[163,166–172]</sup> Dy,<sup>[166]</sup> Tb,<sup>[71]</sup> Gd,<sup>[64,86,166,169–177]</sup> Eu,<sup>[71,178]</sup> Sm,<sup>[74,166,169–172,179–181]</sup> Nd<sup>[75,76,166,170,182,183]</sup> and La doped ceria.<sup>[169]</sup> Fourth order polynomials were fitted to the data with exception of the data of Zajac and Molenda to show the general trend of the data (dashed lines).



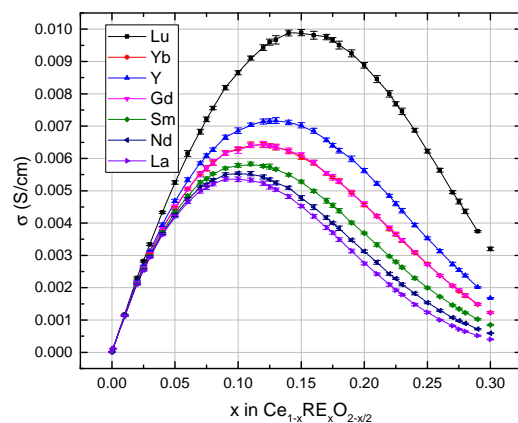
(a) all interactions



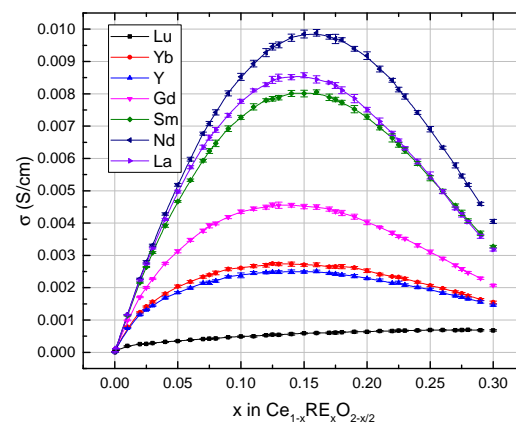
(b) no trapping



(c) no blocking



(d) only different Ce-RE edge



(e) only different  $1_{NN} \leftrightarrow 2_{NN}$  RE-V jump

Figure 9.13: Calculated ionic conductivity of rare-earth doped ceria at 500 °C without considering RE-V interactions around the start and destination position (left) or without considering different migration edges (right). Lines are a guide to the eye only.

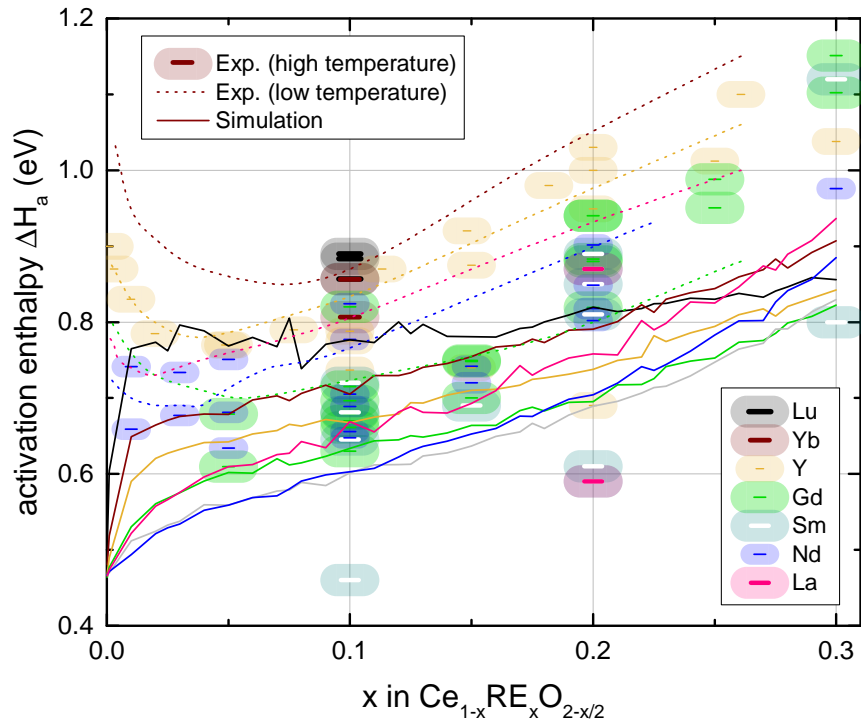


Figure 9.14: Activation enthalpy in KMC simulation in this work (lines) and experiments between room temperature and 330 °C (dashed lines)<sup>[163]</sup> or higher temperatures up to 1000 °C (dashes) for Lu,<sup>[165,166]</sup> Yb,<sup>[166]</sup> Er,<sup>[166]</sup> Y,<sup>[166–170,180]</sup> Dy,<sup>[69,166]</sup> Gd,<sup>[64,166,168–170,173,174,176]</sup> Eu,<sup>[178]</sup> Sm,<sup>[74,166,170,180,195]</sup> Nd<sup>[76,166,170,182,183]</sup> and La doped ceria.<sup>[169]</sup>

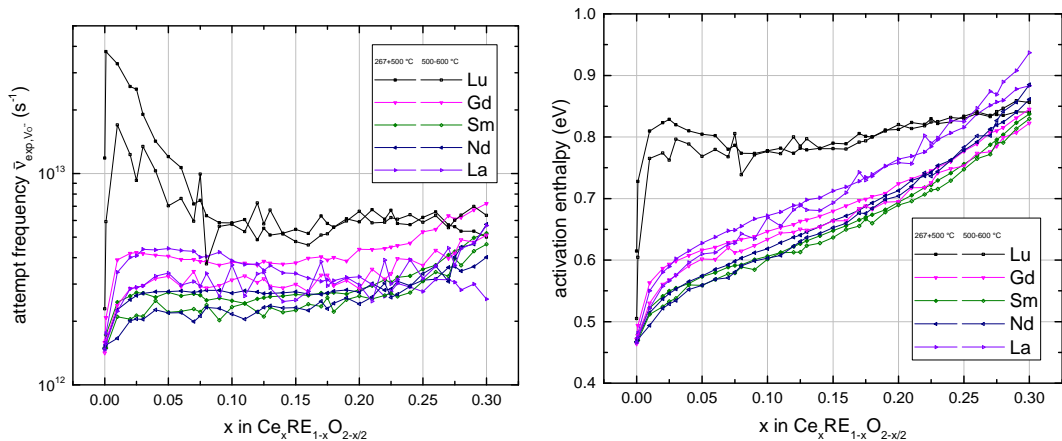
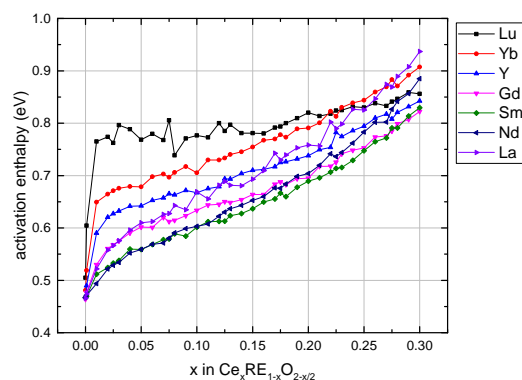
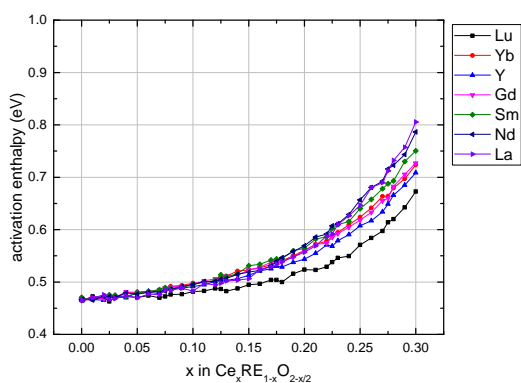


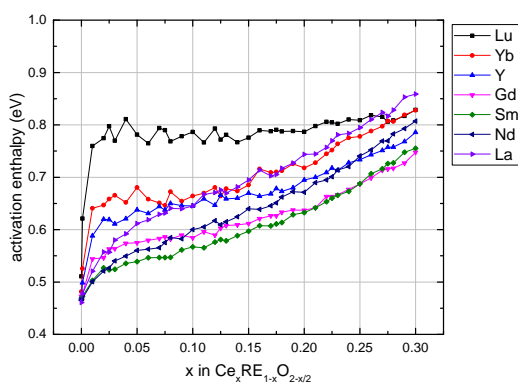
Figure 9.17: Apparent attempt frequency (left) and activation enthalpy (right) for the conductivity of simulated rare-earth doped ceria for the temperatures 267 °C and 500 °C and between 500 °C and 600 °C. Lines are a guide to the eye only.



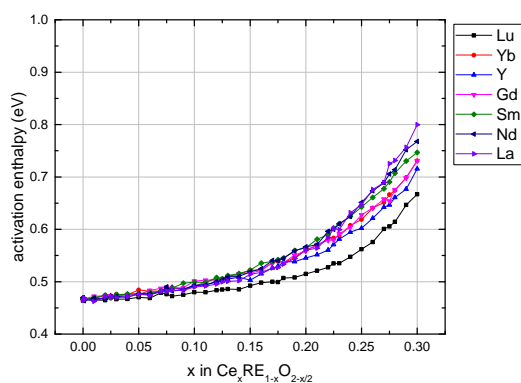
(a) all interactions



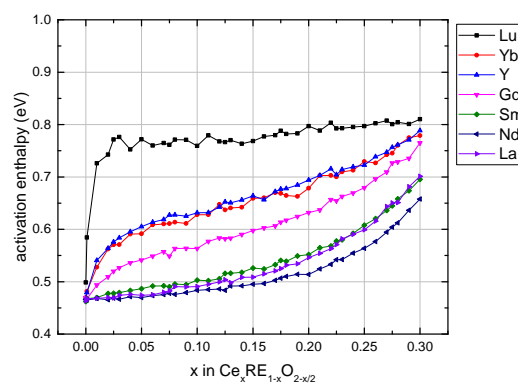
(b) no trapping



(c) no blocking

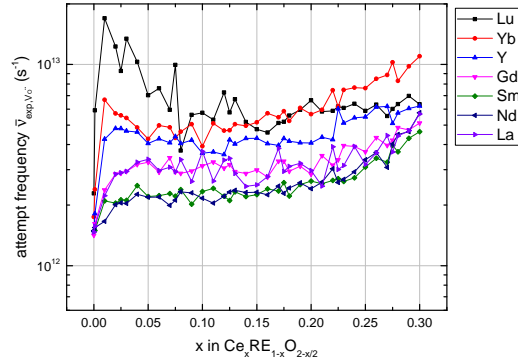


(d) only different Ce-RE edge

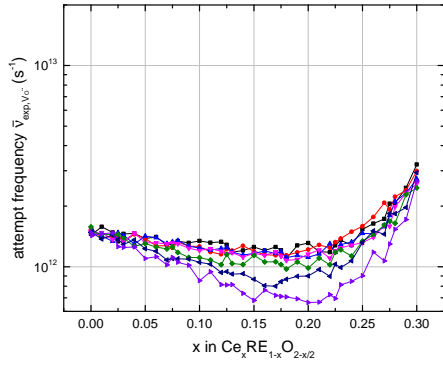


(e) only different  $1_{NN} \leftrightarrow 2_{NN}$  RE-V jump

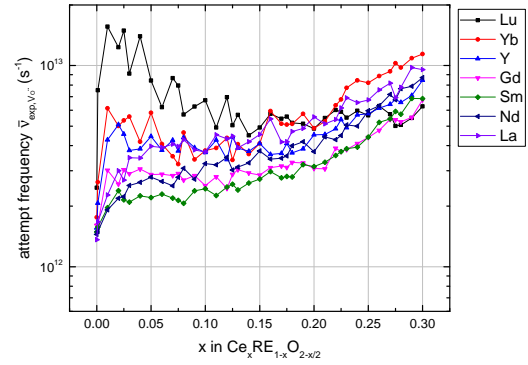
Figure 9.15: Calculated activation enthalpy between 500 °C and 600 °C. All interactions are used (middle) or either RE-V interactions around the start and destination position (left) or different migration edges (right) are neglected. Lines are a guide to the eye only.



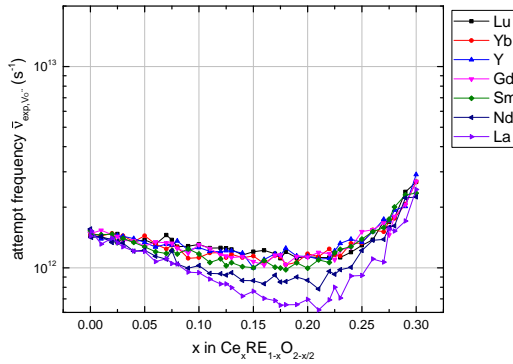
(a) all interactions



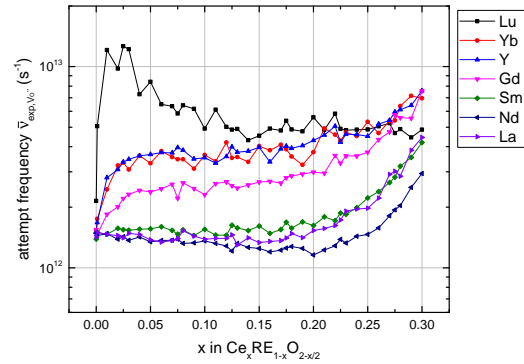
(b) no trapping



(c) no blocking



(d) only different Ce-RE edge



(e) only different  $1_{NN} \leftrightarrow 2_{NN}$  RE-V jump

Figure 9.16: Apparent attempt frequency between 500 °C and 600 °C. All interactions are used (middle) or either RE-V interactions around the start and destination position (left) or different migration edges (right) are neglected. Lines are a guide to the eye only.

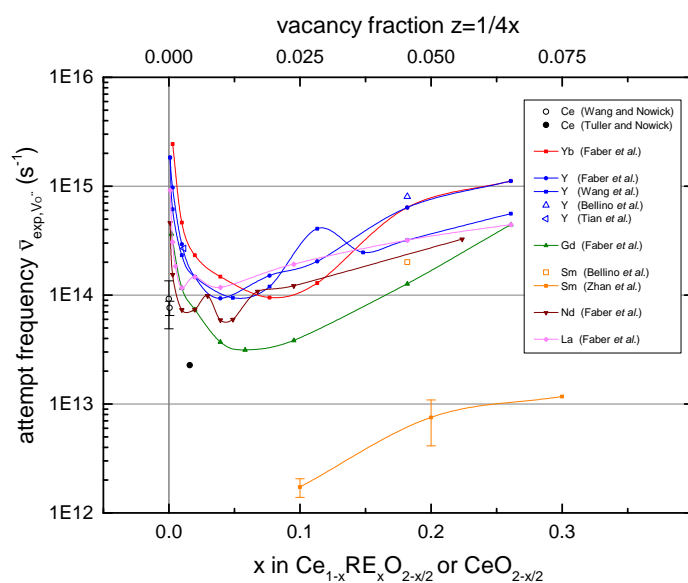


Figure 9.18: Apparent experimental attempt frequency from impedance spectroscopy experiments for stoichiometric or non-stoichiometric ceria,<sup>[83,315]</sup> Yb,<sup>[163]</sup> Y,<sup>[163,167,180,407]</sup> Gd,<sup>[163]</sup> Sm,<sup>[74,180]</sup> Nd<sup>[163]</sup> and La doped ceria.<sup>[163]</sup> Lines are a guide to the eye only.

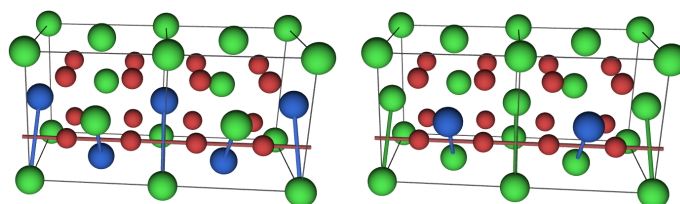


Figure 9.19: Examples for two favored migration paths in yttrium doped ceria according to earlier work.<sup>[55]</sup> The favored migration path of the oxygen is depicted as red line. On the left side there are similar adjacent migration edges while on the right side there are alternating migration edges. Cerium ions (green), yttrium ions (blue) and oxygen ions (red).

# List of Abbreviations

<b>EDX</b>	Energy Dispersive X-ray Spectroscopy
<b>DFT</b>	Density Functional Theory
<b>EXAFS</b>	Extended X-Ray Absorption Fine Structure
<b>GGA</b>	Generalized Gradient Approximation
<b>LDA</b>	Local Density Approximation
<b>NEB</b>	Nudged Elastic Band
<b>PAW</b>	Projector Augmented Wave
<b>SEM</b>	Scanning Electron Microscope
<b>SOFC</b>	Solid Oxide Fuel Cell
<b>VASP</b>	Vienna Ab initio Simulation Package
<b>XANES</b>	X-ray Absorption Near-edge Structure
<b>XRD</b>	X-Ray Diffraction
<b>MMC</b>	Metropolis Monte Carlo
<b>KMC</b>	Kinetic Monte Carlo
<b>XAS</b>	X-ray Absorption Spectroscopy
<b>EQ</b>	Simulation lattice with a cation distribution equilibrated at 1500 K
<b>RND</b>	Simulation lattice with a random cation distribution
<b>NMR</b>	Nuclear Magnetic Resonance
<b>RE</b>	rare-earth
<b>IS</b>	initial state
<b>TS</b>	transition state
<b>DC</b>	direct current
<b>AC</b>	alternating current

## *List of Abbreviations*

---

<b>SIMS</b>	Secondary Ion Mass Spectrometry
<b>GPA</b>	Gas Phase Analysis
<b>MD</b>	molecular dynamics
<b>PBE</b>	Perdew, Burke and Ernzerhof
<b>YSZ</b>	yttria-stabilized zirconia
<b>XPS</b>	X-ray Photoelectron Spectroscopy
<b>TEM</b>	Transmission Electron Microscopy
<b>S-BLM</b>	series brick layer model

# List of Figures

1.1	Configuration of a Solid Oxide Fuel Cell (SOFC). . . . .	2
1.2	Ionic conductivity of Sm doped ceria at 600 °C (left) <sup>[28]</sup> and $\text{Ce}_{0.8}\text{RE}_{0.2}\text{O}_{1.9}$ at 800 °C (right). <sup>[27]</sup> Lines are a guide to the eye only. . . . .	3
2.1	Crystal structure of cerium oxide. Cerium ions (green) and oxygen ions (red). The unit cell of the fluorite structure is highlighted. . . . .	5
2.2	Migration configurations in ceria. Cerium ions (green), oxygen ions (red spheres) and oxygen vacancy (red box). . . . .	6
2.3	Experimental lattice parameter in air at room temperature for Lu, <sup>[65–67]</sup> Yb, <sup>[68]</sup> Dy, <sup>[69,70]</sup> Tb, <sup>[71,72]</sup> Gd, <sup>[64,73]</sup> Eu, <sup>[71]</sup> Sm, <sup>[73,74]</sup> Nd <sup>[75,76]</sup> and La doped ceria. <sup>[63,77]</sup> Lines are a guide to the eye only. . . . .	7
2.4	Ionic and electronic conductivity of $\text{Ce}_{0.8}\text{Gd}_{0.2}\text{O}_{1.9-\delta}$ at 800 °C according to Yokokawa <i>et al.</i> <sup>[101]</sup> . . . . .	9
2.5	Attempt frequency of oxygen ions and vacancies as a function of dopant fraction or non-stoichiometry for a constant oxygen vacancy attempt frequency according to Eq. 2.5. The attempt frequency of the oxygen ions increases with increasing oxygen vacancy fraction. . . . .	10
2.6	Sketch of the electronic energy profile for an oxygen jump in pure ceria according to Eq. 2.9. . . . .	13
2.7	Total ionic conductivity of polycrystalline Sm doped ceria at 600 °C. <sup>[28,73,156–158]</sup> Lines are a guide to the eye only. . . . .	18
2.8	Total ionic conductivity of $\text{Ce}_{1-x}\text{RE}_x\text{O}_{2-x/2}$ for $x = 0.2$ , <sup>[27,29,62,161]</sup> and 0.3. <sup>[162]</sup> The lines show a possible linear relationship between the ionic radius and the conductivity (solid lines) or the logarithm of the conductivity (dashed lines). . . . .	20
2.9	Bulk, grain boundary and total ionic conductivity of Gd doped ceria at 500 °C according to Steele. <sup>[86]</sup> Lines are a guide to the eye only. . . . .	21
2.10	Bulk ionic conductivity of doped ceria at 30 °C (left) and 250 °C (right) according to an Arrhenius fit of the data of Faber <i>et al.</i> for measurements between 30 °C and 330 °C. <sup>[163]</sup> Lines are a guide to the eye only. . . . .	21

2.11	Bulk ionic conductivity at 500 °C for Lu, Yb, Er, Y, Dy, Tb, Gd, Eu, Sm, Nd and La doped ceria. Forth order polynomials were fitted to the data with exception of the data of Zajac and Molenda (in parentheses) as a guide to the eye only to show the general trend of the data (dashed lines). . . . .	22
2.12	Bulk ionic conductivity at 400 °C of $Ce_{1-x}RE_xO_{2-x/2}$ for $x = 0.1$ , and $0.2$ . The lines show a possible linear relationship between the ionic radius and the conductivity (solid lines) or the logarithm of the conductivity (dashed lines). . . . .	23
2.13	Dopant fractions that lead to the highest ionic conductivity for $Ce_{1-x_{max}}RE_{x_{max}}O_{2-x_{max}/2}$ samples in the measured temperature range. Errors bars indicate the nearest measured dopant fraction with lower conductivity. $x_{max}$ for low and high temperature measurements are marked (lines). . . . .	25
2.14	Arrhenius behavior of the ionic conductivity in $Ce_{1-x}Sm_xO_{2-x/2}$ according to Zhan <i>et al.</i> (left). Association energies according to literature (right). For the latter, Lines are a guide to the eye only. . . . .	27
2.15	Activation enthalpy for the bulk ionic conductivity of doped ceria between room temperature and 330 °C according to Faber <i>et al.</i> <sup>[163]</sup> Lines are a guide to the eye only.	28
2.16	Activation enthalpy for the bulk ionic conductivity of doped ceria for various temperature ranges between room temperature and 1000 °C for Lu, <sup>[165,166]</sup> Yb, <sup>[166]</sup> Er, <sup>[166]</sup> Y, <sup>[166-170,180]</sup> Dy, <sup>[69,166]</sup> Gd, <sup>[64,166,168-170,173,174,176]</sup> Eu, <sup>[178]</sup> Sm, <sup>[74,166,170,180,195]</sup> Nd <sup>[76,166,170,182,183]</sup> and La doped ceria. <sup>[169]</sup> . . . . .	28
2.17	The migration energy increases if the oxygen ion jump decreases the association. . .	31
2.18	The migration energy increases for an increasing number of large dopants at the migration edge. . . . .	32
3.1	Setup of a XAS beamline using both X-Ray absorption and fluorescence. . . . .	37
3.2	Schematic representation of an electronic excitation with an X-ray quantum. Here, $j$ is the total angular momentum quantum number of the one electron given by the particle's spin and orbital angular momentum. . . . .	37
3.3	X-ray spectrum of an $Ce_{0.975}Sm_{0.025}O_{1.9875}$ sample, showing the XANES and EXAFS region on the Ce(K)-edge. . . . .	38
4.1	X-ray diffractogram of Gd doped ceria ( $Ce_{0.8}Gd_{0.2}O_{1.9}$ ) in linear (left) and logarithmic (right) representation. . . . .	46
4.2	Density (left) and grain size (right) as a function of sintering temperature in literature. Sintering durations in hours are noted inside the symbols. Lines are a guide to the eye only. . . . .	47
4.3	Density and grain size as a function of sintering temperature and sintering duration for $Ce_{0.85}Sm_{0.15}O_{1.925}$ in comparison with [a] literature ( $Ce_{0.8}Gd_{0.2}O_{1.9}$ ). <sup>[300]</sup> . . . .	48

4.4	SEM measurements of $\text{Ce}_{0.85}\text{Sm}_{0.15}\text{O}_{1.925}$ for different sintering temperatures and durations as well as $\text{Ce}_{1-x}\text{RE}_x\text{O}_{2-x/2}$ with $\text{RE} = \text{Sm}, \text{Lu}$ as a function of dopant fraction. Tonal values are adapted. . . . .	49
4.5	Evaluation of an EXAFS measurement of 2.5% Sm doped ceria as a function of the incident X-Ray energy. . . . .	50
4.6	Normalized X-Ray Absorption at the Ce(K)-edge (XANES) of $\text{Ce}_{1-x}\text{Sm}_x\text{O}_{2-x/2}$ . . .	51
4.7	Evaluation of an EXAFS measurement of 2.5% Sm doped ceria. . . . .	52
4.8	Modeling an EXAFS measurement of 2.5% Sm doped ceria. . . . .	53
4.9	Equivalent circuit models. . . . .	54
4.10	Nyquist plot with fitted equivalent circuit model for $\text{Ce}_{0.75}\text{Sm}_{0.25}\text{O}_{1.875}$ at 200 °C. .	56
4.11	Equivalent circuit and schematic representation of the brick layer models. . . . .	57
4.12	Total energy difference between $1_{\text{NN}}$ and $6_{\text{NN}}$ RE-V and corresponding lattice sites for RE doped ceria in a $2 \times 2 \times 3$ supercell taken from an earlier work. <sup>[1]</sup> Distances between $1_{\text{NN}}$ and $6_{\text{NN}}$ RE-V were calculated. The dashed line shows the Coulomb energy. Other Lines are a guide to the eye only. Cerium ions are green spheres, dopants are blue spheres, the oxygen ions are red spheres and the oxygen vacancy is a red cube. . . .	61
5.1	RE-V interaction for different supercell sizes and $\Delta E_{\text{RE-V}}^3 = 0$ . . . . .	66
5.2	RE-V interaction for the infinitely large supercell (left and right) or the $3 \times 3 \times 3$ supercell (right). For the former, association energies are extrapolated for either $2 \times 2 \times 2$ and $3 \times 3 \times 3$ supercells (model 2015) or variable supercell sizes (model 2014). <sup>[55]</sup> The RE-V interaction is calculated relative to $3_{\text{NN}}$ (model 2015) or infinite distances (model 2014). . . . .	68
5.3	RE-V association energy in comparison with other theoretical studies. <sup>[44,224,275,350]</sup> For Dholabhai <i>et al.</i> a termination at $3_{\text{NN}}$ is assumed. . . . .	69
5.4	V-V interaction lattice sites. Cerium ions are green spheres, oxygen ions are red spheres and oxygen vacancies are red cubes. . . . .	70
5.5	V-V interaction for different supercell sizes. . . . .	71
5.6	V-V interaction extrapolated for $2 \times 2 \times 2$ and $3 \times 3 \times 3$ supercells (model 2015) or variable supercell sizes (model 2014). <sup>[55]</sup> The V-V interaction is calculated relative to $5_{\text{NN}}$ (model 2015) or infinite distances (model 2014). . . . .	71
5.7	Sm-V association energy difference between $x_{\text{NN}}$ and $1_{\text{NN}}$ for one oxygen vacancy and either one or two Sm dopants. . . . .	72
5.8	Model and DFT association energies with intuitive parameters. The jumping oxygen vacancy interacts with both dopants and vacancies. Both sublattices interact. Association energies around the moving oxygen vacancy up to $2_{\text{NN}}$ RE-V and $4_{\text{NN}}$ V-V (5.41 Å) are added up. Intuitive parameters are chosen for the extrapolated supercell according to Chapter 7.2 with the termination $E_{\text{ass}}(3_{\text{NN}} \text{ RE-V}) = 0$ and $E_{\text{ass}}(5_{\text{NN}} \text{ V-V}) = 0$ . Sm doped ceria in $3 \times 3 \times 3$ supercell. . . . .	73

5.9	Coordination numbers according to NMR <sup>[210–212]</sup> and XRD experiments <sup>[376]</sup> for Y doped ceria (left) and according to XRD experiments <sup>[377,378]</sup> for Gd doped ceria (right). For Gd doped ceria, Bevan <i>et al.</i> sintered the samples at 1600 °C and Nakamura <i>et al.</i> at 1450 °C. Additionally, MMC simulations according to the models 2014 <sup>[55]</sup> and 2015 are shown. . . . .	74
5.10	Coordination numbers for Sm doped ceria (left) according to XRD experiments <sup>[376]</sup> and MMC simulations for the models 2014 <sup>[55]</sup> and 2015 are shown. Additionally, MMC simulations for Y, Gd and Sm doped ceria according to the model 2015 are compared (right). . . . .	76
5.11	Radial Distribution Function at Ce(K)-edge of $\text{Ce}_{1-x}\text{Sm}_x\text{O}_{2-x/2}$ . . . . .	77
5.12	Coordination number of Ce-O for Sm doped ceria. XRD experiments according to Nakamura. <sup>[376]</sup> MMC simulations according to an earlier work. <sup>[55]</sup> . . . . .	78
5.13	Normalized X-Ray Absorption near the Sm(K)-edge (XANES) of $\text{Ce}_{1-x}\text{Sm}_x\text{O}_{2-x/2}$ . . . . .	79
5.14	Radial Distribution Function at Sm(K)-edge of $\text{Ce}_{1-x}\text{Sm}_x\text{O}_{2-x/2}$ . . . . .	80
5.15	Coordination number of Sm-O for Sm doped ceria. XRD experiments according to Nakamura. <sup>[376]</sup> MMC simulations according to an earlier work. <sup>[55]</sup> . . . . .	80
6.1	Possible migration edge configurations in samarium doped ceria. Ce-Ce edge (left), Ce-Sm edge (middle) and Sm-Sm edge (right). Cerium ions (green), samarium ions (blue), oxygen ions (red spheres) and oxygen vacancies (red boxes). . . . .	84
6.2	Phonon dispersions of the initial state $\text{V}_{\text{O}_1}^{\bullet\bullet} - \text{O}_{\text{O}_2}^{\times}$ (left, space group $P\bar{4}m2$ ) and the transition state $\text{V}_{\text{O}_1}^{\bullet\bullet} - \text{O}_{\text{TS}}'' - \text{V}_{\text{O}_2}^{\bullet\bullet}$ (right, space group $Pmmm$ ) in ceria according to Eq. 2.9. . . . .	85
6.3	Vibrational free energy difference $\Delta F_{\text{vib}}$ , vibrational energy difference $\Delta E_{\text{vib}}$ and entropy difference $\Delta S_{\text{vib}}$ of initial and transition state in ceria in harmonic approximation for a $6 \times 6 \times 6$ phonon mesh. For comparison $-k_{\text{B}}T$ is shown, which is similar to $\Delta E_{\text{vib}}$ . . . . .	85
6.4	Oxygen vacancy attempt frequency $\nu_0$ in ceria in harmonic approximation for different phonon mesh sizes. Lines are calculated using the Eyring method, squares are the results of the generalized Vineyard formula (Eq. 2.22). The dashed line shows the result according to the Eyring method without zero point energy (ZPE). . . . .	86
6.5	Phonon calculations for pure and Sm, Gd and Yb doped ceria in harmonic approximation calculated using the Vineyard method. . . . .	89
6.6	Migration energies (left) and attempt frequencies (right) in phonon supercells as a function of dopant fraction. . . . .	89

6.7	Oxygen vacancy attempt frequency $\nu_0$ in harmonic (squares) and quasi-harmonic approximation (circles) in samarium doped ceria with different number of dopants at the migration edge, using the generalized Vineyard method at a temperature of 900 K. For comparison also the results of the simple displacement approximation (triangles) are shown. . . . .	92
6.8	Oxygen vacancy attempt frequency $\nu_0$ in pure ceria in harmonic and quasi-harmonic approximation calculated using the Eyring (lines) and generalized Vineyard (squares) method at a temperature of 900 K at constant volume ( $V = \text{const.}$ ) and constant pressure ( $p = 0$ ). . . . .	92
6.9	Jump environment with a dopant in nearest neighborhood to the start position of the migrating oxygen vacancy (left). Cerium ions are green spheres, dopants are blue spheres, the oxygen ion is a red sphere and the oxygen vacancy is a red cube. On the right, the positions of the migrating oxygen vacancies are labeled start (s), center (c) and destination (d). . . . .	94
6.10	Attempt frequencies for Sm doped ceria with dopants at migration edge and in nearest neighborhood to the start position of the migrating oxygen vacancy. . . . .	94
6.11	Experimental (a) oxygen vacancy diffusion coefficients and (b) resulting attempt frequencies of pure ceria using bulk <sup>[315]</sup> and total <sup>[83,84,248,258-260]</sup> domain. Though experimental attempt frequencies vary over several orders of magnitude, all experiments are probably based on the same elemental frequency for a jump process. . . . .	98
6.12	The (a) ionic conductivity for the simple model and regression according to Eqs. 2.3 and 2.4. The fit parameters are the (b) apparent oxygen vacancy attempt frequency and (c) the apparent activation enthalpy. . . . .	103
6.13	The ionic conductivity for the simple model and regression (lines) according to Eqs. 2.3 and 2.4 between 500 and 700 K. The values for infinite temperatures were chosen according to an educated guess. . . . .	104
6.14	KMC simulations of the ionic conductivity for Sm doped ceria with fixed and varying attempt frequencies. Lines are a guide to the eye only. . . . .	106
6.15	KMC simulations of the ionic conductivity for Sm doped ceria at 500 °C with fixed and varying attempt frequencies. Experimental values according to Zhan <i>et al.</i> <sup>[74]</sup> and Sanghavi <i>et al.</i> <sup>[179]</sup> Lines are a guide to the eye only. . . . .	107
7.1	Examples of migration configurations including only the six nearest cation sites around a jump (6-cation environment). Cerium ions are green spheres, dopants are blue spheres, the oxygen ion is a red sphere and the oxygen vacancy is a red cube. .	110
7.2	Migration energy and widening of the edges cation distance for all jump configurations in the 6-cation environment. The widening is the difference of distances of the edges cations in transition and initial state. Confidence region (95 %) is shown. Y, Sm and Nd doped ceria, $2 \times 2 \times 2$ supercell. . . . .	112

7.3	Migration energy and widening of the edges cation distance for different jump configurations in the $3 \times 3 \times 3$ supercell. The widening is the difference of distances of the edges cations in transition and initial state. . . . .	113
7.4	Migration energy of a single oxygen vacancy in pure ceria as a function of used potential, lattice parameter and supercell size. The electronic energy difference at absolute zero is shown. Calculations are labeled with the used temperature-dependent experimental lattice parameters. . . . .	115
7.5	Migration energy in Sm doped ceria at different supercell sizes at constant volume. .	118
7.6	Migration energy of Ce-Ce, Ce-RE and RE-RE edge as a function of ionic radius. . .	119
7.7	Migration energy in Sm doped ceria at different supercell sizes at constant volume (lines) and pressure (dashed lines). . . . .	120
7.8	Migration energy with two oxygen vacancies at different supercell sizes. . . . .	121
7.9	Migration energies of an oxygen vacancy jump with an additional vacancy present. The repulsion between vacancies leads to low $E_{\text{mig}}$ 's for the detachment from the additional vacancy and high $E_{\text{mig}}$ 's if the additional vacancy is approached. For large distances the migration energy without an additional vacancy is approached, especially for larger supercell sizes. . . . .	122
7.10	DFT migration energies in $3 \times 3 \times 3$ supercell of ceria including two oxygen vacancies.	122
7.11	V-V association energy as a function of oxygen vacancy distance for an infinitely large supercell. Arrows show the differences between the jump for the approach and detachment of the additional vacancy. Black arrows are exact values, blue arrows are constructed by the termination $E_{\text{ass}}(5_{\text{NN}} \text{ V-V}) = 0$ . The V-V distances are based on the DFT lattice parameter. . . . .	123
7.12	Centers of Interaction: start (s), center (c) and destination (d) . . . . .	128
7.13	Cation sublattice around an oxygen ion jump. Oxygen ion (red sphere), oxygen vacancy (red box) and Cerium ions (all other spheres). Non-transparent ions with the same color possess the same distance to the migrating oxygen ion in either the initial or final state. . . . .	130
7.14	RE-V (green) and V-V interactions (red) that are considered, if spheres are expanded around the start, destination (up) or center position (down). All interactions are labeled according to their distance to the oxygen vacancy before and after the jump. For example, "1-1,2" refers to $1_{\text{NN}} \rightarrow 1_{\text{NN}}$ and $1_{\text{NN}} \rightarrow 2_{\text{NN}}$ jumps, while "1-4;2-3" refers to $1_{\text{NN}} \rightarrow 4_{\text{NN}}$ and $2_{\text{NN}} \rightarrow 3_{\text{NN}}$ jumps. . . . .	131
7.15	Migration energy model. . . . .	132
7.16	Migration energies in a $3 \times 3 \times 3$ supercell with a dopant and a migrating oxygen vacancy. . . . .	133

7.17 Migration energy for different number of dopants at the migration edge. Beside the migrating oxygen vacancy, no other defect is present. Sm and Y doped ceria in $3 \times 3 \times 3$ supercell. . . . .	135
7.18 Migration energy for different numbers of dopants at the migration edge with varying dopants in the 2 <sup>nd</sup> shell. $3 \times 3 \times 3$ supercell. . . . .	136
7.19 Migration energy for different numbers of dopants near the start ( $1_{NN} \leftrightarrow 2_{NN}$ ) or destination position ( $2_{NN} \leftrightarrow 1_{NN}$ ) of the migrating oxygen. No other defect is present. Sm and Y doped ceria in $3 \times 3 \times 3$ supercell. . . . .	137
7.20 Migration energy for different numbers of dopants near the <i>start</i> (upper row, $1_{NN} \leftrightarrow 2_{NN}$ ) and the <i>destination</i> position (lower row, $2_{NN} \leftrightarrow 1_{NN}$ ) of the migrating oxygen. Other defects are present. $3 \times 3 \times 3$ supercell. . . . .	138
7.21 RE-V (green) and V-V interactions (red). The asymmetric and symmetric influence of the $1_{NN} \leftrightarrow 2_{NN}$ jump is marked. . . . .	140
7.22 Initial and final state energy for an oxygen ion jump relative to the transition state energy. Sm (left) and Y doped ceria (right) in $3 \times 3 \times 3$ supercell. If only the difference between dopants near start and destination of the oxygen vacancy is relevant, all lines connecting initial and final state should intersect at TS. Lines are a guide to the eye only. . . . .	141
7.23 Migration energy for different numbers of dopants near <i>both</i> start and destination position ( $1_{NN} \leftrightarrow 2_{NN}$ and $2_{NN} \leftrightarrow 1_{NN}$ ) of the migrating oxygen. Other defects are present. $3 \times 3 \times 3$ supercell. . . . .	142
7.24 Model (see Table 7.7) and DFT migration energies for 6-cation environment with fitted (left) and intuitive parameters (right). The left and right graph use identical models with different parameter values. While the left graph indicates the quality of the model, the right graph illustrates how well the model can predict migration energies using only a few calculations. Intuitive parameters for the infinite supercell. DFT energies for Sm doped ceria in $3 \times 3 \times 3$ supercell. . . . .	146
7.25 $\bar{R}^2$ and standard derivation for different models in 6-cation environment. Sm doped ceria in $3 \times 3 \times 3$ supercell. . . . .	146
7.26 Model (see Table 7.7) and DFT migration energies for 6-cation environment with fitted (left) and intuitive parameters (right). Intuitive parameters for the infinite supercell. DFT energies for Y doped ceria in $3 \times 3 \times 3$ supercell. . . . .	148
7.27 $\bar{R}^2$ and standard derivation for different models in 6-cation environment. Y doped ceria in $3 \times 3 \times 3$ supercell. . . . .	148
7.28 4 parameters model (c1+sd [ds] up to $2_{NN}$ RE-V) for 6-cation environment. DFT migration energies in Sm doped ceria for the infinite large, $3 \times 3 \times 3$ and $2 \times 2 \times 2$ supercell as well as intuitive parameters chosen from the corresponding supercell size as described in the last section. . . . .	149

7.29	Semiempirical <sup>[282,283]</sup> and DFT migration energies in La doped ceria for the $4 \times 4 \times 4$ and $2 \times 2 \times 2$ supercell, respectively. The three selected interatomic potentials are labeled. <sup>[232,386,427]</sup> . . . . .	150
7.30	Migration energies according to Murray, <sup>[41]</sup> DFT and model migration energies. The models are based on intuitive parameters from the Murray migration energies in the 6-cation environment. Y doped ceria in $2 \times 2 \times 2$ supercell. . . . .	151
7.31	Migration energy for different numbers of dopants at the next nearest edge position ( $2_{NN} \leftrightarrow 2_{NN}$ ). Beside the migrating oxygen vacancy, no other defect is present. Sm and Y doped ceria in $3 \times 3 \times 3$ supercell. . . . .	152
7.32	Migration energy for different numbers of dopants at the $2_{NN} \leftrightarrow 3_{NN}$ and $2_{NN} \leftrightarrow 4_{NN}$ position. Beside the migrating oxygen vacancy, no other defect is present. Sm and Y doped ceria in $3 \times 3 \times 3$ supercell. . . . .	153
7.33	DFT and model migration energies. Intuitive parameters are chosen according to the model 2014 and 2015 as discussed above. Sm doped ceria in $3 \times 3 \times 3$ supercell. . . .	155
7.34	Model and DFT migration energies for jumps between $1, 2_{NN} \leftrightarrow 1, 2, 3, 4_{NN}$ cation shells with fitted (left) and intuitive parameters (right). Models <b>c1+sd</b> [ <b>ds</b> ] and <b>c1+c5+sd</b> [ <b>ds</b> ] with 4.48 Å RE-V interaction radius. Intuitive parameters for the infinite supercell according to model 2014 and 2015. DFT energies for Sm doped ceria in $3 \times 3 \times 3$ supercell. . . . .	155
7.35	Migration energy for different numbers of dopants at the $3_{NN} \leftrightarrow 4_{NN}$ and $3_{NN} \leftrightarrow 5_{NN}$ position. Beside the migrating oxygen vacancy, no other defect is present. Sm doped ceria in $3 \times 3 \times 3$ supercell. . . . .	156
7.36	Migration energy for different numbers of dopants. Beside the migrating oxygen vacancy, no other defect is present. Sm doped ceria in $3 \times 3 \times 3$ supercell. The range of the migration energy is marked on the right side. . . . .	158
7.37	Migration energy for different numbers of oxygen vacancies. The moving vacancy is included in the number of vacancies. No other defect is present. Lines show a linear fit. $3 \times 3 \times 3$ supercell. . . . .	159
7.38	Migration energy for different numbers of oxygen vacancies. The moving vacancy is included in the number of vacancies. No other defect is present. Points show DFT results for the $3 \times 3 \times 3$ supercell. Lines show model migration energies for linear scaling using the association energy from the extrapolated (left) and $3 \times 3 \times 3$ supercell (right).160	
7.39	$\bar{R}^2$ and standard derivation for different models (c1 is categorical). The jumping oxygen vacancy interacts with either dopants or vacancies. Jumps up to the 23 <sup>th</sup> shell (6.76 Å) are included. Sm doped ceria in $3 \times 3 \times 3$ supercell. . . . .	161

7.40	$\bar{R}^2$ for selected models (c1 is categorical). The jumping oxygen vacancy interacts with either dopants or vacancies. Jumps up to the 23 <sup>th</sup> shell (6.76 Å) are included. If a minimal number of parameters is desired, a model with a single symmetrical influence (c1) and an interaction radius of 5.41 Å is sufficient. Sm doped ceria in $3 \times 3 \times 3$ supercell.	162
7.41	$\bar{R}^2$ and standard derivation for different models (c1 is categorical). The jumping oxygen vacancy interacts with both dopants and vacancies. Both sublattices interact. Interactions up to the 13 <sup>th</sup> shell (5.41 Å) are included in the model. Sm doped ceria in $3 \times 3 \times 3$ supercell. . . . .	163
7.42	Model and DFT migration energies with fitted and intuitive parameters. The jumping oxygen vacancy interacts with both dopants and vacancies. Both sublattices interact. The model <b>c1+sd [ds]</b> up to the 13 <sup>th</sup> shell (5.41 Å) is used. Intuitive parameters are chosen for the infinite supercell as discussed above with the termination $E_{\text{ass}}(3_{\text{NN}} \text{ RE-V}) = 0$ and $E_{\text{ass}}(5_{\text{NN}} \text{ V-V}) = 0$ . A proportional behavior with a deviation of 0.1 eV is marked. Sm doped ceria in $3 \times 3 \times 3$ supercell. . . . .	164
7.43	Simulated ionic conductivity of Sm doped ceria at 500 °C (left) using different interaction radii as shown on the right for the RE-V (green) and V-V interaction (red). Around the jump center at most the first interaction is used with categorical scaling. Intuitive parameters are used as described above. . . . .	167
7.44	Association energies as intuitive model parameters as a function of interactions radius.	168
7.45	Simulated ionic conductivity of Sm doped ceria at 500 °C (left) using blocking, trapping and V-V interactions with an interaction radius of 5.41 Å as shown on the right for the RE-V (green) and V-V interaction (red). Additionally, interactions are switched off individually. . . . .	170
8.1	Ionic conductivity of $\text{Ce}_{0.85}\text{Sm}_{0.15}\text{O}_{1.925}$ at 173 °C based on MMC and KMC simulations as a function of cation equilibration temperature. The infinite cation equilibration temperature is marked with ‘inf’. . . . .	174
8.2	Ionic conductivity of bulk (left) and grain boundary domain (right) for different sintering temperatures after $t_{\text{sinter}} = 10$ h according to impedance experiments. . . . .	175
8.3	Ionic conductivity at 173 °C according to impedance experiments as a function of sintering temperature after $t_{\text{sinter}} = 10$ h (left) and for all measurements as a function of grain size (right). Lines are a guide to the eye only. . . . .	176
8.4	Grain boundary contribution to the resistivity according to impedance experiments as a function of measuring temperature (left) and grain size (right) for $\text{Ce}_{0.85}\text{Sm}_{0.15}\text{O}_{1.925}$ with data from [a] Wang <i>et al.</i> , <sup>[297]</sup> [b] Zhan <i>et al.</i> <sup>[300]</sup> and [c] Zhan <i>et al.</i> <sup>[74]</sup> Lines are a guide to the eye only. . . . .	177
8.5	Activation enthalpy according to impedance experiments as a function of sintering temperature for $t_{\text{sinter}} = 10$ h (left) and grain size (right). Lines are a guide to the eye only. . . . .	177

8.6	Conductivity at 267 °C and activation enthalpy according to impedance experiments as a function of grain size. Bulk and grain boundary (gb) domain is shown. Lines are a guide to the eye only. . . . .	179
8.7	Macroscopic and microscopic conductivity at 173 °C according to impedance experiments as well as grain boundary thickness for different grain sizes. Lines are a guide to the eye only. . . . .	180
8.8	Ionic conductivity of rare-earth doped ceria at 500 °C with RE = Lu, Yb, Y, Gd, Sm, Nd and La calculated using KMC simulations. Lines are a guide to the eye only. . .	181
8.9	Ionic conductivity of rare-earth doped ceria at 267 °C and 600 °C with RE = Lu, Yb, Y, Gd, Sm, Nd and La calculated using KMC simulations. Lines are a guide to the eye only. . . . .	182
8.10	Simulated and experimental ionic conductivity of $Ce_{1-x}RE_xO_{2-x/2}$ at 400 °C for $x = 0.1$ , and $0.2$ . The lines show a possible linear relationship between the ionic radius and the conductivity (solid lines) or the logarithm of the conductivity (dashed lines). . . . .	184
8.11	Simulated ionic conductivity of rare-earth doped ceria at 600 °C without considering RE-V interactions around the start and destination position (left) or without considering different migration edges (right). Lines are a guide to the eye only. . . .	186
8.12	Relationship between blocking and trapping and the simulated ionic conductivity for different dopants at 600 °C. A comparison between the Ce-RE migration edge energy (blocking) and the dopant fraction of the maximum (left) or the the RE-V association energy difference (trapping) and the ionic conductivity of the maximum (right) is shown. For comparison, interactions are switched off individually. Lines are a guide to the eye only. . . . .	189
8.13	Apparent attempt frequency (left) and activation enthalpy (right) for the simulated conductivity of rare-earth doped ceria at 500 °C and 600 °C. Lines are a guide to the eye only. . . . .	190
8.14	Apparent attempt frequency as a function of activation enthalpy for simulations at 500 °C and 600 °C (left). A fit according to Eq. 6.5 for infinite large temperature (constant attempt frequency) and 3000 K is shown. Experimental association energy calculated from the activation enthalpy difference between 500 °C and 600 °C as well as 267 °C and 500 °C (right). For comparison, a 80 % confidence interval of a linear fit is shown. . . . .	191
8.15	Arrhenius behavior of the ionic conductivity in $Ce_{1-x}Sm_xO_{2-x/2}$ according to impedance experiments. . . . .	194
8.16	Ionic conductivity of Sm doped ceria according to impedance experiments. Lines are a guide to the eye only. . . . .	195

---

8.17	Experimental attempt frequency (left) and activation enthalpy (right) of Sm doped ceria for all temperatures (solid symbols) or low and high temperatures according to impedance experiments. Lines are a guide to the eye only. . . . .	195
8.18	Total ionic conductivity of polycrystalline Sm and Gd doped ceria according to experiments at 600 °C. Lines are a guide to the eye only. . . . .	196
8.19	Bulk ionic conductivity of Sm <sup>[74,166,169–172,179–181]</sup> and Gd doped ceria <sup>[64,86,166,169–177]</sup> according to experiments at 500 °C. Fourth order polynomials were fitted to the data with exception of the data of Zajac and Molenda to show the general trend of the data (dashed lines) other Lines are a guide to the eye only. . . . .	197
8.20	Bulk ionic conductivity of Sm and Gd doped ceria according to impedance experiments. <sup>[64,74,163,166,179,185]</sup> . . . . .	198
8.21	Grain boundary (left) and total ionic conductivity (right) of Sm and Gd doped ceria according to experiments. <sup>[64,74,156,161,185,317]</sup> . . . . .	199
8.22	Experimental attempt frequency (left) and activation enthalpy (right) for different domains of Sm and Gd doped ceria according to experiments. Lines are a guide to the eye only. . . . .	200
8.23	Ionic conductivity for the bulk domain of Sm-Zr doped ceria according to impedance experiments. Both, polycrystalline samples and agglomerates of single crystals are investigated. Doping with Zr decreases the conductivity. . . . .	202
8.24	Macroscopic grain boundary (left) and total (right) conductivity of Sm-Zr doped ceria according to impedance experiments. Both, polycrystalline samples and agglomerates of single crystals are investigated. . . . .	203
8.25	Ionic conductivity for the bulk, grain boundary and total domain of Gd-Zr doped ceria according to impedance experiments. Both, polycrystalline samples and agglomerates of single crystals are investigated. . . . .	204
8.26	Arrhenius behavior of the bulk conductivity in $Ce_{1-x}Lu_xO_{2-x/2}$ according to experiments by Dück <sup>[295]</sup> in comparison with literature. <sup>[165,166]</sup> . . . . .	205
8.27	Arrhenius behavior of the macroscopic grain boundary (left) and total conductivity (right) in $Ce_{1-x}Lu_xO_{2-x/2}$ according to experiments by Dück <sup>[295]</sup> in comparison with literature. <sup>[62]</sup> . . . . .	205
8.28	Ionic conductivity of bulk domain in Lu doped ceria according to experiments by Dück. <sup>[295]</sup> Lines are a guide to the eye only. . . . .	206
8.29	Macroscopic ionic conductivity of grain boundary domain according to experiments by Dück (left) <sup>[295]</sup> and total conductivity (right) in Lu doped ceria. Lines are a guide to the eye only. . . . .	207
8.30	Experimental attempt frequency (left) and activation enthalpy (right) of Lu doped ceria according to impedance experiments. Lines are a guide to the eye only. . . . .	207

8.31	Simulated ionic conductivity of rare-earth doped ceria at 267 °C and 368 °C with RE = Lu, Gd and Sm. In comparison, ionic conductivities according to impedance experiments are shown. Lines are a guide to the eye only. . . . .	208
8.32	Degradation of the ionic conductivity of the bulk domain of Ce <sub>0.8</sub> Sm <sub>0.2</sub> O <sub>1.9</sub> at 500 K as a function of equilibration time at 800 K according to impedance experiments. . .	210
8.33	Ionic conductivity of bulk domain in Ce <sub>0.8</sub> Sm <sub>0.2</sub> O <sub>1.9</sub> at 500 K as a function of equilibration time at 800 K according to impedance experiments. . . . .	211
9.1	Calculating the dopant fraction in RE <sub>1</sub> O <sub>1.5</sub> mol% and RE <sub>2</sub> O <sub>3</sub> mol%. . . . .	241
9.2	Radial Distribution Function at Ce(K)-edge of Ce <sub>0.8</sub> RE <sub>0.2</sub> O <sub>1.9</sub> . . . . .	241
9.3	Radial Distribution Function at RE(K)-edge of Ce <sub>0.8</sub> RE <sub>0.2</sub> O <sub>1.9</sub> . . . . .	242
9.4	Oxygen vacancy diffusion coefficient (above), apparent attempt frequency (left) and activation enthalpy (right) for the conductivity of simulated rare-earth doped ceria. ‘high trapping/blocking’ refers to a virtual material with possess association energies according to Sc and migration edges according to La. Lines are a guide to the eye only.	243
9.5	Apparent attempt frequency (left) and activation enthalpy (right) for the conductivity of simulated Sm doped ceria using different microscopic attempt frequencies between 500 °C and 1100 °C. Lines are a guide to the eye only. . . . .	243
9.6	Migration energy of Ce-RE edge at different supercell sizes. . . . .	244
9.7	Migration energy of RE-RE edge at different supercell sizes. . . . .	244
9.8	Model (4, 5 and 30 parameters model) and DFT migration energies for 6-cation environment with intuitive parameters for the infinite large or 3 × 3 × 3 supercell. DFT energies for Sm doped ceria in 3 × 3 × 3 supercell. . . . .	245
9.9	Model and DFT migration energies with fitted parameters. The jumping oxygen vacancy interacts with either dopants and vacancies. Both sublattices do not interact. The model c1+vn [vn] up to the 13 <sup>th</sup> shell (5.41 Å) is used. Sm doped ceria in 3 × 3 × 3 supercell. . . . .	245
9.10	Model and DFT migration energies with fitted parameters. The jumping oxygen vacancy interacts with both dopants and vacancies. Both sublattices interact. The model c1+vn [vn] up to the 13 <sup>th</sup> shell (5.41 Å) is used. Sm doped ceria in 3 × 3 × 3 supercell.	246
9.11	Ionic conductivity of rare-earth doped ceria at 500 °C with RE = Lu, Yb, Y, Gd, Sm, Nd and La. . . . .	246
9.12	Bulk ionic conductivity at 500 °C in KMC simulation in this work (lines) and experiments (dots) for Lu, <sup>[165,166]</sup> Yb, <sup>[166]</sup> Er, <sup>[166]</sup> Y, <sup>[163,166–172]</sup> Dy, <sup>[166]</sup> Tb, <sup>[71]</sup> Gd, <sup>[64,86,166,169–177]</sup> Eu, <sup>[71,178]</sup> Sm, <sup>[74,166,169–172,179–181]</sup> Nd <sup>[75,76,166,170,182,183]</sup> and La doped ceria. <sup>[169]</sup> Forth order polynomials were fitted to the data with exception of the data of Zajac and Molenda to show the general trend of the data (dashed lines).	247

---

9.13	Calculated ionic conductivity of rare-earth doped ceria at 500 °C without considering RE-V interactions around the start and destination position (left) or without considering different migration edges (right). Lines are a guide to the eye only. . . .	248
9.14	Activation enthalpy in KMC simulation in this work (lines) and experiments between room temperature and 330 °C (dashed lines) <sup>[163]</sup> or higher temperatures up to 1000 °C (dashes) for Lu, <sup>[165,166]</sup> Yb, <sup>[166]</sup> Er, <sup>[166]</sup> Y, <sup>[166–170,180]</sup> Dy, <sup>[69,166]</sup> Gd, <sup>[64,166,168–170,173,174,176]</sup> Eu, <sup>[178]</sup> Sm, <sup>[74,166,170,180,195]</sup> Nd <sup>[76,166,170,182,183]</sup> and La doped ceria. <sup>[169]</sup> . . . . .	249
9.17	Apparent attempt frequency (left) and activation enthalpy (right) for the conductivity of simulated rare-earth doped ceria for the temperatures 267 °C and 500 °C and between 500 °C and 600 °C. Lines are a guide to the eye only. . . . .	249
9.15	Calculated activation enthalpy between 500 °C and 600 °C. All interactions are used (middle) or either RE-V interactions around the start and destination position (left) or different migration edges (right) are neglected. Lines are a guide to the eye only. .	250
9.16	Apparent attempt frequency between 500 °C and 600 °C. All interactions are used (middle) or either RE-V interactions around the start and destination position (left) or different migration edges (right) are neglected. Lines are a guide to the eye only. .	251
9.18	Apparent experimental attempt frequency from impedance spectroscopy experiments for stoichiometric or non-stoichiometric ceria, <sup>[83,315]</sup> Yb, <sup>[163]</sup> Y, <sup>[163,167,180,407]</sup> Gd, <sup>[163]</sup> Sm, <sup>[74,180]</sup> Nd <sup>[163]</sup> and La doped ceria. <sup>[163]</sup> Lines are a guide to the eye only. . . . .	252
9.19	Examples for two favored migration paths in yttrium doped ceria according to earlier work. <sup>[55]</sup> The favored migration path of the oxygen is depicted as red line. On the left side there are similar adjacent migration edges while on the right side there are alternating migration edges. Cerium ions (green), yttrium ions (blue) and oxygen ions (red). . . . .	252



# List of Tables

2.1	Dopant fractions that lead to the highest total ionic conductivity for polycrystalline $\text{Ce}_{1-x_{\max}}\text{Sm}_{x_{\max}}\text{O}_{2-x_{\max}/2}$ samples in the measured temperature range. . . . .	19
2.2	Dopant fractions that lead to the highest <i>total</i> ionic conductivity for $\text{Ce}_{1-x_{\max}}\text{RE}_{x_{\max}}\text{O}_{2-x_{\max}/2}$ samples in the measured temperature range. . . . .	24
2.3	Dopant fractions that lead to the highest <i>bulk</i> ionic conductivity for $\text{Ce}_{1-x_{\max}}\text{RE}_{x_{\max}}\text{O}_{2-x_{\max}/2}$ samples in the measured temperature range. . . . .	26
4.1	Samples investigated by EXAFS. . . . .	50
6.1	Electronic migration energies for different migration configurations (Eq. 2.10), distances of the edge cations in the initial and the transition state and oxygen vacancy attempt frequencies $\nu_0(V,T)$ (Vineyard, Eq. 2.22) at constant volume ( $V = \text{const.}$ ) .	87
6.2	Electronic migration energies for different migration configurations, distances of the edge cations in the initial and the transition state and oxygen vacancy attempt frequencies $\nu_0(V,T)$ (Vineyard) at constant volume ( $V = \text{const.}$ ) . . . . .	88
6.3	Electronic migration energies for different migration configurations, changes in volume between transition state and initial state $\Delta V$ and oxygen vacancy attempt frequencies $\nu_0(p,T)$ (Vineyard) at constant pressure ( $p = 0$ ) and 900 K . . . . .	91
6.4	Electronic migration energies for different migration configurations, changes in volume between transition state and initial state $\Delta V$ and oxygen vacancy attempt frequencies $\nu_0(p,T)$ (Vineyard) at constant pressure ( $p = 0$ ) and 900 K . . . . .	93
6.5	Electronic migration energies for different migration configurations, distances of the edge cations in the initial and the transition state and oxygen vacancy attempt frequencies $\nu_0(V,T)$ (Vineyard) at constant volume ( $V = \text{const.}$ ) . . . . .	95
6.6	Electronic migration energies for different migration configurations, changes in volume between transition state and initial state $\Delta V$ and oxygen vacancy attempt frequencies $\nu_0(p,T)$ (Vineyard) at constant pressure ( $p = 0$ ) . . . . .	95

6.7	Experimental oxygen vacancy attempt frequency $\bar{\nu}_{\text{exp},V_{\text{O}}^{\bullet\bullet}}$ of pure ceria for polycrystalline samples (poly) and single crystals (sc) calculated based on impedance spectroscopy (AC), direct current (DC), Secondary Ion Mass Spectrometry (SIMS) and Gas Phase Analysis (GPA) measurements. The number of charge carriers is based on the purity (hp = high, lp = low) of the starting material or the non-stoichiometry for [a] $\text{CeO}_{1.992}$ and [b] $\text{CeO}_{1.96}$ . The error of the attempt frequency is given according to the linear regression. . . . .	96
7.1	Electronic migration energies for different migration configurations and distances of the edge cations in the initial and the transition state for the $2 \times 2 \times 2$ supercell at constant volume. . . . .	111
7.2	Electronic migration energies for different migration configurations and distances of the edge cations in the initial and the transition state for the $3 \times 3 \times 3$ supercell at constant volume. . . . .	113
7.3	Calculated migration energy in pure ceria according to literature. . . . .	114
7.4	Calculated migration energy in pure ceria. The supercell extrapolated to infinite volume is called ‘inf’. . . . .	115
7.5	Experimental activation enthalpy $\Delta H_a$ of pure ceria for polycrystalline samples (poly) and single crystals (sc) calculated based on impedance spectroscopy (AC), direct current (DC), Secondary Ion Mass Spectrometry (SIMS) and Gas Phase Analysis (GPA) measurements. The number of charge carriers is chosen constant for all temperatures as discussed in Chapter 6.3. Samples differ in purity (hp = high, lp = low) or non-stoichiometry with [a] $\text{CeO}_{1.992}$ and [b] $\text{CeO}_{1.96}$ . . . . .	116
7.6	Experimental activation enthalpy $\Delta H_a$ of lightly Y doped ceria for the bulk of polycrystalline samples calculated based on $^{17}\text{O}$ -NMR lattice relaxation, dielectric relaxation and impedance spectroscopy (AC) measurements. . . . .	117
7.7	Migration energy models for 6-cation environment including start and destination equally. . . . .	144
7.8	Number of parameters of migration energy models for 6-cation environment. . . . .	145
9.1	Fit results of the EXAFS data of $\text{Ce}_{1-x}\text{Sm}_x\text{O}_{2-x/2}$ at the Ce-edge. The amplitude $amp_i$ and the distance to the scattering ion $R_i$ is shown. . . . .	242